Transport Properties of Flow over Spatially Non-Uniform Boundary Conditions

Zur Erlangung des akademischen Grades eines

Doktors der Ingenieurwissenschaften (Dr.-Ing.)

von der KIT-Fakultät für
Maschinenbau
des Karlsruher Instituts für Technologie (KIT)

angenommene

Dissertation

von

M.Sc. Jonathan Neuhauser

Tag der mündlichen Prüfung:	20.07.2026
Hauptreferentin:	Prof. Dr.-Ing. Bettina Frohnapfel
Korreferenten:	Prof. Dr.-Ing. Thomas Wetzel
	Prof. Luca Marocco

Abstract

Many flows of engineering and geophysical interest occur in the vicinity of solid walls, which exchange momentum and heat with the fluid. Under canonical conditions, engineering correlations for global momentum and heat transfer exist for a wide range of parameters. Spatially inhomogeneous boundary conditions, such as non-uniform surface roughness or non-uniform heat flux, present an engineering challenge, because existing correlations are not readily applicable and high-quality reference data are rare.

This work aims to improve the understanding of heat and momentum transport over non-uniform boundary conditions. Two related configurations are considered: turbulent channel flow over streamwise-aligned roughness strips, and pipe flow subject to azimuthally non-uniform heat flux. Starting from a detailed analysis of the governing equations, novel relationships for the global transport properties are derived analytically. In particular, it is shown that the global heat transfer (characterised by the Nusselt number) is independent of the azimuthal variation of the wall heat flux, assuming temperature variations are small (i.e. buoyancy effects are negligible). Furthermore, an analytical relationship for the skin friction coefficient of inhomogeneous surface conditions is obtained in the limit of large homogeneous patches.

The theoretical analysis is complemented by well-resolved numerical simulations for both configurations. For channel flow over streamwise-aligned ridges, a wall boundary condition is developed to mimic the influence of roughness on the turbulent flow while maintaining scale separation between roughness elements and the mean flow. The spatial development of the resulting flow topology is investigated to elucidate the link between global drag, the spanwise distribution of streamwise momentum, and turbulent secondary motions. For turbulent pipe flow with azimuthally varying heat flux, a well-resolved numerical database is generated that covers two Prandtl numbers ($\mathrm{Pr} \in \{0.025, 0.71\}$) and two bulk Reynolds numbers ($\mathrm{Re}_b \in \{5300, 19000\}$), including the thermal inlet region and conjugate heat transfer. The impact of the azimuthal wavelength of the boundary condition on mean temperature statistics is examined in detail, and parallels between the two configurations are highlighted.

Kurzfassung

Strömungen von technischem oder geophysikalischem Interesse befinden sich häufig in der Nähe fester Wände, mit denen die Strömung Impuls und Wärme austauscht. In wohldefinierten Standardgeometrien sind Korrelationen für den globalen Wärme- und Impulstransfer für einen großen Parameterbereich bekannt. Räumlich inhomogene Randbedingungen, wie etwa ungleichmäßige Oberflächenrauheit oder ungleichmäßiger Wärmestrom, stellen aus technischer Sicht eine Herausforderung dar, weil bestehende Korrelationen nicht direkt anwendbar sind und qualitativ hochwertige Referenzdaten fehlen.

Diese Arbeit trägt dazu bei, das Verständnis der Wärme- und Impulsübertragung von Strömungen über räumlich variierende Randbedingungen zu verbessern. Zwei verwandte Konfigurationen werden betrachtet: turbulente Kanalströmungen über in Strömungsrichtung ausgerichteten Rauheitsstreifen und Rohrströmung mit in Umfangsrichtung ungleichförmigem Wärmestrom. Ausgehend von einer detaillierten Analyse der Grundgleichungen werden neuartige Beziehungen für die globalen Transporteigenschaften analytisch hergeleitet. Im Besonderen wird gezeigt, dass die globale Wärmeübertragung, quantifiziert durch die Nusselt-Zahl, unabhängig von der Verteilung des Wärmestroms über den Umfang ist – unter der Annahme, dass die Temperaturdifferenzen klein genug sind, um Auftriebseffekte vernachlässigen zu können. Weiterhin wird eine analytische Beziehung für den Reibungsbeiwert über inhomogenen Oberflächen für den Grenzfall sehr großer homogener Wandabschnitte hergeleitet.

Für beide Konfigurationen wird die theoretische Analyse durch hochaufgelöste numerische Simulationen ergänzt. Für eine Kanalströmung über in Strömungsrichtung ausgerichteten Rauheitsstreifen wird eine effektive Randbedingung für die Wand entwickelt, die den Einfluss der Wandrauheit auf die Turbulenz abbilden kann und gleichzeitig die Skalentrennung zwischen mittlerer Strömung und Rauheitselementen aufrechterhält. Die räumliche Entwicklung der Strömungstopologie wird untersucht, um den Zusammenhang zwischen globaler Reibung, der spannweitigen Verteilung des Impulses in Strömungsrichtung und der entstehenden turbulenten Sekundärströmung

besser zu verstehen. Für eine turbulente Rohrströmung mit in Umfangsrichtung variablem Wärmestrom wird eine numerische Datenbank erstellt, die zwei Prandtl-Zahlen ($\mathrm{Pr} \in \{0.025, 0.71\}$) und zwei Reynolds-Zahlen ($\mathrm{Re}_b \in \{5300, 19000\}$) umfasst und außerdem den Effekt des thermischen Einlaufs sowie die konjugierte Wärmeübertragung berücksichtigt. Der Einfluss der Wellenlänge der Randbedingung in Umfangsrichtung auf die mittleren Temperaturstatistiken wird detailliert untersucht, und Parallelen zwischen beiden Konfigurationen werden aufgezeigt.

Acknowledgements

To Bettina and Davide. Your great teaching made me join the ISTM crew as a student after my 3rd semester of studies, the welcoming atmosphere you created kept me hooked during my under- and postgraduate studies and the scientific exchange with you helped me grow into the researcher I am today.

To my collaborators Carola, Jan-Henrik, Jonathan, Kay, Leo, and Luca; and the master students I had the pleasure to co-supervise over the years.

To all my colleagues at ISTM for the supporting and friendly environment everyone of you contributes to, every day.

To Prof. Sergio Pirozzoli for many inspiring discussions during my research stay in Rome.

To my family.

This work was supported by the German Research Foundation (DFG) under research project 423710075.

Simulations in chapter 3 were performed on BWUniCluster 2.0. The author acknowledges support by the state of Baden-Württemberg through bwHPC.

Simulations in chapter 4 were performed on the national supercomputer HPE Cray EX4000 Hunter at the High Performance Computing Center Stuttgart (HLRS) under the grant number `ctbctpf`.

The research stay at University La Sapienza Rome (Prof. Pirozzoli) was funded by Karlsruhe House of Young Scientists (KHYS).

Note on AI Use. GPT 5.1 by OpenAI has been used for selective stylistic improvement of the language throughout the thesis.

List of Publications

The content of the thesis is based on the following references published during the PhD study. In particular, results from the publications *Simulation of Turbulent Flow over Roughness Strips* [NSGF22b], *Predicting the Global Drag of Turbulent Channel Flow over Roughness Strips* [NSGF25], *Solution of the Extended Graetz Problem for Nonuniform Heat Flux* [NMGF25], and *Thermal Entry Effects in Turbulent Pipe Flows* [NGF26] are presented and direct quotations from these publications are indicated with a vertical line in the page's margin. At the end of the quoted section, the source article is indicated; the quoted section may span multiple pages. Major omissions from and additions to the quoted content are indicated with [...] or [in brackets]. The nomenclature of the quoted content is silently adapted to the remainder of the dissertation. Minor typographical or language adjustments are made without indication. The plural form of the pronoun referring to the authors is preserved.

Results preliminary to chapter 4, particularly the parts pertaining to turbulent flows, have been presented in the conference contributions [NS+24]; [NM+25]; [NBGF25].

The publication [NSGF22b] is based on preliminary results obtained during the author's own master thesis.

The contribution of the co-authors of the publications is highly acknowledged.

Peer-reviewed journal publications

[NSGF22b] J. Neuhauser, K. Schäfer, D. Gatti, and B. Frohnapfel (2022b). "Simulation of Turbulent Flow over Roughness Strips". In: *Journal of Fluid Mechanics* 945, A14.

[NMGF25] J. Neuhauser, J.-H. Metsch, D. Gatti, and B. Frohnapfel (2025c). "Solution of the Extended Graetz Problem for Nonuniform Heat Flux". In: *International Journal of Heat and Mass Transfer* 249, p. 127198.

[NSGF25] J. Neuhauser, C. Schmidt, D. Gatti, and B. Frohnapfel (2025d). “Predicting the Global Drag of Turbulent Channel Flow over Roughness Strips”. In: *International Journal of Heat and Fluid Flow* 115, p. 109848.

Conference contributions

[NSGF22c] J. Neuhauser, K. Schäfer, D. Gatti, and B. Frohnapfel (2022c). “Slip-Type Boundary Conditions for Turbulent Flows over Heterogeneous Roughness”. In: *Proceedings of the 12th International Symposium on Turbulence and Shear Flow Phenomena*.

[NGSF24] J. Neuhauser, D. Gatti, C. Schmidt, and B. Frohnapfel (2024a). “Predicting the Global Drag of Turbulent Channel Flow over Roughness Strips”. In: *Proceedings of the 13th International Symposium on Turbulence and Shear Flow Phenomena*.

[NS+24] J. Neuhauser, J. Schmitt, D. Gatti, L. Marocco, and B. Frohnapfel (2024b). “Conjugate Heat Transfer in Turbulent Liquid Metal Flows in Pipes”. In: 1st European Fluid Dynamics Conference.

[NBGF25] J. Neuhauser, L. Bürk, D. Gatti, and B. Frohnapfel (2025a). “Non-Uniform Heating Effects in Thermally Developing Turbulent Pipe Flows”. In: *Progress in Turbulence XI*. iTi Conference on Turbulence. Peer-reviewed conference proceeding.

[NM+25] J. Neuhauser, J.-H. Metsch, L. Bürk, D. Gatti, and B. Frohnapfel (2025b). “Thermal Entrance Region of Laminar and Turbulent Pipe Flows Subject to Nonuniform Heating”. In: 2nd European Fluid Dynamics Conference.

[NGF26] J. Neuhauser, D. Gatti, and B. Frohnapfel (2026). “Thermal Entry Effects in Turbulent Pipe Flows”. In: *Proceedings of the 14th International Symposium on Turbulence and Shear Flow Phenomena*.

Only first-author publications and conference contributions related to the thesis’ contents are listed above.

Datasets

J. Neuhauser, K. Schäfer, D. Gatti, and B. Frohnapfel (2022a). *Dataset: Simulation of Turbulent Flow over Roughness Strips*. KITopen.

J. Neuhauser (2025). *Analytical Solutions of the Laminar (Extended) Graetz Problem*. GitHub repository. GitHub. URL: https://github.com/joneuhauser/graetz (visited on 05/05/2026).
– (2026a). *Dataset: Conjugate Heat Transfer in Turbulent Pipe Flows with Non-Uniform Heating Effects at Two Prandtl Numbers*. Karlsruhe Institute of Technology.
– (2026b). *Dataset: Developing Turbulent Secondary Flow over Streamwise-Aligned Roughness Strips*. Karlsruhe Institute of Technology.
– (2026c). *Dataset: Simulation of the Turbulent Graetz Problem with Neumann Boundary Conditions at Two Reynolds and Prandtl Numbers*. Karlsruhe Institute of Technology.

Contents

1

Introduction

1.1 Motivation

Many technical and environmental flows are turbulent and bounded by solid surfaces (walls), where momentum (via friction and pressure forces) and heat are transported between fluid and wall. For a number of canonical wall-bounded flows, such as single-phase flow between infinitely long parallel smooth plates (plane channel flow) or in a long circular pipe, the associated heat and momentum transport properties are well characterised by experimental and numerical data. In most practical situations, however, the boundary conditions (e.g. surface roughness, elevation, wall heat flux, or temperature) vary in space. Introducing such spatial non-uniformity modifies the velocity and temperature fields and thus the transport properties of the system. This thesis focuses on such flows with non-uniform boundary conditions.

To make this general problem of spatially varying boundary conditions more tractable, this thesis focuses on two simplified settings: flow over spatially varying roughness, and passive-scalar transfer in flows subject to spatially non-uniform wall heat flux.

Flow over rough walls has a long research history in fluid mechanics. Examples include internal flows in pipes with deposits or corrosion, ice accretion on wings, river flows over natural beds, and the atmospheric boundary layer over heterogeneous terrain (e.g. desert, forest, or urban canopy). Even for *homogeneous* rough walls, the interaction between turbulence and the surface geometry remains an area of active research. When the roughness varies in the streamwise or spanwise directions (see fig. 1.1 for illustration), additional phenomena arise, such as internal boundary layers

(a) Spatially non-uniform corrosion in a gas pipeline. Image: Ghorbani and Zadeh (2020), reproduced with the authors' permission.

(b) Spatially inhomogeneous surface properties in the Fanny-Hensel-Anlage in Karlsruhe-Mühlburg. The primary wind direction roughly aligns with the park's axis. Image: Tim Carmele for KA-News, reproduced with the photographer's permission.

Figure 1.1: Examples for flows over spatially non-uniform roughness.

and turbulent secondary motions (mean transport perpendicular to the primary flow direction). The global transport properties (such as drag) of such composite surfaces must be understood for engineering design and for parameterisations in, for example, climate models.

Most existing rough-wall models and correlations are calibrated using data from uniformly driven flow over surfaces that feature small-scale inhomogeneity, but are homogeneous on the large scale (i.e. effectively the same roughness everywhere). As a result, such models cannot reliably predict the overall drag and mean-flow organisation over non-uniform rough surfaces. The first class of problems addressed in this thesis therefore concerns plane channel flow over rough walls featuring macroscopic inhomogeneity in both the streamwise and spanwise directions.

Flows with non-uniform thermal boundary conditions are also an established subject. In practice, it is difficult to find a heat-transfer device in which the wall temperature or heat flux is uniform: heaters and coolers often have strong spatial variations owing to non-uniform heating elements or radiation. Classical work in this area goes back to Graetz (1882) on the thermal inlet problem that now bears his name. There, a streamwise change of the wall boundary condition creates a developing region where convection and diffusion are out of balance and the mean temperature field evolves in the streamwise direction until the global heat-transfer properties (such as Nusselt number) no longer change with streamwise position, at least asymptotically.

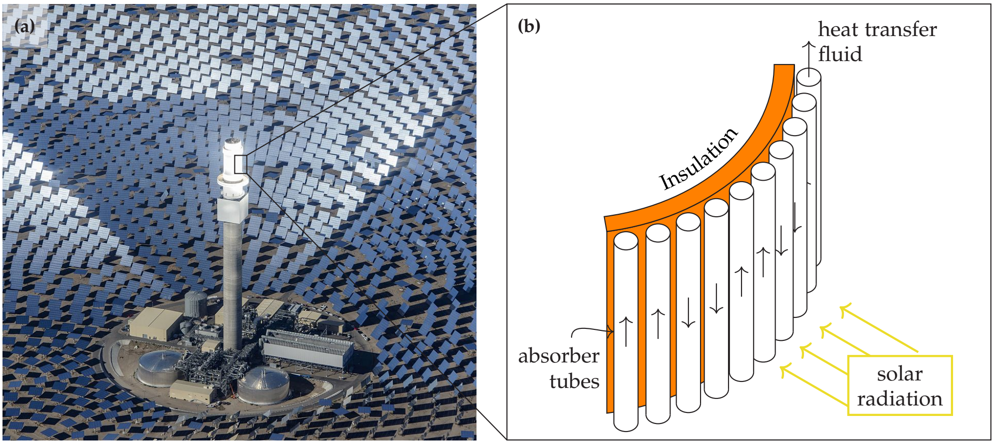

Figure 1.2: (a) Aerial photo of the Crescent Dunes solar power plant in Nevada, United States. Image by user Marygrikas on Wikimedia (CC-BY-SA 4.0). (b) Sketch of the receiver surface. A heat transfer fluid flows through the absorber tubes, which are heated by the solar radiation from one side. The flow direction may change between pipes.

Non-uniformity in the *cross-stream* direction, such as azimuthal heat flux variations in pipe flow, was first analysed in the 1960s under thermally fully developed conditions and has recently received renewed attention in the context of concentrated solar power (CSP, X. Yang et al. (2012)), where concentrated solar irradiation heats only part of the circumference of the absorber pipes within the central receiver (see fig. 1.2). In such flows, local heat-transfer characteristics (e.g. the Nusselt number) become position-dependent, and their accurate prediction is essential for thermal design.

Standard correlations for heat transfer typically assume uniform wall temperature or uniform heat flux, and the errors associated with applying them to conditions where the wall heat flux varies strongly in the cross-stream direction are unknown. The second class of problems addressed in this thesis thus concerns pipe flow with streamwise- and azimuthally varying heat flux, motivated in part by solar receiver applications.

Both of these configurations – turbulent channel flow over inhomogeneous rough walls and turbulent pipe flow with non-uniform wall heat flux – are examples of flows with spatially varying boundary conditions in which global drag and heat transfer are not yet well understood.

The next section reviews the current state of knowledge on these two classes of problems, after which the methodological framework and high-level objectives of the thesis are stated. Following a brief introduction of the governing equations and numerical methods in chapter 2, chapter 3 discusses momentum transfer in channel flow, and chapter 4 deals with heat transfer in pipe flow. Finally, chapter 5 ties the results from both geometries together.

1.2 State of the art

1.2.1 Flow over spatially non-uniform roughness

Drag predictions for flows over rough surfaces rely on the prescription of a homogeneous roughness length scale, i.e. an equivalent sand grain roughness k_s. This quantity can be obtained empirically from drag measurements (physical experiments or numerical experiments based on direct numerical simulations, DNS), through existing correlations with statistical surface properties (Chung et al. 2021) or recently also based on data-driven approaches (S. Lee et al. 2022; J. Yang et al. 2023). All approaches rely on reference data in form of Nikuradse-type curves, i.e. a friction coefficient (e.g. C_f) as a function of Reynolds number.

[NSGF25] For rough surfaces whose roughness properties vary in space, there is no common understanding of how to predict the resulting global drag, and reference data are scarce.

Heterogeneous surface roughness is typically studied using idealised model problems. These model problems can be broadly categorised according to whether the surface properties vary primarily in the streamwise or in the spanwise direction, and they have been investigated in various canonical flow configurations (plane and open channel flows, as well as boundary layers).

Streamwise heterogeneity of the surface. Streamwise-varying roughness has mainly been studied through smooth-to-rough and rough-to-smooth surface transitions and the associated downstream relaxation towards a new fully developed state (Elliott 1958; Rouhi et al. 2019). For shorter streamwise length scales of the surface variations, configurations such as smooth-rough-smooth transitions (Jacobi and McKeon 2011) and periodically spaced, spanwise-aligned roughness elements (S.-H. Lee and Sung 2007; Ismail et al. 2018) have been considered. These flows are characterised by the formation of internal layers and transient responses of the wall shear stress, including overshoots (for smooth-to-rough) and undershoots (for rough-to-smooth) relative to their fully developed rough- or smooth-wall values.

Since the concept of *fully developed* flow – and deviations from it – is central to this thesis, it requires a more careful introduction. A flow is said to be fully developed (in the streamwise direction, which is implied) if it can be described by a set of key statistical quantities – such as mean profiles, mean fluxes, or turbulence statistics – that are invariant in the streamwise direction, possibly after an appropriate rescaling.

In statistically homogeneous rough-wall channels or pipes, a fully developed flow in this sense has statistics and associated viscous and turbulent momentum fluxes that are constant along the streamwise direction, while, for example, the pressure varies linearly. Consequently, the face-normal momentum fluxes through the streamwise faces of a suitably chosen control volume cancel out. Classical equilibrium boundary layers exhibit analogous behaviour after a similarity rescaling of the profiles.

In the thermally fully developed state of a pipe subject to uniform wall heat flux, the molecular and turbulent axial heat fluxes are invariant along the streamwise direction, while the mean temperature field varies linearly. Again, the face-normal heat fluxes through the streamwise faces of a suitably chosen control volume cancel out. In some cases, rescaling is necessary for this definition as well, as for conditions sufficiently far downstream of a step change in wall temperature.

Relatedly, the flow is said to be in *local equilibrium* with the wall properties or boundary condition if the statistics at a given wall location are identical to those of a fully developed flow above a spatially uniform boundary condition with the same local properties. If a non-uniform boundary condition varies on length scales much greater than the outer scale of the flow, it is natural to assume that fields governed by a convective–diffusive equation attain local equilibrium sufficiently far away from where the boundary condition changes.

Spanwise heterogeneity of the surface. Problems in the second category, i.e. spanwise-heterogeneous roughness, have been studied since Hinze (1967). Two model problems are typically discussed: strip-type and ridge-type roughness (Colombini and Parker 1995; Wang and Cheng 2006). Strip-type roughness features lateral heterogeneity via longitudinal strips of alternating wall conditions. Numerical strategies for this geometry include spanwise-alternating wall shear stress conditions (Anderson et al. 2015; Chung et al. 2018), volume-force approaches (Schäfer et al. 2022), or directly resolving the roughness elements (Stroh et al. 2020b). Ridge-type roughness is defined as a series of protruding longitudinal ridges (Vanderwel et al. 2019), and explicitly emphasises the wall-normal elevation of (deposition-type) roughness strips. This is in contrast to strip-type roughness, where a large scale separation between roughness height and boundary-layer thickness is assumed, such that local elevation differences between smooth and rough surface areas are negligible.

In both of these streamwise-homogeneous configurations, secondary flows of Prandtl's second kind are observed. These consist of non-zero mean velocity components perpendicular to the main flow direction, accompanied by a spanwise redistribution of streamwise momentum. The resulting mean flow features low-momentum pathways (LMP) and high-momentum pathways (HMP). The sense of rotation of the secondary vortices and the relative positioning of LMPs with respect to the rough patches depend on the type of heterogeneity (strip versus ridge) (Wang and Cheng 2006; Vanderwel and Ganapathisubramani 2015; Hwang and J. H. Lee 2018), the spanwise wavelength (Chung et al. 2018) and, when a clear scale separation between outer scales of the flow and size of the roughness elements is absent, the elevation of the rough surface patch (Stroh et al. 2020b).

The impact of these turbulent secondary motions on skin friction drag remains unclear. Some studies attribute a significant drag penalty to the secondary flow (Nikora et al. 2019; Stroh et al. 2020a), whereas others find only a minor influence on the global drag (Modesti et al. 2018; Modesti and Pirozzoli 2022).

Streamwise development of the flow over spanwise heterogeneous surfaces. Most studies have focused on fully developed conditions, in which the spanwise surface heterogeneity persists over a long streamwise distance. However, the development from a smooth-wall inflow has been considered experimentally, e.g. by Studerus (1982) and Vermaas et al. (2011). Well-resolved numerical studies include those of Hwang and J. H. Lee (2018), who examined boundary-layer flows over streamwise-aligned ridges, and of Andreolli et al. (2025), who analysed the temporal decay of secondary motions once the spanwise inhomogeneity in the boundary condition is removed. The latter observed that the mean in-plane velocity components decay faster than the non-uniformity of the streamwise momentum.

Despite the extensive body of work on spanwise-alternating boundary conditions, a shared understanding of how such heterogeneous roughness distributions affect the global drag, and how this drag modification is related to the presence of turbulent secondary flows, has not yet emerged. This knowledge gap motivates the present study.

1.2.2 Non-uniform thermal boundary conditions

Spatially non-uniform thermal boundary conditions form an important class of thermo-fluid problems and, analogous to spatially inhomogeneous roughness, they are most naturally classified by the direction of inhomogeneity relative to the mean flow. This again leads to two broad families: azimuthally (or spanwise) varying, streamwise-homogeneous conditions, and axially varying (thermal entrance) conditions.

Azimuthally non-uniform conditions, thermally fully developed flow. Thermal boundary conditions with non-uniformity perpendicular to the mean flow direction were first considered in pipe flow by Reynolds (1963a). In that study, an analytical solution was derived for the temperature field in thermally fully developed laminar flow subject to azimuthally non-uniform wall heat flux, using a Fourier decomposition in the azimuthal direction. This analysis was later extended to conjugate heat transfer by Reynolds (1963b). For turbulent flow, Reynolds (1963a) and Sparrow and Lin (1963) proposed solutions based on a turbulent thermal diffusivity model, which was assumed to be isotropic, i.e. equal radial and azimuthal components.

On the basis of experiments, Black and Sparrow (1967) argued that isotropy of the turbulent thermal diffusivity α_t is a reasonable approximation in the pipe core, however near the wall, its azimuthal component is much larger than the radial one, i.e. $\alpha_{t,\varphi} \gg \alpha_{t,r}$. This anisotropy was later confirmed numerically by Antoranz Perales (2017), who provided DNS data for thermally fully developed turbulent pipe flow at friction Reynolds numbers $\mathrm{Re}_\tau \in \{180, 360\}$, and by Straub et al. (2019a), who used well-resolved large-eddy simulation (LES) up to $\mathrm{Re}_\tau \approx 1000$. However, it is still unclear how the azimuthal and radial turbulent thermal diffusivities depend on the imposed azimuthal heat flux distribution, as both studies considered only one or two specific patterns.

Within their modelling framework, Reynolds (1963a) and Sparrow and Lin (1963) showed that the global Nusselt number Nu is independent of the azimuthal variation of wall heat flux: 'the average heat-transfer performance is equal to that of the axisymmetric heat-transfer situation.' (Sparrow and Lin 1963). Later studies raised doubts about the applicability of this conclusion to low-Prandtl-number fluids (e.g. liquid metals), arguing that these fluids obey a different heat transfer regime (Marocco et al. 2016). However, all subsequent numerical and experimental investigations (Marocco et al. 2016; Straub et al. 2019a; Laube et al. 2022) have consistently reported that Nu remains independent of the azimuthal heat flux distribution. Nevertheless, a clear theoretical rationale specifying under which conditions this Nu-independence must hold – in terms of fluid properties, mean-flow parameters and the type of non-uniformity in the boundary condition – is still lacking.

Buoyancy and temperature-dependent properties. In several studies on azimuthally varying heat flux, the standard assumptions of purely forced convection and temperature-independent properties are relaxed. Barletta et al. (2003) and Barletta and Lazzari (2007) extended the laminar fully developed solution of Reynolds (1963a) to include buoyancy effects when gravity is aligned with the pipe axis, considering both azimuthally varying wall temperature and wall heat flux. Buoyancy in the form of aided mixed convection was further investigated by Dachwitz et al. (2022) using DNS, and mixed convection in a horizontal pipe with azimuthally inhomogeneous heating was studied experimentally by Elmlinger et al. (2026). In addition, Antoranz et al. (2025) examined fully developed turbulent pipe flow with azimuthally varying heat flux and temperature-dependent thermal diffusivity and viscosity, thereby coupling in-plane motion and temperature field.

Conjugate heat transfer and idealised boundary conditions. In applications with essentially uniform heat input along the axial direction – such as CSP receiver tubes – the thermal boundary condition in the thermally fully developed state is often idealised as either a prescribed heat flux (Neumann condition) or a prescribed mean wall heat flux with inhibited temperature fluctuations at the wall (mixed boundary condition, MBC, see Piller (2005)). Both are applied directly at the fluid. In real systems, by contrast, the external heat flux is specified on the outer surface of a solid pipe, and the fluid temperature fluctuations are coupled to unsteady heat conduction in the solid. This fully coupled situation is referred to as *conjugate heat transfer* (CHT).

For channel flow, DNS data for CHT were first presented by Tiselj et al. (2001), while for pipe flow, Vicente Cruz and Lamballais (2023) reported CHT results using an immersed boundary method on a Cartesian grid. All well-resolved CHT studies to date consider uniform thermal boundary conditions on the solid. The influence of *non-uniform* thermal boundary conditions at the outer solid surface – especially in azimuthally varying configurations – on the coupled solid-fluid system has not yet been explored numerically.

If the solid is excluded from the computational domain, approximate agreement with full CHT can be recovered by choosing a suitable effective boundary condition (uniform heat flux, MBC, or a Robin-type condition), depending on the solid-fluid pairing and wall thickness (Flageul et al. 2015; Straub et al. 2019b). In CHT cases, the fully developed mean temperature profile in the fluid is only weakly sensitive to the solid properties, an observation which is correctly captured by the limiting effective boundary conditions. However, the thermal development length after a step change in the boundary condition is strongly influenced by the solid’s thermal inertia and thickness.

Axially varying conditions and thermal entrance region. For scalar boundary conditions varying in the streamwise direction, classical work goes back to Graetz (1882), who solved the thermal entrance problem for laminar pipe flow with a step change in wall temperature and negligible axial conduction.[1] In the second half of the 20th century, this solution to the ‘Graetz problem’, based on expanding the temperature field in radial eigenfunctions, was extended in many directions. Notable extensions include Neumann-type boundary conditions, incorporation of turbulent thermal diffusivity (Sparrow et al. 1957; Siegel et al. 1958), and inclusion of axial conduction (Papoutsakis et al. 1980). Using a turbulent thermal diffusivity model, Notter and Sleicher (1972) provided thermal entrance data over a wide range of Pr and Re, and observed that the thermal development length increases significantly with Re only for $\mathrm{Pr} \ll 1$.

Well-resolved numerical studies of thermally developing internal flows are scarce. Rousta and Lessani (2022) performed DNS of thermally developing turbulent channel flow at $\mathrm{Pr} \in \{0.71, 1, 3, 7\}$ and $\mathrm{Re}_\tau = 180$ for a step change in wall temperature. However, their computational domain is too short for even first-order statistics to reach a fully developed state. More recently, Vicente Cruz et al. (2025) presented preliminary data of thermally developing turbulent pipe flow (mixed and forced convection, imposed wall heat flux, implicit LES) at a single $(\mathrm{Pr}, \mathrm{Re}_b)$ combination[, which is insufficient to systematically test the trends reported in Notter and Sleicher (1972).] [NGF26]

To the best of the author’s knowledge, no studies – either laminar or turbulent – have addressed the thermal entrance problem for azimuthally non-uniform wall heat flux. Such a regime is unavoidable in any experiment in which azimuthally non-uniform heat flux is imposed, and it is relevant for applications such as solar receivers. Consequently, both analytical theory and high-fidelity numerical data are missing for this class of flows.

1 Graetz’s analysis already accounted for conjugate heat transfer.

1.3 Research objectives and procedure

The primary objective of this thesis is to improve the physical understanding of flow-induced transport phenomena driven by non-uniform boundary conditions. It examines spatially varying roughness features and spatially non-uniform heat flux. Motivated from the engineering application, a focus is placed on *global* transport metrics, i.e. friction coefficient C_f and heat transfer coefficient (Nusselt number Nu).

Boundary effects are isolated from geometric complexities by studying the flow in two canonical geometries, each with a variation in a single direction: (i) a plane channel with spanwise-varying roughness and (ii) a circular pipe with azimuthally-varying heat flux (laminar and turbulent, including conjugate heat transfer). The respective fully developed state is compared to the corresponding homogeneous reference (i.e. smooth- or rough-walled channel, uniformly heated pipe). A subsequent step systematically studies the development of the flow between homogeneous and spanwise/azimuthally inhomogeneous fully developed states.

The work addresses the following research questions:

1. How do spanwise/azimuthal variations in boundary conditions alter global and local flow statistics in the fully developed state relative to the homogeneous reference case, and which physical mechanisms are responsible for these changes?
2. Is it possible to predict global transport metrics (C_f and Nu) based on homogeneous reference data?
3. How does a flow adapt when it encounters a region of different (and spatially non-uniform) boundary condition? What governs the length of the ensuing development region and what are the associated transport phenomena?

To answer these questions, the thesis employs theoretical analyses and high-fidelity numerical simulations.

The theoretical work is based on the partial differential transport equations of mass, momentum and energy. For channel flow, the analysis yields a predictive model for flow over non-uniform roughness. For pipe flow with azimuthally non-uniform heat flux, an analytical temperature solution is obtained in the developing regime under laminar flow conditions, and an exact expression for the influence of azimuthally non-uniform heat flux on global heat transfer is derived under turbulent flow conditions. Data from physical and numerical experiments are used to calibrate and verify the analysis.

High-fidelity numerical data for turbulent flow cases are generated and analysed for a range of Reynolds and Prandtl numbers. The governing equations of fluid motion and energy conservation are solved numerically with two high-order schemes, implemented in high-performance open-source solvers: the spectral element method (SEM) via NekRS (Fischer et al. 2022) for pipe flow (non-uniform thermal boundary condition) and the method of compact finite differences via Xcompact3D (Bartholomew et al. 2020) for channel flow (inhomogeneous roughness). The data enable detailed flow examination and reveal the transport mechanisms governing flow states with non-uniform boundary conditions.

The thesis delivers three main contributions: (i) predictive frameworks for global transport in case of non-uniform boundary conditions, (ii) high-fidelity numerical databases quantifying global and pointwise flow statistics – including in the development region – and (iii) physical insight into the mechanisms governing global transport both within and outside of the equilibrium state.

The thesis first addresses the questions for channel flow with spanwise inhomogeneous roughness in chapter 3, and then for pipe flow with azimuthally non-uniform heat flux in chapter 4.

The numerical data are published open-access in the KITOpen repository to support further research.

2

Fundamentals

2.1 Governing equations of fluid dynamics

This section briefly recapitulates the transport equations of fluid dynamics, following the textbooks of Batchelor (2010) and Pope (2000).

At the microscopic scale, a fluid consists of discrete particles whose dynamics can be treated by means of molecular or kinetic theory (e.g., the Boltzmann equation for a statistical description). When the molecular mean free path is much smaller than the scale of macroscopic variations (local thermodynamic equilibrium), the fluid can be considered a *continuum*. This scale separation allows one to assign well-defined local fields – such as velocity $\vec{u}(\vec{x}, t)$, pressure $p(\vec{x}, t)$ or temperature $T(\vec{x}, t)$ – throughout the domain, with $\vec{x}$ denoting a fixed spatial position and t denoting time. The statistical description then admits a formulation in terms of the equations of continuum mechanics. In this Eulerian viewpoint, the principle of mass conservation can be written in differential form as

$$\frac{\partial \rho}{\partial t} + \nabla \cdot (\rho \vec{u}) = 0, \tag{2.1}$$

where ρ is the density of the fluid. Equation (2.1) can be expanded as

$$\frac{\partial \rho}{\partial t} + (\vec{u} \cdot \nabla)\rho + \rho \nabla \cdot \vec{u} = \frac{\mathrm{D}\rho}{\mathrm{D}t} + \rho \nabla \cdot \vec{u} = 0. \tag{2.2}$$

$\mathrm{D}/\mathrm{D}t = \partial/\partial t + (\vec{u} \cdot \nabla)$ denotes the material derivative. This thesis only considers incompressible fluids. Consequently, density variations of a material fluid element are negligible, such that the continuity equation simplifies to a kinematic constraint on the velocity field:

$$\boldsymbol{\nabla} \cdot \vec{u} = 0. \tag{2.3}$$

The acceleration of a material fluid element is given by Newton's second law from the combined effect of all acting forces:

$$\rho \frac{\mathrm{D}\vec{u}}{\mathrm{D}t} = \boldsymbol{\nabla} \cdot \boldsymbol{\sigma} + \rho \vec{f}, \tag{2.4}$$

where surface forces are represented by the divergence of the stress tensor $\boldsymbol{\sigma}$, and volume forces by the volumetric force density vector $\vec{f}$. The isotropic (spherical) component of the stress tensor is identified with the pressure, and a linear relationship between the deviatoric component of the stress tensor and the strain rate tensor is assumed. This material law is commonly associated with Newtonian fluids assuming Stokes' hypothesis (negligible bulk viscosity):

$$\boldsymbol{\sigma} = -p\boldsymbol{I} + \boldsymbol{\tau}, \quad \text{with } \boldsymbol{\tau} = \mu \left(\boldsymbol{\nabla}\vec{u} + \boldsymbol{\nabla}\vec{u}^T \right), \tag{2.5}$$

where μ is the dynamic viscosity. For constant-property fluids, this further simplifies to

$$\frac{\mathrm{D}\vec{u}}{\mathrm{D}t} = -\frac{1}{\rho} \boldsymbol{\nabla} p + \nu \nabla^2 \vec{u} + \vec{f}, \tag{2.6}$$

where ν is the kinematic viscosity. Equation (2.6) together with eq. (2.1) are the well-known Navier-Stokes equations for an incompressible Newtonian fluid with constant properties.

An additional advection-diffusion equation is required to model the transport of a passive scalar. For a domain without scalar sources, such an evolution equation is given by Pope (2000) as

$$\frac{\mathrm{D}\phi}{\mathrm{D}t} = D \nabla^2 \phi \tag{2.7}$$

for a constant-property flow, where D is the diffusivity. Importantly, the scalar does not affect the velocity field; hence the term 'passive'. If the scalar ϕ is understood as temperature, eq. (2.7) corresponds to the energy conservation equation for constant-property Newtonian fluids, under the assumption of negligible viscous heating (Bird et al. 2007). In this case, D is the thermal diffusivity $\alpha = \lambda / (\rho c_p)$, where λ is the thermal conductivity and c_p the heat capacity at constant pressure.

2.2 Numerical methods

The numerical solution of eqs. (2.1), (2.6) and (2.7) on a given domain, subject to appropriate boundary and initial conditions, requires two major steps: spatial and temporal discretisation.

This thesis considers flow and heat transfer in the idealised geometries of a plane channel and a circular pipe. These geometries cannot be represented directly in a numerical simulation due to their infinite extent in at least one spatial direction. Instead, a finite, but sufficiently large computational domain is used, provided it captures the relevant physics of the problem. If the flow is translationally invariant in a given direction (e.g. in hydraulically fully developed flow), periodic boundary conditions can be imposed, which removes the need for a turbulence generator at the inlet. This choice inevitably modifies the representation of turbulent structures larger than the computational box: the equations effectively perceive them as infinitely extended. Nevertheless, Lozano-Durán and Jiménez (2014) showed that their interaction with the well-resolved scales is accurately represented for reasonably sized domains.

High-order spatial schemes offer sufficiently small discretisation errors at reasonable computational cost (Toosi et al. 2024) and are therefore used for the turbulent flow simulations in this thesis, with the specific method chosen according to the domain geometry. For plane channel flow, compact finite differences on a three-dimensional staggered Cartesian grid are employed, as implemented in the open-source solver XCompact3D (Laizet and Li 2011). For the pipe geometry, following El Khoury et al. (2013), the spectral element method (SEM) is used as implemented in the open-source code NekRS (Fischer et al. 2022).

In the following subsections, both spatial discretisation methods are briefly introduced, followed by a discussion of the temporal discretisations used.

2.2.1 Compact finite differences

Compared to ordinary finite differences for the evaluation of spatial derivatives, compact finite differences as introduced by Lele (1992) yield higher-order schemes with smaller stencil size, at the cost of having to invert a linear system for each derivative. Conceptually, the scheme is derived as a linear combination of Taylor expansions at neighbouring points, where the coefficients are chosen such that some of the outermost terms cancel (making the stencil 'compact').

The schemes for first and second derivatives are expressed implicitly as follows, where $i \in [1, n_x]$:

$$\alpha_{1,i} f'_{i-1} + f'_i + \alpha_{1,i} f'_{i+1} = a_{1,i} \frac{f_{i+1} - f_{i-1}}{2\Delta x} + b_{1,i} \frac{f_{i+2} - f_{i-2}}{4\Delta x}, \tag{2.8}$$

$$\begin{aligned} \alpha_{2,i} f''_{i-1} + f''_i + \alpha_{2,i} f''_{i+1} = a_{2,i} \frac{f_{i+1} - 2f_i + f_{i-1}}{\Delta x^2} + b_{2,i} \frac{f_{i+2} - 2f_i + f_{i-2}}{4\Delta x^2} \\ + c_{2,i} \frac{f_{i+3} - 2f_i + f_{i-3}}{9\Delta x^2}. \end{aligned} \tag{2.9}$$

Here, Δx is the distance between grid points in the x-direction, and f_i (f'_i, f''_i) denotes the value of the function (first, second derivative in x direction) at grid point i. The parameters $\alpha_{1,i} = \frac{1}{3}$, $a_{1,i} = \frac{14}{9}$, $b_{1,i} = \frac{1}{9}$ for the first derivative, and $\alpha_{2,i} = \frac{2}{11}$, $a_{2,i} = \frac{12}{11}$, $b_{2,i} = \frac{3}{11}$, $c_{2,i} = 0$ for the second derivative yield formally sixth-order schemes. For non-periodic directions, these parameters are used for $i \in [3, n_x - 2]$ (first derivative) and $i \in [5, n_x - 4]$ (second derivative); boundary points are treated with one-sided or non-centred stencils (see Laizet and Lamballais (2009) for details).

Numerical dissipation. Numerical schemes lose accuracy at small scales, which leads to unphysical small-scale oscillations. Lamballais et al. (2011) suggested enlarging the right-side-stencil for the second derivative to 7 points (i.e. $c_{2,i} \neq 0$) to provide numerical dissipation that damps these small-scale oscillations.

Consider $f_i = e^{jkx_i} = e^{jk(i-1)\Delta x} = e^{j(i-1)\kappa}$ with the scaled wavenumber $\kappa = k\Delta x$, and note that the coordinates x_i are given by $x_i = (i-1)\Delta x$. The exact second derivative at grid point i is $f''_{i,\text{exact}} = -\frac{\kappa^2}{\Delta x^2} f_i$, while the scheme produces $\tilde{f}''_i = -\frac{(\kappa''_s)^2}{\Delta x^2} f_i$, where κ''_s is called the modified wavenumber for the second derivative. Inserting into eq. (2.9), and using $f_{i\pm m} = f_i e^{\pm jm\kappa}$, one finds

$$(\kappa''_s)^2(\kappa) = 2 \frac{a_{2,i}(1 - \cos\kappa) + \frac{b_{2,i}}{4}(1 - \cos 2\kappa) + \frac{c_{2,i}}{9}(1 - \cos 3\kappa)}{1 + 2\alpha_{2,i}\cos\kappa}. \tag{2.10}$$

Requiring $(\kappa''_s)^2 = \pi^2$ at the cutoff wavenumber $\kappa = \pi$ as well as formal sixth order accuracy (see equation (2.2) of Lele (1992)) yields

$$\begin{aligned} \alpha_{2,i} = \frac{272 - 45\pi^2}{416 - 90\pi^2} \approx 0.36448, \quad a_{2,i} = \frac{3}{2} - \frac{9}{4}\alpha_{2,i} \approx 0.67991, \\ b_{2,i} = \frac{3}{5}(8\alpha_{2,i} - 1) \approx 1.1495, \quad c_{2,i} = \frac{1}{20}(1 - 11\alpha_{2,i}) \approx -0.11047. \end{aligned} \tag{2.11}$$

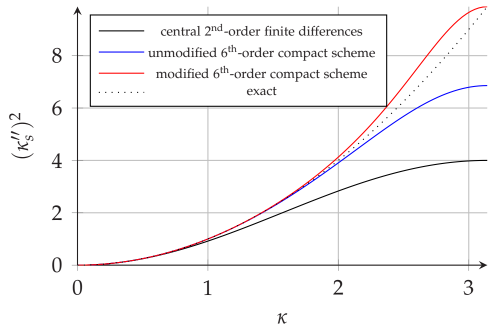

Figure 2.1: Comparison of $(\kappa_s'')^2$ for the second derivative.

Figure 2.1 displays $(\kappa_s'')^2$ for the original scheme by Lele (1992), the modified scheme by Lamballais et al. (2011), and a second-order central difference scheme for comparison. The original scheme has $(\kappa_s'')^2 < \kappa^2$, i.e. it is under-dissipative, while the modified scheme eq. (2.11) remains closer to the exact differentiation at high wavenumbers and provides over-dissipation at in this range, with negligible additional computational cost. This scheme is selected for the simulations performed with XCompact3D in this thesis.

2.2.2 Spectral element method

The spectral element method (SEM) is a high-order method for solving differential equations numerically on arbitrarily-shaped domains. It is conceptually related to the finite element method (FEM) and was became popular following Patera (1984). This section briefly recapitulates the method. For a more general and formal introduction, the reader is referred to Deville et al. (2002); this section adopts the nomenclature used there.

The wave equation for the displacement $\vec{u}$ with forcing $\vec{f}$ on a domain $\mathcal{D}$ serves as an example:

$$\rho \frac{\partial^2 \vec{u}}{\partial t^2} = \nabla \cdot (\mu \nabla \vec{u}) + \vec{f}(\vec{x}, t), \qquad \vec{x} \in \mathcal{D} \tag{2.12}$$

which is considered in one dimension for simplicity. Locally, the solution $u(x,t)$ is approximated by a weighted sum of $N_p + 1$ basis functions φ_i (to be defined later):

$$u(x,t) \approx \sum_{i=0}^{N_p} u_i(t) \varphi_i(x), \tag{2.13}$$

with fixed-in-time basis functions and fixed-in-space coefficients u_i.

Weak form. As with all Galerkin-type methods, the weak form of the PDE eq. (2.12) is required, which is obtained by multiplying the PDE with a test function $v \in L^2(\mathcal{D})$, then integrating both sides over the domain $\mathcal{D}$ and finally performing integration by parts on terms involving spatial derivatives, i.e. for eq. (2.12),

$$\int_{\mathcal{D}} \rho \frac{\partial^2 u}{\partial t^2} v \mathrm{d}x + \int_{\mathcal{D}} \mu \frac{\partial u}{\partial x} \frac{\partial v}{\partial x} \mathrm{d}x = \int_{\mathcal{D}} f v \mathrm{d}x + \int_{\partial\mathcal{D}} \mu \frac{\partial u}{\partial x} v \mathrm{d}x \tag{2.14}$$

Any boundary conditions other than homogeneous Neumann boundary conditions require special treatment that depends on the choice of basis functions; in the latter case the boundary term vanishes identically, which is assumed in this basic introduction (for details on boundary treatment, see (Deville et al. 2002)). Next, eq. (2.13) is inserted into the weak form eq. (2.14):

$$\sum_{i=0}^{N_p} \frac{\partial^2 u_i(t)}{\partial t^2} \int_{\mathcal{D}} \rho \varphi_i(x) v \mathrm{d}x + \sum_{i=0}^{N_p} u_i(t) \int_{\mathcal{D}} \mu \frac{\partial \varphi_i(x)}{\partial x} \frac{\partial v}{\partial x} \mathrm{d}x = \int_{\mathcal{D}} f v \mathrm{d}x \tag{2.15}$$

The spectral element method uses the basis functions as test functions. In particular, the following equation holds for $j = 0..N_p$:

$$\sum_{i=0}^{N_p} \frac{\partial^2 u_i(t)}{\partial t^2} \int_{\mathcal{D}} \rho \varphi_i(x) \varphi_j(x) \mathrm{d}x + \sum_{i=0}^{N_p} u_i(t) \int_{\mathcal{D}} \mu \frac{\partial \varphi_i(x)}{\partial x} \frac{\partial \varphi_j(x)}{\partial x} \mathrm{d}x = \int_{\mathcal{D}} f \varphi_j(x) \mathrm{d}x \tag{2.16}$$

Spatial discretisation. The domain is subdivided into an arbitrary number of *elements* (which are connected by shared faces), typically hexahedral. In the simplest 1D case, the domain $\mathcal{D}$ is split into equally sized linear elements:

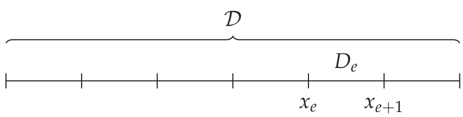

The basis functions are defined on a reference element $r \in [-1,1]$ (or $r,s \in [-1,1] \times [-1,1]$ in 2D, etc.). A mapping (ideally affine to preserve the accuracy of the numerical quadrature) relates each element's coordinates to the reference, i.e. $F_e : [-1,1] \to D_e$:

$$x(r) = x_e + \frac{x_{e+1} - x_e}{2}(r+1), \qquad r(x) = 2\frac{x - x_e}{x_{e+1} - x_e} - 1 \tag{2.17}$$

The Jacobian of the mapping is readily evaluated, which will be used for integration by substitution:

$$\frac{\mathrm{d}x}{\mathrm{d}r} = \frac{x_{e+1} - x_e}{2}, \qquad \frac{\mathrm{d}r}{\mathrm{d}x} = \frac{2}{x_{e+1} - x_e} \tag{2.18}$$

The method is formulated in element-local coordinates (i.e. $r(,s,t)$).

Choice of basis functions φ_i. Polynomial interpolants in the form of the Lagrange polynomials of order N_p are an obvious choice for the basis functions ℓ_i:

$$\varphi_i(r) = \ell_i^{(N_p)}(r) = \frac{(r - r_0)}{(r_i - r_0)} \cdots \frac{(r - r_{i-1})}{(r_i - r_{i-1})} \frac{(r - r_{i+1})}{(r_i - r_{i+1})} \cdots \frac{(r - r_{N_p})}{(r_i - r_{N_p})} = \prod_{\substack{0 \le j \le N_p \\ i \ne j}} \frac{r - r_j}{r_i - r_j}. \tag{2.19}$$

In particular, $\ell_i^{(N_p)}(r_j) = \delta_{ij}$, where δ_{ij} is the Kronecker delta; hence the coefficients $u_i(t)$ become the values of u at the (mapped) collocation points r_i, which remain to be chosen.

Choice of collocation points. The Gauss-Lobatto-Legendre (GLL) points are the $n-1$ extrema of the Legendre polynomial $P_n(x)$ of order $n = N_p$, plus the boundary points ($r_0 = -1, r_{N_p} = 1$). The Legendre polynomials are given, for example, by Rodrigues' formula

$$P_n(x) = \frac{1}{2^n n!} \frac{\mathrm{d}^n}{\mathrm{d}x^n} \left(x^2 - 1\right)^n \tag{2.20}$$

These points satisfy a few useful properties. They yield, together with the GLL weights

$$w_0 = w_{N_p} = \frac{2}{N_p(N_p+1)}, \qquad w_i = \frac{2}{N_p(N_p+1)[P_{N_p}(r_i)]^2}, \quad i = 1, \ldots, N_p - 1, \tag{2.21}$$

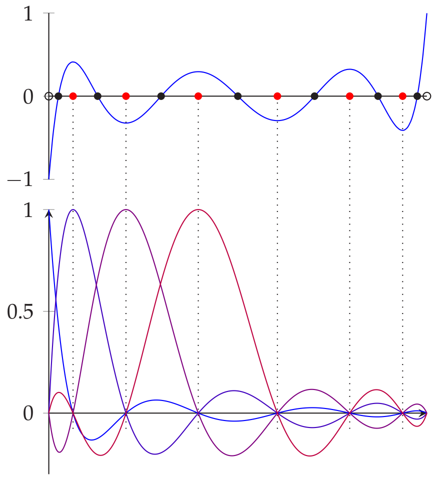

Figure 2.2: $N_p = 7$ Legendre polynomial and its roots (black points) and extrema (red points), with additional points at the boundary. The resulting Lagrange polynomials are displayed below: note that their values are bounded by $[-1, 1]$. Only the left half of them is shown; the others follow by symmetry.

the optimal numerical quadrature formula for $N_p + 1$ points that include the boundary, providing exact integration for polynomials of degree up to $2N_p - 1$:[1]

$$\int_{-1}^{1} f(r)\mathrm{d}r \approx \sum^{i} w_i f(r_i). \tag{2.22}$$

Choosing the same points for interpolation and quadrature leads to a diagonal (and hence trivial to invert) mass matrix.

Furthermore, for each non-boundary GLL point, the derivative of the corresponding basis function vanishes: $\left.\mathrm{d}\ell_i^{(N_p)} \middle/ \mathrm{d}r \right|_{r_i} = 0$ for $i \in [1, N_p - 1]$, and all interpolant polynomials are bounded: $|\ell_i^{(N_p)}(r)| < 1$ for $r \in [-1, 1]$, which reduces the interpolation error. For $N_p = 7$ (the polynomial degree used in the present simulations), the Legendre polynomial, resulting GLL points and interpolants are visualised in fig. 2.2.

[1] Low-order GLL quadratures have commonly-known names: For $N_p = 1$, one obtains the trapezoidal rule, which is exact for linear functions. $N_p = 2$ yields the Simpson rule which integrates cubic functions exactly.

Numerical quadrature. Applying Gauss-Lobatto quadrature to the individual integrals in eq. (2.16) and exploiting the properties of the basis functions yields

$$\int_D \rho \ell_i(r(x))\ell_j(r(x))\mathrm{d}x \approx w_j \rho(x(r_j))\delta_{ij} \left.\frac{\mathrm{d}x}{\mathrm{d}r}\right|_{r_j} =: M^e_{ij}, \tag{2.23a}$$

$$\int_D f(x,t)\ell_j(r(x))\mathrm{d}x \approx w_j f(x(r_j),t) \left.\frac{\mathrm{d}x}{\mathrm{d}r}\right|_{r_j} =: f^e_j(t), \tag{2.23b}$$

$$\int_D \mu \frac{\partial \ell_i(r(x))}{\partial x}\frac{\partial \ell_j(r(x))}{\partial x}\mathrm{d}x \approx \sum_{k=0}^{N_p} w_k \mu(x(r_k))\ell'_j(r_k)\ell'_i(r_k) \left.\frac{\mathrm{d}r}{\mathrm{d}x}\right|^2_{r_k} \left.\frac{\mathrm{d}x}{\mathrm{d}r}\right|_{r_k} =: K^e_{ij}. \tag{2.23c}$$

M^e_{ij}, $f^e_j(t)$ and K^e_{ij} are the (diagonal) mass matrix, forcing vector and (symmetric) stiffness matrix, respectively. The latter contains the matrix of derivatives $\ell'_i(r_j)$, which is identical for all elements and can be computed analytically.

For each element, eq. (2.16) becomes, due to eqs. (2.23a) to (2.23c),

$$\sum_{i=0}^{N_p} \frac{\partial^2 u_i(t)}{\partial t^2} M^e_{ij} + \sum_{i=0}^{N_p} u_i(t) K^e_{ij} = f^e_j(t), \quad j = 0..N_p. \tag{2.24}$$

Assembly of the global system. The local equation systems of each element (eq. (2.24)) are joined together using *direct stiffness summation*, which is closely related to the *direct stiffness method* from FEM: for all collocation points that are shared between two or more elements, their respective equations are added together. This ensures that the resulting solution u is continuous at the element interfaces.

For a 2-element domain of 1D elements, the global equation system could be written as follows (without boundary terms), where $\vec{u}$ is now the global solution vector:

$$\begin{pmatrix} M^{(0)}_{0,0} \\ \vdots \\ M^{(0)}_{N_p,N_p} + M^{(1)}_{0,0} \\ \vdots \\ M^{(1)}_{N_p,N_p} \end{pmatrix} \cdot \ddot{\vec{u}} = \begin{pmatrix} f^{(0)}_0 \\ \vdots \\ f^{(0)}_{N_p} + f^{(1)}_0 \\ \vdots \\ f^{(1)}_{N_p} \end{pmatrix} - \begin{pmatrix} K^{(0)}_{0,0} & \cdots & K^{(0)}_{0,N_p} & & 0 \\ & \ddots & \vdots & & \\ & & K^{(0)}_{N_p,N_p} + K^{(1)}_{0,0} & \cdots & K^{(1)}_{0,N_p} \\ & & & \ddots & \vdots \\ \text{sym.} & & & & K^{(1)}_{N_p,N_p} \end{pmatrix} \vec{u}. \tag{2.25}$$

In practice, only the *action* of the stiffness matrix on the solution vector is required, which is element-local except for exchanging boundary data through a gather-scatter operation.

Extension to two and three spatial dimensions. The mapping defined in eq. (2.17) generalises to higher dimensions d by multiplying each corner $\vec{x}_j$, $j = 1..N_c$ ($N_c = 4$ for $d = 2$ and $N_c = 8$ for $d = 3$), with a shape function S_j,

$$\vec{x}(\vec{r}) = \sum_{j=1}^{N_c} S_j(\vec{r})\vec{x}_j, \quad \text{where } \vec{r} = \begin{pmatrix} r & s \end{pmatrix}^T \ (d = 2) \text{ and } \vec{r} = \begin{pmatrix} r & s & t \end{pmatrix}^T \ (d = 3),$$

where the shape functions are tensor products of the linear Lagrange polynomials ℓ_i^1. For $d = 2$, the mapping that maps $(r, s) \in [-1, 1] \times [-1, 1]$ to physical space can be defined as follows, where the corners $\vec{x}_i$ are labelled counter-clockwise:

$$\begin{aligned}\vec{x}(r,s) &= \ell_0^1(r)\ell_0^1(s)\vec{x}_0 + \ell_1^1(r)\ell_0^1(s)\vec{x}_1 + \ell_1^1(r)\ell_1^1(s)\vec{x}_2 + \ell_0^1(r)\ell_1^1(s)\vec{x}_3 \\ &= \frac{1}{4}\left[(1-r)(1-s)\vec{x}_0 + (1+r)(1-s)\vec{x}_1 + (1+r)(1+s)\vec{x}_2 + (1-r)(1+s)\vec{x}_3\right].\end{aligned}$$

Similarly, convex 3D hex elements are mapped using triple products of Lagrange polynomials. The basis functions for interpolation are taken from the tensor-product basis of Lagrange polynomials, i.e. for $d = 2$:

$$\varphi_{pq}(x, y) = \ell_p(r(x, y))\ell_q(s(x, y)). \tag{2.26}$$

The collocation points for both directions are identical, i.e. $r_i = s_i$ (the Gauss-Lobatto-Legendre points). For each element, $(N_p + 1)^2$ basis functions are formed this way, which are then inserted into the weak form. The remainder is analogous to the 1D case.

2.2.3 Temporal discretisations

XCompact3D. The time advancement of the momentum equation eq. (2.6), here re-framed as

$$\frac{\partial \vec{u}}{\partial t} = \vec{F}(\vec{u}) - \frac{1}{\rho}\boldsymbol{\nabla} p, \tag{2.27}$$

and its spatially discretised variant, is constrained by mass conservation (eq. (2.3)). One common solution is the fractional step method, as used by Laizet and Lamballais (2009). For each Runge-Kutta substep k, one first advances the explicit terms to obtain an intermediate velocity $\vec{u}^*$, then solves a pressure-Poisson equation, and finally projects $\vec{u}^*$ onto a divergence-free velocity field by pressure correction:

$$\vec{u}^* = \vec{u}^k + \Delta t (a_k \vec{F}^k + b_k \vec{F}^{k-1}), \tag{2.28}$$

$$\nabla \cdot \nabla \tilde{p}^{k+1} = \frac{\rho}{c_k \Delta t} \nabla \cdot \vec{u}^*, \tag{2.29}$$

$$\vec{u}^{k+1} = \vec{u}^* - \frac{c_k \Delta t}{\rho} \nabla \tilde{p}^{k+1}. \tag{2.30}$$

The values of $a_k = \{\frac{8}{15}, \frac{5}{12}, \frac{3}{4}\}$, $b_k = \{0, -\frac{17}{60}, -\frac{5}{12}\}$, and $c_k = a_k + b_k$ are used; they represent a low-storage, three-step Runge-Kutta scheme (Orlandi 2000).

NekRS. The spectral element discretisation is integrated in time with the implicit backward difference (BDFk) method developed by Couzy (1995), where in particular the nonlinear term is extrapolated (EXTk). The method is not reiterated here in detail; it is described in Fischer et al. (2022). For all NekRS simulations in chapter 4, BDF2/EXT2 is used.

2.3 Description of turbulent flows

The numerical solution methods described in section 2.2 are deterministic; hence for the same initial conditions and identical floating point round-off behaviour, all obtained solutions are bitwise reproducible. Under turbulent flow conditions, however, altering the initial state slightly (or allowing round-off errors to accumulate in a different way) will completely alter the solution after a sufficient time separation: indeed, one of the core properties of turbulence is its chaotic nature (Pope 2000). This also means that the time series of an experiment and a numerical solution of the same turbulent flow will generally not agree, in contrast to typical laminar flow scenarios.

While the instantaneous fields at a given time are not reproducible, the statistical properties of the solution (such as the mean and variance of temperature at a certain position) are. Hence, a statistical description of the turbulent fields is common. For a field ϕ with probability density function (PDF) $p(\phi, \vec{x}, t)$, the mean is defined as

$$\langle \phi \rangle = \int_{-\infty}^{\infty} \phi p(\phi, \vec{x}, t) \mathrm{d}\phi, \tag{2.31}$$

and the fluctuation as $\phi' = \phi - \langle\phi\rangle$. Often, one-point correlations between different quantities are sought, e.g. in the forms of Reynolds stresses (see below), and then the joint PDF $p(\phi, \vec{u}, \vec{x}, t)$ is integrated in a similar way. Similarly, two-point correlations (of, e.g., the velocity) are obtained from the joint PDF of the velocities at two distinct locations.

In practice, $p(\dots)$ is not readily available; it can be estimated through repeated experiments (ensemble averaging) or, in the present case, through time averaging, as the flow is statistically steady (so $\partial\langle\phi\rangle/\partial t = 0$). The time means $\langle\phi\rangle_T$ obtained in this way are themselves random variables and associated with their own variance, which can be estimated by various methods (Yao et al. 2023). Nevertheless, provided the averaging time is large enough, $\langle\phi\rangle_T$ is a reasonable approximation of $\langle\phi\rangle$. Within this thesis, $\langle\phi\rangle$ denotes the statistical mean (and indeed some derivations do not assume statistically steady conditions). Whenever data from turbulent simulations are evaluated, $\langle\phi\rangle$ is to be understood as the time mean used as an estimate of the statistical mean.

The above decomposition of a statistical quantity into a mean and a fluctuation can also be applied to the governing equations themselves, giving rise to the Reynolds-averaged Navier-Stokes equations (RANS) and the mean temperature equation:

$$\boldsymbol{\nabla} \cdot \langle\vec{u}\rangle = 0, \tag{2.32a}$$

$$\rho\left(\frac{\partial\langle\vec{u}\rangle}{\partial t} + (\langle\vec{u}\rangle \cdot \boldsymbol{\nabla})\langle\vec{u}\rangle\right) = -\boldsymbol{\nabla}\langle p\rangle + \mu\nabla^2\langle\vec{u}\rangle - \boldsymbol{\nabla} \cdot (\rho\langle\vec{u}' \otimes \vec{u}'\rangle), \tag{2.32b}$$

$$\rho\left(\frac{\partial\langle T\rangle}{\partial t} + (\langle\vec{u}\rangle \cdot \boldsymbol{\nabla})\langle T\rangle\right) = \boldsymbol{\nabla} \cdot (\lambda\boldsymbol{\nabla}\langle T\rangle) - \boldsymbol{\nabla} \cdot (\rho c_p\langle\vec{u}'T'\rangle). \tag{2.32c}$$

Solving these equations for the mean fields is possible if the additional terms on the right hand side – namely the divergence of the Reynolds stress tensor and the divergence of the turbulent heat flux vector – are closed by means of a turbulence model and a turbulent heat flux model, respectively. Transport equations for these terms and other one-point statistics (such as $\langle T'T'\rangle$) can also be derived. In appendix A.1, this is shown exemplarily in general tensor notation for $\langle\vec{u}'T'\rangle$, $\langle T'T'\rangle$ and the dissipation of $\langle T'T'\rangle$, which is then also reduced for cylindrical coordinates.

3

Momentum transport in channel flows with spanwise-alternating surface features

3.1 Problem description

In this chapter, plane channel flow over structured and rough walls is studied under both laminar and turbulent conditions. The conservation equations of mass (eq. (2.1)) and momentum (eq. (2.6)) for a constant-property Newtonian fluid are solved both semi-analytically and by means of DNS. Streamwise, wall-normal and spanwise directions are denoted by x, y and z, whereas u, v and w are the respective velocity components.

The channel walls are modified by inserting streamwise-aligned strips of altered surface properties (either elevation or roughness). These strips cover 50% of the surface in a spanwise-periodic arrangement, see fig. 3.1. The strip width and the surface properties are treated as parameters. The surface conditions modify the drag exerted by the surface onto the fluid as well as the flow topology, for example by generating turbulent secondary motions and preferential momentum pathways.

Even predicting the drag of a *homogeneous* rough surface remains an active research topic (Chung et al. 2021). The additional spatial inhomogeneity and anisotropy of the present strip-type surfaces introduce further complexity. Yet, roughness *strips* – either streamwise or spanwise – only introduce a single extra dimensionless parameter (namely the strip width) compared to a homogeneous rough surface, and have therefore been established in the literature as a basic test case for non-uniform surface roughness.

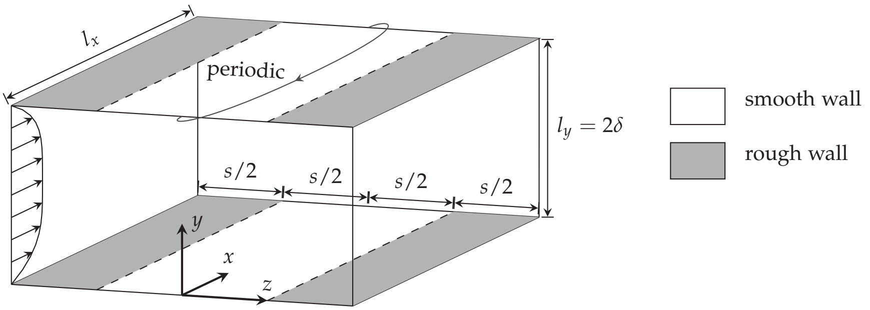

Figure 3.1: Illustration of the setup for streamwise-aligned roughness strips. This unit cell is periodically repeated in the spanwise direction.

For turbulent cases, the statistically steady state is considered, i.e. $\langle \partial q/\partial t\rangle = 0$ for any field q. Here, $\langle\cdot\rangle$ denotes a statistical average, which is, for numerical evaluations, approximated by averaging over statistically homogeneous directions and time. For fully developed flow, this includes the streamwise direction x and time; for developing flows, only time averaging is used. Symmetry about the channel centreplane ($y = \delta$) and the statistical periodicity in the spanwise direction are exploited when computing $\langle\cdot\rangle$. Consequently, mean quantities depend on y (and on x for developing cases) and on the relative spanwise position above the wall pattern, $-1 \leq z/s \leq 1$, where s is the spanwise period. Spanwise averages are denoted by an overbar, e.g. $\overline{\langle u\rangle} = \frac{1}{2}\int_{-1}^{1}\langle u\rangle(y, z/s)\,\mathrm{d}(z/s)$. For composite quantities such as the average friction velocity $\overline{u_\tau}$, this notation is extended in such a way that spanwise averaging is applied to the source quantity, in this case $\langle u\rangle$, from which the mean wall shear stress $\langle\tau_w\rangle$ is computed. The average friction velocity $\overline{u_\tau}$ then follows from $\langle\tau_w\rangle = \rho\,\overline{u_\tau}^2$, where ρ is the fluid density.

Unless stated otherwise, non-dimensionalisation in viscous units (superscript $^+$) uses $\overline{u_\tau}$, e.g. $\langle u\rangle^+ = \langle u\rangle/\overline{u_\tau}$. For developing cases, the friction velocity of the initially smooth-wall inflow, $u_{\tau 0}$, is used instead, unless explicitly noted.

In the remainder of the chapter, three main aspects of channel flow over structured rough walls are addressed; the first two are mainly based on the papers [NSGF25] and [NSGF22b]. First, section 3.2 introduces an analytical drag prediction for spanwise-inhomogeneous surfaces (including ridge-type and strip-type roughness), assuming the drag curves $C_f(\mathrm{Re}_b)$ of the constituent homogeneous surfaces are known. The prediction is found to be valid in the limit of very wide strips, where the flow is in equilibrium with the local surface conditions. Deviations from this limit at finite strip widths are quantified for both laminar and turbulent flow, leading to a simplified model for the drag of flows over strip-type roughness based on the hydraulic channel height.

Second, for DNS of flow over homogeneous and heterogeneous rough surfaces, section 3.3.2 introduces a slip-length boundary condition, following the general numerical setup. The resulting flow topology and comparisons with experimental data are discussed in section 3.4.

Third, section 3.5 investigates the onset of the flow topology induced by a strip-type surface by starting from a statistically fully developed smooth-wall flow and tracking its evolution over streamwise-aligned roughness strips.

3.2 Analytical results

3.2.1 The wide-strip limit

Based on an equilibrium assumption (the flow is in local equilibrium with the boundary condition above each surface patch), an averaging procedure can be derived in which the global drag of the heterogeneous surface is predicted based on the drag behaviour of the homogeneous reference surfaces. The resulting predictive curves for global drag are expected to be valid only for heterogeneous surfaces consisting of [strips] whose size significantly exceeds the boundary layer thickness. For the present case of streamwise-aligned rough strips (spanwise heterogeneous roughness) we refer to the global drag prediction based on the local equilibrium assumption as the *wide-strip limit*. [NSGF25]

In this section, the wide-strip limit concept is introduced and applied to streamwise-aligned ridges in laminar and turbulent channel flow. Numerical simulations are used to assess the effect of finite ridge sizes for both flow regimes. The analogy of the hydraulic channel height is then introduced, enabling drag-increase information to be transferred from the ridge-type to the strip-type case. This leads to a predictive model for the global drag, which is compared to experimental data.

The wide-strip limit provides a drag prediction for straight ducts with complex cross section under a local equilibrium assumption, fundamentally different from the constant wall-shear-stress approach of Pirozzoli (2018), which is clearly not fulfilled in the present geometry at large s/δ. Furthermore, Hutchins et al. (2023) presented a version of the wide-strip limit for turbulent boundary layers, which is of much simpler form than for internal flows.

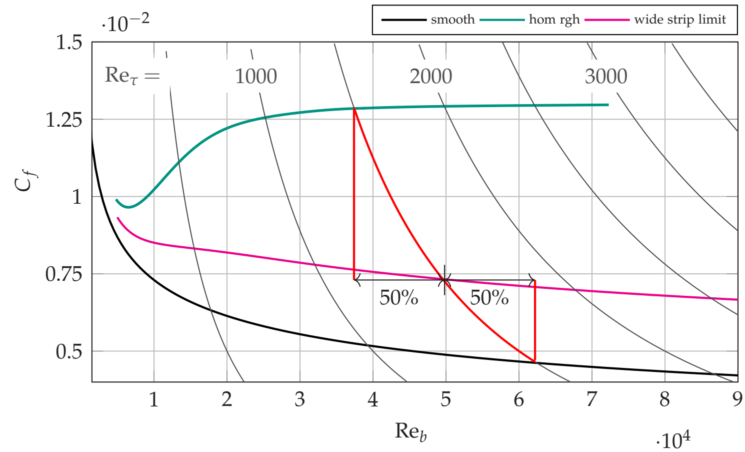

Figure 3.2: Friction coefficient versus Re_b for the wide-strip limit at 50% roughness surface coverage, which is based on input from the homogeneous smooth and rough reference curves only. The global $\overline{C_f}$ for the wide-strip limit is obtained based on $C_{f,\mathrm{rgh}}$ and $C_{f,\mathrm{smooth}}$ at the same Re_τ. The grey lines in the background are lines of constant Re_τ. Adapted from [NSGF25]; figure created by C. Schmidt.

In the following, we refer to the global skin friction coefficient $\overline{C_f}$ in the case of a heterogeneous rough surface, and the related quantities, with an overbar, whereas global quantities for homogeneous surfaces are written without an overbar.

For a [laminar or turbulent] channel flow, the streamwise pressure gradient at different spanwise positions must be identical to allow for fully developed flow conditions. Hence, the wide-strip limit for spanwise alternating smooth and rough strips is derived based on the idea that this identical pressure gradient will induce different flow rates depending on whether the surface is rough or smooth.[1]

The pressure drop–flow rate relation for each type of surface is obtained from the available $C_f(\mathrm{Re}_b)$ relation for the homogeneous smooth and rough surfaces. These are valid for the subsurfaces of the heterogeneous surface if the assumption of local equilibrium holds. Figure 3.2 depicts the idea of how an average of the homogeneously smooth and rough Re_b–C_f curves (i.e. the wide-strip limit) is constructed based on the assumption of the same friction Reynolds number Re_τ, which is the consequence of assuming an equal streamwise pressure gradient if the channel height of both sections is the same.

[1] A streamwise heterogeneous rough surface consisting of *spanwise*-aligned roughness strips will feature identical flow rates in the rough and smooth surface sections (due to continuity) with a varying pressure gradient. Therefore, the present prediction for $\overline{C_f}$ is not meaningful in this context.

Since the channel half-height[2] h of the smooth and the rough surface parts of the considered strip-type surfaces is the same, a constant mean streamwise pressure gradient $\Pi(= -\partial p/\partial x)$ corresponds to a constant friction Reynolds number Re_τ along both surface parts, as this is defined as

$$\mathrm{Re}_\tau = \frac{u_\tau h}{\nu} = \sqrt{\frac{\tau_w}{\rho}}\frac{h}{\nu} = \sqrt{\frac{\Pi h}{\rho}}\frac{h}{\nu}, \tag{3.1}$$

with the fluid density ρ and kinematic viscosity ν.

The friction Reynolds number is not included in the classical Re_b–C_f visualisation. Therefore, the definition of the friction coefficient is reshaped such that it includes the bulk Reynolds number $\mathrm{Re}_b = 2hu_b/\nu$ and the friction Reynolds number Re_τ:

$$C_f = \frac{\tau_w}{\frac{\rho}{2}u_b^2} = 8\frac{\mathrm{Re}_\tau^2}{\mathrm{Re}_b^2}. \tag{3.2}$$

This relation is plotted for several constant values of Re_τ in fig. 3.2. Whilst the friction Reynolds number is the same for both subsurfaces, the volume flow rate, and thus the local bulk Reynolds numbers, differ. Using the plotted relation, the local bulk Reynolds numbers are determined at the intersection points with the homogeneous curves. Volume-weighted averaging of the two values yields the global bulk Reynolds number in the channel. As the surfaces of interest are covered by 50 % with roughness, the global volume flow rate, and thus the global bulk Reynolds number, is obtained by taking the mean between the two local Reynolds numbers (if the roughness surface coverage was 30 %, the effective Reynolds number would be calculated by $\mathrm{Re}_{\mathrm{eff}} = 0.3\,\mathrm{Re}_{\mathrm{rgh}} + 0.7\,\mathrm{Re}_{\mathrm{smooth}}$). The corresponding global friction coefficient still has to fulfil eq. (3.2) and thus is the value on the plotted curve. Repeating this procedure for all friction Reynolds numbers results in the wide-strip limit, which is drawn in magenta in fig. 3.2.

Summarising this averaging procedure mathematically results in a predicted friction coefficient based on a power mean as suggested by [NSGF22b]:

$$\overline{C_f} = \left(\frac{1}{2}\left(\frac{1}{\sqrt{C_{f,\mathrm{rgh}}}} + \frac{1}{\sqrt{C_{f,\mathrm{smooth}}}}\right)\right)^{-2}, \tag{3.3}$$

[2] In this section and appendix A.2, the channel half-height is denoted with h as opposed to δ, for consistency with [NSGF25]. δ is used for the DNS investigations in sections 3.4 and 3.5 for consistency with DNS literature and [NSGF22b].

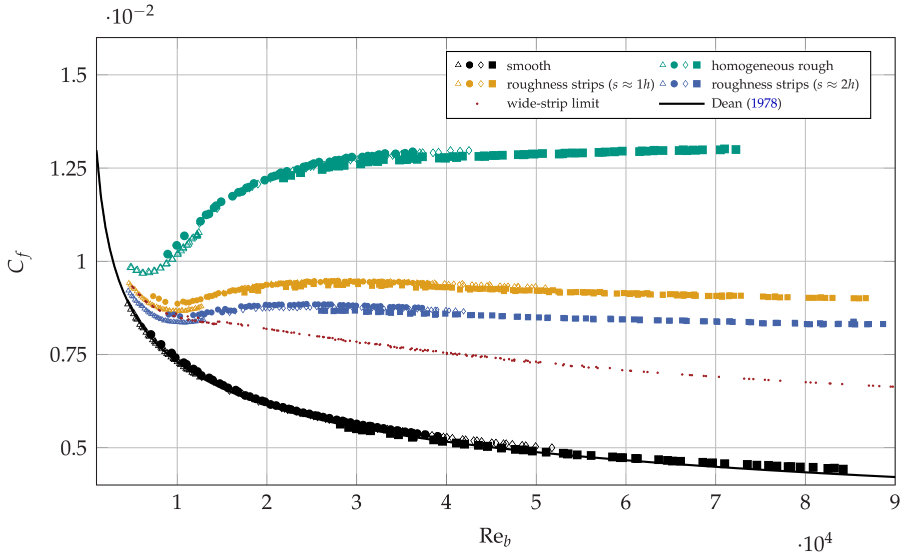

Figure 3.3: Measurement data from Frohnapfel et al. (2024) (thick symbols for smooth and rough references and roughness strips with two different s) and wide-strip limit. Different symbols within each colour correspond to different flow rate measurement procedures within the experiment, which is not in focus here. The roughness strips are symmetrically placed on the channel top and bottom wall and are inserted in such a way that the average channel height in the rough channel parts is identical to the one in the smooth channel parts. The evaluation of the plotted C_f is based on this average channel height. Adapted from [NSGF25].

where $C_{f,\mathrm{rgh}}$ and $C_{f,\mathrm{smooth}}$ are taken at the same Re_τ.[3]

[Eventually, the aim is to give an a-priori estimate of the global drag of] turbulent channel flow with streamwise-aligned roughness strips (i.e. finite spanwise extension of the individual surface patches but quasi-infinite extension in streamwise direction), for which we have high-quality reference data from Frohnapfel et al. (2024) available. The surfaces considered consist of streamwise-aligned roughness strips (P60 sandpaper) which alternate with smooth surface parts of the same width. The width in terms of the channel half-height h is set to $s \approx h$ and $s \approx 2h$. The dataset contains $C_f(\mathrm{Re}_b)$ for these strip-type rough surfaces and for the homogeneous rough and smooth reference cases over a Reynolds number range $4500 < \mathrm{Re}_b < 85000$ (where $\mathrm{Re}_b = u_b 2h/\nu$ with bulk velocity u_b and kinematic viscosity ν).

3 This is valid as long as the smooth and rough channel parts have the same channel half-height. As will be discussed later, different channel height definitions are possible. For eq. (3.3) to be (strictly) valid, the channel height chosen for data evaluation is the one that needs to be identical in both sections of the channel. Otherwise, a different formulation for $\overline{C_f}$ is required; see Frohnapfel et al. (2024).

The results shown in fig. 3.3 were previously published in Frohnapfel et al. (2024). The alternating rough and smooth surface parts are arranged such that they have the same mean height, which corresponds to the case of submerged rough strips in this previous publication. In this case, the (average) channel height is identical for rough and smooth sections of the surface. As can be seen in fig. 3.3, the drag curves for two different strip widths differ, despite the fact that 50% of the surface is rough in both cases. In addition, the data do not indicate fully rough behaviour (i.e. a Re-independent C_f) for the rough strips within the Reynolds number range considered. However, there is an intermediate Reynolds number range in which the data appear to remain at a constant C_f similar to a fully rough behaviour before dropping again to lower values.

The wide-strip limit for a turbulent channel flow according to [NSGF22b] is included in fig. 3.3. It can be seen that it clearly underpredicts the measured C_f curves, indicating that the assumption of local equilibrium is indeed not valid. In fact, the wide-strip limit underestimates the drag for both s and most Reynolds numbers. While both cases have a 50% surface coverage their global drag differs, indicating that both surfaces induce different deviations from the wide-strip limit and the underlying equilibrium assumption. [NSGF25]

In the following sections, a simpler, better-defined geometry – streamwise-aligned ridges – is studied to analyse these deviations from the wide-strip limit in more detail, first for laminar and then for turbulent flow.

3.2.2 Global drag of laminar flow over streamwise-aligned ridges

We aim to estimate the global skin friction coefficient $\overline{C_f} = 2\overline{u_\tau}^2/\overline{u_b}^2$ (where $\overline{(\cdot)}$ denotes spanwise-averaged quantities), expressed in terms of the friction velocity u_τ and bulk velocity u_b, for a channel with structured walls. The global friction coefficient can also be expressed in terms of the mean pressure gradient Π,

$$\overline{C_f} = \frac{2\Pi\tilde{h}}{\rho\overline{u_b}^2} = \frac{8\Pi\tilde{h}^3}{\rho\overline{\dot{V}}^2}, \tag{3.4}$$

where ρ is the fluid density, $\tilde{h}$ is a reference channel half-height (to be defined later) and $\overline{\dot{V}}$ is the spanwise-averaged flow rate per unit width. As discussed before, we postulate that two flows which are both in local equilibrium with their respective boundary conditions need to have the same mean streamwise pressure gradient in order to co-exist without a separating wall.

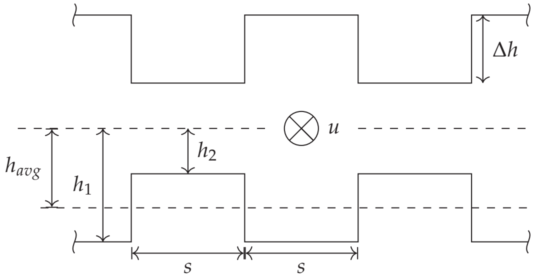

Figure 3.4: Sketch of the spanwise-periodic ridge-type setup. Mean flow direction is perpendicular to the drawing plane. Adapted from [NSGF25].

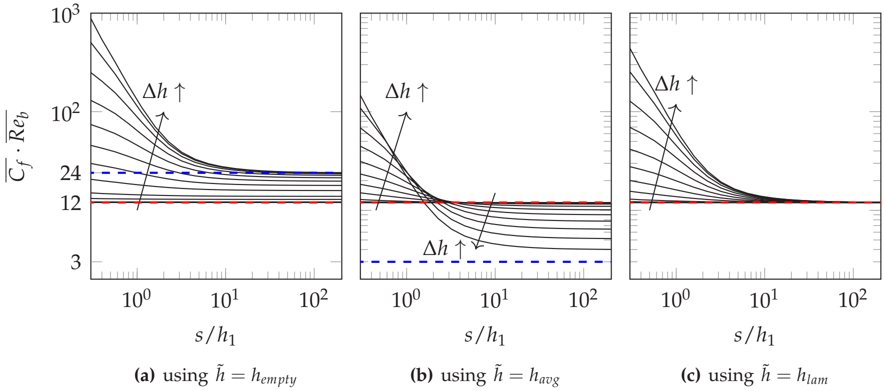

Figure 3.5: Product of $\overline{Re_b}$ and $\overline{C_f}$ for laminar flow over streamwise-aligned ridges. Displayed are $\Delta h/h_1 = 0.1, 0.2, ..., 0.9$, (dashed red) the value from the canonical laminar relation, $\overline{Re_b} \cdot \overline{C_f} = 12$ and (dashed blue) the $s \to \infty$ asymptote for the case $h_2 \to 0$. Adapted from [NSGF25].

For a laminar channel with spanwise alternating channel half-heights h_1 and $h_2 < h_1$ (see fig. 3.4), in the limit of $s/h_i \gg 1$ (i.e. the additional surface area of the step and interface transients are negligible), the resulting skin friction coefficient may be computed analytically using the classical Hagen–Poiseuille relation:

$$\overline{C_f} = \frac{12}{\overline{\mathrm{Re}_b}} \cdot \frac{\tilde{h}^3}{\frac{1}{2}(h_1^3 + h_2^3)} \quad \text{with} \quad \overline{\mathrm{Re}_b} = \frac{\overline{u_b} 2\tilde{h}}{\nu}, \tag{3.5}$$

where $\tilde{h}$ is any reference height (to be defined). Note that $\overline{u_b}$ is the volumetric flow rate per unit width divided by $\tilde{h}$. Therefore, $\overline{\mathrm{Re}_b}$ is independent of the choice of $\tilde{h}$ for a known flow rate. [Equation (3.5) thus provides the wide-strip limit for laminar flow over streamwise-aligned rectangular ridges.]

The choice of the reference height $\tilde{h}$ is relevant when comparing the skin friction coefficient of different setups, and poor understanding of the influence of the reference height may prompt problematic statements regarding changes in drag. Therefore, we consider different choices for $\tilde{h}$ in the evaluation of $\overline{C_f}$. The corresponding results are shown in fig. 3.5. All plots show the numerically evaluated $\overline{C_f \mathrm{Re}_b}$ for different ridge dimensions. The ridge geometry is characterised by its height $\Delta h = h_1 - h_2$ and its width s/h_1.

Three different choices for the reference channel half-height are considered. The first is the 'empty channel height' $\tilde{h} = h_{empty} = h_1$ (fig. 3.5a) and the second is a 'meltdown height' [(or average height)] $\tilde{h} = h_{avg} = \frac{1}{2}(h_1 + h_2)$ (fig. 3.5b). The dashed red line in these plots corresponds to the analytical solution of a smooth-wall laminar channel flow, $\overline{C_f \mathrm{Re}_b} = 12$, and the blue dashed line represents the limit for very tall ridges [blocking most of the available space ($s/h_1 \gg 1$, $h_2 \to 0$)] according to eq. (3.5). The obtained results in these two plots can easily lead to different conclusions for one and the same numerical results.

Using $\tilde{h} = h_{empty}$ (fig. 3.5a) yields an increase in $\overline{C_f}$ with increasing ridge height Δh, while using $\tilde{h} = h_{avg}$ (fig. 3.5b) yields a decrease in $\overline{C_f}$ with increasing ridge height (for the limiting case of $h_2 \to 0$, a 'skin friction reduction' of 75% can be observed).[4]

A third alternative is shown in fig. 3.5c. It is introduced to recover the smooth-wall solution $\overline{C_f \mathrm{Re}_b} = 12$ for very wide ridges. Here, the reference channel half-height is defined as:

$$\tilde{h} = h_{lam} = \sqrt[3]{\frac{1}{2}\left(h_1^3 + h_2^3\right)}, \tag{3.6}$$

h_{lam} is the half-height of the (homogeneous smooth-wall) channel that has the same relationship between $\dot{V}$ and Π as the channel with ridge heights h_1 and h_2, for $s/h_i \gg 1$.

As anticipated, $\overline{C_f}$ is independent of the ridge height in the limit of large s when evaluated based on h_{lam} (fig. 3.5c), and $\overline{C_f} = 12/\overline{\mathrm{Re}_b}$ is recovered in this case. The visible deviation from $\overline{\mathrm{Re}_b} \cdot \overline{C_f} = 12$ for smaller strip sizes s/h_1 and large ridge heights $\Delta h/h_1$ stems from the fact that the flow is not in local equilibrium. This plot thus provides a measure of the impact of the transition region between the two flow regions on the global drag.

[4] This statement generally also holds for walls that are not shaped like a step function, e.g. Türk et al. (2014) reported a 50% 'drag reduction' for a channel with sinusoidal walls at the limit of large wavelengths, where the skin friction is evaluated with h_{avg}.

[NSGF25] In addition, we observe that, for a given pressure gradient, the flow rate per unit width $\dot{V}$ tends towards the [respective fully developed state] in the thinner part of the channel, but not equally so in the thicker part of the channel (since $h_1 > h_2 \rightarrow s/h_1 < s/h_2$) where it remains below the [corresponding fully developed] condition. In consequence, for finite ridge widths, the global flow rate for a given pressure gradient is lower than in the case of very wide ridges.

3.2.3 Global drag of turbulent flow over streamwise-aligned ridges

In the following, we compare these results to the case of turbulent flow over ridges. Similar to the laminar case, an explicit expression for the global friction coefficient for the case of $s \gg h_i$ can be given based on the correlation of Dean (1978), $C_f = 0.073\,\mathrm{Re}_b^{-1/4}$. We find

$$\overline{C_f} = 0.073\overline{\mathrm{Re}_b}^{-1/4} \frac{\tilde{h}^3}{\left(\frac{1}{2}\left(h_1^{12/7} + h_2^{12/7}\right)\right)^{7/4}}. \tag{3.7}$$

In analogy to the laminar case it is possible to define a channel half-height that recovers the smooth wall correlation (which is given by the Dean correlation $\overline{C_f \mathrm{Re}_b}^{1/4}/0.073 = 1$ for turbulent flow) for very wide ridges:

$$\tilde{h} = h_{turb} = \left(\frac{1}{2}\left(h_1^{12/7} + h_2^{12/7}\right)\right)^{7/12}. \tag{3.8}$$

In order to investigate the influence of finite s under turbulent flow conditions, DNS simulations of channel flow with streamwise-aligned ridges have been performed for the cases listed in table 3.1. The employed numerical code is NekRS [...] (Fischer et al. 2022). The simulations were set up using a body-conformal mesh and streamwise periodicity, with streamwise box length $L_x = 4\pi h_1$. Element order $n = 7$ and BDF3 / EXT3 time-stepping was used. The simulations were conducted at a prescribed constant global flow rate.

Figure 3.6 shows the resulting skin friction coefficients for different choices of $\tilde{h}$ in analogy to the laminar results shown in fig. 3.5. The smooth-wall reference $\overline{C_f}\ \overline{\mathrm{Re}_b}^{1/4}/0.073 = 1$ is indicated by a black line in these plots. The coloured horizontal lines (orange, green, blue) on the right ordinate of each panel depict the limiting case of very wide ridges for the three considered values of Δh. For increasing s, the computed values for $\overline{C_f}$ clearly decrease towards the respective limiting cases, which collapse onto the smooth-wall reference when using h_{turb}. Similar to the laminar results

s/h_1	$\Delta h/h_1$	L_z/h_1	N_{el}	Re_b
—	0	4	153600	8000
1	0.132	4	475200	12000
1	0.25	4	124800	8000
1	0.5	4	110400	8000
2	0.25	4	124800	8000
2	0.5	4	123200	8000
8	0.25	16	499200	8000
8	0.5	16	492800	8000

Table 3.1: Metadata for discussed cases of fully developed turbulent flow over streamwise-aligned ridges. From [NSGF25].

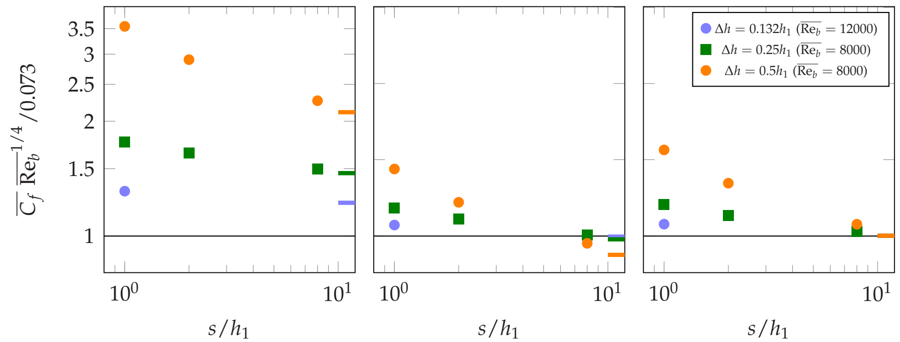

(a) using $\tilde{h} = h_{empty}$ **(b)** using $\tilde{h} = h_{avg}$ **(c)** using $\tilde{h} = h_{turb}$

Figure 3.6: Diagnostic function $\overline{C_f}\,\overline{\mathrm{Re}_b}^{-1/4}/0.073$ for the considered turbulent cases. Displayed are $\Delta h/h_1 =$ 0.25 (green), 0.5 (orange) and 0.132 at a higher Reynolds number. The coloured horizontal lines on the right-hand axis of each subplot indicate the expected value for very large s, i.e. the wide-strip limit for the ridge geometry. The subplots are evaluated with different definitions for $\tilde{h}$. Due to the definition of h_{turb}, the wide-strip limit is equal to 1 for all cases in subplot (c). Adapted from [NSGF25].

discussed before, a 'skin friction drag reduction' can be obtained for high s, when evaluating the numerical data using h_{avg}. We note that there is no right or wrong choice for $\tilde{h}$ in the evaluation of C_f. The different choices simply lead to a presentation of the results that are likely to be interpreted differently. For any data evaluation of this type it is thus of utmost importance to communicate how an evaluation of $\overline{C_f}$ was performed.

For the present study it is important to realise that there is a qualitative similarity between laminar (fig. 3.5) and turbulent (fig. 3.6) cases, irrespective of the choice of $\tilde{h}$, which suggests that the effect of finite s on $\overline{C_f}$ is mostly a geometric one. This is also supported by closer investigation of the spanwise distribution of streamwise velocity as

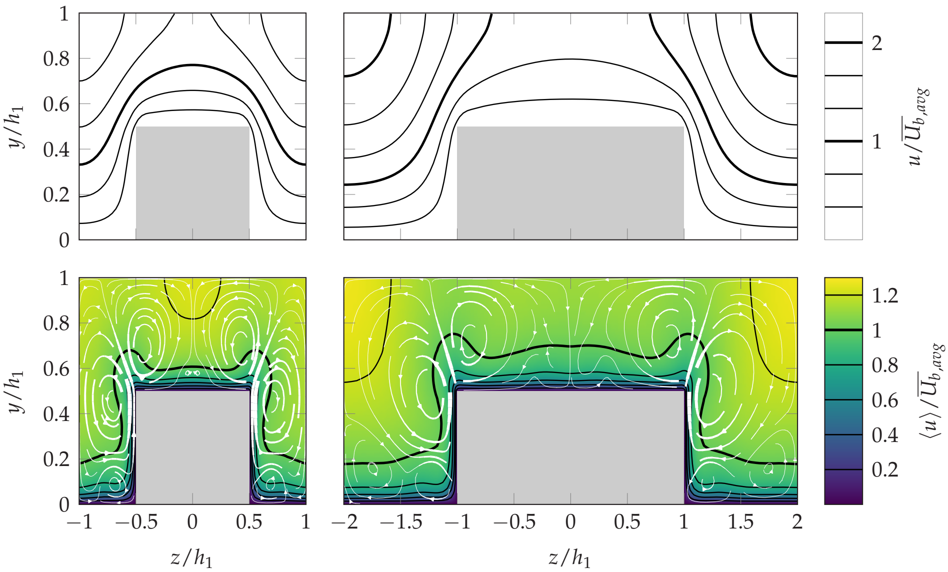

Figure 3.7: Comparison of laminar (top) and turbulent (bottom) flow over streamwise-aligned ridges for $\Delta h = 0.5h_1$. Left: $s/h_1 = 1$, Right: $s/h_1 = 2$. Top: Laminar flow at constant bulk flow rate, Bottom: Turbulent flow at constant bulk flow rate ($\overline{\mathrm{Re}_b} = 8000$). The resulting secondary flow is indicated with streamlines; line thickness of the streamlines indicates magnitude. The maximum magnitude is 5.3% $\overline{u_{b,avg}}$ ($s/h_1 = 1$) and 5.5% $\overline{u_{b,avg}}$ ($s/h_1 = 2$). Adapted from [NSGF25].

discussed in the following. Figure 3.7 depicts contours of streamwise velocity in part of the channel cross-section for the laminar (top) and turbulent (bottom) case for two different ridge widths. We recall that the width of the ridge and of the valley between the ridges is always identical in the present study since the ridges resemble surface roughness that covers 50% of the surface. The velocity contours in the turbulent flow case are significantly more complex than the laminar one since turbulent secondary flow develops in the presence of ridges. This mean flow in the spanwise and wall-normal velocity components is indicated by the white in-plane streamlines in fig. 3.7 (bottom), which are placed in front of a colour map of the streamwise mean velocity. The turbulent secondary flow clearly impacts the streamwise velocity distribution. Nevertheless, the laminar and turbulent contours of streamwise velocity carry some similarities when one considers the changes that occur with increasing ridge width.

Consider the wall-normal gradient of the streamwise mean velocity (i.e. the local wall shear stress) for $s/h_1 = 1$ (left) and $s/h_1 = 2$ (right). For each flow condition, laminar and turbulent, the wall shear stress distribution on the ridge sides and the ridge top, close to the edge, remains very similar when doubling the ridge width. On top of the

s/h_1	$\Delta h/h_1$	$R_{\dot{V}}$ (turbulent)	$R_{\dot{V}}$ (laminar)
1	0.132	0.0393	0.0332
1	0.25	0.1024	0.1125
1	0.5	0.2568	0.3468
2	0.25	0.0679	0.0580
2	0.5	0.1661	0.1837
8	0.25	0.0141	0.0133
8	0.5	0.0390	0.0448

Table 3.2: Relative flow rate loss $R_{\dot{V}} = 1 - \overline{\dot{V}_{actual}}/\overline{\dot{V}_{expected,\ limit}}$ for the pressure gradient encountered in the respective simulations in which Re_b was prescribed. Note that for the laminar case, $R_{\dot{V}}$ is independent of pressure gradient or Reynolds number. From [NSGF25].

ridge the flow rate decreases with increasing s (fewer contours in the laminar case, lower values of $\overline{u}$ in the turbulent case), which also results in a reduction of the shear stress in the ridge centre. With increasing s there is a flow rate increase above the valley for laminar and turbulent flow, which is mostly located further away from the wall while the wall shear stress remains similar. This results in a smaller total wall shear stress for the wider ridge, as reflected by the decrease in the diagnostic function ($\overline{\mathrm{Re}_b C_f}$ for the laminar case, $\overline{\mathrm{Re}_b}^{1/4}\overline{C_f}$ for the turbulent case) with increasing s for laminar and turbulent flow conditions.

The observed increase in the diagnostic function with smaller s can be translated into a 'flow rate loss'. In the limiting case of very wide ridges (and valleys) the maximum achievable global flow rate for a given pressure gradient is realised. The finite width of ridges (and valleys) reflects in a reduction of the achievable flow rate compared to the expected maximum one. The relative flow rate loss is thus defined as

$$R_{\dot{V}} = 1 - \frac{\overline{\dot{V}_{actual}}}{\overline{\dot{V}_{expected,\ limit}}}. \tag{3.9}$$

Table 3.2 shows the results for all considered laminar and turbulent cases. As expected, $R_{\dot{V}}$ is positive, indicating that the achievable flow rate for ridges (and valleys) with finite width is lower than the expected one for very wide ridges. The data show that $R_{\dot{V}}$ increases with larger Δh and smaller s for both laminar and turbulent flow conditions. To first approximation, the obtained values for $R_{\dot{V}}$ agree reasonably well for laminar and turbulent flow, which supports the hypothesis that the friction increase due to narrower ridges (i.e. the deviation from the local equilibrium state) is mainly a geometric and not a turbulent effect, despite the emergence of strong secondary flow in

[NSGF25] the turbulent case. Stated differently, the deviation from the limiting [local] equilibrium case is mainly caused by the transients between the subdomains, and those transients and their effect are comparable in magnitude for the laminar and turbulent regimes. In addition, we note that $R_{\dot{V}}$ is independent of the prescribed pressure gradient (and thus the Reynolds number) in the laminar regime while a (small) Reynolds number dependency is expected for turbulent flow conditions.

3.2.4 A-priori prediction of inhomogeneous skin friction from homogeneous reference data

In the previous sections, the wide-strip limit has been introduced as the consequence of local equilibrium above each channel segment. For the example of finite-width ridges, the effect of finite s was quantified in terms of a relative loss of flow rate. In a next step, the wide-strip limit for a heterogeneous surface is augmented with information about how the finite strip width affects global drag.

The extended modelling approach is based on the idea of a hydraulic channel height which is introduced in the following. Similar to a hydraulic diameter for duct flows, the hydraulic channel height refers to an effective channel height of a non-smooth channel that recovers the $C_f(\mathrm{Re}_b)$-relation for a smooth-wall channel. In contrast to the hydraulic diameter for ducts, the hydraulic channel height is not defined based on geometric properties, but is derived as a result from a pressure drop and volume flow rate measurement (Von Deyn et al. 2022; Frohnapfel et al. 2024). A rough-walled channel reduces the flow rate at a given pressure gradient Π compared to a smooth channel with the same (average) channel height. The hydraulic channel height corresponds to the reduced height of a smooth-wall channel in which the flow rate measured for the rough-wall channel is found for the same Π. Consequently, the hydraulic channel height is not only a function of the roughness (e.g. in terms of the equivalent sand grain size k_s) but also of the operating condition (in terms of Re_b or Π). The hydraulic channel half-height h_{hyd} normalised by the geometrical channel half-height h is shown in fig. 3.8 for the homogeneous rough surface (P60 sandpaper). It can be seen that P60 sandpaper (placed homogeneously on both channel walls in our channel flow facility) induces a reduction of h_{hyd}/h by approx. 10% (almost 30%) at $\mathrm{Re}_b = 1 \times 10^4$ (7×10^4).

This observation is used to construct a modelling approach for the global friction coefficient of surfaces with streamwise-aligned roughness strips. We assume that the combination of rough and smooth strips in a channel can be represented by a local narrowing of the channel. The idea is sketched in fig. 3.9. The rough-wall section

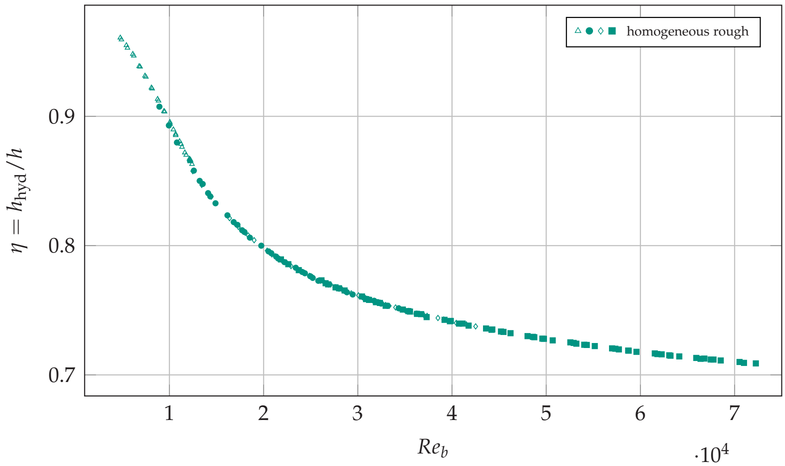

Figure 3.8: Hydraulic channel height ratio $\eta = h_{\mathrm{hyd}}/h$ for P60 sandpaper. Data from Frohnapfel et al. (2024). Adapted from [NSGF25].

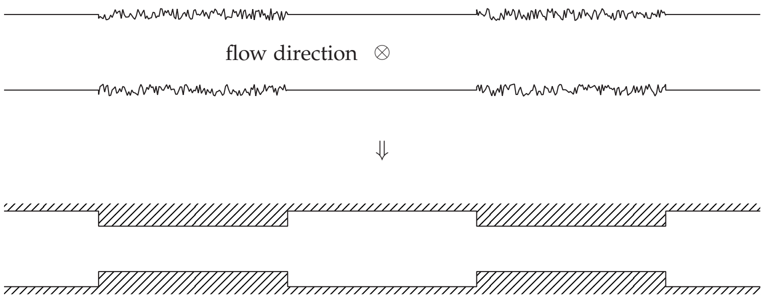

Figure 3.9: Sketch of the modelling approach: rough strips are identified with a locally narrower channel. Adapted from [NSGF25].

of the channel is modelled as a channel with reduced height in such a way that a streamwise-aligned ridge is inserted instead of the rough strip. We thus obtain a channel with streamwise-aligned ridges in which the ridge height depends on the operating conditions, i.e. the applied pressure drop, in the channel. The width of the ridges corresponds to the width of the rough strips. Accordingly, the wide-strip limit is modelled by two neighbouring (very wide) channels with different height. The same pressure gradient is applied to each of these channels, resulting in different flow rates: the channel with smaller channel height yields less flow rate for the same pressure gradient.

In the next step, we employ $R_{\dot{V}}$ as a correction factor to the existing global drag prediction for the wide-strip limit (see eq. (3.3)). This correction factor leads to a surface-specific flow rate reduction for a prescribed pressure drop or – in other words – to an increase in $\overline{C_f}$ for a certain $\overline{\mathrm{Re}_b}$. This general tendency is in agreement with our observations for fig. 3.3: the measured values of $\overline{C_f}$ are higher than those predicted by the wide-strip limit and indicate a surface-specific global drag.

Based on the observed similarity in the relative flow rate loss for laminar and turbulent flows over streamwise-aligned ridges, we decide to employ the laminar reference data to formulate a new predictive model for the global drag of spanwise heterogeneous rough surfaces. [...]

We hypothesise that the friction behaviour, in particular the spanwise transients before a local equilibrium with the wall boundary condition is reached, is similar to that found in a channel flow with streamwise-aligned ridges.[5] Due to the discussed similarity between turbulent and laminar data with respect to these transients, we rely on the laminar data for the model formulation. While h_1 is defined by the geometrical channel half-height and s by the strip width, a definition for the ridge height $\Delta h = h_1 - h_2$ remains to be chosen. This is done in the following way: The prediction of the global drag coefficient in the wide-strip limit relies on two contributions to the global flow rate: one in the smooth section of the channel $\dot{V}_{smooth}$ and one in the rough section of the channel $\dot{V}_{rough}$. The ratio of these two contributions, $\dot{V}_{rough}/\dot{V}_{smooth}$, can be easily computed for any Reynolds number. Similar ratios are computed for the laminar flow in the structured channel with very wide ridges (and valleys). In this case, the global flow rate consists of the flow rate in the channel section with height h_1 ($\dot{V}_{h1}$) and the flow rate in the channel section with height h_2 ($\dot{V}_{h2}$). This yields a flow rate ratio $\dot{V}_{h2}/\dot{V}_{h1}$ for every $\Delta h = h_1 - h_2$. The remaining model parameter Δh is now chosen such that

$$\frac{\dot{V}_{rough}}{\dot{V}_{smooth}} = \frac{\dot{V}_{h2}}{\dot{V}_{h1}}.$$

Since $\dot{V}_{rough}/\dot{V}_{smooth}$ depends on the applied pressure gradient, Δh is not constant for one particular type of roughness, but depends on the operating condition Π.

Once h_1, s and Δh are fixed for each Π, the correction factor $R_{\dot{V}}$ is extracted for the corresponding laminar database of the structured channel. This correction factor is used to compute the actual flow rate that enters eq. (3.4) following eq. (3.9). The reduced global flow rate results in an increase of the predicted global friction coefficient which depends on the operating conditions and the strip width.

[5] This requires that the additional drag introduced by the ridge side walls does not dominate, as is the case for $s \to 0$.

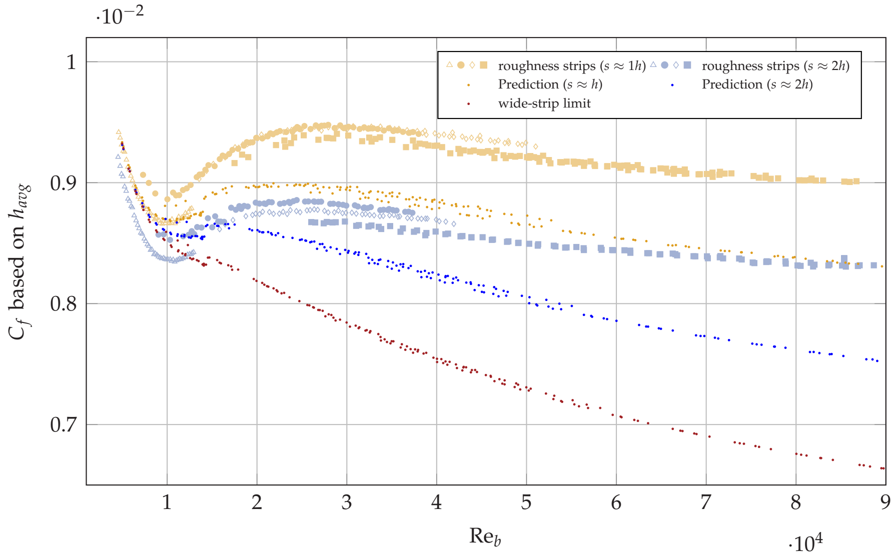

Figure 3.10: Model predictions for the friction coefficient of rough strips of width $s \approx h$ and $s \approx 2h$ in comparison to the wide-strip limit and the measurement data of Frohnapfel et al. (2024). While light yellow and blue colours represent the measurement data for $s \approx h$ and $s \approx 2h$, respectively, the different symbols within each colour correspond to different flow rate measurement procedures within the experiment. Adapted from [NSGF25].

When comparing the prediction with the measurement data, attention must be paid to the choice of $\tilde{h}$, which appears directly in eq. (3.4). For the presented experimental results, [C_f and Re_b were evaluated based on the geometrical (average) channel height. The same choice is used] in the model-based prediction to ensure comparability.

Figure 3.10 shows the obtained predictions for $\overline{C_f}$ for two different values of s along with the experimental data. Results for the narrower strips $s \approx h$ are displayed in yellow and for the wider strips $s \approx 2h$ in blue. It can clearly be seen that the agreement with experimental data is significantly improved compared to the wide-strip limit (in brown). We note that the scatter in the experimental data is mainly related to uncertainties in the volume flow rate measurement; details can be found in the appendix of Gatti et al. (2015). [...]

The new prediction correctly captures the measured effect of larger $\overline{C_f}$ for smaller s. In fact, the obtained agreement between prediction and measurements is surprising considering the strong simplifications introduced in the model formulation. Therefore, the quantitative agreement might be coincidental to some degree. In our opinion, the observed qualitative agreement of the predicted drag behaviour is the most important result. The predictive model captures different regimes of the $\overline{C_f}(\overline{\mathrm{Re}_b})$-curve. This

[NSGF25]

includes effects at low Re_b (small difference between different values for s since homogeneous flow rates also differ less), intermediate Re (near-constant C_f over a limited Re range) and high Re_b (decreasing C_f).

Based on these model results, the emergence of an apparent fully rough condition in an intermediate Reynolds number range can be related to a strongly simplified interplay of the two subsurfaces, in which only a spanwise flow rate variation is considered. The model suggests that a range of constant $\overline{C_f}$ will be more pronounced for narrow surface structures and less pronounced for wider ones.

3.3 Numerical setup

The flow inside a plane channel whose walls feature streamwise-aligned roughness strips is computed numerically by means of direct numerical simulation (DNS). Two configurations are considered:

- fully developed turbulent channel flow with periodic boundary conditions in the streamwise direction, and
- spatially developing turbulent channel flow obtained by a recycling approach.

In both cases, streamwise-aligned roughness strips are modelled via a slip-length boundary condition (cf. section 3.3.2), applied symmetrically on the top and bottom walls and periodically in the spanwise direction. The channel half-height is denoted by $\delta = \frac{1}{2} l_y$.

[NSGF22b]

The DNS in this work are performed using the open-source solver XCompact3D (Laizet and Lamballais 2009; Laizet and Li 2011; Bartholomew et al. 2020), which adopts sixth-order compact finite differences for computing spatial derivatives. In the streamwise and spanwise directions, the mesh is homogeneous; in the wall-normal direction stretching is used to refine the mesh towards the wall such that the first node is placed at $y^+ = 1$.

The flow is advanced in time with an explicit third-order Runge–Kutta scheme with a fixed time step, yielding a CFL number of approximately 0.4 in the wall-normal direction. Statistics are then collected during runtime; the averaging time is given in tables 3.4 and 3.5. For the fully developed data first presented in [NSGF22b], the flow is driven by a constant pressure gradient (CPG), so that the average wall shear stress $\overline{\tau_w}$ is fixed. This amounts to prescribing the friction Reynolds number, $\mathrm{Re}_\tau = \frac{\delta \overline{u_\tau}}{\nu} = 180$,

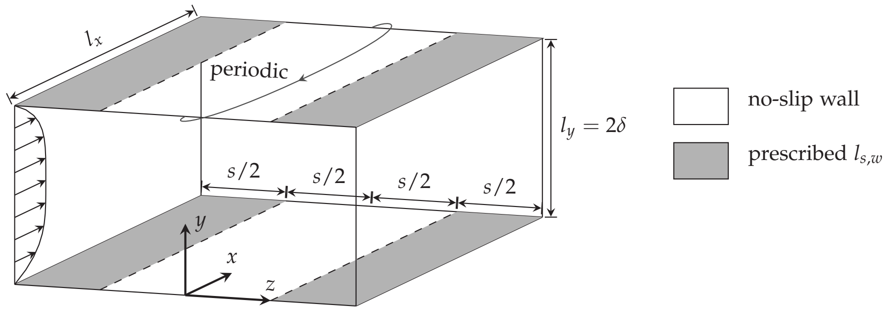

Figure 3.11: Illustration of the numerical setup for the fully developed cases, as well as location of the coordinate system for plots. This unit cell is repeated in spanwise direction as indicated in table 3.4.

Re_τ	s/δ	Grid resolution	l_x	l_y	l_z	Δy^+
180	hom., $0.25, 0.5, 1$	$256 \times 193 \times 128$	8δ	2δ	4δ	$1.001 \cdots 3.513$
180	$0.75, 1.5, 3$	$256 \times 193 \times 384$	8δ	2δ	12δ	$1.001 \cdots 3.513$
180	$2, 4, 5, 8, 10, 16$	$256 \times 193 \times (32 l_z/\delta)$	8δ	2δ	$4 \cdot s$	$1.001 \cdots 3.513$
540	hom.	$768 \times 451 \times 384$	8δ	2δ	4δ	$1.003 \cdots 5.741$

Table 3.3: Grid properties for fully developed cases. Adapted from [NSGF22b].

Case	Re_τ	s/δ	$l^+_{s,z}$	$T\overline{u_\tau}/\delta$
`NSBC180`	180	hom.	0	31.9
`NSBC540`	540	hom.	0	35.3
`SLW180`	180	hom.	1..10	127.8
`SLW540`	540	hom.	0.5..10	12.8
`SLW180_inhom`	180	$0.25, 1, 4$	9	153.3
		$0.5, 0.75, 1.5, 2, 3, 5, 8, 10, 16$		127.8

Table 3.4: Statistical averaging times for fully developed cases. Adapted from [NSGF22b].

where ν is the kinematic viscosity of the fluid. This is advantageous for determining the wide-strip limit (see section 3.2.1), where the flow rate corresponding to a given imposed pressure gradient is required. For the developing channel-flow cases, a velocity-recycling approach is used instead, corresponding to constant bulk flow rate (CFR) forcing.

In order to model streamwise-aligned alternating strips of rough and smooth surfaces, a spanwise slip $l_{s,w} > 0$ is prescribed as a function of z [(and, for developing flow, x)] in order to model strip type roughness. [The roughness modelling by means of the slip length boundary condition is elaborated on in section 3.3.2.] The present formulation ensures that the boundary condition does not have any influence on laminar flow

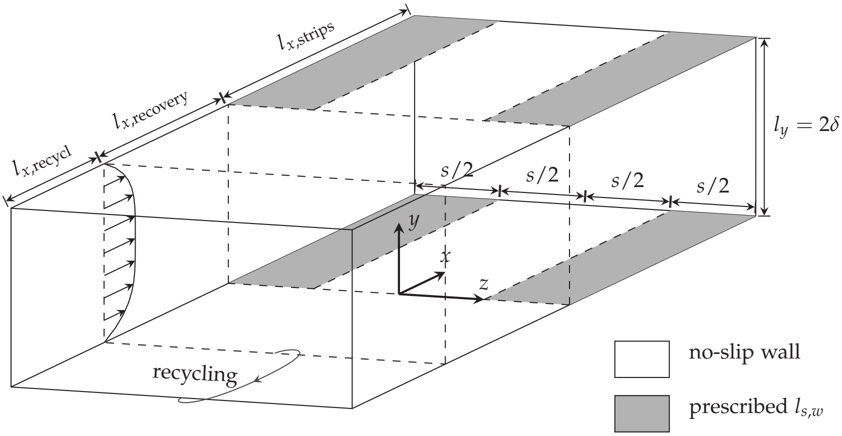

Figure 3.12: Illustration of the numerical setup for developing channel flow, as well as location of the coordinate system for plots. This unit cell is repeated in spanwise direction as indicated in table 3.5. The streamwise lengths are not drawn to scale.

Type	Re_b	s/δ	grid resolution	l_x	l_y	l_z	$Tu_{\tau 0}/h$
developing	4240	1, 2, 4	$4097 \times 193 \times 256$	128δ	2δ	8δ	380
		1.5	$4097 \times 193 \times 288$			9δ	
periodic	4240	1, 2, 4	$512 \times 193 \times 256$	16δ	2δ	8δ	414
		1.5	$512 \times 193 \times 288$			9δ	

Table 3.5: Grid and averaging parameters for developing and corresponding (CFR) periodic cases. $^+$ indicates non-dimensionalisation with $u_{\tau 0}$ and ν.

[NSGF22b]

conditions but leads to enhanced drag for turbulent flow only. Note that under CPG conditions this drag enhancement corresponds to a reduction of the flow rate. [For $x > 0$, and in the fully developed case,] 50 % of the surface area has a fixed spanwise slip length applied, and no-slip boundary conditions are applied to the other half. The strip width s/δ varied over two orders of magnitude. [...] A slip length of $l_{s,w} = 0.05\delta$ ($l^+_{s,w} = 9$) chosen, corresponding to a roughness function of $\Delta U^+ \approx 3$ for a homogeneously rough surface at $\mathrm{Re}_\tau = 180$ (see section 3.3.2).

3.3.1 Developing turbulent flow

For the developing cases, the simulation domain is split into three streamwise sections, see fig. 3.12. The first section with no-slip boundary condition (length $l_{x,\text{recycl}}$) serves as velocity-recycling region: the velocity at $x = l_{x,\text{recycl}} = 8\delta$ is imposed as the inlet velocity in the next time step, rescaled to enforce a fixed bulk flow rate. $l_{x,\text{recycl}}$ lies within the recommended range for the streamwise length used in periodic channel flow simulations (Lozano-Durán and Jiménez 2014). The periodicity imposed by the velocity recycling modifies the two-point correlation $\langle u_i'(x,t)u_j'(x+\Delta x,t)\rangle$, introducing an artificial maximum at $\Delta x = l_{x,\text{recycl}}$ and its multiples. Through numerical, turbulent and molecular diffusion, this peak decays with streamwise distance from the recycling plane; precursor simulations indicated a decay to background levels by a streamwise separation of $\Delta x = 4l_{x,\text{recycl}}$. Accordingly, $l_{x,\text{recovery}} = 4l_{x,\text{recycl}}$ is chosen. At the end of the recovery section a fully developed turbulent flow at $\text{Re}_{\tau 0} \approx 180$ in equilibrium with the smooth wall is obtained.[6]

Downstream, the flow enters the inhomogeneous section with a length of $l_{x,\text{strips}} = 88\delta$. The inhomogeneous section features streamwise-aligned roughness strips with 50 % surface coverage, again symmetric on top and bottom walls. The rough sections of the wall are also modelled through the spanwise slip-length boundary condition, later detailed in section 3.3.2. Unlike in the fully developed cases, the viscous length scale $\delta_v = \nu/u_\tau$ varies along x; consequently, the smooth-wall section and the various strip sizes yield different (spanwise-averaged) viscous length scales, which are unknown a priori. The spanwise slip length $l_{s,w}$ is therefore prescribed as constant in outer units, $l_{s,w} = 0.05\delta$. Strip widths $s/\delta = 1, 1.5, 2$, and 4 are investigated, as these dimensions lead to the most significant changes in global skin friction drag (cf. section 3.4.2).

The domain is periodic in the spanwise direction. The unit cell displayed in fig. 3.12 is repeated along z to obtain a spanwise box size of at least 8δ. A zero-gradient boundary condition is imposed on the outlet.

The simulations are initialised by tiling a snapshot from a periodic, smooth-wall case at $\text{Re}_\tau = 180$. After an initial transient of $T_{trans.}u_{\tau 0}/\delta = 60$, statistics are collected for at least $Tu_{\tau 0}/\delta = 380$ large-eddy turnover times. The lack of a statistically homogeneous streamwise direction dictates a high sampling frequency: the decorrelation time of pointwise velocity statistics is $\mathcal{O}(t_v)$ where $t_v = \delta_v^2/\nu$, and run-time statistics are sampled every $0.38t_{v0}$. To further improve collected statistics, they are phase-averaged in z and y; however, the z symmetry was not enforced. The deviation from this symmetry therefore indicates the statistical uncertainty of the obtained mean values.

Two validation steps are performed. First, the implementation of the velocity recycling is validated by asserting that the terms of the Reynolds stress transport equation within

[6] Smooth-wall references are denoted with a '0' subscript.

the recovery region coincide with those of a fully developed (no-slip) reference case. Second, the statistics at the end of the inhomogeneous section are compared against a periodic reference case with the same boundary condition and run at the same bulk flow rate (see table 3.5). The grid resolution is identical to that used in the corresponding periodic simulations.

3.3.2 Slip length roughness model

Following the suggestion by Luchini (2013) we employ a spanwise slip length to model the drag increasing effect of small roughness onto the turbulent flow field. [...] A slip length (Navier 1823) relates the wall slip velocity with the wall-normal velocity gradient at the wall. It can be understood as the distance between a virtual wall, where no-slip is thought to apply, and the actual wall, which then has a non-zero velocity. For spanwise slip the boundary conditions are given by

$$w_{y=0} = l_{s,w}(z) \left.\frac{\partial w}{\partial y}\right|_{y=0}, \quad w_{y=2\delta} = -l_{s,w}(z) \left.\frac{\partial w}{\partial y}\right|_{y=2\delta}, \tag{3.10}$$

where $l_{s,w}(z)$ denotes the spanwise slip length, which is the quantity that can vary along the spanwise direction. We note that a slip in streamwise direction can be inserted in an analogous way with $l_{s,u}$ as streamwise slip length. [...]

Especially from research on turbulent drag reduction via riblets, it is established knowledge that the change in drag is related to the difference $\Delta l = l_{s,u} - l_{s,w}$ between streamwise and spanwise slip length, so that drag is reduced when Δl is positive. In this context, slip length is typically referred to as 'protrusion height' and Δl for streamwise and spanwise flow can be used to predict the achievable drag reduction rate for small riblets (Luchini et al. 1991; Bechert and Bartenwerfer 1989). In contrast, an increase of the spanwise slip length leads to enhanced near-wall turbulence and thus drag increase (Min and Kim 2004; Fukagata et al. 2006; Busse and Sandham 2012; Gómez-de-Segura and García-Mayoral 2020). In [the present chapter], we employ $l_{s,u} = 0$ and $l_{s,w} > 0$ (and therefore a negative Δl) as a simple model for a rough surface. Standard no-slip $(u = 0)$ and impermeability $(v = 0)$ conditions are applied for the streamwise and wall-normal velocity components at both walls.

Fukagata et al. (2006) and Busse and Sandham (2012) suggested a relation between the dimensionless spanwise slip length and the resulting drag increase. Assuming only minor modifications of the shape of the turbulent velocity profile due to the imposed boundary condition, the corresponding reduction of u_b^+ can be translated into

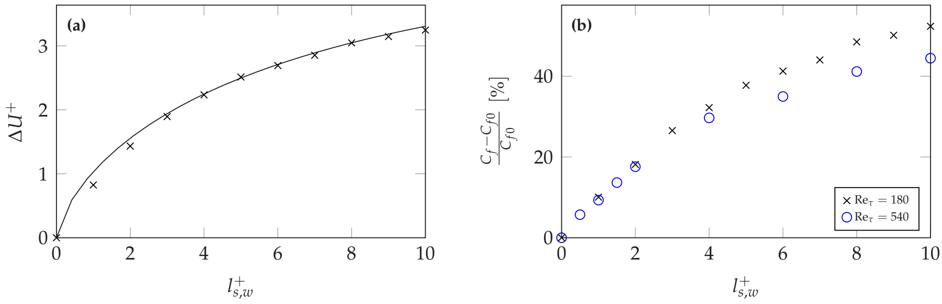

Figure 3.13: (a): Relative velocity deficit $\Delta U^+ = \langle u \rangle^+|_\delta - \langle u \rangle^+|_{\delta,\mathrm{NSBC}}$ for $\mathrm{Re}_\tau = 180$ for different (uniform) values of $l^+_{s,w}$. and (solid line) Relationship suggested by Fukagata et al. (2006), adapted. (b): Relative change in skin friction coefficient C_f compared to the no-slip reference case (denoted by index 0) at the same Re_τ evaluated for $\mathrm{Re}_\tau = 180$ and $\mathrm{Re}_\tau = 540$. Adapted from [NSGF22b].

the Hama roughness function ΔU^+, which is widely used to characterise turbulent flow over rough surfaces. Figure 3.13a shows the correlation proposed by Fukagata et al. (2006) translated into ΔU^+ for the present CPG conditions in comparison with simulation results.[7] They are in excellent agreement. As noted by Fukagata et al. (2006), the observed changes in ΔU^+ are almost independent of Reynolds number, which we confirmed with additional simulations at $\mathrm{Re}_\tau = 540$ (not shown here). For a rough surface, ΔU^+ is expected to increase with Reynolds number. Therefore, it should be noted that simulations with constant l^+_s at different Reynolds numbers do not mimic the Reynolds number dependence of real rough surfaces. For such a study, the prescription of a Reynolds number dependent $l^+_{s,w}$ would be required. In fig. 3.13a it can furthermore be seen that the relationship between ΔU^+ and the spanwise slip length is non-linear. This saturation effect was previously reported by Gómez-de-Segura and García-Mayoral (2020) and is in agreement with the finding of Luchini (2013) that this type of boundary condition is suited for the representation of small roughness only. Nevertheless, a roughness function in the present order of magnitude corresponds to a significant drag increase.

The related increase of C_f under CPG conditions is in the order of 50% for $l^+_{s,w} \approx 10$ ($\Delta U^+ \approx 3$) at $\mathrm{Re}_\tau = 180$ as shown in fig. 3.13b. An increase in Reynolds number leads to a smaller change in skin friction drag coefficient for a fixed ΔU^+ as discussed by Gatti and Quadrio (2016). This is confirmed for the present boundary condition at $\mathrm{Re}_\tau = 540$ where $l^+_{s,w} \approx 10$ corresponds to a drag increase of approximately 45%.

[7] It was confirmed that the present implementation of the slip lengths reproduces the data presented in Min and Kim (2004).

[NSGF22b]

The [uniform] prescription of a spanwise slip length can thus reproduce the mean velocity profile of a turbulent flow over rough surfaces with roughness functions in the order of $\Delta U^+ < 4$ (Fukagata et al. 2006). We note that the spanwise slip length has no direct relation to the roughness topography and cannot reproduce the specific flow signatures of a roughness sublayer (Chung et al. 2021) which is also the case for other roughness models employed in DNS, see e.g. Busse and Sandham (2012). While a slip-length based roughness model has the advantage of replicating the roughness effect of not influencing the drag of laminar flows, the model requires a priori knowledge about the main flow direction as slip is prescribed for the transversal velocity component only.

Finally, the slip-length model assumes scale separation of the roughness and the outer scales of the flow. This greatly simplifies the data analysis and interpretation (see the discussion on defining an appropriate reference height in section 3.2.1 as well as Stroh et al. (2020b) for the consequences of a lack of scale separation), and the resulting unambiguous definition of the wall location makes the slip length model an ideal candidate for a fundamental study of spanwise inhomogeneous surfaces. For example, 'suddenly switching on' the rough wall in a temporal (Andreolli et al. 2025) or spatial sense – as in section 3.5) is possible without introducing an obstacle to the flow (in the Stokes limit).

3.4 Numerical results: Fully developed turbulent flow

3.4.1 Flow organisation

The resulting velocity profiles for selected heterogeneous case are presented in fig. 3.14. The left column of plots is scaled with the global friction velocity $\overline{u_\tau}$ which is defined by the prescribed pressure gradient. Since the pressure gradient is equal in all considered cases, the plots in this column allow to deduce statements on the flow rate in a given section of the inhomogeneous channel. The plots in the right column are scaled with the local friction velocity $u_\tau(z)$, which makes it possible to compare local flow conditions with the homogeneous reference cases.

For $s \ll \delta$, the change in the boundary condition only affects the near-wall region; Townsend's outer layer similarity hypothesis holds (Townsend 1976). For $y > s$, the mean velocity profiles at different z positions collapse when scaled with the global friction velocity $\overline{u_\tau}$ (fig. 3.14a), implicating spanwise homogeneity. The velocity profile in the outer layer falls between the limiting homogeneous cases. For $s \gg \delta$, the flow in each patch centre is barely affected by the change in the boundary condition. [The flow conditions above each patch appear mostly unaffected by the presence of the other patch.] As a consequence, the local velocity profile agrees well with the respective homogeneous cases when scaled with the local friction velocity (which is higher in the $l_{s,w} > 0$ region), see fig. 3.14f. This suggests that the flow above the patches is in near equilibrium with the respective boundary condition, which is not the case for the narrower strips, see figs. 3.14b and 3.14d. Since scaling the velocity profile with the local friction velocity $u_\tau(z)$ represents normalisation with the actual near-wall gradients of these profiles, the observed near-wall collapse of the profiles is expected.

As indicated in fig. 3.14e, the no-slip region provides a preferred pathway to the flow for $s \gg \delta$ due to the (relatively) lower skin friction. Therefore, a high-momentum pathway is located above the no-slip region; i.e. the blue curve is located above the red one. For $s \approx \delta$, the opposite is observed, and the blue curve is located below the red one in fig. 3.14c. The redistribution of momentum due to the secondary motion obviously dominates over the effect of locally lower skin friction drag and a LMP is located over the no-slip region.

The corresponding mean momentum distribution and secondary flow are presented in fig. 3.15. As expected, for $s/\delta = 0.25$, the secondary motions are restricted to a region close to the wall. For $s = \delta$, the secondary vortices expand towards the channel centreplane and give rise to a high momentum pathway over the rough region.

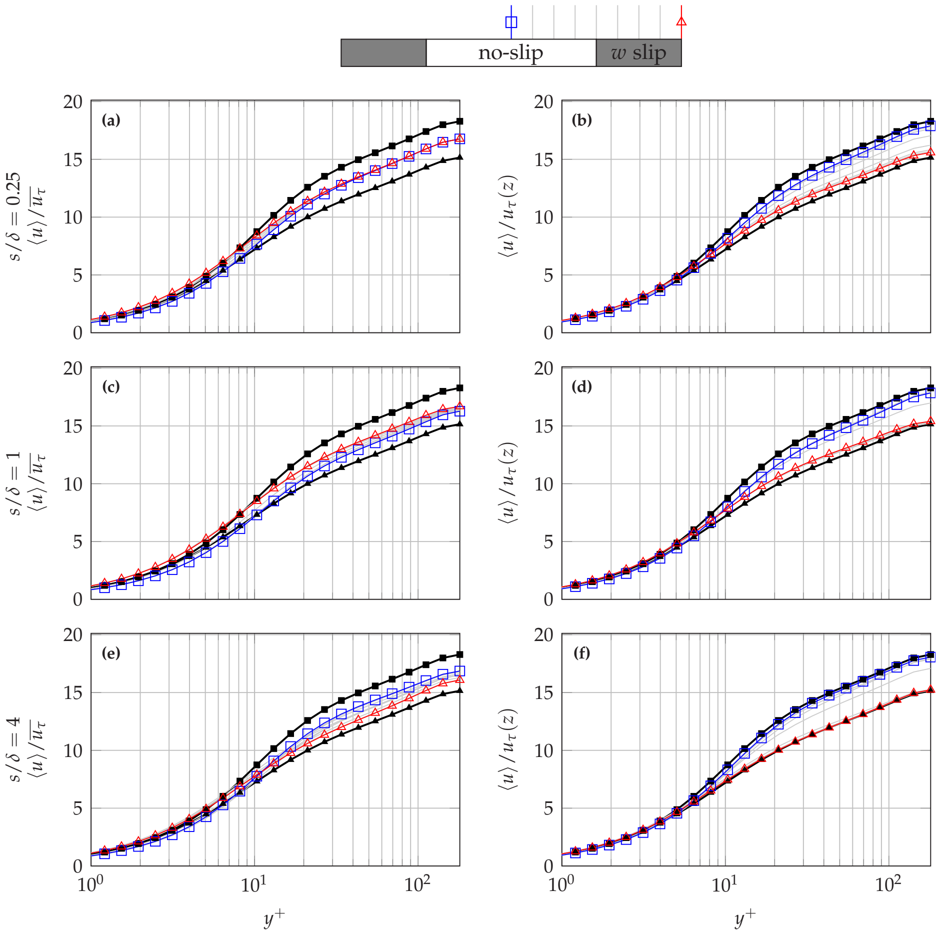

Figure 3.14: Velocity profile for different z positions, scaled with [(a), (c), (e)] the mean friction velocity $\overline{u_\tau}$ and [(b), (d), (f)] the local friction velocity $u_\tau(z)$. Centre of the patch with $l_{s,w} = 0.05$ (—△—), centre of the no-slip patch (—□—). Homogeneous reference profiles: no-slip (—■—), $l_{s,w} = 0.05$ (—▲—). Adapted from [NSGF22b].

For $s/\delta = 4$, the secondary motions and the corresponding momentum transport is restricted to an approximately square region centred at the patch interface, giving rise to a weak local HMP on the rough side of the interface and a weak local LMP on the no-slip side. Such a configuration was also observed experimentally by Wangsawijaya et al. (2020). [...] The orientation and size of the secondary vortices observed in the cited experiments are correctly represented by the slip-length boundary condition in all cases. [...]

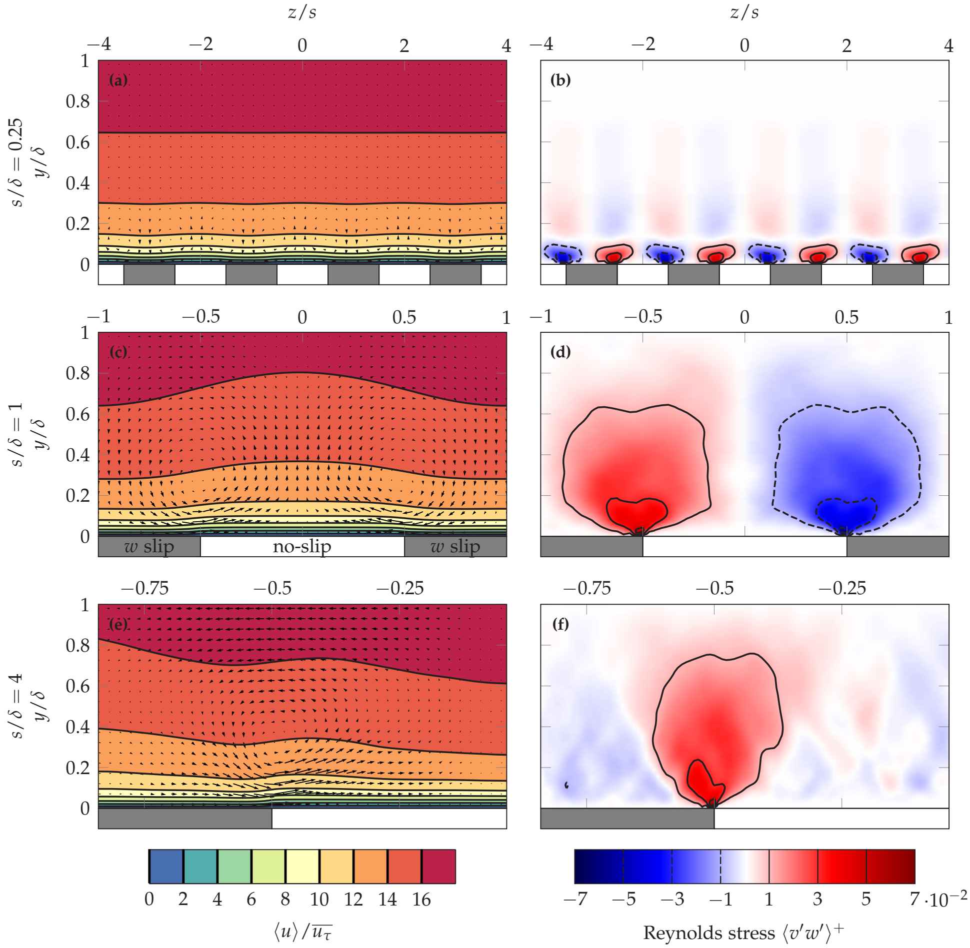

Figure 3.15: Resulting streamwise velocity, in-plane velocity and $\langle v'w' \rangle$ Reynolds stress for differently sized patches of spanwise alternating w slip length and no-slip walls. (a), (c), (e): Mean streamwise velocity in the y-z plane (contours). The secondary flow $[\langle v \rangle, \langle w \rangle]/\overline{u_\tau}$ in the plane is indicated with vectors. The z limits are chosen to enable comparison with the experiments of Wangsawijaya et al. (2020), panels 8(c), (e), (g). (b), (d), (f): Reynolds stress $\langle v'w' \rangle^+$. Top row: $s/\delta = 0.25$, middle row: $s/\delta = 1$, bottom row: $s/\delta = 4$. Adapted from [NSGF22b].

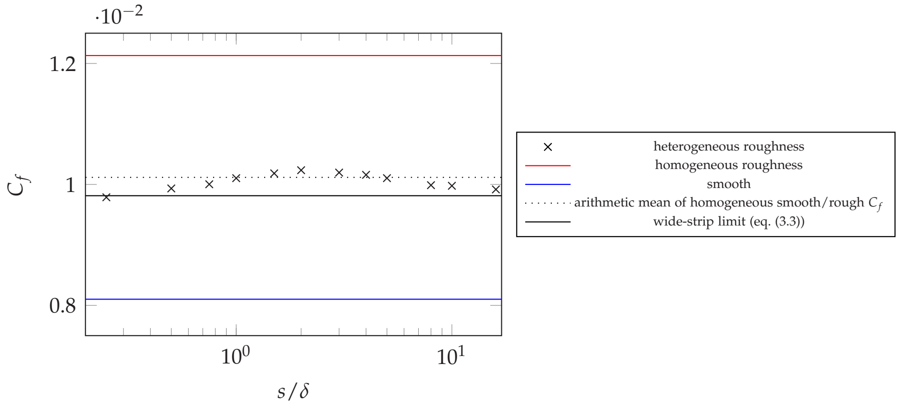

Figure 3.16: Skin friction coefficient C_f as a function of the strip width s/δ with step-wise change of the boundary condition and $l^+_{s,w} = 9$ in the rough patch. C_f for the standard smooth wall, the homogeneous rough case with $l^+_{s,w} = 9$ and the wide-strip limit (eq. (3.3)) are included for reference. Adapted from [NSGF22b].

[NSGF22b]

The spatial distribution of the Reynolds stress component $\langle v'w' \rangle$ is shown in figs. 3.15b, 3.15d and 3.15f. It is in [good] qualitative agreement with DNS results in which streamwise aligned roughness strips are resolved based on an IBM approach or modelled through a parametric forcing approach (PFA) (Schäfer et al. 2022). In particular, the qualitative agreement is achieved for the case of non-protruding roughness strips (cf. Fig. 8(c,k) in Schäfer et al. (2022) vs. fig. 3.15b). Note that the spanwise wavelengths are different: Schäfer et al. (2022) present results for $s/\delta = 0.5$. Therefore, Appendix A [of [NSGF22b] (not reproduced here)] contains a direct comparison at $s/\delta = 0.5$ with the IBM resolved reference data.

3.4.2 Global flow properties

As established in section 3.2, the resulting skin friction coefficient of a spanwise heterogeneous surface can be approximated by means of the wide strip limit eq. (3.3). The wide-strip limit typically underestimates the true drag, particularly if the strip width is not much larger than the channel half-height, as finite-s effects – to which secondary flows contribute – are present. The wide-strip limit and the actual C_f value for the considered s/δ is displayed in fig. 3.16, which also includes the respective reference cases for the homogeneous surfaces (rough and smooth).

For very wide strip ($s \gg \delta$), the global skin friction coefficient as determined from the simulations match the computed wide-strip limit (eq. (3.3)). Interface effects only occupy a small volume fraction of the channel, as can also be seen from the secondary flow in fig. 3.15e, hence most of the channel is in local equilibrium with the respective surface conditions.

Decreasing s/δ, finite-s effects become dominant, to which the secondary flows contribute.[8] Relative to the wide-strip limit, the observed drag increases by 2.9 % and 3.5 % for $s/\delta = 1$ and $s/\delta = 4$, respectively. At very small s/δ, the observed values decrease again, even slightly below the wide-strip limit. Indeed, for $s \to 0$, smooth-wall behaviour should be obtained again: the smallest turbulent structures become larger in the spanwise direction than the wall sections that permit spanwise slip. Consequently thence these vortices cannot penetrate the wall anymore, effectively leading to no-slip behaviour.

For a direct comparison with the C_f-changes presented in Schäfer et al. (2022) we note that both Reynolds number and roughness function are larger than in the present case while the strip width is smaller. In addition, equation (3.3) was not applied in this case. Instead, the arithmetic mean of C_f for smooth and rough wall was used as reference. Irrespective of the reference definition, i.e. as arithmetic mean or according to equation (3.3), the data of Schäfer et al. (2022) indicate a much higher contribution of the secondary flow to drag increase than the present data. At the same time the [curvature of velocity iso-contours] due to the secondary flow is similar for the present data and non-protruding roughness strips of Schäfer et al. (2022) (see their figure 5 (c) and (j,k) or the appendix of [NSGF22b]).

We suspect that this difference is related to drag effects on the protruding lateral sides of the smooth surface patches [as well as the non-zero streamwise protrusion height of the roughness that were present] in the IBM resolved and PFA modelled roughness DNS (Stroh et al. 2020b; Schäfer et al. 2022). Those effects should disappear for large scale separation between the roughness length scale and the channel half height (boundary layer thickness), which cannot be achieved with roughness resolving DNS. However, this scale separation is a likely property of engineering or environmental rough-wall flows and can be realized experimentally. In fact, recent wind tunnel experiments with rough surface strips carried out in our lab indicate a smaller global drag increase when surface elevation differences between rough and smooth wall strips are minimized (Frohnapfel et al. 2024). [NSGF22b]

8 [NSGF22b] attempted an estimation of the actual drag contribution of the secondary flow, which is not reproduced here.

3.5 Numerical results: Developing turbulent flow

The origin of turbulent secondary flows has seen considerable attention in the literature (cf. section 1.2.1). Typically, secondary flows are studied under statistically steady, fully developed conditions. In this section, a previously under-explored approach will be used to approach the problem, namely their emergence when spanwise homogeneous flow enters a geometry with spanwise inhomogeneity. While experimental studies have treated this matter out of necessity (e.g. Studerus (1982) and Vermaas et al. (2011)), it has seen little attention from the numerical side. For streamwise-aligned ridges, Hwang and J. H. Lee (2018) studied the onset of the secondary flow in a turbulent boundary layer. For strip-type surfaces, only the study of Andreolli et al. (2025) is available, who considered the *temporal decay* of turbulent secondary motions using the same slip-length boundary condition proposed by [NSGF22b]. The slip-length boundary condition introduced in section 3.3.2 is well suited for this investigation, as it does not modify the streamwise velocity component directly, and thus the step change in boundary condition does not behave like an obstacle to the flow.

3.5.1 Flow organisation and mean flow properties

Upon entering the structured part of the channel, the fully developed turbulent flow adjusts[9] to the changed surface properties. With increasing x/δ, streamwise gradients of all mean properties decay until the flow is effectively translationally invariant in the streamwise direction, i.e. fully developed. The streamwise location at which this state is attained depends on the geometry (s/δ) and flow conditions (Re_b). The convergence length (or entry length) of different variables (e.g. skin friction coefficient C_f, mean velocity field $\langle u\rangle(y,z)$, and TKE budget terms such as pseudo-dissipation $\tilde{\epsilon}$) differs. This establishes an observable sequence in which the secondary flow, the change in global skin friction, and the locations of HMP/LMP are first detected. The adjustment

[9] In the incompressible limit, the pressure equation is elliptic, so changes at a given position influence the entire domain instantly (i.e. an obstacle in the flow affects it arbitrarily far upstream). This makes it difficult to establish cause and effect in such flows. Consider, for example, the flow around a stationary sphere: the low-pressure zone on the leeward side and the flow separation arise simultaneously as mutually consistent aspects of the flow field, even though it is tempting to discuss them in causal terms. For this reason, the present section does not attempt to construct a causal chain between the different observations. Instead, it records which features occur and at which streamwise locations they are first observed. In the next section, these observations are then used to formulate a plausible formation mechanism for the developing secondary flow.

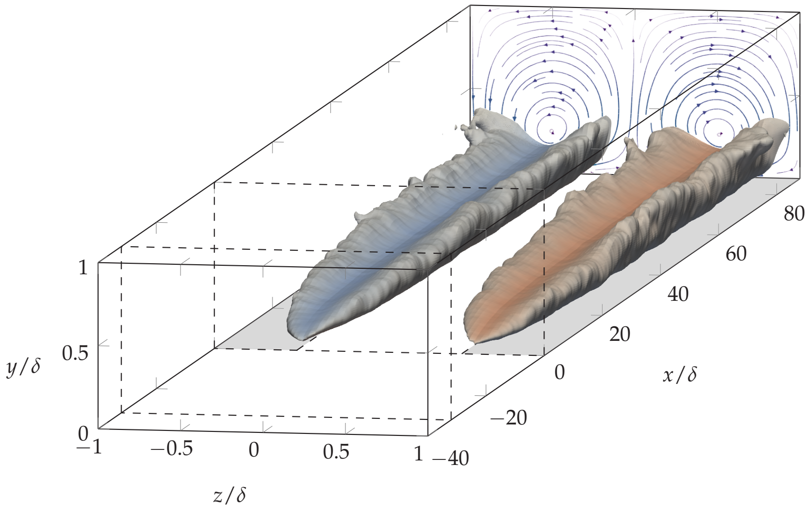

Figure 3.17: Resulting flow topology ($s/\delta = 1$), bottom channel half only. Shown is an iso-surface of the mean in-plane velocity magnitude $\sqrt{\langle v\rangle^2 + \langle w\rangle^2}$ at 0.5% $\overline{u_b}$, coloured by the mean streamwise vorticity to distinguish the opposite sense of rotation. On the $x = x_{max}$ plane, the streamlines of the mean in-plane velocity at that location are displayed. The shaded areas on the $y = 0$ plane indicate the locations of nonzero spanwise slip.

of the flow to the change in surface properties is exemplarily visualised in fig. 3.17 for $s/\delta = 1$.

In this section, four different perspectives on the flow organisation are presented: the perspective of an integral mass balance (as in Vermaas et al. (2011)), the perspective of near-wall turbulence (exemplified by the balance of turbulent kinetic energy), the perspective of a developing 'internal boundary layer' above the rough patch, and a probabilistic perspective on large-scale vorticity. These perspectives are linked in section 3.5.2 to a mechanistic view.

Integral mass balance. Immediately after the change in boundary condition, a significant mean spanwise velocity $\langle w\rangle$ is observed near the wall at the smooth-rough interface (the plane defined by $z = s/2$ for $x > 0$, hereafter referred to as the smooth-rough interface plane); see figs. 3.18a and 3.18d which display wall-normal profiles of $\langle w\rangle$ at the smooth-rough interface plane for various streamwise locations x/δ. The mean spanwise velocity at this plane is negative, i.e. directed from the rough towards the smooth patch. Over the centre of the rough patch, a negative $\langle v\rangle$ and a near-wall peak of $\langle u\rangle - \langle u\rangle_0$ (i.e. an acceleration of the mean flow above the wall) are observed (see

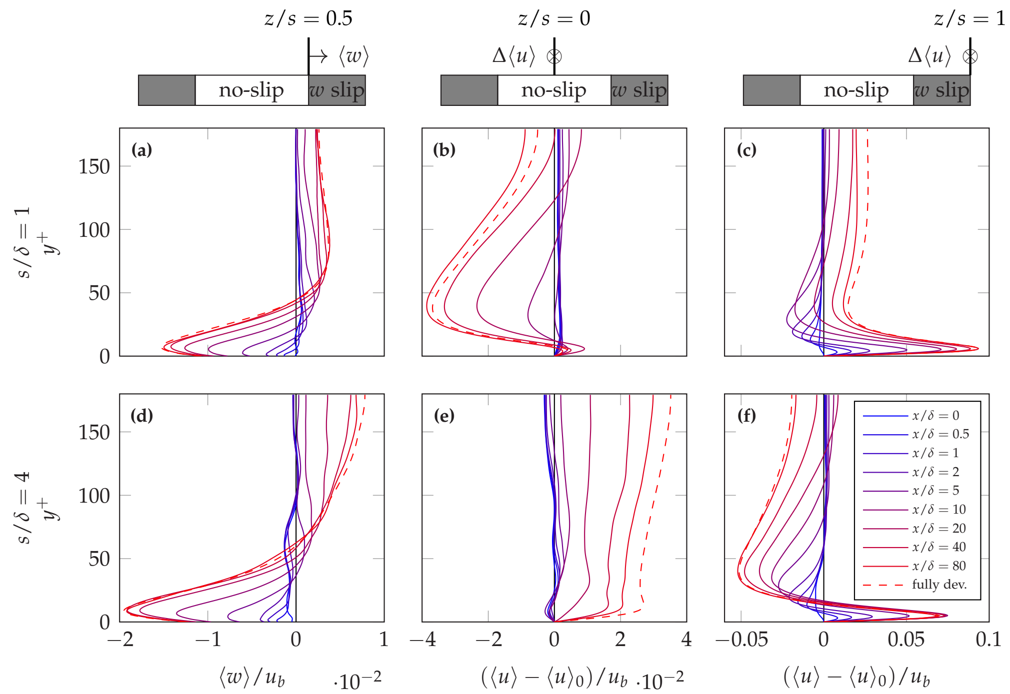

Figure 3.18: Wall-normal profiles of $\langle w \rangle$ (panels (a), (d); at the interface between the smooth and rough patch) and $\langle u \rangle$ (relative to the smooth reference $\langle u \rangle_0$; panels (b), (e) at the centre of the smooth patch; panels (c), (f) at the centre of the rough patch). Streamwise positions are colour-coded; see panel (f) for the positions. The fully developed reference is shown with a dashed line. Top row: $s = \delta$, bottom row: $s = 4\delta$.

figs. 3.18c and 3.18f). These three changes are already present immediately downstream of $x = 0$ and are consistent with continuity of the mean flow there.

The negative near-wall mean spanwise velocity at the smooth-rough interface plane persists for all $z > 0$ and reaches about half of its fully developed magnitude by $x/\delta = 5$ (figs. 3.18a and 3.18d). In contrast, significant deviations of $\langle u \rangle$ at the centre of the smooth patch (figs. 3.18b and 3.18e) are only observed for $x \gtrsim 10\delta$. Overall, the spanwise velocity at the interface, and with it the overall topology of the turbulent secondary flow, resemble the fully developed distributions by $x \approx 5\delta$, whereas the mean streamwise momentum adjusts more gradually and still deviates from the fully developed state at the end of the numerical domain; see fig. 3.18e.

Initially, the net mass flux through the smooth-rough interface plane is negative, i.e. directed from the rough patch to the smooth patch. Further downstream, the secondary flow (whose sense of rotation matches this near-wall motion) is associated with a

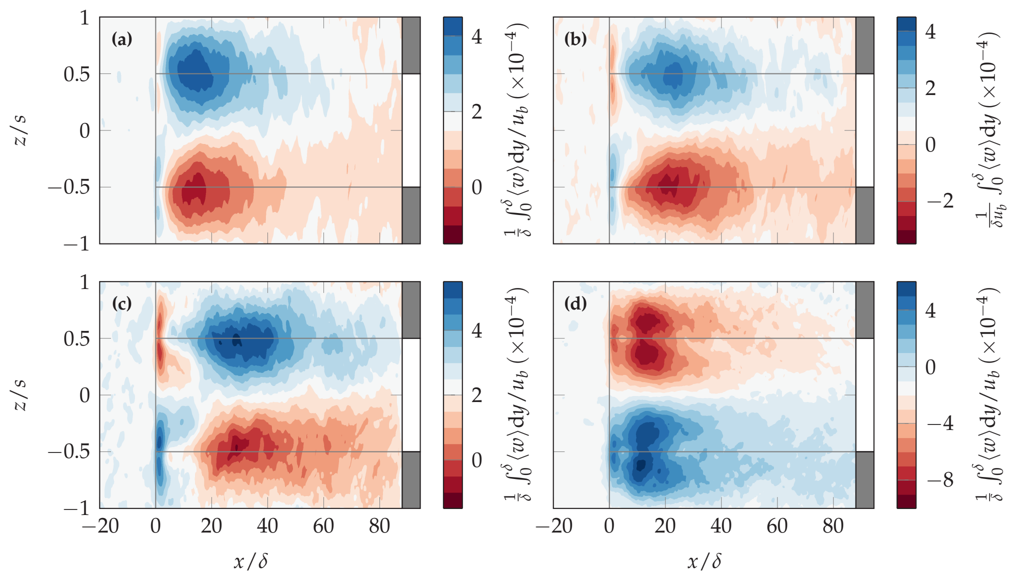

Figure 3.19: Wall-normal integral of $\langle w \rangle$ along x and z. (a): $s/\delta = 1$, (b): $s/\delta = 1.5$, (c): $s/\delta = 2$, (d): $s/\delta = 4$. The resulting values are small compared to u_b, and the plots would be affected by residual background spanwise velocity; the colourbars are therefore chosen to highlight deviations from the background level of $\langle w \rangle$ (which is of the order of $10^{-4}u_b$).

high-momentum pathway over the rough patch for $s/\delta \lesssim 2$ (see section 3.4.1, e.g. for $s/\delta = 1$). In the fully developed state the flow rate is therefore higher over the rough patch, while the net mass flux through the smooth-rough interface plane must vanish. Taken together, these observations imply that the net spanwise flux across the interface changes sign at some downstream position x and becomes positive before ultimately tending to zero in the fully developed regime. This is visualised in fig. 3.19, which displays the mean flow rate in spanwise direction through each wall-normal line. The described sign change is observed for $s/\delta \in \{1, 1.5, 2\}$, and its streamwise location increases with s/δ, as does the location of the maximum spanwise flow rate, which lies between $x = 15\delta$ and $x = 35\delta$.

For cases where no sign reversal of the mean spanwise flow rate occurs along x (as for $s/\delta = 4$, see fig. 3.19d), the control volume encompassing the flow above the rough patch continuously loses flow rate to the smooth side through the interface plane. In that regime, no HMP is observed over the rough patch, and the flow decelerates relative to the smooth reference.

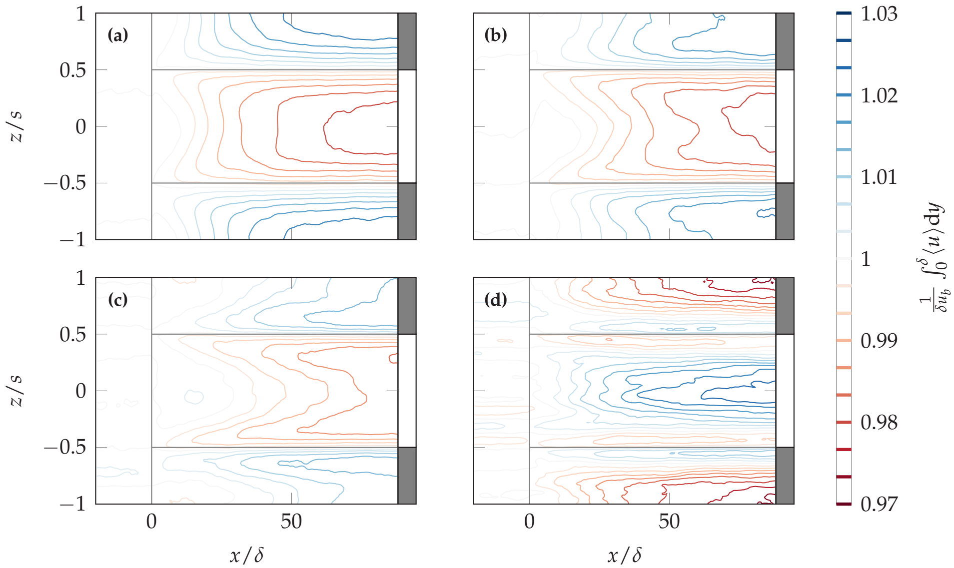

Figure 3.20: Wall-normal integral of $\langle u \rangle$ along x and z. (a): $s/\delta = 1$, (b): $s/\delta = 1.5$, (c): $s/\delta = 2$, (d): $s/\delta = 4$.

A spanwise acceleration of the flow is already observed upstream of the boundary condition, e.g. at $x = -2\delta$ for $s/\delta = 4$, consistent with upstream momentum diffusion.

The wall-normal integral of $\langle u \rangle$ (i.e. the streamwise flow rate at each x-z location) is shown in fig. 3.20. The aforementioned near-wall outflow from the rough patch into the smooth patch is, for all s/δ cases, associated with an initial mean-flow acceleration over the smooth patch and a deceleration over the rough patch (best visible in fig. 3.20c). As the secondary vortex associated with this near-wall outflow expands towards the channel centre, it begins to transport high-momentum fluid: away from the wall over the smooth region (establishing an LMP there) and towards the wall over the rough region (HMP). For large s/δ (fig. 3.20d) the secondary vortices have a spanwise extent of roughly 2δ, consistent with the observation of near-interface HMP/LMP, together with an overall deceleration (acceleration) over the rough (smooth) patch. Since the magnitude of the secondary flow is small ($\approx 2\%\, u_b$), the associated cross-stream transport requires a large streamwise extent. This is consistent with the observed development length of the streamwise momentum, which exceeds the simulation domain.

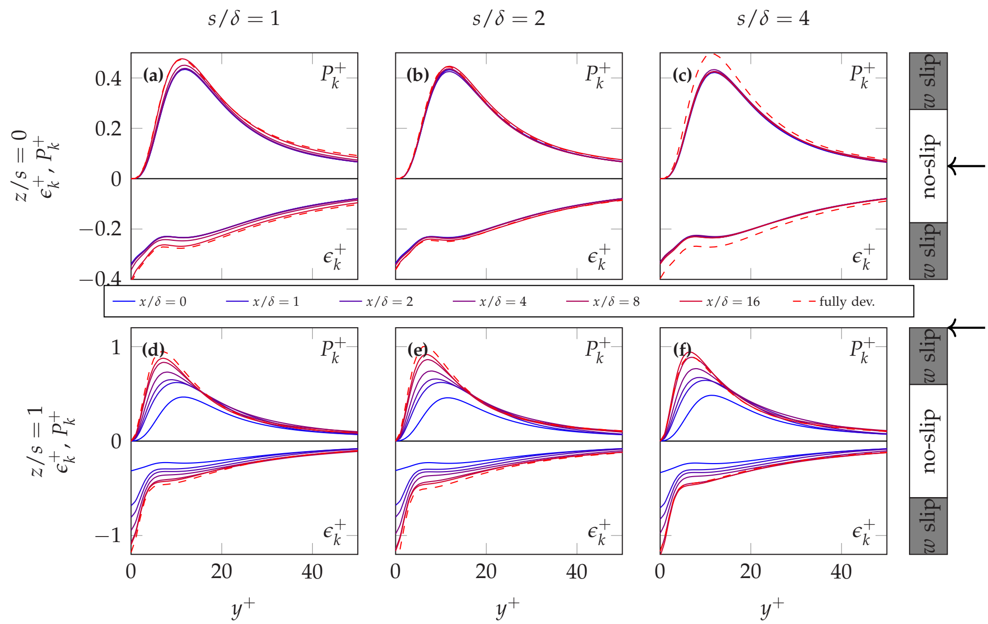

Figure 3.21: Production and dissipation of TKE at the centre of the smooth patch (top row) and the centre of the rough patch (bottom row) for various streamwise locations (legend). Left column: $s/\delta = 1$, centre column: $s/\delta = 2$, right column: $s/\delta = 4$. TKE terms are non-dimensionalised with viscous units of the smooth case ($u_{\tau 0}$).

Near-wall turbulence. The production and dissipation terms of the turbulent kinetic energy are shown in fig. 3.21 for the centres of each patch. The production and dissipation terms are defined as

$$P_k = -2\langle u_i' u_k' \rangle \frac{\partial \langle u_i \rangle}{\partial x_k}, \qquad \epsilon_k = 2\nu \langle \frac{\partial u_i{}'}{\partial x_k} \frac{\partial u_i{}'}{\partial x_k} \rangle. \tag{3.11}$$

Immediately downstream of $x = 0$, the production and dissipation above the rough patch adjust to the new surface conditions. This is best seen for $s/\delta = 4$ (fig. 3.21f), where the production and dissipation terms are close to the fully developed profiles by $x = 8\delta$. In contrast, the TKE budget above the smooth patch (fig. 3.21c) is essentially unaffected by the change in surface conditions even at $x = 16\delta$. For smaller $s/\delta = \{1, 2\}$, similar trends are observed (cf. figs. 3.21a and 3.21d and figs. 3.21b and 3.21e), but (instantaneous) spanwise momentum diffusion reduces spanwise gradients of the involved quantities, thereby delaying the adjustment of near-wall turbulence over the rough patch and accelerating it over the smooth patch. Near-wall turbulence therefore responds very quickly to the change in boundary conditions.

Internal boundary layer. In boundary layer flows, a so-called *internal boundary layer* (IBL) forms following a streamwise step change of the boundary condition (Garratt 1990). While there is a vast literature on this phenomenon in boundary layers and some on open channel flows, few studies have considered internal flows; notable exceptions are an experimental study on a rough-to-smooth streamwise surface inhomogeneity in turbulent pipe flow (Van Buren et al. 2020) and a wall-modelled LES study of smooth-rough-smooth transition in a channel flow (Saito and Pullin 2014).

The core concept of an internal boundary layer, i.e. 'the IBL is the layer within which significant changes from upstream conditions occur, in $u(x)$ and $\tau(x)$' (Garratt 1990), can only be transferred to internal flows in an approximate sense, as the response of, e.g., channel flow to a step change in boundary condition fundamentally differs from that of a boundary layer.

Consider a spanwise-homogeneous channel with a step change from smooth to rough at $x = 0$ and a control volume of streamwise, wall-normal and spanwise extent $\mathrm{d}x \times 1 \times \mathrm{d}z$. The only surfaces of the control volume that can contribute to the integral mass balance are the streamwise ones: on all other surfaces, mass fluxes vanish due to symmetry or boundary conditions. Hence, if the flow accelerates (in streamwise direction) at one wall-normal location of the control volume, it must decelerate at another to satisfy continuity. A change of the boundary condition therefore immediately influences the flow along the entire wall-normal axis. Such a constraint is not imposed on boundary layer flows or open channel flows (where the height of the boundary layer or the water level can change, respectively). For this reason, Van Buren et al. (2020) avoid the terminology of an internal layer altogether. Consequently, this section borrows some concepts from the IBL literature, fully aware that they are not applicable to internal flows in an exact sense. In particular, it is examined whether features reminiscent of an IBL can be observed following the smooth-to-rough transition at the centre of the rough patch.

The height of the internal boundary layer δ_i is typically related to the streamwise coordinate by a power law, $\delta_i \propto x^\alpha$. Various definitions of δ_i have been proposed in the literature. Rouhi et al. (2019) compared these definitions based on data from channel flow DNS over IBM-resolved roughness. Considerable scatter of the exponent α was found, and α was observed to be rather sensitive to the definition of δ_i.

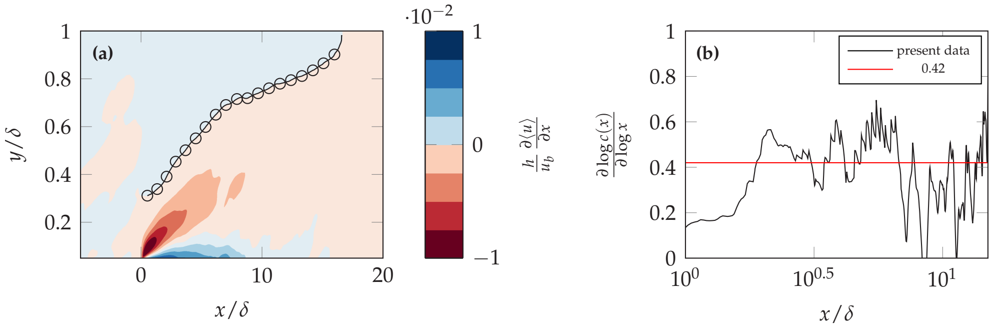

Figure 3.22: Evaluation of δ_{AW} for the centre of the rough patch, $s/\delta = 4$. To reduce statistical noise, the spanwise mean of a 0.5δ-wide region centred around $z/\delta = 4$ is shown. (a) Contours of $\partial u/\partial x$, with the zero isocontour $c(x)$ considered for (b) highlighted. (b) Diagnostic plot for the power-law growth of $c(x)$. Rouhi et al. (2019) reported $\delta_{AW} \propto x^{0.42}$ for their channel DNS.

From the aforementioned article, only δ_{AW} (after Andreopoulos and Wood (1982)[10]) is readily evaluated. It is based on the location where $\partial\langle u\rangle/\partial x$ changes sign. From their figs. 14(e) and 16 it is clear that $\partial\langle u\rangle/\partial x = 0$ at two y positions over the rough patch, with acceleration near the wall and near the centreline and, to satisfy continuity, deceleration over an intermediate range of y values that expands in x. They selected the upper boundary of that region to define δ_{AW}, which is reproduced in fig. 3.22 for the present data.

Figure 3.22 shows δ_{AW} for the centre of the rough patch for $s/\delta = 4$. While the shape of the isoline $c(x)$ roughly matches that observed by Rouhi et al. (2019), the statistical noise is too large to determine the growth rate reliably; see fig. 3.22b.

The other definitions of δ_i present even greater difficulties for evaluation. Unlike in a smooth-wall turbulent boundary layer, $\partial\langle u'u'\rangle/\partial x$ vanishes in fully developed channel flow; hence the sign change of that quantity (on which δ_{SP} is based) is ill-defined in the present case. δ_{BMP} is only applicable to streamwise-periodic smooth-rough(-smooth) cases with 50% surface coverage. δ_E (after Elliott (1958)) cannot be evaluated as the Reynolds number is too low to distinguish multiple logarithmic regions in the velocity profile; δ_{AL} suffers from similar evaluation problems.

For a transition of the surface conditions, Ismail et al. (2018) suggested the diagnostic quantity

$$X_q = \frac{q - q_s}{q_r - q_s}, \tag{3.12}$$

[10] Note that Rouhi et al. (2019) appear to misreport the value of α from Andreopoulos and Wood (1982); it should be 0.8 for a smooth-to-rough transition, while Rouhi et al. (2019) cite it as 0.48.

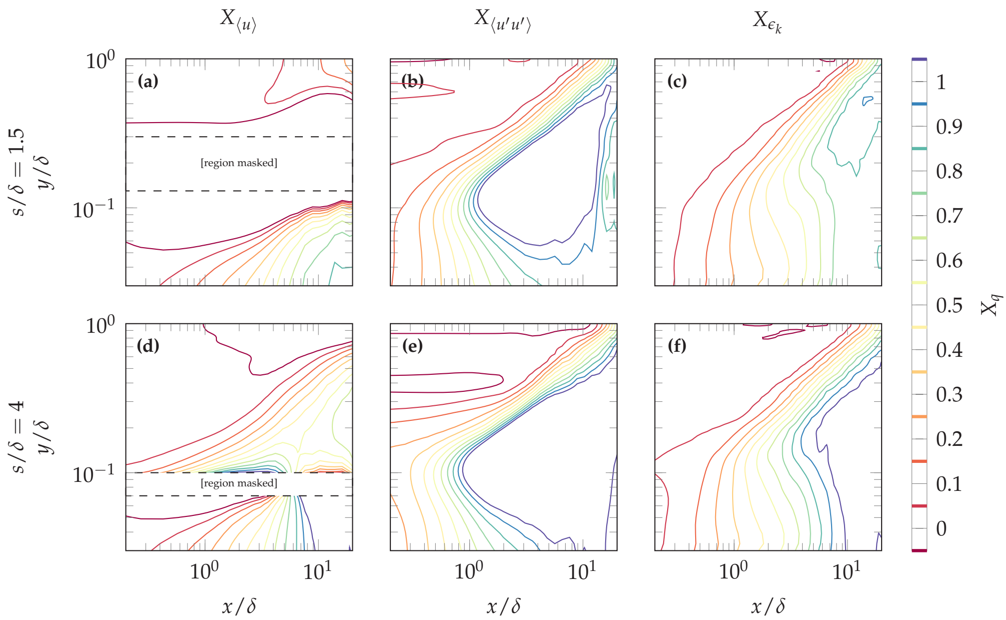

Figure 3.23: Recovery magnitude, evaluated according to (3.12). Columns (left to right): $X_{\langle u \rangle}$, $X_{\langle u'u' \rangle}$, X_{ϵ_k}. Top row: $s/\delta = 1.5$, bottom row: $s/\delta = 4$. In the masked regions of (a) and (d), $X_{\langle u \rangle}$ has a singularity as smooth and rough references are close.

where q is any quantity of interest, such as $\langle u \rangle$ or ϵ_k, and the indices s and r denote fully developed smooth and rough states, respectively. Adapting this to the present geometry, q_r is taken as the (spanwise inhomogeneous) fully developed value at a given spanwise and wall-normal position. X_q thus tends to 0 for $x \to -\infty$ and to 1 for $x \to \infty$; values outside of $[0, 1]$ are admissible. Contours of X_q for various statistics are displayed in fig. 3.23 in log-log scaling. For $s/\delta = 4$, turbulence-associated quantities like $\langle u'u' \rangle$ and ϵ_k have isocontours for $0 < X_q < 1$ that are straight and almost parallel for $0.15 \lesssim y \leq 1$ (figs. 3.23e and 3.23f), indicating a power-law-type downstream propagation of turbulence-related changes with exponent $\alpha \approx 0.65$. For $s/\delta = 1.5$, a similar parallelism of isocontours is observed (figs. 3.23b and 3.23c). For $X_{\langle u \rangle}$ a clear power-law-type growth cannot be identified (figs. 3.23a and 3.23d).

In the classical literature on streamwise surface-property changes, an overshoot of the wall shear stress is often reported; that is, following a smooth-to-rough transition, τ_w converges from above to the fully developed value and has a pronounced maximum within a few δ downstream of $x = 0$ (Garratt 1990). Both experimental data and theoretical considerations have supported this hypothesis. Modern studies present

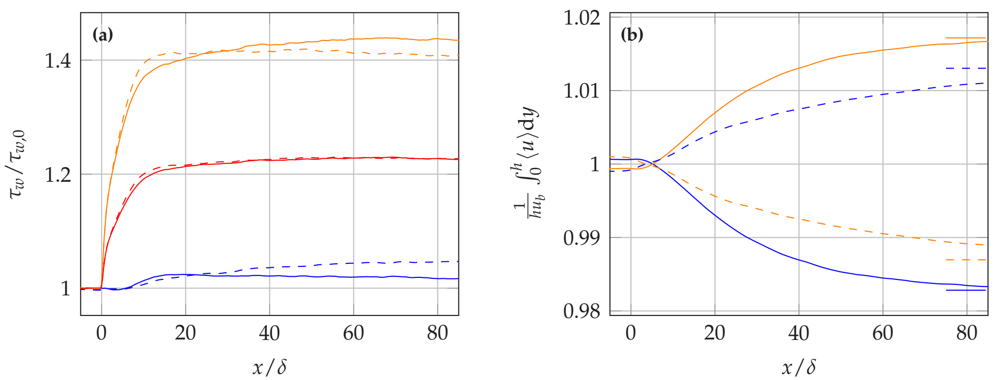

Figure 3.24: Comparison of (a) shear stress increase and (b) fractional flow rate over the smooth patch (——), rough patch (——) and globally (——). Solid lines: $s/\delta = 1$, dashed lines: $s/\delta = 4$. Panel (b) also includes the fully developed values as markers on the right-hand side.

conflicting evidence about whether the overshoot is present. Jacobi and McKeon (2011) observed the overshoot in boundary-layer experiments, and the studies of Saito and Pullin (2014) and Van Buren et al. (2020) reported it in internal flows (LES of channel flow and experiments of pipe flow, respectively). On the other hand, the experiments of Chen and Chiew (2003) and Rathore et al. (2022) did not exhibit an overshoot of τ_w. Nezu and Nakagawa (1991) and Carravetta and Della Morte (2004) studied the question more systematically in open-channel-flow experiments; they found the presence of the overshoot to depend on the roughness size k_s^+ and the emersion height of the roughness elements relative to the smooth wall. In the present dataset, a significant overshoot of the skin friction coefficient is not observed, neither globally nor for any specific z coordinate.

The change of wall shear stress is reported in fig. 3.24a for two strip widths. The secondary flow (which fully affects the channel width for small s/δ) can be linked to a reduction of the shear stress increase over the smooth patch. This is consistent with the sense of rotation of the in-plane components, which can be compared to a blowing/suction effect. However, the global shear stress is virtually unaffected by s/δ.

The wall shear stress, particularly the global quantity, converges rather quickly to the fully developed state (development length of approximately 20δ). This contrasts with the fractional flow rate, whose development length exceeds the streamwise domain length; see fig. 3.24b, particularly for $s/\delta = 4$.

Instantaneous large-scale vorticity. One common interpretation of secondary flow is given in the review of Kawahara et al. (2012): '[I]n a statistical sense, mean secondary-flow vorticity can be understood as a footprint of the preferential spatial occurrence of streamwise vortices', and a statistical evaluation of those vortices has been used to connect instantaneous events to secondary flows (Pinelli et al. 2010). The present setup enables a test of this re-positioning hypothesis, as the flow undergoes a transition from a statistically homogeneous (smooth) state to the inhomogeneous state featuring secondary motion. The central question is whether large-scale vorticity statistics (in viscous units) remain invariant under this transition, as the re-positioning hypothesis would suggest.

Small-scale structures dominate the overall statistics of vorticity and of commonly used vortex-identification criteria. To emphasise large-scale rotational motion, a spatial filtering approach is employed to track large-scale structures (Bürger et al. 2023). The streamwise vorticity is

$$\omega_x = \frac{\partial w}{\partial y} - \frac{\partial v}{\partial z}. \tag{3.13}$$

A filtered vorticity field $\tilde{\omega}_x$ is defined by taking the mean in a $\Delta_y \times \Delta_z = \delta \times \delta$ window for each x and z position. More precisely, one convolves ω_x with a two-dimensional box kernel of size $\Delta_y = \delta$ and $\Delta_z = \delta$, evaluated separately on both channel halves:

$$\tilde{\omega}_x(x,y,z,t) = \frac{1}{\delta^2} \int_{z-\delta/2}^{z+\delta/2} \int_{y-\delta/2}^{y+\delta/2} \omega_x(x,y',z',t) \mathrm{d}y' \mathrm{d}z', \quad \text{for } y \in \left\{ \tfrac{1}{2}\delta, \tfrac{3}{2}\delta \right\}. \tag{3.14}$$

This definition yields a measure of the mean streamwise vorticity over $\delta \times \delta$ windows in the y-z plane, computed separately in each channel half. The spanwise extent $\Delta z = \delta$ is chosen to match the characteristic spanwise width of the secondary motions. In the DNS, a histogram of these values is collected online for each x and z, removing the y dependency by averaging over the two channel halves with flipped bins on the upper half.

For all cases considered, $\tilde{\omega}_x(x,y,z,t)$ is well approximated by a univariate normal distribution: throughout the entire domain, the skewness values satisfy $-0.15 < E[((\tilde{\omega}_x - \mu)/\sigma)^3] < 0.15$ (where E is the expectation value, μ the mean and σ the standard deviation at each location) and the excess kurtosis values satisfy $-0.2 < E[((\tilde{\omega}_x - \mu)/\sigma)^4] - 3 < 0.5$ (for $z < 0$, the excess kurtosis is ≈ 0.15, and the kurtosis is 3-5% lower over the rough strips). The mean and variance of the distribution vary with position.

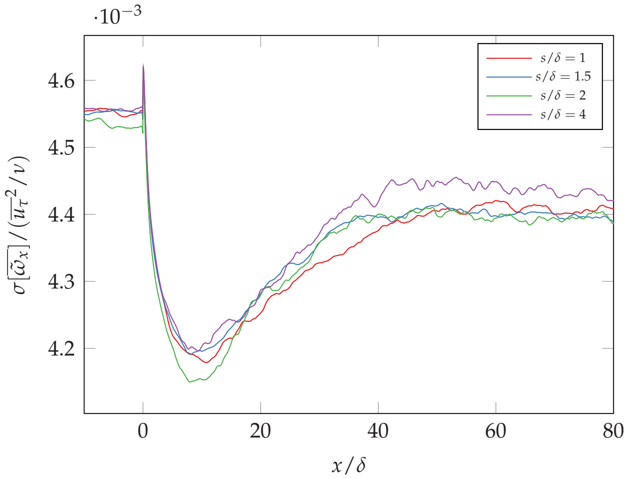

Figure 3.25: Standard deviation of the spanwise-averaged PDF of $\tilde{\omega}_x$, normalised in spanwise-averaged wall units, for the various cases of s/δ.

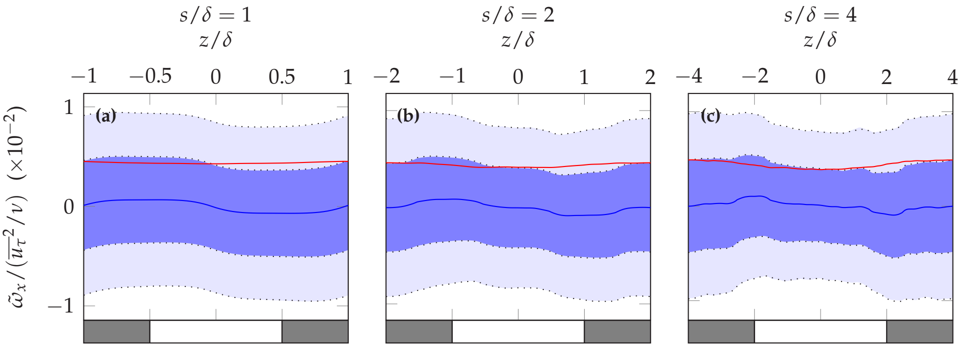

Figure 3.26: Distribution of $\tilde{\omega}_x$ at the end of the domain (averaged over $x \in [60\delta, 80\delta]$) for $s/\delta = 1$ (a), $s/\delta = 2$ (b) and $s/\delta = 4$ (c). Shown are the mean (solid blue line) and centred intervals that contain 68.27% (dark blue) and 95.45% (light blue) of observed values. 1σ and 2σ intervals around the mean are displayed with dotted lines; they coincide with the percentage-based intervals, indicating that $\tilde{\omega}_x$ is approximately modelled by a univariate normal distribution. The red line indicates the standard deviation.

The variance of $\tilde{\omega}_x$ is increased by up to 40 % over the rough patch ($s/\delta = 4$). However, the variance of the spanwise-averaged PDF, when scaled in local wall units $\overline{u_\tau}^2/\nu$, changes by only about -3 % between the two fully developed states. This indicates that *global* large-scale vorticity is approximately in balance with $\overline{u_\tau}(x)$ and is only weakly affected by the spanwise heterogeneity. Indeed, the curves of $\sigma[\widetilde{\omega}_x]/(\overline{u_\tau}^2/\nu)$ are quite similar for all s/δ cases, as displayed in fig. 3.25. The development length of $\sigma[\widetilde{\omega}_x]$ is significantly longer than that of $\overline{u_\tau}$ (cf. fig. 3.24).

Figure 3.26 displays the distribution of $\tilde{\omega}_x$, averaged over $x = [60\delta, 80\delta]$, for $s/\delta \in \{1, 2, 4\}$. The variation of $E[\tilde{\omega}_x]$ in the spanwise direction is much smaller than the standard deviation of $\tilde{\omega}_x$; hence the secondary flow is difficult to detect in instantaneous fields (without in-plane components, the mean of $\tilde{\omega}_x$ would be identically zero). In the mean of $\tilde{\omega}_x$, the secondary flow can be clearly identified: the mean departs from zero over roughly a δ-wide interval around the interface. Such an impact is not seen in the standard deviation of $\tilde{\omega}_x$ (red line in fig. 3.26): the presence of the secondary flow is not associated with a globally (cf. fig. 3.25) nor locally increased probability of extreme events in large-scale vorticity.

3.5.2 A possible formation mechanism of the secondary flow

The observations in the previous section can be combined into a mechanistic picture of the changes in the mean flow field downstream of $x = 0$, i.e. of the secondary flow, the global drag, and the deformation of the streamwise mean velocity field. In line with the caveats formulated at the beginning of section 3.5.1, the different development lengths of these quantities suggest a plausible sequence of events, but the discussion in this section remains interpretative rather than causal.

Immediately downstream of $x = 0$, the near-wall turbulence hitting the rough strip adjusts to the new boundary condition, as indicated by the increased production and dissipation of TKE (fig. 3.21). The importance of TKE production in the formation of secondary currents was already emphasised by Hinze (1967). An increase in surface roughness typically leads to an increase in total drag. In the present configuration, where pressure drag is absent, this manifests as an increase in skin-friction drag, i.e. an increase of the wall-normal gradient of streamwise velocity at the wall. Hence, the mean flow above the rough patch accelerates near the wall (figs. 3.18 and 3.21).

The near-wall flow then encounters the increased resistance over the rough patch and is deflected towards the smooth patch (figs. 3.18 and 3.19). This near-wall spanwise motion provides a preferential location for the already-present large-scale structures in the flow: they re-position to support the near-wall outflow from the rough patch. The associated organisation of large-scale vorticity develops over a streamwise extent of roughly $x \approx 40\delta$ (fig. 3.25). Throughout this process, there is no substantial increase in the variance of large-scale vorticity, either globally (when scaled with the streamwise-varying $\overline{u_\tau}$, fig. 3.25) or locally in the regions most affected by the secondary flow (fig. 3.26). This supports the view that the secondary flow is the statistical footprint of a preferential positioning of pre-existing large-scale structures, rather than the emergence of fundamentally stronger structures (that would require additional energy input to sustain). In line with this interpretation, the global drag changes little once $x \gtrsim 10\delta$ (fig. 3.24), even though the mean drag on the individual smooth and rough surfaces continues to evolve.

By $x/\delta \approx 5{-}10$ (depending on s/δ), the modifications of the flow have reached the centre of the smooth patch (figs. 3.18, 3.21 and 3.24a). This streamwise extent is comparable to the effective growth of an internal-boundary-layer-like region above the rough patch, inferred from turbulence-related quantities (fig. 3.23) and conceptually mapped into the spanwise direction.

The fractional flow rate over the smooth and rough patches requires a much larger streamwise distance to approach its fully developed value (figs. 3.20 and 3.24b). This long development length is consistent with the small magnitude of the mean in-plane velocity components, which implies that the momentum pathways are a consequence of $\langle v \rangle$. For decaying secondary motions, Andreolli et al. (2025) observed that the in-plane components decay faster than the momentum pathways, at least for $s/\delta > 1$. The present study confirms the reverse ordering for the growth of secondary motions.

3.6 Discussion and summary

This chapter investigates how heterogeneous surface properties affect momentum transfer in laminar and turbulent channel flows, using theoretical analysis and direct numerical simulation (DNS). Roughness is modelled via a simplified boundary condition that avoids resolving individual roughness elements, enabling simulations at conditions with scale separation between roughness height and channel height.

For channel flow over streamwise-aligned strips of differing surface properties (e.g. height, roughness, or active/passive flow control), the global drag is derived in the limit of a large strip width s in the spanwise direction (the *wide-strip limit*). The derivation assumes local equilibrium and requires only the homogeneous skin friction curves, $C_f(\mathrm{Re}_b)$, of the constituent surfaces. The limit is validated for two idealised spanwise-heterogeneous cases (spanwise heterogeneous roughness and streamwise-aligned ridges) in both laminar and turbulent flow conditions. An extension to heat transfer is derived and validated for laminar flow over streamwise-aligned ridges (see appendix A.2).

In general, C_f is sensitive to the definition of the channel height (e.g. $h_{\text{avg}}, h_{\text{empty}}$), especially when the characteristic height of the surface features (e.g. the height of roughness peaks or the height of a ridge) and the outer scales of the flow are not well separated. This property is discussed for laminar and turbulent flow over streamwise-aligned ridges. For example, it is found that blocking part of the channel can reduce C_f by a factor of four if h_{avg} is used. Hence, for cases without scale separation, it is crucial to report the height definition used for drag evaluations.

For strips of finite width s, the global drag increases compared to the wide-strip limit (for any chosen channel height definition). This is due to a combination of various factors, such as increased wetted surface area per unit width, transients between strips, and turbulent secondary flows. Comparison of laminar and turbulent flow over streamwise-aligned ridges shows that this increase is mainly geometric rather than caused by changes in turbulent properties. This observation motivates a model for the global drag of turbulent flow over finite-width roughness strips. Comparison with experimental data shows that the model reproduces a local maximum in $C_f(\text{Re}_b)$ and how its location changes with s/δ.

To study turbulent flow over streamwise-aligned roughness strips numerically without scale-separation issues, a slip-length boundary condition is used. By locally allowing for a spanwise slip velocity, near-wall turbulence is enhanced (increasing drag), and the (purely streamwise) laminar flow is unaffected. The model yields a secondary flow topology in the fully developed regime that is consistent with the experiments of Wangsawijaya et al. (2020) for various s/δ. Indeed, even the effects of a smooth-to-rough transition in the streamwise direction are well reproduced with the slip-length model. This includes the power-law adaptation of the flow to the new surface conditions and the formation of an internal layer. An overshoot of the global drag immediately after the change in surface conditions, which is often reported in the literature, has not been observed. The presence of such an overshoot is linked in the literature to Re_b and the protrusion of the rough-walled section from the smooth-wall reference.

For fully developed flow, it is observed that the global drag tends towards the wide-strip limit for $s \to \infty$. For $s/\delta \approx 2$, drag increases over the wide-strip limit by a few percent. A turbulent secondary flow is present. It is weak in magnitude (at most $\approx 2\% u_b$) and aligned to flow away from the wall above the smooth strip. This is accompanied by a low-momentum pathway over the smooth strip and a high-momentum pathway over the rough strip, consistent with experimental data. The in-plane components are non-zero for an approximately square section around the interface. This section is limited by the channel half-height δ in the spanwise direction for large strip widths. Thus, the overall fractional flow rate is higher over the smooth strip in this case.

To investigate the mechanisms behind secondary-flow formation, novel DNS of the streamwise flow development over spanwise-heterogeneous roughness, starting from a fully developed, smooth-wall state, are performed. The order of observations in the streamwise direction suggests a logical succession of events: (i) adaptation of the near-wall turbulence over the rough strip, (ii) near-wall deflection of flow from rough to smooth, (iii) growth of the secondary motion in the spanwise direction, (iv) redistribution of the streamwise momentum fluxes by the secondary flow. A statistical analysis of large-scale vorticity supports the observation of Kawahara et al. (2012): the secondary flow is the 'statistical footprint of a preferential spatial occurrence of streamwise vortices', which are already present in the flow. The global drag reaches its fully developed value far before the secondary flow attains its final magnitude. Both of these findings indicate that global drag is, if at all, only weakly affected by the secondary flow. From an engineering perspective focused on global drag, the secondary flow thus appears to be a statistical artifact of the turbulent flow with little practical importance.

In summary, this chapter advances the understanding of momentum transfer in flows over heterogeneous surfaces. A new theoretical baseline for drag evaluation – the wide-strip limit – has been proposed and validated. A simplified roughness model has been employed to study these flows using DNS in various settings, showing consistent results with experiments. The streamwise development analysis offers insight into the formation mechanism of secondary flows and their weak coupling to the global drag.

4

Passive scalar transport in pipe flows with azimuthally varying heat flux

4.1 Problem description

In this chapter, hydraulically fully developed pipe flow is considered under both laminar and turbulent flow conditions. The conservation equations of mass (eq. (2.1)), momentum (eq. (2.6)) and energy (eq. (2.7)) for a constant-property Newtonian fluid with a passive scalar field are solved analytically for the case of laminar pipe flow and numerically for turbulent pipe flow using the spectral element code NekRS (Fischer et al. 2022). The statistically steady state is considered, e.g. $\langle \partial q / \partial t \rangle = 0$ for any field q. No mean in-plane velocity components ($\langle u_r \rangle$, $\langle u_\varphi \rangle$) are present.

The transport of a passive scalar T subject to axially and azimuthally varying heat flux is considered. The boundary condition is of the type $\partial T / \partial r \big|_w \propto h(z) f(\varphi)$, where $h(z)$ is the unit step function; the streamwise, radial and azimuthal coordinates are denoted with z, r and φ, respectively. A sketch of the configuration is given in fig. 4.1. Over the course of the current chapter, multiple variations of this problem will be discussed, i.e. laminar/turbulent, conjugated/non-conjugated. The base configuration, i.e. the conjugated turbulent Graetz problem for non-uniform heat flux in the azimuthal direction, is introduced first and then simplified for the respective cases.

The heat transfer problem in a thick-walled pipe is set up as follows. Constant material properties for the fluid (index 'f') and solid (index 's') phases are assumed, respectively. Heating through viscous dissipation, thermal expansion and radiation are neglected.

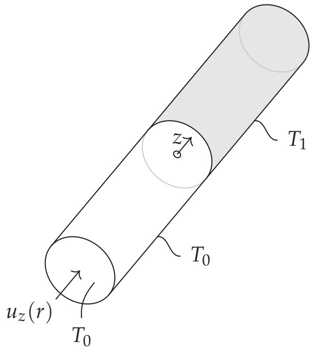

(a) Graetz problem with Dirichlet boundary conditions

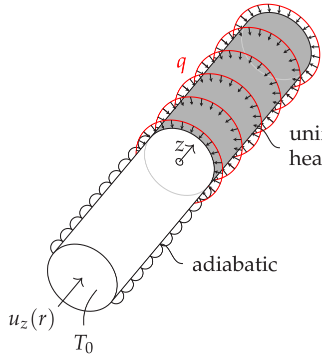

(b) Graetz problem with homogeneous Neumann boundary conditions

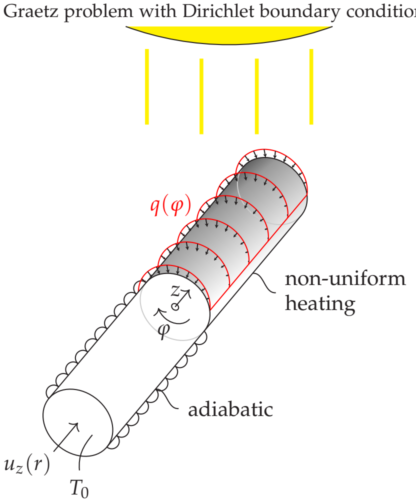

(c) Graetz problem with inhomogeneous Neumann boundary conditions

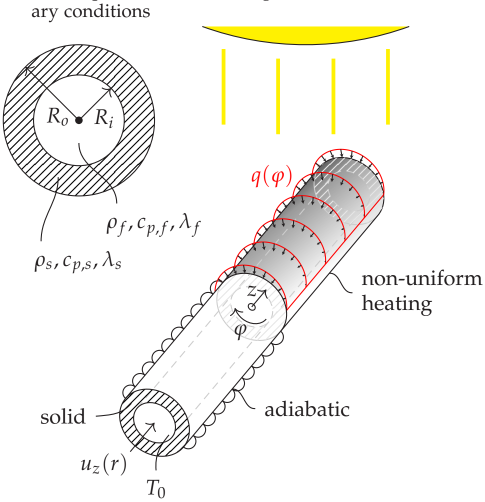

(d) Conjugated Graetz problem with inhomogeneous Neumann boundary conditions

Figure 4.1: Sketch of the typical configurations of the Graetz problem (figs. 4.1a and 4.1b), as well as the non-uniform heating case and conjugated case considered in this chapter. Adapted from [NMGF25].

ρ, c_p and λ denote density, specific heat capacity at constant pressure and thermal conductivity, respectively. Under these conditions, the conservation equation for the (instantaneous) temperature T_i (i / phase being fluid or solid) is given in each phase by

$$\rho_i c_{p,i}\left(\frac{\partial T_i}{\partial t}+u_r\frac{\partial T_i}{\partial r}+\frac{u_\varphi}{r}\frac{\partial T_i}{\partial \varphi}+u_z\frac{\partial T_i}{\partial z}\right)=\lambda_i\left[\frac{1}{r}\frac{\partial}{\partial r}\left(r\frac{\partial T_i}{\partial r}\right)+\frac{1}{r^2}\frac{\partial^2 T_i}{\partial \varphi^2}+\frac{\partial^2 T_i}{\partial z^2}\right] \tag{4.1}$$

A boundary condition prescribing the wall-normal heat flux is applied to the outer perimeter of the solution domain, while a constant inlet temperature is maintained far upstream of the heated section. The thermal boundary conditions are given by

$$\lim_{z\to-\infty} T_i(r,\varphi,z) = T_0, \quad \text{for a constant } T_0, \tag{4.2a}$$

$$T_f(0,\varphi,z) \text{ is regular in } z \text{ and } \varphi, \tag{4.2b}$$

$$\lambda_s \left.\frac{\partial T_s}{\partial r}\right|_{R_o} = \begin{cases} q_w(\varphi) & \text{for } \varphi\in[0,2\pi) \text{ and } z\geq 0,\\ 0 & \text{for } \varphi\in[0,2\pi) \text{ and } z<0,\end{cases} \tag{4.2c}$$

with a heating function $q_w(\varphi) \in L^2$ applied at the outer diameter R_o. The fluid-solid interface is coupled by prescribing continuous temperature and heat flux at the interface $r = R_i$:

$$\lambda_s \left.\frac{\partial T_s}{\partial r}\right|_{R_i} = \lambda_f \left.\frac{\partial T_f}{\partial r}\right|_{R_i} \qquad \text{for all } z\in\mathbb{R} \text{ and } \varphi\in[0,2\pi), \tag{4.3a}$$

$$T_f(R_i,\varphi,z) = T_s(R_i,\varphi,z) \qquad \text{for all } z\in\mathbb{R} \text{ and } \varphi\in[0,2\pi). \tag{4.3b}$$

General dimensionless form. Various non-dimensionalisations of the problem defined by eqs. (4.1), (4.2c) and (4.3b) are prevalent in the literature, and indeed the author's own publications use different non-dimensionalisations to match the respective core references. Hence, a general one is introduced first and later simplified. Variables are non-dimensionalised as follows:

$$T_i^* = \frac{(T_i - T_0)}{T_{\text{ref}}}, \quad u_i^* = \frac{u_i}{U_{\text{ref}}}, \quad r^* = \frac{r}{R_{\text{ref}}}, \quad z^* = \frac{z}{\alpha R_{\text{ref}}}, \quad t^* = \frac{U_{\text{ref}}}{R_{\text{ref}}}t, \tag{4.4}$$

$$f(\varphi) = \frac{q_w(\varphi)}{q_{w,\text{ref}}}, \quad \lambda^* = \frac{\lambda_i}{\lambda_f} =: \lambda_{sf}, \quad \rho^* = \frac{\rho_i}{\rho_f}, \quad c_{p,i}^* = \frac{c_{p,i}}{c_{p,f}} \tag{4.5}$$

where starred quantities denote dimensionless variables. Equation (4.1) then becomes

$$\begin{aligned}\rho_i^* c_{p,i}^* &\left(\frac{\partial T_i^*}{\partial t^*} + u_r^* \frac{\partial T_i^*}{\partial r^*} + \frac{u_\varphi^*}{r^*} \frac{\partial T_i^*}{\partial \varphi} + \frac{1}{\alpha} u_z^* \frac{\partial T_i^*}{\partial z^*} \right) \\ &= \lambda_i^* \frac{\lambda_f}{R_{\text{ref}} U_{\text{ref}} \rho_f c_{p,f}} \left[\frac{1}{r^*} \frac{\partial}{\partial r^*} \left(r^* \frac{\partial T_i^*}{\partial r^*} \right) + \frac{1}{(r^*)^2} \frac{\partial^2 T_i^*}{\partial \varphi^2} + \frac{1}{\alpha^2} \frac{\partial^2 T_i^*}{\partial z^* \partial z^*} \right]\end{aligned} \tag{4.6}$$

T_i^* inherits the regularity condition eq. (4.2b); the boundary conditions eqs. (4.2a) and (4.2c) give, using the ratio of thermal conductivities $\lambda_{sf} = \lambda_s / \lambda_f$,

$$\lim_{z \to -\infty} T_i^*(r^*, \varphi, z^*) = 0 \qquad \text{for all } r^* > 0 \text{ and } \varphi \in [0, 2\pi), \tag{4.7a}$$

$$\left. \frac{\partial T_s^*}{\partial r^*} \right|_{R_o^*} = \frac{R_{\text{ref}} q_{w,\text{ref}}}{\lambda_{sf} \lambda_f T_{\text{ref}}} \begin{cases} f(\varphi) & \text{for } \varphi \in [0, 2\pi) \text{ and } z \geq 0, \\ 0 & \text{for } \varphi \in [0, 2\pi) \text{ and } z^* < 0. \end{cases} , \tag{4.7b}$$

while the interface conditions eq. (4.3b) simply become

$$\lambda_{sf} \left. \frac{\partial T_s^*}{\partial r^*} \right|_{R_i^*} = \left. \frac{\partial T_f^*}{\partial r^*} \right|_{R_i^*} \qquad \text{for all } z^* \in \mathbb{R} \text{ and } \varphi \in [0, 2\pi), \tag{4.8a}$$

$$T_f^*(r = R_i^*, \varphi, z^*) = T_s^*(r = R_i^*, \varphi, z^*) \qquad \text{for all } z^* \in \mathbb{R} \text{ and } \varphi \in [0, 2\pi). \tag{4.8b}$$

After non-dimensionalisation, the physics of the problem in the fluid domain are governed by the bulk Reynolds number $\text{Re}_b = 2u_b R_i / \nu$, where u_b is the bulk velocity $u_b = 1/A \int_A \langle u_z \rangle \mathrm{d}A$, and the fluid's Prandtl number $\text{Pr} = \nu \rho_f c_{p,f} / \lambda_f$ (which, combined, form the Péclét number $\text{Pe} = \text{Re}_b\,\text{Pr}$). Including the solid in the formulation yields three additional dimensionless properties: a radius ratio $\Gamma = R_o / R_i$, a ratio of thermal conductivities $\lambda_{sf} = \lambda_s / \lambda_f$ and a ratio of effusivities $K = \sqrt{\lambda_f \rho_f c_{p,f} / \lambda_s \rho_s c_{p,s}}$; the latter describing how well temperature fluctuations can travel from the fluid to the solid and is hence only relevant in turbulent flow conditions. Note that in eq. (4.6), $(\rho_s c_{p,s}) / (\rho_f c_{p,f}) = 1/(K^2 \lambda_{sf})$.

Thermally fully developed conditions. For sufficiently large $z > 0$, the PDF of the temperature solution profile becomes translationally invariant in the axial direction, except for a linear shift of the temperature variable in z. This shift is the consequence of the continuous heating along z, and the state is called *thermally fully developed*. Clearly, $\partial T_i^* / \partial z^*$ is constant in this regime. The temperature variable may hence be transformed by subtracting that linear offset, which in particular enables the numerical simulation in a periodic domain:

$$T_i^* = \theta_i^* + C_1 \alpha \overline{f} z^*. \tag{4.9}$$

θ_i^* inherits the heat flux boundary condition eq. (4.7b), the interface conditions eqs. (4.8a) and (4.8b) and the solid temperature equation eq. (4.6) unchanged; the axial convection in eq. (4.6) (fluid) introduces a forcing term into the equation for θ_f^*:

$$\begin{aligned}\left(\frac{\partial \theta_f^*}{\partial t^*} + u_r^* \frac{\partial \theta_f^*}{\partial r^*} + \frac{u_\varphi^*}{r^*}\frac{\partial \theta_f^*}{\partial \varphi} + \frac{1}{\alpha} u_z^* \frac{\partial \theta_f^*}{\partial z^*}\right) \\ = \frac{\lambda_f}{R_{\mathrm{ref}} U_{\mathrm{ref}} \rho_f c_{p,f}} \left[\frac{1}{r^*}\frac{\partial}{\partial r^*}\left(r^* \frac{\partial \theta_f^*}{\partial r^*}\right) + \frac{1}{(r^*)^2}\frac{\partial^2 \theta_f^*}{\partial \varphi^2} + \frac{1}{\alpha^2}\frac{\partial^2 \theta_f^*}{\partial z^* \partial z^*}\right] - u_z^* C_1 \overline{f}.\end{aligned} \tag{4.10}$$

C_1 can be computed a-priori from an integral energy balance. Consider the mean balance equation of T_f^*, which is derived from eq. (4.5) as:

$$\begin{aligned}\frac{1}{\alpha}\langle u_z^* \rangle \frac{\partial \langle T_f^* \rangle}{\partial z^*} &= \frac{\lambda_f}{R_{\mathrm{ref}} U_{\mathrm{ref}} \rho_f c_{p,f}} \left[\frac{1}{r^*}\frac{\partial}{\partial r^*}\left(r^* \frac{\partial \langle T_f^* \rangle}{\partial r^*}\right) + \frac{1}{(r^*)^2}\frac{\partial^2 \langle T_f^* \rangle}{\partial \varphi^2} + \frac{1}{\alpha^2}\frac{\partial^2 \langle T_f^* \rangle}{\partial z^* \partial z^*}\right] \\ &\quad - \left[\frac{1}{r^*}\frac{\partial\left(r^* \langle T_f^{*\prime} u_r^{*\prime} \rangle\right)}{\partial r^*} + \frac{1}{r^*}\frac{\partial \langle T_f^{*\prime} u_\varphi^{*\prime} \rangle}{\partial \varphi} + \frac{1}{\alpha}\frac{\partial \langle T_f^{*\prime} u_z^{*\prime} \rangle}{\partial z^*}\right] \quad \text{fluid,}\end{aligned} \tag{4.11a}$$

$$0 = \frac{\lambda_f \lambda_{sf}}{R_{\mathrm{ref}} U_{\mathrm{ref}} \rho_f c_{p,f}} \left[\frac{1}{r^*}\frac{\partial}{\partial r^*}\left(r^* \frac{\partial \langle T_s^* \rangle}{\partial r^*}\right) + \frac{1}{(r^*)^2}\frac{\partial^2 \langle T_s^* \rangle}{\partial \varphi^2} + \frac{1}{\alpha^2}\frac{\partial^2 \langle T_s^* \rangle}{\partial z^* \partial z^*}\right] \quad \text{solid.} \tag{4.11b}$$

In the thermally fully developed state, there are no mean axial fluxes by construction. Assuming z^* is chosen within the fully developed region, a global energy balance

$$\int_{-\infty}^{z^*} \frac{1}{2\pi} \int_0^{2\pi} \left(\int_0^{R_i^*} (4.11\mathrm{a}) r^* \mathrm{d}r^* + \int_{R_i^*}^{R_o^*} (4.11\mathrm{b}) r^* \mathrm{d}r^*\right) \mathrm{d}\varphi \, \mathrm{d}\tilde{z}^* \tag{4.12}$$

yields, using that the instantaneous velocity at the interface vanishes, the interface condition eq. (4.8a) and the heat flux boundary condition eq. (4.7b),

$$\begin{aligned}\frac{1}{\alpha}\int_0^{R_i^*} \langle u_z^* \rangle \overline{\langle T_f^* \rangle} r^* \mathrm{d}r^* &= \frac{\lambda_f}{R_{\mathrm{ref}} U_{\mathrm{ref}} \rho_f c_{p,f}} \frac{1}{\alpha^2} \left(\int_0^{R_i^*} \frac{\partial \overline{\langle T_f^* \rangle}}{\partial z^*} r^* \mathrm{d}r^* + \lambda_{sf} \int_{R_i^*}^{R_o^*} \frac{\partial \overline{\langle T_s^* \rangle}}{\partial z^*} r^* \mathrm{d}r^*\right) \\ &\quad + \frac{R_i q_{w,\mathrm{ref}} \Gamma}{R_{\mathrm{ref}} U_{\mathrm{ref}} T_{\mathrm{ref}} \rho_f c_{p,f}} \overline{f} z^*\end{aligned} \tag{4.13}$$

Differentiating with respect to z^* and simplifying yields, noting $\frac{\partial T_i^*}{\partial z^*} = \text{const.}$,

$$\frac{\partial \overline{\langle T_f^* \rangle}}{\partial z^*} = \frac{4\alpha R_{\text{ref}} q_{w,\text{ref}} \Gamma}{T_{\text{ref}} \lambda_f \text{Pe}} \overline{f} =: C_1 \alpha \overline{f} \tag{4.14}$$

which gives the $z^* \to \infty$ behaviour of the bulk temperature T_b^*, which is defined as

$$T_b^* = \frac{\int_A \langle u_z^* T_f^* \rangle \mathrm{d}A}{\int_A \langle u_z^* \rangle \mathrm{d}A} = \frac{2U_{\text{ref}} R_{\text{ref}}^2}{u_b R_i^2} \int_0^{R_i^*} \overline{\langle u_z^* T_f^* \rangle} r^* \mathrm{d}r^*, \tag{4.15}$$

where A is the cross-sectional area (θ_b^* is defined analogously) as

$$T_b^* = C_1 \alpha \overline{f} \left(\frac{2R_i}{\text{Pe} R_{\text{ref}} \alpha} (1 + \lambda_{sf}(\Gamma^2 - 1)) + z^* \right) - \int_0^{R_i^*} \overline{\langle u_z'^* T_f^{*\prime} \rangle} r^* \mathrm{d}r^* \tag{4.16}$$

This relationship encodes a simple physical intuition: (i) A low value of Pe leads to a nonzero temperature upstream of $z^* = 0$, giving the heat transfer a 'headstart' compared to a case with low Pe, (ii) a thicker or better-conducting solid increases this 'headstart' and therefore increases the bulk temperature at a given z^* and Pe, (iii) turbulent mixing 'flattens' the temperature profile and hence reduces T_b^*, all else equal.

The inlet condition eq. (4.7a) is not meaningful for θ_i^*. This has two consequences: (i) a unique solution additionally requires the specification of an absolute temperature reference, and (ii) that reference temperature takes the role of T_0 in the non-dimensionalisation of θ^*. In section 4.2.3 that reference temperature will be the global bulk temperature according to eq. (4.16). Another possible choice is the mean interface temperature $\overline{\langle \theta_w^* \rangle}$, which makes it easier to compare temperature profiles, and this will be done for the turbulent cases in section 4.4.

Reference quantities. Various sensible choices for the reference quantities can be made; most references use one of

$$R_{\text{ref}} = \beta R_i, \quad U_{\text{ref}} = \frac{2}{\beta} u_b, \quad T_{\text{ref}} = (-1)^\delta \text{Pe}^\gamma \frac{\Gamma q_{w,\text{ref}}}{\rho_f c_{p,f} U_{\text{ref}}} \tag{4.17}$$

with $\beta \in \{1, 2\}$ and $\gamma, \delta \in \{0, 1\}$.[1]

[1] The same non-dimensionalisation, without CHT and without azimuthally varying heat flux, is used in [NGF26]. Hence, the equations presented in this section and section 4.2.2 are generalized from [NGF26]. A reference to that publication is implied, but not made explicit for every equation.

One then finds, for the diffusion coefficient of the fluid (eqs. (4.6) and (4.10)), the coefficient of the boundary condition eq. (4.7b), the slope C_1 (see eq. (4.10)) and the bulk temperature (see eq. (4.16)):

$$\frac{\lambda_f}{R_{\text{ref}} U_{\text{ref}} \rho_f c_{p,f}} = \frac{1}{\text{Pe}}, \tag{4.18a}$$

$$\frac{R_{\text{ref}} q_{w,\text{ref}}}{\lambda_{sf} \lambda_f T_{\text{ref}}} = (-1)^{\delta} \frac{\text{Pe}^{1-\gamma}}{\lambda_{sf} \Gamma}, \tag{4.18b}$$

$$C_1 = \frac{4\Gamma}{\text{Pe}} \frac{R_{\text{ref}} q_{w,\text{ref}}}{\lambda_f T_{\text{ref}}} = (-1)^{\delta} 4\text{Pe}^{-\gamma}. \tag{4.18c}$$

$$T_b^* = (-1)^{\delta} \overline{f} \left(\frac{8(1 + \lambda_{sf}(\Gamma^2 - 1))}{\text{Pe}^{\gamma+1} \beta} + 4\text{Pe}^{-\gamma} \alpha z^* \right) \tag{4.18d}$$

Indeed, this non-dimensionalisation is used by Straub et al. (2019b) with $\alpha = 1$, $\gamma = 0$ and $\delta = 1$; the main text of that paper uses $\beta = 2$ and appendix A.2 uses $\beta = 1$. In laminar heat transfer problems, the influence of axial conduction can be encoded in the parameter α as it is done in Papoutsakis et al. (1980); they use $\delta = 0$, $\alpha = \text{Pe}$, $\beta = 1$ and $\gamma = 1$ (i.e. $T_{\text{ref}} = q_{w,\text{ref}} \Gamma R_i / \lambda_f$ for $\Gamma = 1$ as there is no CHT in that paper).[2]

The reference heat flux $q_{w,\text{ref}}$ is given by $q_{w,\text{ref}} := F[q_w]$ where F is a functional chosen according to the requirements listed below; we will use in the following

$$q_{w,\text{ref}} := F[q_w] = \begin{cases} \overline{q_w} & \overline{q_w} \neq 0, \\ \sqrt{\frac{1}{\pi} \int_0^{2\pi} q_w(\varphi)^2 \mathrm{d}\varphi} & \overline{q_w} = 0 \end{cases} \tag{4.19}$$

where $\overline{q_w} = 1/(2\pi) \int_0^{2\pi} q_w(\varphi) \mathrm{d}\varphi$. This satisfies four requirements:

$$\text{Nonzero:} \quad q_w \not\equiv 0 \;\Rightarrow\; F[q_w] \neq 0, \tag{4.20a}$$

$$\text{Mean consistency:} \quad \overline{q_w} \neq 0 \;\Rightarrow\; F[q_w] = \overline{q_w}, \tag{4.20b}$$

$$\text{Rotation invariance:} \quad F[q_w(\varphi)] = F[q_w(\varphi + \alpha)] \quad \text{for all } \alpha \in \mathbb{R}, \tag{4.20c}$$

$$\text{Homogeneity:} \quad \begin{cases} F[\alpha\, q_w] = \alpha\, F[q_w], & \text{if } \overline{q_w} \neq 0, \\ F[\alpha\, q_w] = |\alpha|\, F[q_w], & \text{if } \overline{q_w} = 0, \end{cases} \tag{4.20d}$$

[2] Technically, U_{ref} is not specified in that paper; instead the definition of the Péclét number is modified to arrive at the same dimensionless diffusion coefficient in the fluid: $\text{Pe} = U_{\text{ref}} \delta \rho_f c_{p,f} / \lambda_f$.

[NBGF25] the latter reflecting that linear homogeneity is incompatible with requiring both eqs. (4.20a) and (4.20c) for mean-free fields; instead we require absolute linear homogeneity for the zero-mean branch. The requirements are needed for (4.20a) avoiding division by zero, (4.20b) to match the standard definition of the global Nusselt number and (4.20d) an invariant dimensionless solution under scaling of the heat flux in physical dimensions, respectively.

The global Nusselt number Nu is defined as

$$\mathrm{Nu} = 2R_i \left.\overline{\frac{\partial \langle T_f \rangle}{\partial r}}\right|_{R_i} \frac{1}{\overline{\langle T_w \rangle} - T_b(z)} \tag{4.21}$$

where T_w is the wall temperature and T_b is the bulk temperature, for its definition see eq. (4.15). If there is no mean axial conduction in the solid (cf. eq. (4.11b)), eq. (4.21) can be expressed in terms of the boundary condition,

$$\begin{aligned} \mathrm{Nu} &= \frac{2R_i \Gamma q_{w,\mathrm{ref}} \overline{f}}{\lambda_f T_{\mathrm{ref}}} \frac{1}{\left.\overline{\langle T^* \rangle}\right|_{R_i^*} - T_b^*(z^*)} \qquad \text{if } \frac{\partial^2 \langle T_s^* \rangle}{\partial z^* \partial z^*} = 0 \\ &\overset{\text{eq. (4.17)}}{=} (-1)^{\delta} \frac{2\overline{f}}{\beta} \frac{\mathrm{Pe}^{1-\gamma}}{\left.\overline{\langle T^* \rangle}\right|_{1/\beta} - T_b^*(z^*)}, \end{aligned} \tag{4.22}$$

The Nusselt number is therefore only a sensible measure if the azimuthal mean $\overline{f}$ of the dimensionless boundary condition $f(\varphi)$ is not zero. In a similar way, one may define a local Nusselt number

$$\mathrm{Nu}_l(\varphi, z) = 2R_i \left.\frac{\partial T_f}{\partial r}\right|_{R_i} \frac{1}{\langle T_w \rangle - T_{b,l}(\varphi, z)}, \tag{4.23}$$

where $T_{b,l}$ is the bulk temperature of a given azimuthal slice (i.e. eq. (4.15) without the overbar). Since the integral solid energy equation only makes a statement about the relation between $\partial\overline{\langle T_s \rangle}\big/\partial r\Big|_{R_i}$ and $\partial\overline{\langle T_s \rangle}\big/\partial r\Big|_{R_o}$ (note the overline), Nu_l can not be directly related to $f(\varphi)$; if the solid is omitted one obtains equivalently

$$\mathrm{Nu}_l(\varphi, z^*) = (-1)^{\delta} \frac{2f(\varphi)}{\beta} \frac{\mathrm{Pe}^{1-\gamma}}{\langle T^* \rangle|_{1/\beta} - T_{b,l}^*(\varphi, z^*)} \qquad \text{for } z^* > 0, \text{ no CHT} \tag{4.24}$$

Chapter layout. General conclusions from a theoretical viewpoint are presented in section 4.2.1, including the invariance of the global Nusselt number under different boundary conditions with the same mean. A decomposition of the Nusselt number that includes azimuthal and axial conduction is presented in section 4.2.2. Next, the laminar solution to the posed problem is presented: fully developed flow (incl. CHT) in section 4.2.3, and thermally developing flow (excl. CHT) in section 4.2.4. For the cases without CHT, the conservation equation in the solid and the interface conditions are omitted from the equation system; also the heat flux boundary condition (eq. (4.7b)) is applied to the fluid directly (with $\Gamma = \lambda_{sf} = 1$).

Next, section 4.4 considers thermally fully developed turbulent flow. Here, the results from the dissertation of Straub (2020) are extended, in particular to include CHT. Section 4.5 finally treats the case of thermally developing turbulent flow, however without conjugate heat transfer. In those sections, two Prandtl numbers are considered: $\mathrm{Pr} = 0.71$ (air) and $\mathrm{Pr} = 0.025$. Low-Pr fluids are, for example, liquid metals, which are considered as heat transfer fluids for CSP receivers (Marocco et al. 2016).

4.2 Analytical results

4.2.1 The spectral perspective and the global Nusselt number

As the boundary condition and all statistics of temperature are 2π-periodic in φ, it seems natural to employ a spectral decomposition in that direction by means of the Fourier series. This approach was suggested by Reynolds (1963a) to provide a first solution to the non-uniform heating problem in fully developed laminar and turbulent pipe flow (the former analytically, the latter based on a turbulent heat flux model). The spectral perspective not only is the basis for an analytical solution of the Graetz problem with non-uniform heat flux, but also leads to surprisingly strong statements for turbulent flow: in particular, the global Nusselt number can only depend on the mean of the heat flux, not its distribution around the circumference.

Let the complex Fourier coefficients of $f(\varphi)$ be given as

$$f_k = \frac{1}{2\pi} \int_0^{2\pi} f(\varphi) e^{-jk\varphi} \mathrm{d}\varphi, \tag{4.25}$$

where j denotes the imaginary unit. For a given velocity field $u_i^*(r^*, \varphi, z^*, t^*)$, the temperature response is linear in the boundary condition $f(\varphi)$. Consequently, the full

T_i^* can be constructed as a superposition of the responses to individual Fourier modes of $f(\varphi)$. First-order statistical moments in T^* (possibly nonlinear in u_i^*) inherit this linearity with respect to the boundary condition. Formally, for such a moment one can write

$$\langle u_i^{*m} T^* \rangle(\varphi) = \mathcal{L}_{\langle u_i^{*m} T^* \rangle}[f(\varphi)|\varphi], \tag{4.26}$$

where $\mathcal{L}_{\langle u_i^{*m} T^* \rangle}$ is a linear operator encoding the response of the statistic to $f(\varphi)$, evaluated at angle φ. Furthermore, $\mathcal{L}_{\langle u_i^{*m} T^* \rangle}$ is rotation-equivariant: rotating the boundary condition by an angle ψ is equivalent to rotating the moment by ψ:[3]

$$\mathcal{L}_{\langle u_i^{*m} T^* \rangle}[f(\varphi+\psi)|\varphi] = \mathcal{L}_{\langle u_i^{*m} T^* \rangle}[f(\varphi)|\varphi+\psi]. \tag{4.27}$$

A rotation-equivariant linear operator acts diagonally on the Fourier coefficients of the input (Katznelson 2004, section I.8.5). In other words, the first-order moments of temperature for a single-mode boundary condition $f(\varphi) = \sin(k\varphi)$ can only have a response involving the same wavenumber k (possibly phase-shifted compared to f, e.g., for $\langle u_\varphi^* T^* \rangle$). In particular, the azimuthal mean of all first-order moments of temperature vanishes for $k \neq 0$. Again, due to linearity, a moment that is first-order in temperature for any given composite boundary condition can be computed from the corresponding moments associated with $f(\varphi) = f_k \Re(e^{jk\varphi})$, and only the $k = 0$ mode of φ can contribute to the azimuthal mean of the moment.

Therefore: (i) the Nusselt number, computed from first-order moments of temperature (see eq. (4.21)), can only depend on the mean of $f(\varphi)$ and not its variation over φ, and (ii) if one is interested in first-order moments of temperature, instead of treating arbitrary boundary conditions $f(\varphi) \in L^2[0, 2\pi]$ it is sufficient to consider the response to each Fourier mode $e^{jk\varphi}, k \in \mathbb{Z}$.

Importantly, this argument does *not* require the governing equations to be decoupled in φ, and instantaneous u_φ^* indeed does couple the (time-dependent) modes in turbulent flow. Turbulence is allowed to scramble azimuthal modes in a complex way, but the underlying physics must be rotation-invariant, i.e. invariant under a uniform azimuthal shift. This would be violated for nonzero $\partial\langle u_\varphi^* \rangle \big/ \partial\varphi$ or φ-dependent properties. However, for laminar flow, the governing equations in fact decouple because there is no φ-dependent u_φ^*, and this fact will be exploited for the laminar solutions in sections 4.2.3 and 4.2.4.

[3] If e.g. the conductivity of the solid were different on one side only, this condition would not be fulfilled. Equally so, if $\langle u_\varphi^* \rangle$ depended on φ, this condition would not be not met; a mean swirl would be admissible.

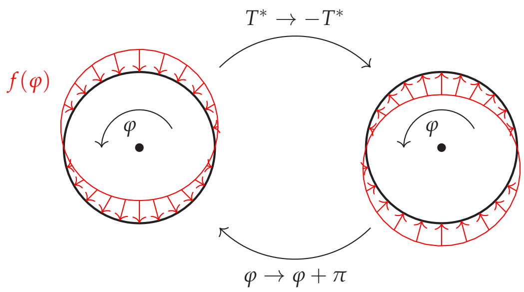

Figure 4.2: Illustration of the transformation for the antisymmetry of the joint PDF. Adapted from [NBGF25].

Note that all terms in the mean temperature equation of $\langle T_f^* \rangle$ (eq. (4.11a)) are first-order in T_f^*, so the same linearity and Fourier-diagonal property applies (and the mean temperature equation can indeed be written in decoupled form, see eq. (4.33c)). Likewise, transport equations for higher moments (such as the turbulent heat flux $\langle T_f^{*\prime} u_i^* \rangle$) also do not include second-order statistics of T_f^*, see appendix A.1.

For second- and higher-order moments, restrictions on the excited modes can be derived, similarly to the approach used in [NBGF25], by exploiting symmetries of the joint velocity-temperature PDF $p(u_r^*, u_\varphi^*, u_z^*, T^*, r^*, \varphi, z^*, t)$. In particular, moments of temperature are given by Pope (2000) for $m, n \geq 0$ as

$$\begin{aligned} &\langle u_i^{*m} T^{*n} \rangle (r^*, \varphi, z^*, t^*) \\ &\quad = \iiint_{-\infty}^{\infty} \int_{-\infty}^{\infty} u_i^{*m} T^{*n} p(u_r^*, u_\varphi^*, u_z^*, T^*, r^*, \varphi, z^*, t^*) \mathrm{d}T^* \mathrm{d}u_r^* \mathrm{d}u_\varphi^* \mathrm{d}u_z^*. \end{aligned} \tag{4.28}$$

Azimuthal integration of $\langle u_i^{*m} T^{*n} \rangle$, weighted with $e^{jl\varphi}$, yields the contribution of the mode corresponding to wavenumber l.

Consider $f(\varphi) = \sin(k\varphi)$ and $f'(\varphi) = -\sin(k\varphi)$. If $T^*(r^*, \varphi, z^*, t^*)$ solves eq. (4.1) with boundary condition f, then $-T^*(r^*, \varphi, z^*, t^*)$ solves eq. (4.1) with boundary condition f' for the same (fixed) velocity field. Thus, the joint PDF for f' is obtained from the joint PDF for f by flipping the sign of T^*:

$$p'(u_r^*, u_\varphi^*, u_z^*, T^*, r^*, \varphi, z^*, t^*) = p(u_r^*, u_\varphi^*, u_z^*, -T^*, r^*, \varphi, z^*, t^*)$$

Moreover, rotating the coordinate system of the solution to f' by π/k yields the solution to f again; this is illustrated in fig. 4.2. Hence,

$$p'(u_r^*, u_\varphi^*, u_z^*, T^*, r^*, \varphi + \pi/k, z^*, t^*) = p(u_r^*, u_\varphi^*, u_z^*, T^*, r^*, \varphi, z^*, t^*).$$

[NBGF25]

Both statements may be combined as

$$p(u_r, u_\varphi^*, u_z^*, -T^*, r^*, \varphi + \pi/k, z^*, t^*) = p(u_r^*, u_\varphi^*, u_z^*, T^*, r^*, \varphi, z^*, t^*). \tag{4.29}$$

This antisymmetry in the joint velocity-temperature PDF can be used to infer useful restrictions on higher-order statistical moments; the argument is similar to showing that the r^*-z^* and $r^*-\varphi$ components of the Reynolds stress tensor must be zero (Pope 2000). The moment $\langle u_i^{*m} T^{*n} \rangle$ has a weighted mean of $\frac{1}{2\pi}\int_0^{2\pi} e^{jl\varphi}\langle u_i^{*m} T^{*n}\rangle(r^*, \varphi, z^*, t^*)\mathrm{d}\varphi = \iiint_{-\infty}^{\infty} A \mathrm{d}u_r^* \mathrm{d}u_\varphi^* \mathrm{d}u_z^*$, where A is given by

$$\begin{aligned}
A &:= \frac{1}{2\pi}\int_0^{2\pi} e^{jl\varphi}\int_{-\infty}^{\infty} u_i^{*m} T^{*n} p(u_j^*, T^*, r^*, \varphi, z^*, t^*)\mathrm{d}T^*\mathrm{d}\varphi \\
&= \sum_{a=0}^{k-1}\frac{1}{2\pi}\int_0^{2\pi/k} e^{jl(\varphi+2\pi a/k)}\int_{-\infty}^{\infty} u_i^{*m} T^{*n} p(u_j^*, T^*, r^*, \varphi, z^*, t^*)\mathrm{d}T^*\mathrm{d}\varphi \\
&= \left(\sum_{a=0}^{k-1}\left(e^{2\pi jl/k}\right)^a\right)\frac{1}{2\pi}\int_0^{2\pi/k} e^{j\varphi l}\int_{-\infty}^{\infty} u_i^{*m} T^{*n} p(u_j^*, T^*, r^*, \varphi, z^*, t^*)\mathrm{d}T^*\mathrm{d}\varphi
\end{aligned}$$

The geometric sum $S = \sum_{a=0}^{k-1} q^a$ with $q = e^{2\pi jl/k}$ is readily evaluated; if l is a multiple of k (i.e. $l = \alpha k$ with integer α), then $q = 1$ and $S = k$. Otherwise, $S = \frac{1-e^{2\pi jl}}{1-e^{2\pi jl/k}} = 0$ as the numerator is zero and the denominator is nonzero. For $l = \alpha k$ one can split the remaining integral at π/k, substituting $\varphi \to \varphi + \pi/k$ and $T^* \to -T^*$ and finally using eq. (4.29):

$$\begin{aligned}
A &= \frac{k}{2\pi}\int_0^{2\pi/k} e^{j\varphi\alpha k}\int_{-\infty}^{\infty} u_i^{*m} T^{*n} p(u_j^*, T^*, r^*, \varphi, z^*, t^*)\mathrm{d}T^*\mathrm{d}\varphi \\
&= \frac{k}{2\pi}\left(\int_0^{\pi/k} e^{j\varphi\alpha k}\int_{-\infty}^{\infty} u_i^{*m} T^{*n} p(u_j^*, T^*, r^*, \varphi, z^*, t^*)\mathrm{d}T^*\mathrm{d}\varphi\right. \\
&\qquad \left. + \int_{\pi/k}^{2\pi/k} e^{j\varphi\alpha k}\int_{-\infty}^{\infty} u_i^{*m} T^{*n} p(u_j^*, T^*, r^*, \varphi, z^*, t^*)\mathrm{d}T^*\mathrm{d}\varphi\right) \\
&= \frac{k}{2\pi}\left(\int_0^{\pi/k} e^{j\varphi\alpha k}\int_{-\infty}^{\infty} u_i^{*m} T^{*n} p(u_j^*, T^*, r^*, \varphi, z^*, t^*)\mathrm{d}T^*\mathrm{d}\varphi\right. \\
&\qquad \left. + \int_0^{\pi/k} e^{j(\varphi+\pi/k)\alpha k}\int_{-\infty}^{\infty} u_i^{*m} T^{*n} p(u_j^*, T^*, r^*, \varphi+\pi/k, z^*, t^*)\mathrm{d}T^*\mathrm{d}\varphi\right) \\
&= \frac{k}{2\pi}\left(1 + (-1)^n e^{j\pi\alpha}\right)\int_0^{\pi/k} e^{j\varphi\alpha k}\int_{-\infty}^{\infty} u_i^{*m} T^{*n} p(u_j^*, T^*, r^*, \varphi, z^*, t^*)\mathrm{d}T^*\mathrm{d}\varphi
\end{aligned}$$

The combinations (α odd, n even) and (α even, n odd) lead to $A = 0$.[4]. Hence, for $f(\varphi) = \sin(k\varphi)$, the only remaining modes in $\langle T^{*2} \rangle$ are $l \in \{0, 2k, 4k, 6k, \dots\}$ and for $\langle T^{*3} \rangle$ those of $l \in \{k, 3k, 5k, \dots\}$.

In general, for a single-mode boundary condition $f(\varphi) = \sin(k\varphi)$, the structure of the azimuthal spectrum of higher-order temperature statistics is constrained by symmetry considerations: only integer multiples of k are excited, and parity considerations further eliminate some modes depending on the order of the moment.

Consider now a boundary condition $f(\varphi) = \Re(e^{jk\varphi})$, which is even in φ. As per the discussion above, first-order moments of temperature have the same spectral shape, i.e. $\langle T^* \rangle = \Re(\widehat{\langle T^* \rangle}_k e^{jk\varphi})$ and $\langle T^{*\prime} u_i^{*\prime} \rangle = \Re(\widehat{\langle T^{*\prime} u_i^{*\prime} \rangle}_k e^{jk\varphi})$. The coefficient $\widehat{\langle ... \rangle}_k$ is a complex-valued function of r (constant in φ), and encodes both gain and phase change of a moment with respect to the boundary condition. Whether such a phase change occurs can be derived from the symmetry of the problem. With the additional constraint of no mean rotation, i.e. $\langle u_\varphi^* \rangle = 0$, the resulting joint PDF of velocity and temperature transforms under a flip of the φ coordinate as

$$p(u_r^*, u_\varphi^*, u_z^*, T^*, r^*, \varphi, z, t^*) = p(u_r^*, -u_\varphi^*, u_z^*, T^*, r^*, -\varphi, z, t^*). \tag{4.30}$$

Now note that

$$\begin{aligned}
\langle T^* \rangle(r^*, -\varphi, z^*, t^*) &= \int_{-\infty}^{\infty} \iiint_{-\infty}^{\infty} T^* p(u_r^*, u_\varphi^*, u_z^*, T^*, r^*, -\varphi, z, t^*) \mathrm{d}u_r^* \mathrm{d}u_\varphi^* \mathrm{d}u_z^* \mathrm{d}T^* \\
&= \int_{-\infty}^{\infty} \iiint_{-\infty}^{\infty} T^* p(u_r^*, -u_\varphi^*, u_z^*, T^*, r^*, \varphi, z, t^*) \mathrm{d}u_r^* \mathrm{d}u_\varphi^* \mathrm{d}u_z^* \mathrm{d}T^* \\
&= \int_{-\infty}^{\infty} \iiint_{-\infty}^{\infty} T^* p(u_r^*, u_\varphi^*, u_z^*, T^*, r^*, \varphi, z, t^*) \mathrm{d}u_r^* \mathrm{d}u_\varphi^* \mathrm{d}u_z^* \mathrm{d}T^* \\
&= \langle T^* \rangle(r^*, \varphi, z^*, t^*)
\end{aligned}$$

Hence $\langle T^* \rangle$ is even as well, i.e. there is no phase shift between $f(\varphi)$ and $\langle T^* \rangle$. $\langle T^{*\prime} u_r^{*\prime} \rangle$ and $\langle T^{*\prime} u_z^{*\prime} \rangle$ are also in phase with $f(\varphi)$, this follows by multiplying the integrand with u_r^* and u_z^* in the preceding derivation. However, for u_φ^*, one finds

$$\begin{aligned}
\langle T^{*\prime} u_\varphi^{*\prime} \rangle(r^*, -\varphi, z^*, t^*) &= \int_{-\infty}^{\infty} \iiint_{-\infty}^{\infty} T^* u_\varphi^* p(u_r^*, u_\varphi^*, u_z^*, T^*, r^*, -\varphi, z, t^*) \mathrm{d}u_r^* \mathrm{d}u_\varphi^* \mathrm{d}u_z^* \mathrm{d}T^* \\
&= \int_{-\infty}^{\infty} \iiint_{-\infty}^{\infty} T^* u_\varphi^* p(u_r^*, -u_\varphi^*, u_z^*, T^*, r^*, \varphi, z, t^*) \mathrm{d}u_r^* \mathrm{d}u_\varphi^* \mathrm{d}u_z^* \mathrm{d}T^*
\end{aligned}$$

4 Trivially, $A = 0$ for $n = 1$ and $\alpha = 0$, i.e. boundary conditions with $k \neq 0$ lead to first-order temperature statistics with vanishing azimuthal mean.

$$
\begin{aligned}
&= -\int_{-\infty}^{\infty}\iiint_{-\infty}^{\infty} T^* u_\varphi^* p(u_r^*, u_\varphi^*, u_z^*, T^*, r^*, \varphi, z, t^*)\mathrm{d}u_r^*\mathrm{d}u_\varphi^*\mathrm{d}u_z^*\mathrm{d}T^* \\
&= -\langle T^{*\prime} u_\varphi^{*\prime}\rangle(r^*, \varphi, z^*, t^*)
\end{aligned}
$$

i.e. $\langle T^{*\prime} u_\varphi^{*\prime}\rangle$ is odd; therefore $\langle \widehat{T^{*\prime} u_\varphi^{*\prime}}\rangle_k$ must be imaginary. Hence, the phase of $\langle T^{*\prime} u_\varphi^{*\prime}\rangle$ is shifted by $\pi/2$ compared to the BC; for $k = 0$ this component vanishes identically.

To summarize, two independent lines of argumentation have been used to reduce the spectrum of moments of temperature. The first argument establishes the first-order moments of temperature as linear and rotation-invariant operators of the boundary condition; this directly shows that the spectrum of these moments contains the same wavenumbers as the boundary condition itself, and prevents any influence of $k \neq 0$ modes in the boundary condition on the global Nusselt number. The second argument, based on the joint velocity-temperature PDF, can be used to restrict the azimuthal modes in the response of temperature moments *of any order*; the resulting statement is slightly weaker for first-order moments (it still contains the statement regarding the global Nusselt number), but provides selection rules for the spectrogram of those moments for single-wavenumber boundary conditions. However, since higher-order moments are not linear in the temperature, the spectrogram of those moments for arbitrary boundary conditions containing multiple wavenumber components can be populated by nonlinear interactions. Respecting an additional constraint of no mean rotation ($\langle u_\varphi^*\rangle = 0$) determines the phase of the spectrum for each first-order moment a-priori.

It should be noted that the rotational invariance which both arguments use is not unique to pipe flow, but also present in, e.g., (turbulent) plane channel flow (as translational invariance along the spanwise direction). Assuming appropriate care is taken to define the spectrum of the boundary condition on the (infinite) wall plane, both arguments can be extended to that case. This seems unintuitive at first glance, as for channel flow it is known that the global Nusselt number changes between one-sided and both-sided heating (Bergman and Incropera 2011). A one-sided sinusoidal heat flux boundary condition fulfills the requirements of the linearity and symmetry arguments. Consequently, the spanwise mean of all first-order moments of temperature is zero. An arbitrary number of sine waves (including phase shifts) can be added to the boundary condition on both sides of the channel, without impact on the global Nusselt number. Finally, adding the mean temperature profile for one-sided heating (or adding it again, mirrored at the centreline) yields the response to an arbitrary heat-flux boundary condition, and the global Nusselt number is identically given by the response to

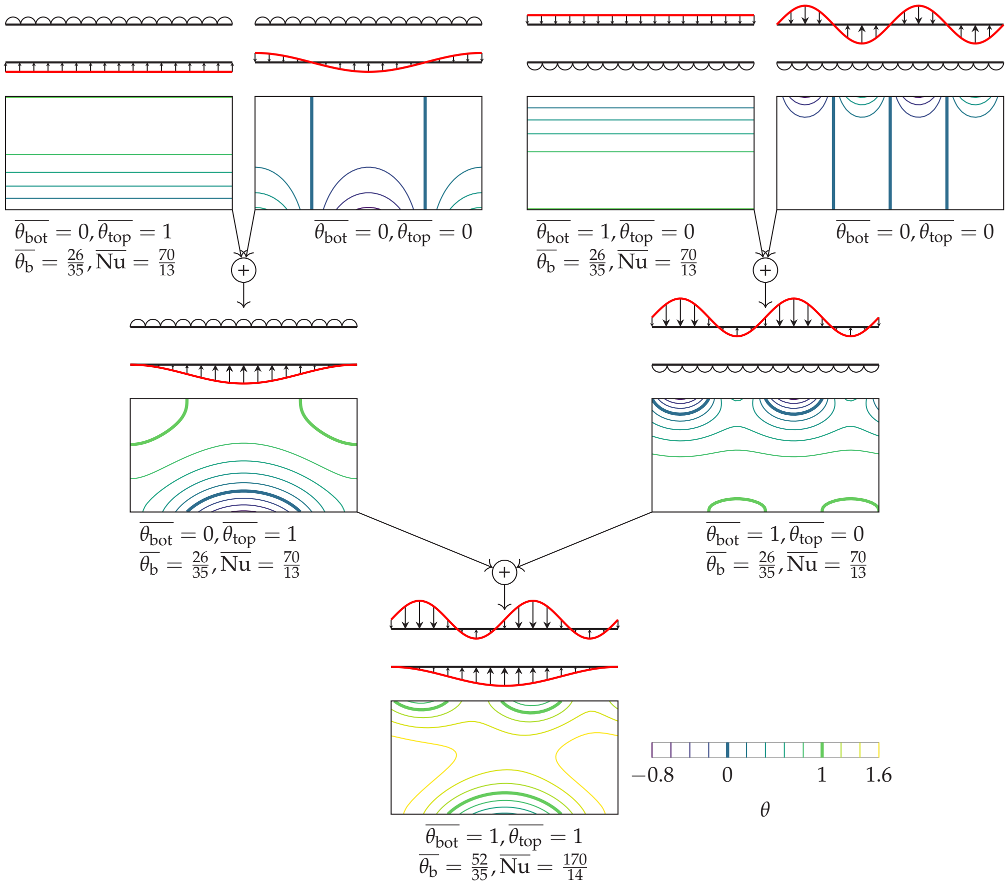

Figure 4.3: Representation of the decomposition of plane channel flow subject to inhomogeneous heating on both sides. Laminar flow, velocity profile $u = \frac{3}{2}(1 - y^2)$. On homogeneously heated walls, $\left|\frac{\partial T^*}{\partial y}\right|_w = 1$. $\overline{q}$ indicates spanwise mean of q. The bulk temperature is given by $\theta_b = \int_A uT^* \mathrm{d}A / \int_A u \mathrm{d}A$, and $\mathrm{Nu} = (D_h \left|\frac{\partial T^*}{\partial y}\right|_w) / (\theta_b - \theta_w)$ is evaluated on the heated wall(s) only (as in Bergman and Incropera (2011)), where $D_h = 4$ is the hydraulic diameter.

homogeneous heating with the mean heat flux of each side. This is visualized in fig. 4.3 for laminar flow.[5]

[5] For symmetric heating on both walls, the modal solution (except $k = 0$ due to different forcing) is identical to those computed for the shear stress boundary condition for the streamwise velocity in laminar flow from [NSGF22b].

4.2.2 Decomposition of the Nusselt number

Similar to the Fukagata-Iwamoto-Kasagi decomposition (Fukagata et al. 2002) of the skin friction coefficient for the purpose of flow control analysis, Straub et al. (2019b) presented a decomposition of the global Nusselt number for azimuthally uniform heat flux. As per section 4.2.1, no additional information will be gained from analysing the *global* Nusselt number of cases with azimuthally non-uniform heat flux, as all terms in the resulting decomposition are first-order moments of temperature, and thus identical to the uniform case. In this section, the analysis is thus expanded to the decomposition of the *local* Nusselt number for a given azimuthal wavenumber k, and the assumption of fully developed flow is dropped (i.e. the thermal inlet); note that (Fukagata et al. 2002) already included (hydrodynamical) development in the original formulation of the FIK identity. It is assumed that there is no mean swirl, i.e. $\langle u_\varphi^* \rangle = 0$, so that the results on the relative phase in section 4.2.1 applies.

In this derivation, the solid is omitted; the result also applies to CHT under the condition of azimuthally uniform heating and fully developed conditions.[6] The 'fluid' subscript is omitted.

Consider $\tilde{T} = -T^* + C_1 \alpha \overline{f} z^*$. Inserting into eq. (4.11a), the mean temperature equation of $\tilde{T}$ follows as

$$\begin{aligned}\frac{1}{\alpha}\langle u_z^* \rangle \frac{\partial \langle \tilde{T} \rangle}{\partial z^*} = \frac{\lambda_f}{R_{\mathrm{ref}} U_{\mathrm{ref}} \rho_f c_{p,f}} \left[\frac{1}{r^*}\frac{\partial}{\partial r^*}\left(r^* \frac{\partial \langle \tilde{T} \rangle}{\partial r^*} \right) + \frac{1}{(r^*)^2}\frac{\partial^2 \langle \tilde{T} \rangle}{\partial \varphi^2} + \frac{1}{\alpha^2}\frac{\partial^2 \langle \tilde{T} \rangle}{\partial z^* \partial z^*} \right] \\ - \left[\frac{1}{r^*}\frac{\partial \left(r^* \langle \tilde{T}' u_r^{*\prime} \rangle \right)}{\partial r^*} + \frac{1}{r^*}\frac{\partial \langle \tilde{T}' u_\varphi^{*\prime} \rangle}{\partial \varphi} + \frac{1}{\alpha}\frac{\partial \langle \tilde{T}' u_z^{*\prime} \rangle}{\partial z^*} \right] + \langle u_z^* \rangle C_1 \overline{f}.\end{aligned} \tag{4.31}$$

Assume a boundary condition $f(\varphi) = \Re(e^{jk\varphi})$ as in section 4.2.1. Each moment in eq. (4.31) has the same spectral content as the boundary condition – only wavenumber k is present – and each phase is known. One has, after regrouping and abbreviating $(R_{\mathrm{ref}} U_{\mathrm{ref}} \rho_f c_{p,f})/\lambda_f = \mathrm{Pe}_{\mathrm{ref}}$,

$$0 = I_r + I_\varphi + I_z, \tag{4.32}$$

[6] The derivation requires that the heat flux on interface is known; this is only the case under the specified conditions, see eq. (4.11b).

where

$$I_r = \frac{1}{r^*}\frac{\partial}{\partial r^*}\left(\frac{r^*}{\mathrm{Pe}_{\mathrm{ref}}}\frac{\partial\widehat{\langle\tilde{T}\rangle}_k}{\partial r^*} - r^*\widehat{\langle\tilde{T}'u_r^{*\prime}\rangle}_k\right) + \langle u_z^*\rangle C_1\overline{f}, \tag{4.33a}$$

$$I_\varphi = -\frac{1}{\mathrm{Pe}_{\mathrm{ref}}}\frac{k^2}{(r^*)^2}\widehat{\langle\tilde{T}\rangle}_k - \frac{jk}{r^*}\widehat{\langle\tilde{T}'u_\varphi^{*\prime}\rangle}_k, \tag{4.33b}$$

$$I_z = -\frac{1}{\alpha}\langle u_z^*\rangle\frac{\partial\widehat{\langle\tilde{T}\rangle}_k}{\partial z^*} + \frac{1}{\mathrm{Pe}_{\mathrm{ref}}}\frac{1}{\alpha^2}\frac{\partial^2\widehat{\langle\tilde{T}\rangle}_k}{\partial z^*\partial z^*} - \frac{1}{\alpha}\frac{\partial\widehat{\langle\tilde{T}'u_z^{*\prime}\rangle}_k}{\partial z^*}, \tag{4.33c}$$

correspond to the radial, azimuthal and axial contributions of the equation, respectively. Similarly, one obtains the boundary condition in the spectral form. From eq. (4.7b) one obtains

$$\left.\frac{\partial\widehat{\langle\tilde{T}\rangle}_k}{\partial r^*}\right|_{R_i^*} = -\frac{R_{\mathrm{ref}}q_{w,\mathrm{ref}}}{\lambda_f T_{\mathrm{ref}}} \qquad \text{for } \varphi\in[0,2\pi) \text{ and } z\geq 0, \tag{4.34}$$

and the spectral form of the local Nusselt number (eq. (4.23)) with the boundary condition inserted, as

$$\mathrm{Nu}_l = 2R_i\left.\frac{\partial\langle T_f\rangle}{\partial r}\right|_{R_i}\frac{1}{\langle T_w\rangle - T_{b,l}(\varphi,z)} = \frac{2R_iq_{w,\mathrm{ref}}}{\lambda_f T_{\mathrm{ref}}}\frac{1}{\widehat{\tilde{T}_{b,l}}_k - \left.\widehat{\langle\tilde{T}\rangle}_k\right|_{R_i^*}}. \tag{4.35}$$

Next, a triple integration $\int_{R_i^*}^0\int_{R_i^*}^{r^*}\int_{R_i^*}^{\tilde{r}^*}$ eq.(4.32)$\bar{r}^*\mathrm{d}\bar{r}^*\frac{1}{\tilde{r}^*}\mathrm{d}\tilde{r}^*\langle u_z^*\rangle r^*\mathrm{d}r^*$ is performed. For a general function $g(r)$ one finds by partial integration, using the fractional flow rate $\Phi = C_2\int_{R_i^*}^{r^*}\langle u_z^*\rangle\bar{r}^*\mathrm{d}\bar{r}^*$, where $C_2 = 2U_{\mathrm{ref}}/u_bR_{\mathrm{ref}}^2/R_i^2$ so that $\Phi(0) = -1$:

$$\int_{R_i^*}^0\int_{R_i^*}^{r^*}\int_{R_i^*}^{\tilde{r}^*} g(\bar{r}^*)\bar{r}^*\mathrm{d}\bar{r}^*\frac{1}{\tilde{r}^*}\mathrm{d}\tilde{r}^*\langle u_z^*\rangle r^*\mathrm{d}r^* = \int_0^{R_i^*}\frac{\Phi+1}{C_2r^*}\int_{R_i^*}^{r^*} g(\tilde{r}^*)\tilde{r}^*\mathrm{d}\tilde{r}^*\mathrm{d}r^*. \tag{4.36}$$

For I_r, one finds after careful integration by parts and insertion of eqs. (4.34) and (4.35)

$$\begin{aligned}&\int_0^{R_i^*}\frac{\Phi+1}{C_2r^*}\int_{R_i^*}^{r^*} I_r\tilde{r}^*\mathrm{d}\tilde{r}^*\mathrm{d}r^*\\ &= \frac{1}{C_2\mathrm{Pe}_{\mathrm{ref}}}\left(-\frac{2R_iq_{w,\mathrm{ref}}}{\lambda_f T_{\mathrm{ref}}}\frac{1}{\mathrm{Nu}_l}\right) - \frac{1}{\mathrm{Pe}_{\mathrm{ref}}}\int_{R_i^*}^0\widehat{\langle u_z^{*\prime}\tilde{T}'\rangle}_k r^*\mathrm{d}r^*\\ &+\int_{R_i^*}^0\frac{\Phi+1}{C_2r^*}\left(\widehat{\langle\tilde{T}'u_r^{*\prime}\rangle}_k r^* - \frac{R_i^*q_{w,\mathrm{ref}}}{U_{\mathrm{ref}}T_{\mathrm{ref}}c_{p,f}\rho_f} - \frac{C_1}{C_2}\overline{f}\Phi\right)\mathrm{d}r^*.\end{aligned} \tag{4.37}$$

Inserting the non-dimensionalisation eq. (4.17) as well as C_2 and C_1 (eq. (4.18c)):

$$
\begin{aligned}
\frac{1}{\mathrm{Nu}_l} = & (-1)^{\delta} 2\beta^2 \mathrm{Pe}^{\gamma-1} \int_0^{1/\beta} \widehat{\langle u_z^{*\prime} \tilde{T}^\prime \rangle}_k r^* \mathrm{d}r^* \\
& - (-1)^{\delta} \frac{\beta}{2} \mathrm{Pe}^{\gamma} \int_0^{1/\beta} (\Phi + 1) \widehat{\langle \tilde{T}^\prime u_r^{*\prime} \rangle}_k \mathrm{d}r^* + \frac{1}{2} \int_0^{1/\beta} \frac{\Phi+1}{r^*} (1 + \overline{f}\Phi) \mathrm{d}r^* \\
& (-1)^{\delta} \frac{\beta}{2} \mathrm{Pe}^{\gamma} \int_0^{1/\beta} \frac{\Phi+1}{r^*} \int_{1/\beta}^{r^*} (I_z + I_\varphi) \tilde{r}^* \mathrm{d}\tilde{r}^* \mathrm{d}r^*
\end{aligned}
$$

Splitting the fractional flow rate into a laminar and turbulent part according to $\langle u_z^* \rangle = 2u_b/U_{\mathrm{ref}}(1 - (R_{\mathrm{ref}}/R_i)^2 (r^*)^2) + \langle u_{z,t}^* \rangle$, hence $\Phi = \Phi_L + \Phi_T = (-1 + 2\beta^2 (r^*)^2 - \beta^4 (r^*)^4) + C_2 \int_{R_i^*}^{r^*} \langle u_{z,t}^* \rangle \overline{r}^* \mathrm{d}\overline{r}^*$, the integral containing the forcing (note that $\overline{f} = 0$ for $k \neq 0$; 1 otherwise) becomes

$$
\begin{aligned}
& \frac{1}{2} \int_0^{1/\beta} \frac{\Phi+1}{r^*} (1 + \overline{f}\Phi) \mathrm{d}r^* \\
& \quad = \frac{3}{8} - \frac{7}{48}\overline{f} + \frac{1}{2} \int_0^{1/\beta} \frac{\Phi_T}{r} \Big((1 - \overline{f}) + \overline{f}(4\beta^2 r^2 - 2\beta^4 r^4 + \Phi_T) \Big) \mathrm{d}r^*
\end{aligned} \tag{4.38}
$$

For $k = 0$, $\overline{f} = 1$ the canonical value for the Nusselt number under laminar, fully developed conditions (fixed heat flux) is recovered (48/11). Indeed, this is the only nonzero contribution under laminar, fully developed conditions for $k = 0$; for $k \neq 0$, the first term of I_φ encodes the azimuthal conduction and hence is present as well in addition to the constant 3/8 (caused by the wall heat flux term). Under axially developing laminar conditions, I_z contributes two additional terms. To summarise, one obtains

$$
\begin{aligned}
\underbrace{\frac{18-7\overline{f}}{48}}_{1/\mathrm{Nu}_{lam}} = \frac{1}{\mathrm{Nu}_l}
&\underbrace{+(-1)^{\delta}\frac{\beta}{2}\mathrm{Pe}^{\gamma}\int_0^{1/\beta}(\Phi+1)\widehat{\langle\tilde{T}'u_r^{*\prime}\rangle}_k \mathrm{d}r^*}_{1/\mathrm{Nu}_{HF,r}} \\
&\underbrace{+\frac{1}{2}\int_0^{1/\beta}\frac{\Phi_T}{r}\left((\overline{f}-1)+\overline{f}(2\beta^4r^4-4\beta^2r^2-\Phi_T)\right)\mathrm{d}r^*}_{1/\mathrm{Nu}_{RSS}} \\
&\underbrace{-2(-1)^{\delta}\beta^2\mathrm{Pe}^{\gamma-1}\int_0^{1/\beta}\widehat{\langle u_z^{*\prime}\tilde{T}'\rangle}_k r^*\mathrm{d}r^*}_{1/\mathrm{Nu}_{HF,z}} \\
&\underbrace{+(-1)^{\delta}\frac{\beta}{2}\frac{\mathrm{Pe}^{\gamma}}{\alpha}\int_0^{1/\beta}\frac{\Phi+1}{r^*}\int_{1/\beta}^{r^*}\left(\langle u_z^*\rangle\frac{\partial\widehat{\langle\tilde{T}\rangle}_k}{\partial z^*}-\frac{1}{\mathrm{Pe}}\frac{1}{\alpha}\frac{\partial^2\widehat{\langle\tilde{T}\rangle}_k}{\partial z^*\partial z^*}+\frac{\partial\widehat{\langle\tilde{T}'u_z^{*\prime}\rangle}_k}{\partial z^*}\right)\tilde{r}^*\mathrm{d}\tilde{r}^*\mathrm{d}r^*}_{1/\mathrm{Nu}_{dev.}} \\
&\Bigg[\underbrace{+(-1)^{\delta}\frac{\beta}{2}\mathrm{Pe}^{\gamma-1}\int_0^{1/\beta}\frac{\Phi+1}{r^*}\int_{1/\beta}^{r^*}\frac{k^2}{\tilde{r}^*}\widehat{\langle\tilde{T}\rangle}_k\mathrm{d}\tilde{r}^*\mathrm{d}r^*}_{1/\mathrm{Nu}_{az.cond.}} \\
&\underbrace{+(-1)^{\delta}\frac{\beta}{2}\mathrm{Pe}^{\gamma}\int_0^{1/\beta}\frac{\Phi+1}{r^*}\int_{1/\beta}^{r^*}jk\widehat{\langle\tilde{T}'u_\varphi^{*\prime}\rangle}_k\mathrm{d}\tilde{r}^*\mathrm{d}r^*}_{1/\mathrm{Nu}_{HF,\varphi}}\Bigg].
\end{aligned}
\tag{4.39}
$$

where I_z and I_φ are given by eq. (4.33c).

The contributions of eq. (4.39) are in order: a laminar part ($Nu_{lam} = 48/11$ in fully developed laminar flow), Nu_l itself, the contribution of the radial turbulent heat flux ($\mathrm{Nu}_{HF,r}$), the modification of the bulk temperature due to the change in the mean velocity profile compared to the laminar one (Nu_{RSS}), the contribution of the axial turbulent heat flux ($\mathrm{Nu}_{HF,z}$) and a developing part ($\mathrm{Nu}_{dev.}$). [The last two terms represent the contributions of azimuthal molecular ($\mathrm{Nu}_{az.cond.}$) and turbulent ($\mathrm{Nu}_{HF,\varphi}$) heat flux (only for $k \neq 0$). Note that for $\gamma = I_z = I_\varphi = 0$, the decomposition of Straub et al. (2019b) is recovered (therein, eq. (B.28) is the resulting form for $\beta = 1$ while eq. (11) is the resulting form for $\beta = 2$).] Crucially, all significant individual terms of the right-hand side of eq. (4.39) are observed to be positive [...]; the only exceptions are the term due to the axial turbulent heat flux and the heat flux through axial conduction; the first is small (Straub et al. 2019b) while the second is negligible for $\mathrm{Pe} \gg 1$. Equation (4.39) is reshaped as

$$1 = \frac{\mathrm{Nu}_{lam}}{\mathrm{Nu}_l} + \frac{\mathrm{Nu}_{lam}}{\mathrm{Nu}_{HF,r}} + \frac{\mathrm{Nu}_{lam}}{\mathrm{Nu}_{RSS}} - \frac{\mathrm{Nu}_{lam}}{\mathrm{Nu}_{HF,z}} + \frac{\mathrm{Nu}_{lam}}{\mathrm{Nu}_{dev.}} \left[+ \frac{\mathrm{Nu}_{lam}}{\mathrm{Nu}_{az.cond.}} + \frac{\mathrm{Nu}_{lam}}{\mathrm{Nu}_{HF,\varphi}} \right]. \quad (4.40)$$

[NGF26] For example, increasing the radial heat flux $\langle \widehat{\tilde{T}' u_r^{*\prime}} \rangle_k$ while keeping all else equal, increases $\mathrm{Nu}_{lam}/\mathrm{Nu}_{HF,r}$, which in turn must decrease the term containing Nu_l, i.e. $\mathrm{Nu}_{lam}/\mathrm{Nu}_l$, hence increasing Nu_l itself.

The decomposition of the Nusselt number will be used for the analysis of turbulent data in sections 4.4.2 and 4.5.

4.2.3 Fully developed solution for laminar flow

The solution for the thermally and hydraulically fully developed state for laminar flow is given in this section, and follows [NMGF25], which in turn is based on Reynolds (1963a), where the case without conjugate heat transfer is discussed (note that Reynolds (1963b) give the wall temperature for the laminar CHT case). Compared to the [NMGF25] paper, the dimensionless temperature variable takes a different label and the non-dimensionalisation of the boundary condition is different to account for the case of zero-mean heat flux.

The boundary value problem for the Graetz problem is given by eq. (4.6) with $\partial\theta^*/\partial t^* = 0$, $u_\varphi^* = u_r^* = 0$, BCs eqs. (4.2b) and (4.7b) and ICs eqs. (4.8a) and (4.8b). For this section and section 4.2.4, the equations are non-dimensionalised according to eqs. (4.5) and (4.17); the parameters $\alpha = \mathrm{Pe}, \beta = 1, \gamma = 0$ and the plus sign in eq. (4.17) are chosen as in Papoutsakis et al. (1980). The resulting dimensionless temperature variables are denoted as $\theta_i^* \to \theta_i$ (fully developed solution) and $T_i^* \to \Theta_i$ (Graetz problem), and star superscripts are omitted. The laminar velocity profile $u_z(r)$ will be specified later. The governing equations are re-stated here for convenience with the chosen non-dimensionalisation:

$$\frac{1}{r}\frac{\partial}{\partial r}\left(r\frac{\partial \Theta_i}{\partial r}\right) + \frac{1}{r^2}\frac{\partial^2 \Theta_i}{\partial \varphi^2} + \frac{1}{\mathrm{Pe}^2}\frac{\partial^2 \Theta_i}{\partial z^2} = \begin{cases} u_z(r)\frac{\partial \Theta_f}{\partial z} & \text{fluid,} \\ 0 & \text{solid,} \end{cases} \quad (4.41a)$$

$$\lim_{z\to-\infty} \Theta_i(r,\varphi,z) = 0 \quad \text{for all } r > 0 \text{ and } \varphi \in [0, 2\pi), \quad (4.41b)$$

$$\Theta_f(0,\varphi,z) \quad \text{regular in } z \text{ and } \varphi, \tag{4.41c}$$

$$\left.\frac{\partial \Theta_s}{\partial r}\right|_{r=\Gamma} = \frac{1}{\Gamma \lambda_{sf}} \begin{cases} f(\varphi) & \text{if } z \geq 0 \text{ and } \varphi \in [0,2\pi) \\ 0 & \text{if } z < 0 \text{ and } \varphi \in [0,2\pi) \end{cases}, \tag{4.41d}$$

$$\lambda_{sf} \left.\frac{\partial \Theta_s}{\partial r^*}\right|_{r=1} = \left.\frac{\partial \Theta_f}{\partial r^*}\right|_{r^*=1} \quad \text{for all } z \in \mathbb{R} \text{ and } \varphi \in [0,2\pi), \tag{4.41e}$$

$$\Theta_f(r=1,\varphi,z) = \Theta_s(r=1,\varphi,z) \quad \text{for all } z \in \mathbb{R} \text{ and } \varphi \in [0,2\pi). \tag{4.41f}$$

In case of the fully developed solution, eq. (4.9) is inserted into eq. (4.41a), so that one obtains instead

$$\frac{1}{r}\frac{\partial}{\partial r}\left(r\frac{\partial \theta_i}{\partial r}\right) + \frac{1}{r}\frac{\partial}{\partial \varphi}\left(\frac{1}{r}\frac{\partial \theta_i}{\partial \varphi}\right) = \begin{cases} 4\overline{f}u_z(r) & \text{fluid,} \\ 0 & \text{solid,} \end{cases} \tag{4.42}$$

where θ_i only depends on r and φ. Therefore, boundary condition eq. (4.41b) is not applicable for the fully developed problem; hence the system is completed by the boundary conditions eqs. (4.41c) to (4.41f) with $\Theta_i \to \theta_i$ substituted. In order to fulfill the ansatz eq. (4.9) in an absolute sense for $z \to \infty$, the offset is determined by the integral energy balance (4.13) like in (4.16).

[As discussed in section 4.2.1,] θ_i can be written as a series of the form

$$\theta_i = \sum_{k=-\infty}^{\infty} \hat{\theta}_{k,i}(r) e^{jk\varphi}. \tag{4.43}$$

Inserting eq. (4.43) into eq. (4.42) yields

$$\sum_{k=-\infty}^{\infty} e^{jk\varphi} \left(\frac{1}{r}\frac{\mathrm{d}}{\mathrm{d}r}\left(r\frac{\mathrm{d}\hat{\theta}_{k,i}}{\mathrm{d}r}\right) - \frac{k^2}{r^2}\right) = \begin{cases} 4\overline{f}u_z(r) & \text{fluid,} \\ 0 & \text{solid.} \end{cases} \tag{4.44}$$

Both sides of Eq. (4.44) are Fourier series – the right hand side only contains the 0-mode. As the Fourier series is unique, we may compare coefficients and deduce

$$0 = \left(\frac{\partial^2 \hat{\theta}_{k,i}}{\partial r^2} + \frac{1}{r}\frac{\partial \hat{\theta}_{k,i}}{\partial r} - \frac{k^2}{r^2}\hat{\theta}_{k,i}\right) + \begin{cases} 4\overline{f}u_z(r) & \text{if } k = 0 \text{ and fluid,} \\ 0 & \text{otherwise.} \end{cases} \tag{4.45}$$

[...] The regularity constraint eq. (4.41c) has two consequences:

$$\left.\frac{\partial \hat{\theta}_{0,f}}{\partial r}\right|_{r=0} = 0, \quad \text{and } \hat{\theta}_{k,f} = 0, \quad k \neq 0. \tag{4.46}$$

Next, let f_k denote the k-th complex Fourier coefficient for $f(\varphi)$ [as in eq. (4.25). Note that $\overline{f} = f_0$.] Inserting eq. (4.43) into the boundary condition eq. (4.41d) and again separating modes, we find

$$\left.\frac{\partial \hat{\theta}_{k,s}(r)}{\partial r}\right|_{r=\Gamma} = \frac{f_k}{\Gamma \lambda_{sf}} \quad \text{for } z \in \mathbb{R} \text{ and } \varphi \in [0, 2\pi). \tag{4.47}$$

The ICs eqs. (4.41e) and (4.41f) can be treated in the same way to obtain

$$\lambda_{sf} \left.\frac{\partial \hat{\theta}_{k,s}}{\partial r}\right|_{r=1} = \left.\frac{\partial \hat{\theta}_{k,f}}{\partial r}\right|_{r=1} \qquad \text{for } z \in \mathbb{R} \text{ and } \varphi \in [0, 2\pi), \tag{4.48a}$$

$$\hat{\theta}_{k,f}(r=1, \varphi, z) = \hat{\theta}_{k,s}(r=1, \varphi, z) \qquad \text{for } z \in \mathbb{R} \text{ and } \varphi \in [0, 2\pi). \tag{4.48b}$$

Finally, eq. (4.13) prescribes

$$\int_0^1 \left(u_z \hat{\theta}_{0,f} - \frac{1}{\mathrm{Pe}^2} \frac{\partial \hat{\theta}_{0,f}}{\partial z} \right) r \mathrm{d}r - \frac{\lambda_{sf}}{\mathrm{Pe}^2} \int_1^\Gamma \frac{\partial \hat{\theta}_{0,s}}{\partial z} r \mathrm{d}r = z. \tag{4.49}$$

For $k = 0$, the solution to the system described by eq. (4.45) and BCs / ICs eqs. (4.46), (4.47), (4.48a), (4.48b) and (4.49) can be computed for any concrete velocity profile $u_z(r)$. [Note that the system is overdetermined; this is as C_1 was already computed from a global energy balance]. For the laminar profile $u_z(r) = 1 - r^2$, we find [...]

$$\hat{\theta}_{0,i} = \overline{f} \left(\frac{8}{\mathrm{Pe}^2} + \frac{8\lambda_{sf}(\Gamma^2 - 1)}{\mathrm{Pe}^2} + \begin{cases} -\frac{1}{4} r^4 + r^2 - \frac{7}{24} & \text{fluid}, \\ \frac{1}{\lambda_{sf}} \ln(r) + \frac{11}{24} & \text{solid}. \end{cases} \right) \tag{4.50}$$

[The offset is as expected by eq. (4.18d)]. For $k \neq 0$, the ODEs for fluid and solid modes are identical. Equation (4.45)'s solutions are $\hat{\theta}_{k,i} = A_{k,i} r^{|k|} + B_{k,i} r^{-|k|}$ with suitable integration constants $A_{k,i}$ and $B_{k,i}$. These are determined from BCs / ICs eqs. (4.46), (4.47), (4.48a) and (4.48b):

$$\hat{\theta}_{k,i} = f_k D_{|k|,i} \tag{4.51a}$$

$$\text{with } D_{|k|,i} = \frac{1}{\Pi_{|k|}|k|} \cdot \begin{cases} 2r^{|k|} & \text{fluid,} \\ \frac{\lambda_{sf}+1}{\lambda_{sf}} r^{|k|} + \frac{\lambda_{sf}-1}{\lambda_{sf}} r^{-|k|} & \text{solid,} \end{cases} \tag{4.51b}$$

$$\text{where } \Pi_{|k|} = (\lambda_{sf}+1)\Gamma^{|k|} - (\lambda_{sf}-1)\Gamma^{-|k|}. \tag{4.51c}$$

Note that $f_{-k} = f_k^*$ since f is real-valued. Exploiting this identity upon inserting eqs. (4.50) and (4.51c) into eq. (4.43), we find [for z sufficiently large, i.e. sufficiently far away from the heated section]

$$\Theta_i = 4z\overline{f} + \hat{\theta}_{0,i}(r) + \sum_{k=-\infty}^{-1} \hat{\theta}_{k,i}(r)e^{jk\varphi} + \sum_{k=1}^{\infty} \hat{\theta}_{k,i}(r)e^{jk\varphi} \tag{4.52a}$$

$$= 4z\overline{f} + \hat{\theta}_{0,i}(r) + \sum_{k=1}^{\infty} 2D_{k,i}(\mathrm{Re}(f_k)\cos(k\varphi) - \mathrm{Im}(f_k)\sin(k\varphi)). \tag{4.52b}$$

In particular, the heat flux at the interface is given by

$$\left.\frac{\partial\theta}{\partial r}\right|_{r=1} = \overline{f} + \sum_{k=1}^{\infty} \frac{4}{\Pi_k}(\mathrm{Re}(f_k)\cos(k\varphi) - \mathrm{Im}(f_k)\sin(k\varphi)). \tag{4.53}$$

For illustration purposes, fig. 4.4 gives the temperature and heat flux distribution (according to eq. (4.52b)) for half-sinusoidal heating, i.e.

$$f(\varphi) = \begin{cases} \pi\sin(\varphi) & \varphi \in [0,\pi], \\ 0 & \text{otherwise,} \end{cases}$$

for a selection of parameters. This heating mode corresponds to a pipe heated by radiation from a far-away point source, isolated on the side facing away from the point source.

Some remarks are in order. First, in eq. (4.51c), the term $r^{|k|}$ is always dominant for increasing r (in both fluid and solid). Hence, high wavenumber contributions are strongly damped the farther away from the outer wall one measures the temperature. This is reminiscent of the St.-Venant principle in solid mechanics, or of the thickness of a Stokes layer depending on the excitation frequency. As a consequence, high k contributions mostly don't travel into the fluid, in particular for thick, well-conducting walls. In general, for solid walls with these properties, the interface heat flux will become increasingly homogeneous, as visualized in fig. 4.5.

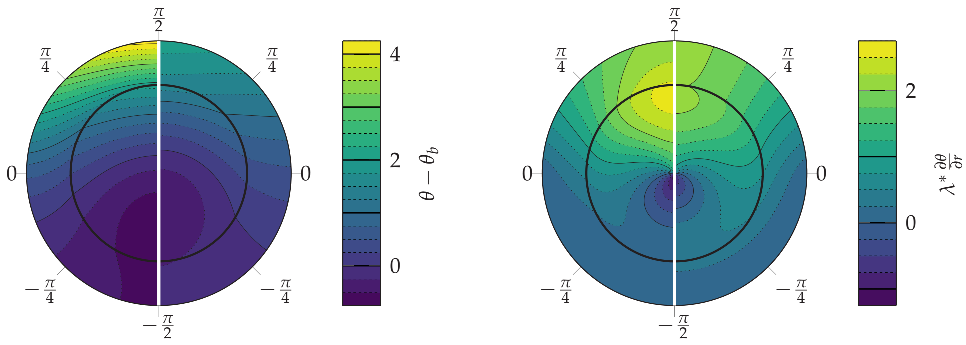

(a) Dimensionless temperature profile $\theta - \theta_b$

(b) Dimensionless radial heat flux $\lambda^* \frac{\partial \theta}{\partial r}$

Figure 4.4: Fully developed solution according to eq. (4.52b) for half-sinusoidal heating, radius ratio $\Gamma = 1.5$ and $\lambda_{sf} = 1/2$ (left semicircle) vs. $\lambda_{sf} = 2$ (right semicircle). The interface between fluid and solid is indicated. Adapted from [NMGF25].

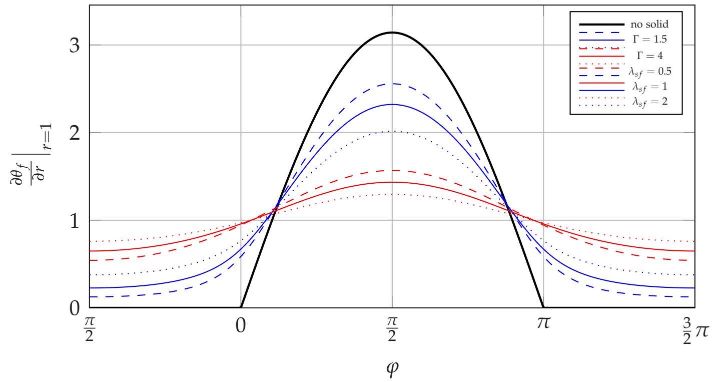

Figure 4.5: Dimensionless heat flux at the fluid-solid interface for various values of λ_{sf} and Γ, assuming half-sinusoidal heat flux. The blue lines ($\Gamma = 1.5$) correspond to the cases displayed in fig. 4.4b. Adapted from [NMGF25].

[NMGF25]

Secondly, the first two terms in eq. (4.50) are only present for finite Pe, and they express the total conductive heat flux into the $z < 0$ region: without these terms present, the bulk temperature at $z = 0$ would be zero. Herein, the first term is the contribution of the fluid region (and thus also present in Papoutsakis et al. (1980)), and the second term is the contribution of the solid region, which vanishes as expected for $\Gamma = 1$ and increases with the solid conductivity (λ_{sf}).

One may alternatively write the solution eq. (4.52b) as a convolution of the boundary condition with a kernel $H(r, \varphi)$:[7]

$$
\begin{aligned}
\theta_i &= 4\bar{f}z + \hat{\theta}_{0,i}(r) + \sum_{k=1}^{\infty} 2D_{k,i}\,\mathrm{Re}\left(f_k e^{jk\varphi}\right) \\
&= 4\bar{f}z + \hat{\theta}_{0,i}(r) + \sum_{k=1}^{\infty} 2D_{k,i}\,\mathrm{Re}\left(\frac{1}{2\pi}\int_0^{2\pi} f(\psi)e^{-jk\psi}\mathrm{d}\psi e^{jk\varphi}\right) \\
&= 4\bar{f}z + \hat{\theta}_{0,i}(r) + \int_0^{2\pi} f(\psi)\sum_{k=1}^{\infty}\frac{1}{\pi}D_{k,i}\cos(k(\varphi-\psi))\mathrm{d}\psi \\
&= 4\bar{f}z + \hat{\theta}_{0,i}(r) + \frac{1}{2\pi}\int_0^{2\pi} f(\psi)H(\varphi-\psi)\mathrm{d}\psi, \quad \text{where } H(\varphi) = 2\sum_{k=1}^{\infty} D_{k,i}\cos(k\varphi).
\end{aligned}
\tag{4.54}
$$

The kernel H is a cosine series with coefficients that carry a dependency on r. At the fluid-solid interface,

$$
\lim_{r\to 1^-}\frac{\partial H(\varphi)}{\partial r} = \sum_{k=1}^{\infty}\frac{4}{\Pi_k}\cos(k\varphi). \tag{4.55}
$$

4.2.4 Thermally developing laminar flow: The case of negligible axial conduction

This section presents the solution to the non-uniform Graetz problem as published in [NMGF25], which is the limiting case of eq. (4.41a) for $\mathrm{Pe} \to \infty$ (no axial conduction).[8] Conjugate heat transfer is not included in this section. As in section 4.2.3, the symbol for the temperature is exchanged to comply with the nomenclature in this chapter, and the non-dimensionalisation of the boundary condition is adapted compared to [NMGF25].

7 Swapping integration and summation here is valid. On the fluid side, Fubini's theorem can be applied since clearly $\sum_{k=1}^{\infty} D_{k,i}\cos(k\varphi)$ converges absolutely; on the solid side the argument requires $f(\varphi) \in L^2$ and some computation and is omitted here.

8 The solution to the extended Graetz problem, i.e. including axial conduction, is omitted in this thesis; it is treated in detail in [NMGF25].

The problem is defined by equations eq. (4.41a), as well as BCs eqs. (4.41b) to (4.41d); in particular, eq. (4.41d) becomes in absence of a solid:

$$\left.\frac{\partial\Theta}{\partial r}\right|_{r=1} = \begin{cases} f(\varphi) & \text{for } z > 0 \text{ and } \varphi \in [0, 2\pi), \\ 0 & \text{for } z < 0 \text{ and } \varphi \in [0, 2\pi). \end{cases} \tag{4.56}$$

Again, the solution is expressed as superposition of Fourier modes, i.e.

$$\Theta = \sum_{k=-\infty}^{\infty} \hat{\Theta}_k(r, z) e^{jk\varphi}.$$

Inserting into eq. (4.41a), yields

$$\frac{1}{r}\frac{\partial}{\partial r}\left(r\frac{\partial\hat{\Theta}_k}{\partial r}\right) - \frac{k^2}{r^2}\hat{\Theta}_k + \frac{1}{\mathrm{Pe}^2}\frac{\partial^2\hat{\Theta}_k}{\partial z^2} = u_z\frac{\partial\hat{\Theta}_k}{\partial z}. \tag{4.57}$$

This problem can be rewritten in terms of a linear operator $\mathcal{L}_k$:

$$\frac{\partial\hat{\Theta}_k}{\partial z} = \underbrace{\left(\frac{1}{ru_z}\frac{\partial}{\partial r}\left(r\frac{\partial}{\partial r}\right) - \frac{k^2}{r^2 u_z}\right)}_{=:\mathcal{L}_k}\hat{\Theta}_k + \frac{1}{\mathrm{Pe}^2 u_z}\frac{\partial^2\hat{\Theta}_k}{\partial z^2}. \tag{4.58}$$

$\mathcal{L}_k$ is self-adjoint and negative semi-definite (even negative definite for $k \neq 0$) on the space

$$\mathcal{D} := \{\varphi \in H^2((0,1)), \varphi'(1) = 0\} \tag{4.59}$$

with respect to the inner product

$$\langle u, v\rangle = \int_0^1 uvru_z \mathrm{d}r. \tag{4.60}$$

These properties are shown in appendix A.3. Therefore, for each k there exists an orthogonal basis of $\mathcal{D}$ consisting of eigenfunctions of $\mathcal{L}_k$. To make use of this, we strive to reformulate the problem in such a way that the solution lies within $\mathcal{D}$. To this end, we subtract a function p_k,

$$\tilde{\Theta}_k = \hat{\Theta}_k - p_k(r, z) \quad \text{where} \quad \frac{\partial p_k}{\partial z} = \mathcal{L}_k(p_k) = p_k' \equiv \text{const.}, \tag{4.61}$$

and choose p_k such that it fulfills the boundary condition eq. (4.56). Hence, we identify p with the fully developed solution eqs. (4.50) and (4.51c) for $z > 0$, and zero for

$z < 0$. The constant p'_k is zero for $k \neq 0$, and $4\overline{f}$ for the zeroth mode. In particular, this transformation asserts $\tilde{\Theta}_k \to 0$ for $z \to \pm\infty$. Equation (4.58) then becomes

$$\frac{\partial \tilde{\Theta}_k}{\partial z} = \mathcal{L}_k \tilde{\Theta}_k + \frac{1}{\mathrm{Pe}^2 u_z} \frac{\partial^2 \tilde{\Theta}_k}{\partial z^2}. \tag{4.62}$$

Initial condition eq. (4.7a), boundary condition eq. (4.56), and regularity condition eq. (4.2b) become, respectively,

$$\lim_{z\to-\infty} \tilde{\Theta}_k(r,\varphi,z) \equiv 0 \quad \text{for } r > 0,\ \varphi \in [0, 2\pi) \text{ and all } k, \tag{4.63a}$$

$$\left.\frac{\partial \tilde{\Theta}_k}{\partial r}\right|_{r=1} = 0, \tag{4.63b}$$

$$\left.\frac{\partial \tilde{\Theta}_0}{\partial r}\right|_{r=0} = 0; \text{ and } \tilde{\Theta}_k(r=0,z) \equiv 0, \text{ for } k \neq 0. \tag{4.63c}$$

Moreover, since $\hat{\Theta}_k$ is continuous at the origin, eq. (4.61) imposes a jump condition onto $\tilde{\Theta}_k$:

$$\tilde{\Theta}_k(r,z)|_{z=0^+} + p_k(r, z=0) = \tilde{\Theta}_k(r,z)|_{z=0^-}. \tag{4.64}$$

For given k, let ϕ_{kj} denote an orthonormal basis of $\mathcal{D}$ consisting of eigenfunctions of the operator $\mathcal{L}_k$, i.e. functions satisfying $\mathcal{L}_k\phi_{kj} = \lambda_{kj}\phi_{kj}$ and $\langle\phi_{kj}, \phi_{kj}\rangle = 1$. Here λ_{kj} are the corresponding eigenvalues for the wavenumber k.

Since the transformed solution $\tilde{\Theta}_k$ lies in $\mathcal{D}$ – the space where the operator $\mathcal{L}_k$ is self-adjoint – it can be expanded into eigenfunctions:

$$\tilde{\Theta}_k = \sum_{j=1}^{\infty} \langle \tilde{\Theta}_k, \phi_{kj}\rangle \phi_{kj}, \tag{4.65}$$

The coefficients $c_{kj}(z) := \langle \tilde{\Theta}_k, \phi_{kj}\rangle$ are dependent on z and determined from the system eqs. (4.62) and (4.63c). To derive expressions for the coefficients, we take the inner product of eq. (4.62) with ϕ_{kj}. Taking the limit $\mathrm{Pe} \to \infty$, we obtain

$$c'_{kj}(z) - \lambda_{kj} c_{kj}(z) = 0 \text{ and thus } c_{kj}(z) = C_{kj} e^{\lambda_{kj} z}. \tag{4.66}$$

From here on, we will restrict ourselves to the case of $k \neq 0$ to enhance the clarity of the presentation.[9] Following the same steps that lead to (4.66), we obtain a boundary condition and a jump condition from eq. (4.63a) and eq. (4.64):

$$\lim_{z \to -\infty} c_{kj}(z) = 0 \tag{4.67a}$$

$$c_{kj}(0^+) + \langle p|_{z=0^+}, \phi_{kj} \rangle = c_{kj}(0^-) \tag{*4.67b}$$

To simplify eq. (*4.67b), we can exploit eq. (A.18) and eq. (4.61) to obtain

$$\langle p|_{z=0^+}, \phi_{kj} \rangle = \frac{1}{\lambda_{kj}} \left(\langle p'_k, \phi_{kj} \rangle - \phi_{kj}(1) \left. \frac{\partial p}{\partial r} \right|_{r=1} \right) = -\frac{\phi_{kj}(1)}{\lambda_{kj}} \left. \frac{\partial p}{\partial r} \right|_{r=1} \tag{*4.68}$$

The second equality is apparent from $p'_k = 0$ for $k \neq 0$. For $z < 0$ we immediately see from eq. (4.67a) that $\langle \tilde{\Theta}_k, \phi_{kj} \rangle = c_{kj} \equiv 0$ due to the operator being negative definite. This was expected because the problem is parabolic for the case $\mathrm{Pe} \to \infty$. For $z > 0$, the integration constant in eq. (4.66) becomes

$$C_{kj} = \langle \tilde{\Theta}_k, \phi_{kj} \rangle|_{z=0^+} = -\langle p, \phi_{kj} \rangle = \frac{\phi_{kj}(1)}{\lambda_{kj}} f_k \tag{*4.69}$$

due to eqs. (4.56), (4.61) and (*4.68).

A Note on the Eigenfunctions. What remains is to determine eigenvalues λ_{kj} and eigenvectors ϕ_{kj}. In general, an analytical expression for the eigenfunctions is not available, however we will sketch how for the case $u_z = 1 - r^2$ this is possible. From the definition of $\mathcal{L}_k$ in eq. (4.58), we find that the self-adjoint eigenvalue problem $\mathcal{L}_k \phi_{kj} = \lambda_{kj} \phi_{kj}$ is given by

$$\frac{1}{r} \left(r \phi'_{kj} \right)' - \frac{k^2}{r^2} \phi_{kj} + u_z \mu_{kj}^2 \phi_{kj} = 0, \tag{4.70}$$

where $\lambda_{kj} = -\mu_{kj}^2$. Using the transformation $\phi_{kj}(r) = r^{|k|} e^{-\eta/2} f(\eta)$, $\eta = \mu_{kj} r^2$, the equation becomes

$$\eta f''(\eta) + (|k| + 1 - \eta) f'(\eta) - \left(-\frac{\mu_{kj}}{4} + \frac{1}{2}(|k| + 1) \right) f(\eta) = 0, \tag{4.71}$$

[9] The $k = 0$ case can be treated in the same framework, but some key simplifications are not possible. We indicate these occurrences with an asterisk in the equation number, and provide their replacements in Appendix C of [NMGF25].

which is Kummer's equation (Slater and Lit 1960). Its solution is the confluent hypergeometric function $M(a_{kj}, b_k, \eta)$ where $a_{kj} = -\frac{\mu_{kj}}{4} + \frac{1}{2}(|k|+1), b_k = 1+|k|$. Therefore, the fundamental solution of eq. (4.70) is

$$\phi_{kj}(r) = r^{|k|} e^{-\frac{\mu_{kj}}{2} r^2} M(a_{kj}, 1+|k|, \mu_{kj} r^2) \tag{4.72}$$

The eigenvalues are then determined by requiring the boundary condition $\phi'_{kj}(1) = 0$, derived from eq. (4.63b) to hold:

$$0 \stackrel{!}{=} 2M'(a_{kj}, 1+|k|, \mu_{kj}) + \left(\frac{|k|}{\mu_{kj}} - 1\right) M(a_{kj}, 1+|k|, \mu_{kj}). \tag{4.73}$$

Note that the eigenfunctions and eigenvalues are equal for k and $-k$. Also note that the eigenfunctions trivially fulfill boundary condition eq. (4.63c).

The Full Solution. Using $p(z)$ from eqs. (4.50) and (4.51c) for $\mathrm{Pe} = \infty$, i.e.

$$p_k(r) = \begin{cases} \bar{f}\left(4z - \frac{1}{4}r^4 + r^2 - \frac{7}{24}\right) & k = 0, \\ f_k \frac{r^{|k|}}{|k|} & k \neq 0, \end{cases} \tag{4.74}$$

we collect the solution Θ from eqs. (4.9), (4.61), (4.65), (4.66) and (*4.69), and find

$$\begin{aligned} \Theta &= \sum_{k=-\infty}^{\infty} \hat{\Theta}_k(r,z) e^{jk\varphi} \\ &= \bar{f}\left(4z - \frac{1}{4}r^4 + r^2 - \frac{7}{24} + \sum_{j=1}^{\infty} \frac{\phi_{0j}(1) e^{\lambda_{0j} z}}{\lambda_{0j}} \phi_{0j}\right) \\ &+ \sum_{k=1}^{\infty} \left(\frac{2r^k}{k} + 2\sum_{j=1}^{\infty} \frac{\phi_{kj}(1) e^{\lambda_{kj} z}}{\lambda_{kj}} \phi_{kj}\right) (\mathrm{Re}(f_k)\cos(k\varphi) - \mathrm{Im}(f_k)\sin(k\varphi)). \end{aligned} \tag{4.75}$$

Two modes $\hat{\Theta}_1$ and $\hat{\Theta}_3$ are displayed exemplarily in fig. 4.6, together with a second-order finite differences approximation, the details of which are given in Appendix D of [NMGF25]. They are in excellent agreement, verifying the analytical solution presented here.

A few remarks follow. Firstly, we observe that the j-th eigenvalue of $\mathcal{L}_k$ increases monotonically in k (that is, $\lambda_{1j} < \lambda_{2j} < ...$), except for the zero-order mode, where the eigenvalues of $\mathcal{L}_0$ and $\mathcal{L}_2$ coincide (apart from the extra eigenvalue $\lambda_{01} = 0$):

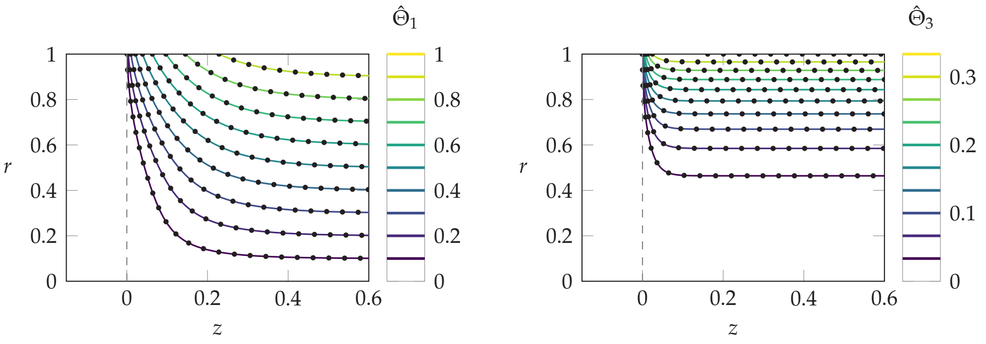

(a) $k = 1$ **(b)** $k = 3$

Figure 4.6: Contour plot of the Fourier modes $\hat{\Theta}_k$ for $k = 1$ and $k = 3$, $\mathrm{Pe} \to \infty$. Lines: solution presented herein. Dots: Finite difference approximation for comparison. Adapted from [NMGF25].

$\lambda_{0(j+1)} = \lambda_{2j}$. Therefore, not only do high-order modes in the azimuthal boundary condition decay quickly in the radial direction (see section 4.2.3), they also reach the fully developed state much faster than lower-order modes. However, it also means that a mode with period of 2π, if present in the boundary condition, significantly increases the length until a fully developed state is reached. This is an important take-away for the design of systems that are heated only on one side, such as heat pipe solar collectors or concentrated solar power plants. There is an intuitive physical explanation for this behaviour: for $k = 0$ and $k = 2$, the information of the changed boundary condition only has to be conducted to the centre of the pipe while for $k = 1$, it has to be conducted to the opposite side of the pipe, which takes longer.

In order to graphically evaluate this behaviour, [the local Nusselt number (eq. (4.24)) is used in its spectral form; one has for the chosen non-dimensionalisation]

$$\mathrm{Nu}_{l,k} = \frac{-2 \left. \frac{\partial \hat{\Theta}_k}{\partial r} \right|_{r=1}}{4 \int_0^1 \hat{\Theta}_k u_z r \mathrm{d}r - \hat{\Theta}_k(r=1)}. \tag{4.76}$$

For $k = 0$, $\mathrm{Nu}_{l,k} = \mathrm{Nu}$. [...] The ratio $\mathrm{Nu}_{l,k}(z)/\mathrm{Nu}_{l,k}(z \to \infty)$ allows us to evaluate how close the radial profile at a given z position is to the fully developed one, hence evaluate thermal entrance lengths for individual modes. This is displayed in fig. 4.7. The $k = 1$ mode actually requires significantly longer to reach the fully developed state than a

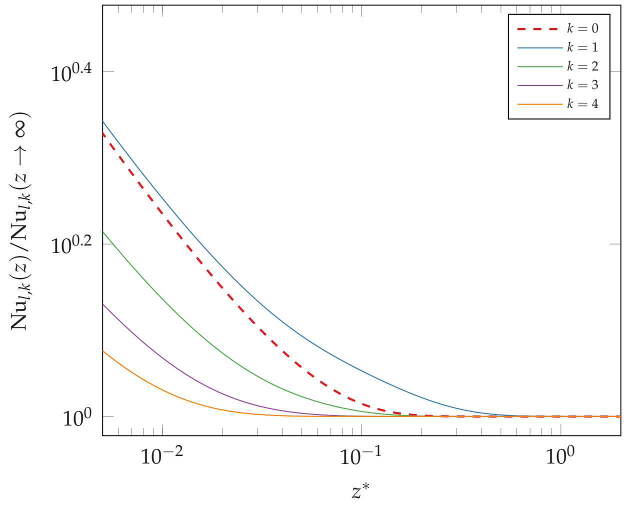

Figure 4.7: Diagnostic plot for the development of $\mathrm{Nu}_{l,k}(z)$ (see eq. (4.76)), different values of k. $k = 0$ is highlighted with dashed linestyle. $\mathrm{Pe} \to \infty$. The ordinate is given in non-dimensional axial length: recall that $z = \mathrm{Pe} R_i z^*$, hence the dimensional thermal entrance length is infinity for $\mathrm{Pe} \to \infty$. Adapted from [NMGF25].

pipe subject to uniform heat flux ($k = 0$). Apart from this, with increasing k, the thermal entrance length decreases.[10] [NMGF25]

Decreasing Pe – i.e. including axial conduction – changes the solution; most notably, the temperature can now be nonzero for $z < 0$. For a detailed treatment, the reader is referred to [NMGF25].

[The thermal entry length of $\mathrm{Nu}_{l,k}$ depending on Pe is displayed in fig. 4.8.[11] It is crucial to remember that z was non-dimensionalised with $\mathrm{Pe} R_i$. If axial conduction is neglected (or negligible), the thermal entrance length (when non-dimensionalised with the pipe radius or diameter) therefore increases linearly with Pe. Considering axial conduction becomes relevant for low Pe, where the solution will ultimately become independent of Pe. This can be seen by [employing the non-dimensionalisation eq. (4.17) with $\alpha = 1$, i.e.] non-dimensionalising z with R_i instead, leading to

$$\frac{1}{r}\frac{\partial}{\partial r}\left(r\frac{\partial \hat{\theta}_f}{\partial r}\right) - \frac{k^2}{r^2}\hat{\theta}_f + \frac{\partial^2 \hat{\theta}_f}{\partial z^2} = \mathrm{Pe} u_z \frac{\partial \hat{\theta}_f}{\partial z}. \tag{4.77}$$

[10] For $k = 1$, $\mathrm{Nu}_{l,k}$ is within 1% of the fully developed value at $z = 0.392$. This position decays roughly with $k^{-2.1\pm0.2}$.

[11] Other quantities follow the same trends with respect to k and Pe.

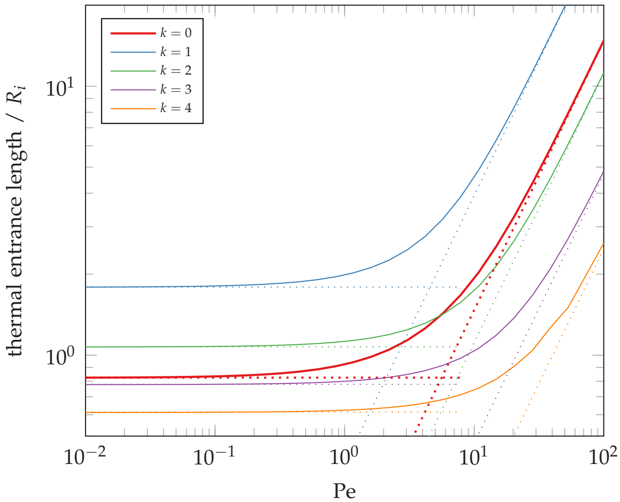

Figure 4.8: Entrance length of the local Nusselt number (defined as the position where $Nu_{l,k}(z)$ deviates 1% from $Nu_{l,k}(z \to \infty)$) for different values of k. Solid lines: including axial conduction. Dotted lines: neglecting axial conduction (right) / axial convection (left). Adapted from [NMGF25].

[NMGF25] For Pe $\to 0$, the convection term is negligible and the problem becomes a purely diffusive one (note that for small, but nonzero Pe the 'outlet condition' – i.e. the fully developed solution for $z \to \infty$ – for $k = 0$ still contains u_z). Hence, the solution becomes independent of Pe, and so does the thermal entrance length when made dimensionless with the pipe radius. Similarly to section 4.2.4, the limiting solution for Pe $\to 0$ is straightforward to derive, as the PDE again gives rise to a (different) self-adjoint operator whose eigenfunctions are the Bessel functions of the first kind J_k. As visible from fig. 4.8, the solution [derived in [NMGF25]] for finite Pe indeed follows nicely both limits for Pe $\to \infty$ and Pe $\to 0$.

4.3 Numerical setup

The turbulent cases are solved numerically using NekRS (Fischer et al. 2022). The mesh of Straub et al. (2019b) is reused. From the perspective of the momentum equation, the present simulations are well-resolved LES simulations, where the required additional dissipation to stabilize the simulation is provided by a high-pass spectral filter as suggested by Schlatter et al. (2004). Since the thermal scales for low-Pr fluids are larger compared to the velocity scales, the thermal fields for that case are effectively fully resolved and no subgrid model is needed for the temperature equation. This approach is called Hybrid LES/DNS or Thermal DNS by some authors (Straub 2020). If a solid domain is included, the azimuthal resolution is the same as in the fluid. The radial element distribution must be fine enough to resolve the decaying thermal fluctuations within the solid (Flageul 2016), and hence the first element on the solid side is mirrored from the fluid side. This choice was confirmed by means of a mesh refinement study, where the same case was run with the resolution of El Khoury et al. (2013); deviation of the mean dimensionless temperature $\langle\vartheta\rangle(r)$ for uniformly heated cases was found to be within 0.2 % for $\mathrm{Pr} = 0.025$ and 0.5 % for $\mathrm{Pr} = 0.71$, while deviation of $\langle\vartheta'\vartheta'\rangle(r)$ was found to be within 2 % for $\mathrm{Pr} = 0.025$ and 5 % for $\mathrm{Pr} = 0.71$.[12] The momentum equation eq. (2.6) is driven by a time-varying pressure gradient to maintain a constant bulk Reynolds number of $\mathrm{Re}_b = 2u_bR/\nu = \{5300, 19000\}$, corresponding to a friction Reynolds number of $\mathrm{Re}_\tau = u_\tau R/\nu \approx \{180, 550\}$.

A streamwise length of $L_z = 50D$ is chosen for the fully developed cases. This length is chosen as Tiselj (2014) and Straub et al. (2019b) showed that for very low Pr, a regular domain length of e.g. $L_z \approx 10D$ underestimates fluctuations of ϑ.

For the developing cases, a velocity recycling boundary condition is used, where the inlet condition of the current timestep is determined by the velocity solution of the previous timestep, $10D$ downstream of the inlet. The recycling length is chosen to produce a hydrodynamically developed flow state at the inlet (Pirozzoli et al. 2021). The temperature is set to zero at the end of the recycling region. Conjugate heat transfer is only considered for the fully developed cases. The metadata of the simulation cases are given in table 4.2.

The timestep is chosen dynamically to ensure $CFL \approx 1$. After an initial transient to the steady state, statistics are collected online. Note that convergence to the steady state can be quite slow (especially for a high thermal inertia within the solid, where no turbulent mixing occurs), so the steady state was asserted by splitting the selected averaging interval and comparing statistics.

In this section, the non-dimensionalisation eq. (4.17) is used with $\alpha = 1, \beta = 2, \gamma = 0$ and a minus sign. The corresponding temperature variables are denoted $T^* \to T$ (developing flow) and $\theta^* \to \vartheta$ (fully developed flow). For ϑ, the arbitrary temperature reference is chosen to be the mean interface temperature, i.e. $\langle\vartheta\rangle|_1 = 0$. Quantities denoted with a $^+$ superscript are given in viscous units; i.e. $U_{\mathrm{ref}} = u_\tau$ and (by means of eq. (4.17))

12 Part of this deviation may be attributed to the significantly shorter averaging time for the DNS case, see table 4.2.

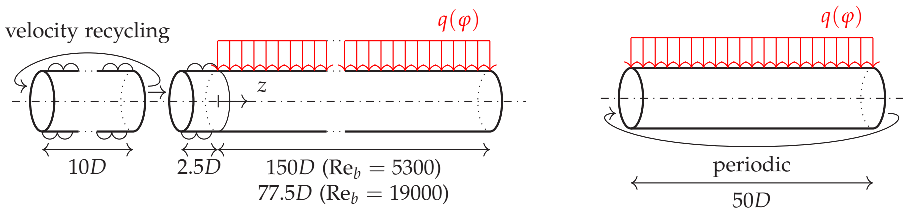

(a) Developing case. Adapted from [NGF26]

(b) Fully developed case

Figure 4.9: Sketch of the numerical domain for thermally developing and thermally fully developed turbulent pipe flow.

<table>
<tr><th>Γ</th><th>λ_{sf}</th><th>K</th><th>Line style</th></tr>
<tr><td colspan="3">MBC</td><td></td></tr>
<tr><td rowspan="5">1.2</td><td rowspan="2">1</td><td>0.25</td><td></td></tr>
<tr><td>4</td><td></td></tr>
<tr><td></td><td rowspan="3">1</td><td></td></tr>
<tr><td>0.5</td><td></td></tr>
<tr><td>2</td><td></td></tr>
<tr><td colspan="3">IF</td><td></td></tr>
</table>

Table 4.1: Considered cases for conjugate heat transfer

Case	Re_b	L_z	$nel_{cs,f}$	$nel_{cs,s}$	nel_z	Δy_0^+	$t_{avg} u_\tau / D$
`cht`	5300	12.5	132	72	54	0.29	269.9
`cht_long` (*)	5300	50	132	72	216	0.29	115.9
`cht_fine`	5300	12.5	384	240	95	0.099	7.0
`dev_180` (*)	5300	150	132	–	702	0.29	199.7
`dev_550` (*)	19000	77.5	828	–	1152	0.26	10.5

Table 4.2: Metadata for the cases presented in this section, including the heated streamwise length L_z, number of fluid (solid) elements per cross section $nel_{cs,f}$ ($nel_{cs,s}$), number of elements in the streamwise direction nel_z, wall distance of the first integration point and averaging time. Data from the cases marked with (*) are used in the various figures. Extended from [NGF26].

$\vartheta^+ = \vartheta u_\tau / u_b$. The wall distance in viscous units is defined as $y^+ = (R_i - r)/\delta_v$ where δ_v is the viscous length scale, i.e. negative values of y^+ denote points inside the solid.

4.4 Numerical results: Thermally fully developed turbulent flow

In this section, conjugate heat transfer is considered. For the additional dimensionless quantities Γ, λ_{sf} and K introduced by the presence of the solid, the values as given in table 4.1 are used. A radius ratio of $\Gamma = 1.2$ is used as in Vicente Cruz and Lamballais (2023), and a similar value of $\Gamma = 1.225$ is used in the experimental facility GALINKA at TVT (Laube et al. 2022). The conductivity ratio λ_{sf} is varied as $\{0.5, 1, 2\}$ for constant $K = 1$, and the thermal activity ratio K is varied as $\{0.25, 1, 4\}$ for constant $\lambda_{sf} = 1$.[13] In addition, a case without the solid, i.e. the heat flux is prescribed on the fluid directly (isoflux – IF), is considered for the various boundary conditions. This corresponds to a very thin solid through which temperature fluctuations can pass through unhindered (very low thermal inertia). For the mixed boundary condition (MBC) case, the same forcing of the temperature equation is applied, prescribing the same mean heat flux, but the wall temperature is kept constant at a uniform value. This corresponds to a very thin solid with very high thermal inertia, which completely blocks temperature fluctuations from passing into the solid and hence from existing at the wall at all, and it is only considered for the case of uniform heat flux.

4.4.1 Uniform heat flux

This subsection considers $f(\varphi) = 1$, and (as per section 4.2.1) the azimuthal mean of first-order statistics in ϑ for non-uniform heat flux are identical to what is shown in this section. This configuration was previously studied in Vicente Cruz and Lamballais (2023) for $\lambda_{sf} \in \{1, 2\}$ and $1/(K^2\lambda_{sf}) \in \{1, 2\}$ using an immersed boundary method implemented in XCompact3D. The present results are in good agreement with those of Vicente Cruz and Lamballais (2023) and Straub et al. (2019b).

Figures 4.10a and 4.10b show the dimensionless mean temperature in inner units, for the various cases defined in table 4.1 for $\mathrm{Re}_b = 5300$. The temperature distribution in the solid is known a priori (linear conduction solution, as can be seen from integrating eq. (4.11b) over z and φ), and hence is only affected by λ_{sf} and not K. Straub et al. (2019b)

[13] Typical values for air at ambient conditions ($\mathrm{Pr} \approx 0.71$) are $\lambda_{sf} \approx 1.6 \times 10^4$ (3.6×10^3), $K \approx 1.5 \times 10^{-4}$ (3.0×10^{-4}) for a Copper (Nickel) wall; for water ($\mathrm{Pr} \approx 7$): $\lambda_{sf} \approx 670$ (157), $K \approx 0.043$ (0.083) and for GaInSn ($\mathrm{Pr} \approx 0.32$): $\lambda_{sf} \approx 17$ (3.9), $K \approx 0.20$ (0.40). Values of $\lambda_{sf} < 1$ and $K > 1$ are obtained for e.g GaInSn paired with steel 1.4828: $\lambda_{sf} \approx 0.49, K \approx 1.1$. Material constants taken from Stephan et al. (2019) and Laube et al. (2023).

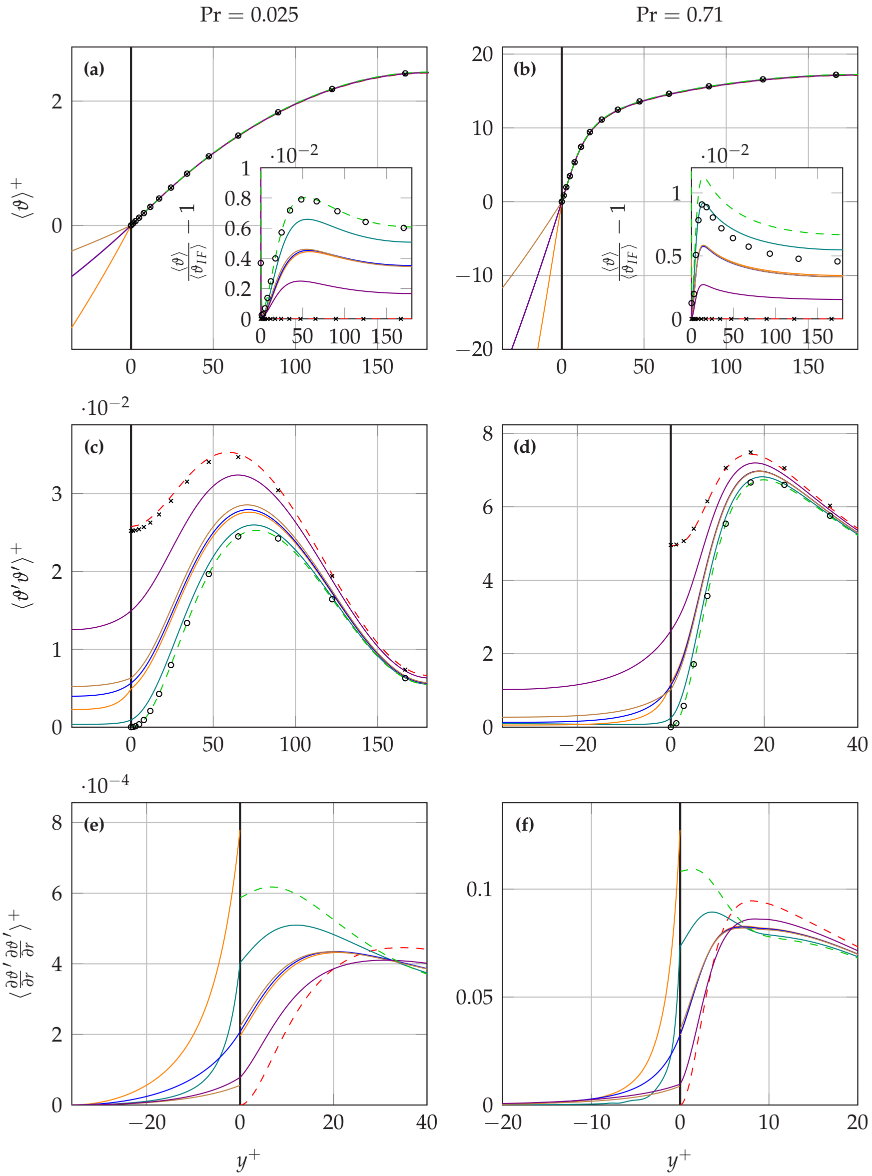

Figure 4.10: Mean profiles of various quantities for homogeneous heat flux at $\mathrm{Re}_b = 5300$ (LES); left: $\mathrm{Pr} = 0.025$, right: $\mathrm{Pr} = 0.71$. First row: Mean profiles of dimensionless temperature and (inset) comparison with IF as baseline. Second row: temperature variance, third row: variance of $\partial\vartheta/\partial r$ (third row). Colors indicate varying solid properties as given in table 4.1. Additionally, data from Straub et al. (2019b) is included if available (DNS, $L_z = 12.5D$): IF (×) and MBC (∘).

observed that the mean temperature profiles are very similar for IF and MBC cases. As IF and MBC are limiting cases ($K \to \infty$ and $K \to 0$ respectively), one would expect that the fluid's temperature profile is only weakly affected by the solid's properties. The data confirms this expectation; in particular there is virtually no dependence on λ_{sf}.

As the effective *mean* boundary condition on the fluid $\langle \partial\vartheta/\partial r \rangle\big|_{r=1/2}$ is identical between cases, eq. (4.11a) shows that a change in ϑ can only come from a change in $\langle u_r'\vartheta' \rangle$. Straub et al. (2019b) showed for the limiting cases of IF and MBC, the near-wall behaviour of $\langle u_r'\vartheta' \rangle$ is quadratic in y^+ for IF, but cubic for MBC. The CHT cases fall in between.

Observing that $\langle u_z'\vartheta' \rangle$ has insignificant contributions to the global Nusselt number (Straub et al. 2019b), the similarity of $\langle \vartheta \rangle$ immediately gives that Nu does not carry a significant dependency on the solid's properties.

The temperature variance $\langle \vartheta'\vartheta' \rangle^+$, however, is strongly affected by the solid's properties: while MBC (and $K \to 0$) removes fluctuations at the wall, they are unrestricted by IF, and indeed an increase of K increases the level of fluctuations in both domains. This quantity is displayed in figs. 4.10c and 4.10d.[14] At least in the fluid domain, there is little influence of λ_{sf} on $\langle \vartheta'\vartheta' \rangle^+$. While low-*Pr* fluids show a reduced overall level of temperature fluctuations, they reach farther into the solid for the same $\{K, \lambda_{sf}\}$. Similar trends can be seen for the variance of the temperature gradient $\langle (\partial\vartheta/\partial r)'^2 \rangle$, displayed in figs. 4.10e and 4.10f. At the wall, this quantity is zero for IF (as $\partial\vartheta/\partial r$ is fixed in time by the boundary condition) and maximum for MBC. If $\lambda_{sf} \neq 1$, this quantity exhibits a jump at the wall, as is expected from eq. (4.8a) which directly translates to an interface condition for the fluctuation of $\partial\vartheta/\partial r$.

$\langle \vartheta'\vartheta' \rangle$ is further analyzed by decomposing it into its (axial) spectral contributions. Streamwise power spectral densities of the temperature field are computed as the product of the streamwise Fourier coefficients of the instantaneous temperature with their complex conjugate (i.e. $E = \hat{\vartheta}\hat{\vartheta}^*$) for both Pr and varying solid properties. The quantity displayed is the premultiplied spectral energy density for the cases IF, MBC and those with $\lambda_{sf} = 1$ (i.e. varying K) for both Pr numbers. Figure 4.11 displays contour lines of the premultiplied power spectral densities (i.e. $k_z E$) at 10 % and 50 % of the maximum value; the horizontal axis is the inner-scaled axial wavelength $\lambda_z^+ = 2\pi/k_z$.

With increasing wall distance, the energy contained in fluctuations of increasingly large axial wavelength becomes independent of K for both Pr. At $\mathrm{Pr} = 0.71$, K has no

[14] Note that in fig. 4.10c, i.e. $\langle \vartheta'\vartheta' \rangle$ for $\mathrm{Pr} = 0.025$, the DNS data by Straub et al. (2019b) is slightly offset from the present data for the IF boundary condition. It has been asserted that this is not an artifact of grid resolution, but rather due to the short domain length used for the reference DNS.

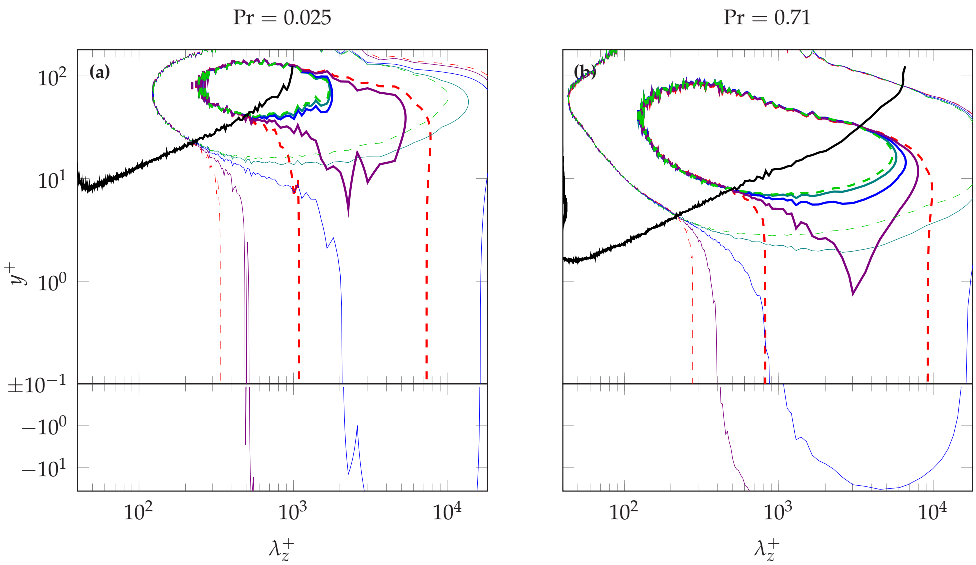

Figure 4.11: Streamwise spectra of the temperature field for $\mathrm{Re}_b = 5300$, LES, $L_z = 50$. (a): $\mathrm{Pr} = 0.025$, (b): $\mathrm{Pr} = 0.071$. Spectra are computed from at least 30 independent snapshots. The figures display the cases of varying K as well as the limiting cases of MBC and IF, where the line styles are given in table 4.1. Contour levels at 0.1 (thin) / 0.5 (thick lines) of the individual maximum are displayed. Note that in the top left of the individual diagrams, the spectral energies of the respective cases are in agreement with each other; the boundary of this region is indicated by the black solid line (5% deviation between IF and MBC).

impact on the spectral energy density in the pipe's core for fluctuations smaller than $\lambda_z^+ \lesssim 6000$ ($\lambda_z/R_i \lesssim 33$). Conceptually, one can imagine the temperature spectrum at a given (sufficiently large) wall distance $\tilde{y}^+$ as the near-wall spectrum viewed through the lens of the accumulated turbulent mixing up to $\tilde{y}^+$; making all but the largest axial fluctuations indistinguishable from an MBC reference. For $\mathrm{Pr} = 0.025$, the same effect is observed; but the enhanced conduction reduces the effectiveness of the imagined filter: near-wall, instantaneous temperature information can travel further towards the pipe's core by means of conduction. In this case, the spectral energy density in the pipe's core becomes independent of K for $\lambda_z^+ \lesssim 1000$ ($\lambda_z/R_i \lesssim 5.5$). Consequently, there is stronger effect of the solid's properties on the temperature fluctuations in the pipe's core for $\mathrm{Pr} = 0.025$, as seen in the overall profiles (figs. 4.10c and 4.10d).

4.4.2 Non-uniform heat flux

First-order temperature statistics in response to an arbitrary boundary condition $f(\varphi)$ may be obtained by superposition of the response to a boundary condition composed of only a single azimuthal wavenumber (monochromatic boundary condition). In this subsection, first-order moments are presented for azimuthal wavenumbers up to $k = 10$, and the impact of solid and fluid properties on those is characterised.

Following the arguments of section 4.2.1, such an analysis can be made based on the response to a boundary condition containing a variety of azimuthal modes, as the Fourier-diagonal property of $\mathcal{L}_{\langle u_i^m \vartheta \rangle}$ (see eq. (4.26)) allows to split the response to such a test boundary condition. This is conceptually similar to characterising a dynamical system by its impulse response. For simplicity, this test boundary condition is chosen as

$$f(\varphi) = \sum_{k=1}^{10} \sin(k\varphi), \tag{4.78}$$

yielding the response to the first ten wavenumbers. As a validation step, the expected response to the half-sinusoidal boundary condition (section 4.2.3) is computed based on the response to the test boundary condition and the response to homogeneous heating, and compared to the actual response to the half-sinusoidal boundary condition. For $\langle \vartheta \rangle$, the root mean square of the deviation was less than 0.5 % of the centreline temperature. The main cause of the deviation is the omission of wavenumbers $k > 10$ which is only relevant near the wall as these decay fast with increasing $y^+ > 0$ (in section 4.2.4, the same was observed for laminar flow).

Mean temperature. Figure 4.12 displays selected azimuthal temperature modes $\widehat{\langle \vartheta \rangle}_k$ (see section 4.2.1); those modes can be superimposed to obtain the solution to a composite boundary condition. For a monochromatic boundary condition $\Re(e^{ik\varphi})$, the curve displayed in fig. 4.12 multiplied with the boundary condition is the resulting temperature distribution as a function of r and φ; hence $\langle \hat{\vartheta} \rangle_k$ is identified with the temperature profile (modulo a complex exponential) of a monochromatic boundary condition with appropriate heat flux scaling.

Firstly, one observes that for $k \geq 1$, $\langle \hat{\vartheta} \rangle_k |_{r=0} = 0$ due to the compatibility condition (and only the $k = 1$ mode can have a non-zero gradient at the centreline). Secondly, for a given fluid-solid configuration and nonzero k, increasing k reduces the magnitude of the solution; and it quickly tends towards zero in the bulk of the flow. As in the laminar

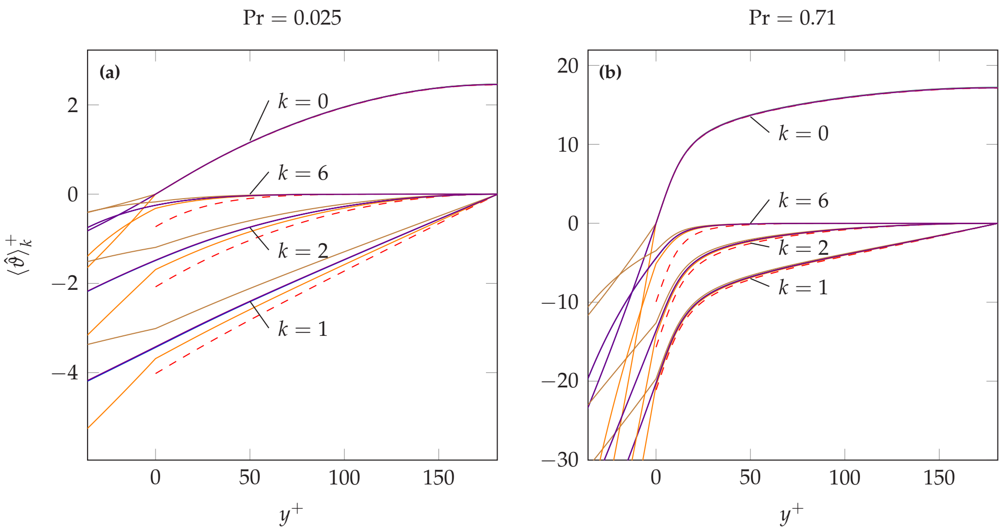

Figure 4.12: Selected azimuthal modes of the mean temperature operator at $\mathrm{Re}_b = 5300$. (a): $\mathrm{Pr} = 0.025$, (b): $\mathrm{Pr} = 0.71$. Line styles correspond to different solid properties; see table 4.1.

case (see section 4.2.3), the bulk of the flow does not participate in the heat transfer for sufficiently large k.

Unlike for homogeneous heating ($k = 0$), the presence of the solid does alter the fluid's mean temperature profile significantly (cf. solid vs. dashed lines for $k \neq 0$ in fig. 4.12). Azimuthal conduction in the solid reduces the variation of the mean heat flux at the interface, thus reducing the magnitude of $\widehat{\langle\vartheta\rangle}_k$ within the fluid. This effect is particularly strong for large k and small Pr, whereas for larger Pr radial turbulent transport dominates the azimuthal conduction. As in the laminar case, a thick, well-conducting solid enhances this effect (cf. curves for different λ_{sf} in fig. 4.12). However, modifying K only has a minor effect on the mean temperature profile also for $k > 0$. Figure 4.13 exemplifies this observation for half-sinusoidal heat flux; it displays contours of radial heat flux $(\partial\vartheta/\partial r)$ for various K (left side of each subplot) and λ_{sf} (right side); clearly the overall temperature distribution is only weakly affected by variations of K.

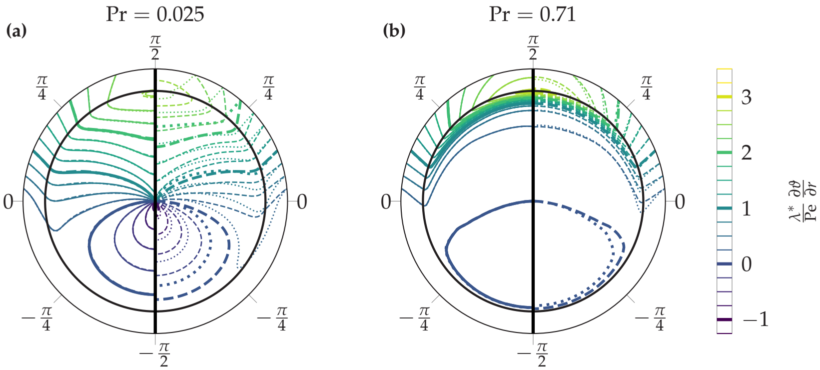

Figure 4.13: Comparison of $\partial\vartheta/\partial r$, normalised with λ^*/Pe as in fig. 4.4, for half-sinusoidal heat flux and $\mathrm{Re}_b = 5300$. Left side of each subplot: different K for $\lambda_{sf} = 1$: 1 (solid), 0.25 (dotted), 4 (dashed). Right side of each subplot: different λ_{sf} for $K = 1$: 0.5 (dashed) and 2 (dotted).

Turbulent Prandtl number. The direct solution of eq. (4.11a) requires modeling of the terms $\langle u_r'\vartheta'\rangle$ and $\langle u_\varphi'\vartheta'\rangle$. The gradient diffusion hypothesis (Pope 2000) leads to the following closure (here in the dimensional form):

$$\langle u_r' T'\rangle = -\alpha_{t,r}\frac{\partial\langle T\rangle}{\partial r}, \qquad \langle u_\varphi' T'\rangle = -\alpha_{t,\varphi}\frac{1}{r}\frac{\partial\langle T\rangle}{\partial\varphi} \tag{4.79}$$

where $\alpha_{t,r}$ and $\alpha_{t,\varphi}$ are the turbulent thermal diffusivities in the radial and azimuthal direction, respectively. They are often expressed in terms of the turbulent Prandtl number (Kays 1994):

$$\mathrm{Pr}_{t,r} = \frac{\nu_t}{\alpha_{t,r}}, \quad \mathrm{Pr}_{t,\varphi} = \frac{\nu_t}{\alpha_{t,\varphi}} \tag{4.80}$$

where ν_t is the turbulent eddy viscosity, here defined via the Boussinesq approximation $\langle u_r' u_z'\rangle = -\nu_t\,\partial\langle u_z\rangle/\partial r$. In common turbulent heat flux models such as the Kays correlation (Kays 1994) or the $k{-}\epsilon{-}k_\theta{-}\epsilon_\theta$ model proposed by Manservisi and Menghini (2014), the turbulent Prandtl number is assumed scalar (i.e. $\mathrm{Pr}_{t,r} = \mathrm{Pr}_{t,\varphi}$), although it is known that this is an incorrect assumption especially near the wall (Black and Sparrow 1967).

In fig. 4.14, the turbulent Prandtl numbers are presented for wavenumbers $k = \{0, 1, 2, 4\}$. According to eq. (4.79), evaluation of $\alpha_{t,i}$ requires dividing by the temperature gradient, i.e. $\partial\widehat{\langle\vartheta\rangle}_k\big/\partial r$ and $\partial\widehat{\langle\vartheta\rangle}_k\big/\partial\varphi = kj\widehat{\langle\vartheta\rangle}_k$. As shown in fig. 4.12, both gradients vanish for $k > 1$ as $r \to 0$. Accordingly, the turbulent Prandtl number becomes ill-defined near the pipe centre and those regions are excluded from plotting.

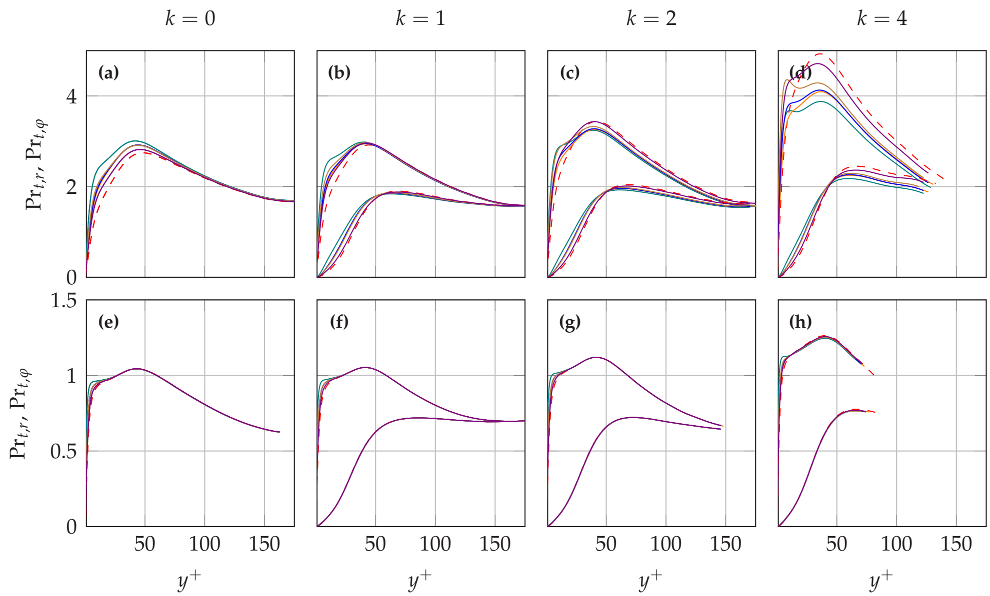

Figure 4.14: Turbulent Prandtl number Pr_t in radial and azimuthal direction for selected modes at $\mathrm{Re}_b = 5300$. (a-d): $\mathrm{Pr} = 0.025$, (e-h): $\mathrm{Pr} = 0.71$. Columns from left to right: $k = \{0, 1, 2, 4\}$. In each subplot, the top cluster of curves correspond to $\mathrm{Pr}_{t,r}$ and the bottom cluster of curves correspond to $\mathrm{Pr}_{t,\varphi}$. For $k = 0$ (a, e), only $\mathrm{Pr}_{t,r}$ is relevant. Line styles correspond to different solid properties; see table 4.1.

Previous studies (Antoranz Perales 2017; Straub et al. 2019a) have reported that for azimuthally inhomogeneous heating (of the half-sinusoidal type), the assumption of a scalar eddy diffusivity is clearly violated, even though isotropy is recovered near the channel centre. Figure 4.14 confirms these observations for all $k > 0$ and Pr considered, at least as far as it can be evaluated. In particular, $\mathrm{Pr}_{t,r} \sim y$ and $\mathrm{Pr}_{t,\varphi} \sim y^2$ is observed for all wavenumbers at the wall. For $\mathrm{Pr} = 0.71$, subfigures (e-h) show that $\mathrm{Pr}_{t,i}$ is virtually independent of the solid properties across all wavenumbers, except in a thin region near the wall. In contrast, for $\mathrm{Pr} = 0.025$ (subfigures (a-d)) the solid properties influence $\mathrm{Pr}_{t,i}$ throughout the entire domain. For such low Prandtl numbers, instantaneous fluctuations of temperature near the wall (whose spectrum is strongly affected by the solid properties) are transported into the bulk primarily by molecular diffusion. This modifies the turbulent heat flux vector and, consequently, Pr_t.

Both aforementioned studies observed that for a half-sinusoidal boundary condition, there is only a weak dependency of $\mathrm{Pr}_{t,i}$ on the azimuthal coordinate. If this statement held exactly, it would imply that $\mathrm{Pr}_{t,i}$ is independent of the wavenumber k, which is not the case. However, $\mathrm{Pr}_{t,i}$ is indeed very similar for $k = 0$ and $k = 1$, which are the

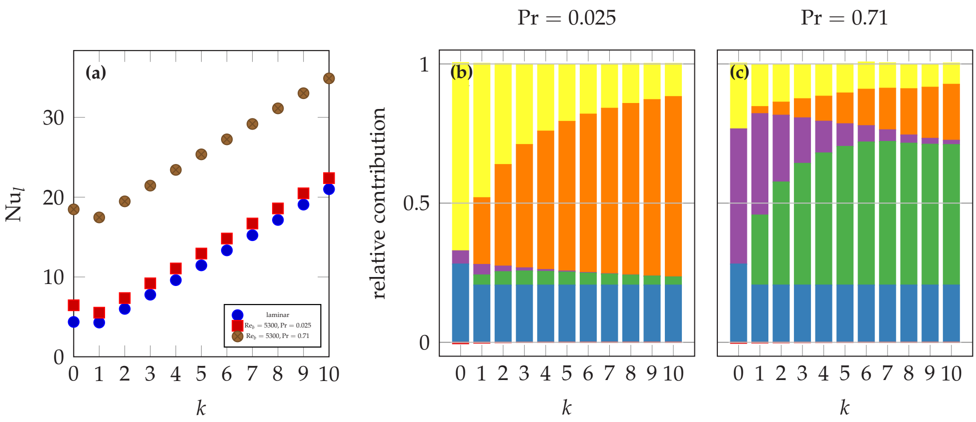

Figure 4.15: a) Local Nusselt number as function of k for different Pr considered. b), c): Individual contributions to Nu_l according to the decomposition eq. (4.40). ■: $\mathrm{Nu}_{lam}/\mathrm{Nu}_l$, ■: $\mathrm{Nu}_{lam}/\mathrm{Nu}_{RSS}$, ■: $\mathrm{Nu}_{lam}/\mathrm{Nu}_{HF,r}$, ■: $\mathrm{Nu}_{lam}/\mathrm{Nu}_{HF,\varphi}$, ■: $\mathrm{Nu}_{lam}/\mathrm{Nu}_{az.cond}$, ■: $\mathrm{Nu}_{lam}/\mathrm{Nu}_{HF,z}$. b): $\mathrm{Pr} = 0.025$, c): $\mathrm{Pr} = 0.71$.

dominant modes of a half-sinusoidal boundary condition. $\mathrm{Pr}_{t,i}$ increases systematically with k, and this increase is particularly pronounced for the low-Pr case. This observation might be explained as follows: As the scalar field is driven at increasingly small azimuthal scales with growing k, azimuthal scalar gradients increase. This enhances molecular diffusion, which increases $\mathrm{Pr}_{t,i}$ in particular for low-Pr fluids. At the same time, these azimuthal scales become to small to be effectively mixed by the dominant scales of turbulence, reducing the turbulent heat flux. Both effects contribute to the observed increase of $\mathrm{Pr}_{t,i}$ with k. One might foresee this to be an interesting test case for a turbulent heat flux model.

Local Nusselt number and its decomposition. The local Nusselt number, as defined by eq. (4.24), can be evaluated for each wavenumber k. In the given setting, it can be understood as a measure of how uniform the (modal) temperature profile is within the pipe. It aggregates the effect of all heat transfer mechanisms, i.e. radial and azimuthal transport, due to both mean conduction and turbulent diffusion. Figure 4.15a displays Nu_l for the wavenumbers considered. After a global minimum at $k = 1$, Nu_l increases monotonically in k, approximately linear with slope $\mathrm{dNu}_l/\mathrm{d}k \approx 2$, equal for all considered cases.[15]

15 For reference, $\mathrm{Nu}_l = 2k + 16/(k+6)$ for $k > 0$, $48/11$ otherwise for laminar flow.

While Nu_l aggregates all heat transfer mechanisms, the decomposition derived in section 4.2.2 provides insight into the relative importance of the various heat transfer mechanisms. Figures 4.15b and 4.15c display the individual contributions to the decomposition eq. (4.40) for $k = 0..10$. The term $\mathrm{Nu}_{lam}/\mathrm{Nu}_{RSS}$ depends only on the turbulent velocity profile (fixed for a given Re_τ). It is therefore essentially independent of Pr and k (the $k = 0$ term differs because of the mean temperature forcing). For homogeneous heating ($k = 0$), turbulent mixing is stronger for $\mathrm{Pr} = 0.71$ than for $\mathrm{Pr} = 0.025$. Consequently, $\mathrm{Nu}_{lam}/\mathrm{Nu}_{HF,r}$ is larger, and thus the overall Nusselt number Nu_l (which coincides with Nu at $k = 0$) increases.

For $\mathrm{Pr} = 0.025$, the contribution associated with azimuthal conduction increases with k, while the radial and turbulent heat flux terms remain small. Hence the rise of Nu_l is primarily driven by molecular conduction in the azimuthal direction. For $\mathrm{Pr} = 0.71$, the azimuthal conduction term also grows with k, but is dominated by turbulent azimuthal transport, which appears to saturate at higher k. At low k, radial turbulent transport contributes significantly, but its relative importance diminishes as k increases.

In summary, the decomposition of Nu_l highlights distinct heat transfer mechanisms under non-uniform heating. For the low-Pr fluid, the main transport mechanism at this Re_b is azimuthal molecular conduction. For $\mathrm{Pr} = 0.71$, the main driver of azimuthal transport is turbulence, while radial (turbulent) transport is only important at low wavenumbers. For both Pr numbers, the relative importance of azimuthal transport through molecular diffusion increases with k compared to azimuthal transport through turbulent heat flux.

Temperature fluctuations. Unlike for first-order statistics, nonlinear effects prohibit a convenient, general modal analysis of the temperature variance $\langle \vartheta' \vartheta' \rangle$. Instead, figs. 4.16a and 4.16b display cross-sectional profiles of $\langle \vartheta' \vartheta' \rangle$ for the half-sinusoidal heating case; linestyles indicate different solid properties. Figures 4.16a and 4.16b show contour plots, while figs. 4.16c and 4.16d present the azimuthally averaged variance as a function of wall distance. Straub et al. (2019a) presented data for the same setup without conjugate heat transfer.

Straub et al. (2019a) observed that non-uniform heating increases the maximum value of the temperature variance by approximately a factor of 10 compared to the case of homogeneous heating at the same Re_b and Pr. For $\mathrm{Pr} = 0.71$, the maxima of wall heat flux and wall temperature variance coincide, whereas for $\mathrm{Pr} = 0.025$ they are offset by approx. $\pi/4$ in either direction. Motivated by this observation, a simple model for the temperature variance production can be constructed based on truncating the modal

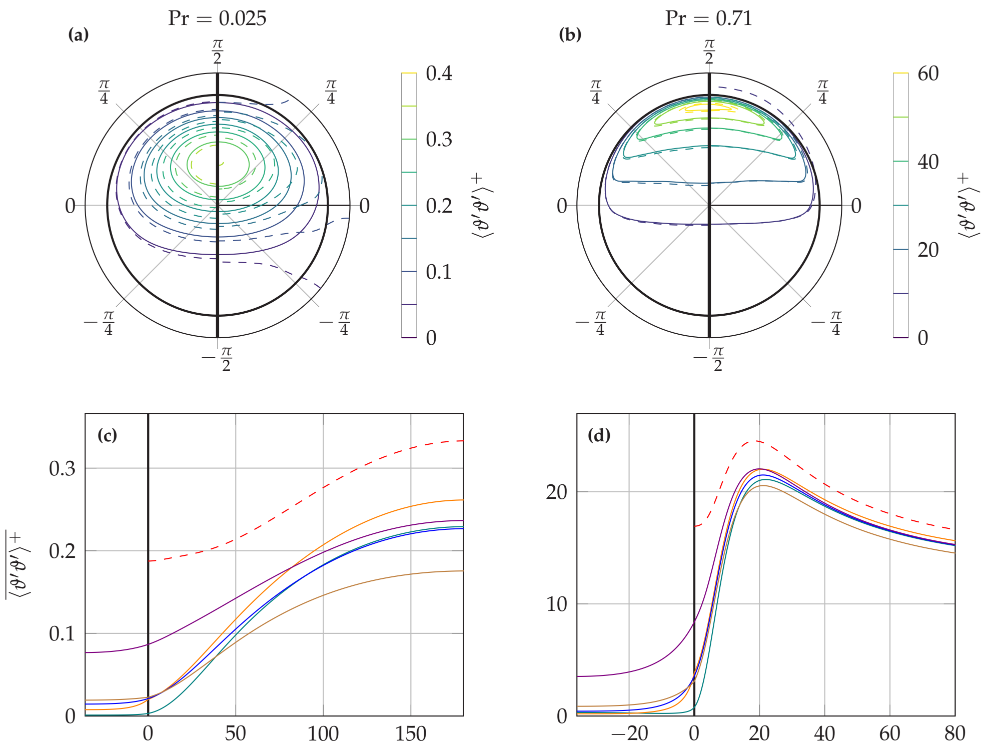

Figure 4.16: Variance of ϑ for half-sinusoidal heating, $\mathrm{Re}_b = 5300$. The left column ((a), (c)) displays $\mathrm{Pr} = 0.025$, the right column ((b), (d)) $\mathrm{Pr} = 0.71$. Top row (a-b): Contour lines of $\langle \vartheta' \vartheta' \rangle^+$, comparing the effect of varying solid properties (line style). Solid lines: $K = \lambda_{sf} = 1$. Left semicircle: $K = 1$, $\lambda_{sf} = 0.5$, right semicircle: $K = 4$, $\lambda_{sf} = 1$. Bottom row (c-d): Azimuthally averaged temperature variance. Line styles correspond to different solid properties; see table 4.1.

representation. First, inserting the definition of the turbulent eddy diffusivity eq. (4.79) into eq. (A.11e) and observing from fig. 4.14 that its value is similar for the first (and dominant) wavenumbers $k = 0, 1, 2$, one has

$$
\begin{aligned}
P_{\vartheta'\vartheta'} &= \langle \vartheta' u'_r \rangle \frac{\partial \langle \vartheta \rangle}{\partial r} + \frac{\langle \vartheta' u'_\varphi \rangle}{r} \frac{\partial \langle \vartheta \rangle}{\partial \varphi} \\
&\approx -\alpha_{t,r} \left(\frac{\partial \langle \vartheta \rangle}{\partial r} \right)^2 - \frac{\alpha_{t,\varphi}}{r^2} \left(\frac{\partial \langle \vartheta \rangle}{\partial \varphi} \right)^2 \\
&= -\alpha_{t,r} \left(\frac{\partial \widehat{\langle \vartheta \rangle}_0}{\partial r} + \frac{\pi}{2} \sin \varphi \frac{\partial \widehat{\langle \vartheta \rangle}_1}{\partial r} - \frac{2}{3} \cos 2\varphi \frac{\partial \widehat{\langle \vartheta \rangle}_2}{\partial r} + \ldots \right)^2 \\
&\quad - \frac{\alpha_{t,\varphi}}{r^2} \left(\frac{\pi}{2} \cos \varphi \widehat{\langle \vartheta \rangle}_1 + \frac{4}{3} \sin 2\varphi \widehat{\langle \vartheta \rangle}_2 + \ldots \right)^2
\end{aligned}
$$

where the numerical coefficients (1, $\pi/2$, $2/3$) arise from the Fourier representation of the half-sinusoidal boundary condition, truncated after $k = 2$. Finally, fig. 4.12 indicated that, in the outer half of the pipe (where the peak of temperature variance production is located), the magnitudes of the radial gradients of the first three modes are comparable, i.e. $\mathcal{O}(\partial\widehat{\langle\vartheta\rangle}_0 \big/ \partial r) = \mathcal{O}(\partial\widehat{\langle\vartheta\rangle}_1 \big/ \partial r) = \mathcal{O}(\partial\widehat{\langle\vartheta\rangle}_2 \big/ \partial r)$, and that $\widehat{\langle\vartheta\rangle}_1 \approx 2\widehat{\langle\vartheta\rangle}_2$. Inserting, one finds

$$\begin{aligned} P_{\vartheta'\vartheta'} &\approx -\alpha_{t,r}\left(\frac{\partial\widehat{\langle\vartheta\rangle}_0}{\partial r}\right)^2\left(1+\frac{\pi}{2}\sin\varphi-\frac{2}{3}\cos 2\varphi\right)^2 \\ &\quad -\frac{\alpha_{t,\varphi}}{r^2}\left(\widehat{\langle\vartheta\rangle}_1\right)^2\left(\frac{\pi}{2}\cos\varphi+\frac{2}{3}\sin 2\varphi\right)^2 \\ &\approx -\alpha_{t,r}\left(\frac{\partial\widehat{\langle\vartheta\rangle}_0}{\partial r}\right)^2 f(\varphi)^2-\frac{\alpha_{t,\varphi}}{r^2}\left(\widehat{\langle\vartheta\rangle}_1\right)^2 f'(\varphi)^2 \end{aligned} \tag{4.81}$$

For half-sinusoidal heating, $f(\varphi)^2$ attains its maximum value $\pi^2 \approx 9.86$ at $\varphi = \pi/2$, while $f'(\varphi)^2$ has the same maximum at the inflection points of $f(\varphi)$, i.e. at $\varphi = 0$. The Prandtl number alters the relative importance of the azimuthal and radial production terms: increasing Pr enhances Nu_l and thus increases radial production (first term). For $y^+ \lesssim 20$, the near-wall behaviour implies $\alpha_{t,\varphi} \gg \alpha_{t,r}$, so the azimuthal production (second term) is locally amplified near the wall. To summarize, a production peak is expected at $\varphi = \pi/2$, while for low Pr, secondary near-wall peaks are expected offset from $\pi/2$ by $\Delta\varphi \leq \pi/2$ – the actual position is determined by the balance of azimuthal and radial contributions to the production, and indeed it varies slightly between cases of different solid properties. Interestingly, the low-order model captures nicely the peak locations and $\mathcal{O}(10)$ increase of temperature variance compared to the homogeneous case, which was also observed by Straub et al. (2019a) – even though the precise level of temperature variance is not only governed by its production, but also dissipation and (turbulent and molecular) diffusion.

Returning to the influence of λ_{sf} and K, figs. 4.16c and 4.16d displays the azimuthally averaged temperature variance for the different solid configurations and Pr numbers. As in the case of uniform heating, increasing the effusivity ratio K amplifies temperature fluctuations within the solid; this effect is particularly pronounced for low Pr. The temperature variance in the bulk of the flow is only weakly affected by K. Unlike for uniform heat flux, λ_{sf} has a strong impact on temperature fluctuations. A thick, well conducting wall reduces mean temperature gradients at the interface in both radial and azimuthal directions, directly decreasing the production of temperature variance within the fluid (see eq. (4.81)); this effect is, as discussed, more pronounced for small

Pr. As λ_{sf} increases, temperature fluctuations in the fluid are reduced, while they are amplified in the solid. These observations have a direct engineering implication for applications employing low-Pr fluids under non-uniform heating conditions. By adjusting the wall thickness and/or solid properties, one can substantially reduce the variance of temperature fluctuations in the fluid, thereby making more efficient use of the heat transfer fluid while keeping it within safe operating limits. Such modifications leaves the global heat-transfer coefficient essentially unchanged (see fig. 4.10b), but they increase temperature fluctuations in the solid and thus, potentially, thermal stresses.

4.5 Numerical results: Thermally developing turbulent flow

In section 4.4, it was shown that, in the turbulent fully developed state, azimuthally non-uniform heating affects certain properties strongly (e.g. temperature fluctuations), while others change little or not at all (e.g. the global Nusselt number, when compared to uniform heat flux). In engineering applications, however, the fully developed state does not occur in isolation. It is an idealised asymptotic state, representing the limit in which net axial fluxes (i.e. axial molecular and turbulent diffusion) have decayed. In real systems, the fully developed state is only approximated 'sufficiently far downstream' of a change in boundary condition. This section aims to quantify 'sufficiently far downstream' in terms of Re_b, Pr and the azimuthal wavenumber that characterises non-uniform heating.

Section 4.2.3 discussed the thermal entry section in the laminar regime and found that the thermal entry length (of any quantity) scales linearly in both Re_b and Pr for $\mathrm{Pe} \gg 1$. With respect to the azimuthal wavenumber of the boundary condition, increasing k generally reduces the thermal entry length of the local Nusselt number, except for $k = 1$, where the entry length increased by a factor of 2-3 over that of $k = 0$. In turbulent flow, turbulent mixing reduces the development length, which makes the dependence on Re and Pr is more complex, but the dependence on k is qualitatively similar to the laminar case.

Relationship between development length and fully developed state. In general, one may expect all (mean) flow properties $q(z)$ to converge exponentially to their fully developed values. This is explicitly seen in laminar flow (see eq. (4.75)). It is reasonable to make the same assumption for turbulent flow, at least beyond an initial transient region. Mathematically, this implies that the fully developed state is reached only in the limit $z \to \infty$. For engineering purposes, however, it is useful to identify regions where the fully developed state is a good approximation of the actual behaviour, and to compare such development lengths between different configurations and parameter sets.

A common definition of the development length $\hat{z}$ is based on the relative deviation of $q(z)$ from its asymptotic value:

$$\left| \frac{q(z)}{\lim_{q\to\infty} q(z)} - 1 \right| < c \qquad \forall\, z > \hat{z}, \tag{4.82}$$

where c is a prescribed tolerance (in this section, $c = 1\,\%$). Different authors choose different values of c, but for relative comparison of $\hat{z}$ between cases, the exact choice of c is inconsequential, provided that $q(z)$ is in form of an exponential (plus a constant). If fully developed data are not available, one may fit an exponential function $\tilde{q}(z)$ numerically and use $\lim_{z\to\infty} \tilde{q}(z)$ as a surrogate. Both approaches become unreliable for quantities that are small or zero in the fully developed state, or even zero everywhere. For this reason, development lengths are best evaluated for quantities that remain finite, such as the (global or local) Nusselt number.

It is important to note that the development length evaluated in this way can differ substantially between quantities. Consider a trivial example: a wall heat flux proportional to $\sin(\varphi)$ does not affect the centreline temperature. The development length *of the centreline temperature* is then zero (for any c), whereas other quantities, such as the wall temperature), have a non-zero development length (see e.g. fig. 4.6 for a laminar illustration). Global quantities such as the Nusselt number are also subject to this behaviour. The Nusselt number may be within 1 % of its asymptotic value, while the (mean) temperature at a given (r, φ)-location still deviates by 50 % or more from its fully developed value (e.g. in the presence of a strong $k = 1$ mode in the boundary condition).[16] Even if the local mean temperature is within 1 % of its fully developed value everywhere in the (r, φ) plane, the temperature variance may deviate by 10 % or more.

It is therefore crucial to distinguish between the development length of a specific quantity and the onset of the fully developed state in a broader sense.

[16] In terms of the decomposition of the Nusselt number: From $\hat{z}$ on, the sum of all terms in eq. (4.40) except $\mathrm{Nu}_{lam}/\mathrm{Nu}_l$ is approximately constant, although individual contributions may still be exchanged between the other terms. For some engineering applications, only the development length of the global Nusselt number is relevant, if only mean heat transfer is of interest.

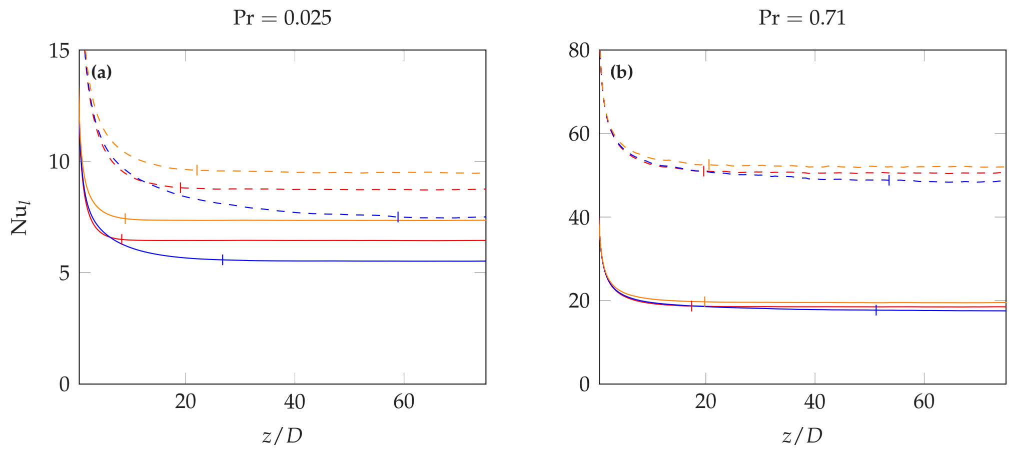

Figure 4.17: Azimuthal mean of the local Nusselt number as a function of z for (left) $\mathrm{Pr} = 0.025$ and (right) $\mathrm{Pr} = 0.71$ at $\mathrm{Re}_b = 5300$ (solid lines) and 19000 (dashed lines) for (coloured) azimuthal heating modes $k = 0$ (constant, ——), $k = 1$ (——) and $k = 2$ (——). Additionally marked is the 1% thermal entry length. Adapted from [NBGF25].

Global and local Nusselt number As discussed in section 4.2.1, the global Nusselt number is not affected by variations of the boundary condition in φ. This result was obtained without any restriction on the variation of the boundary condition in z (and even time t). The conclusions of section 4.2.1 therefore also hold in developing flow: Nu depends on the streamwise location z, but not on the azimuthal $f(\varphi)$ except for its mean.

All statistics that are linear in T can be obtained as linear combination of the responses to monochromatic boundary conditions. Accordingly, such statistics are presented for the azimuthal modes $k \in \{0, 1, 2\}$.

As in sections 4.2.4 and 4.4, the local Nusselt number $\mathrm{Nu}_l(z)$ is used to characterise the global scalar transport for varying k and z, and is later decomposed according to eq. (4.40). Figure 4.17 shows Nu_l as a function of z for $k \in 0, 1, 2$ and both Reynolds and Prandtl numbers.

In all cases, Nu_l exhibits a strong maximum at $z = 0$. At the start of the heated section, the heat flux is fixed, but the [modal] temperature profile is still nearly uniform, which results in a very high Nu_l. Downstream, Nu_l decreases monotonically towards its

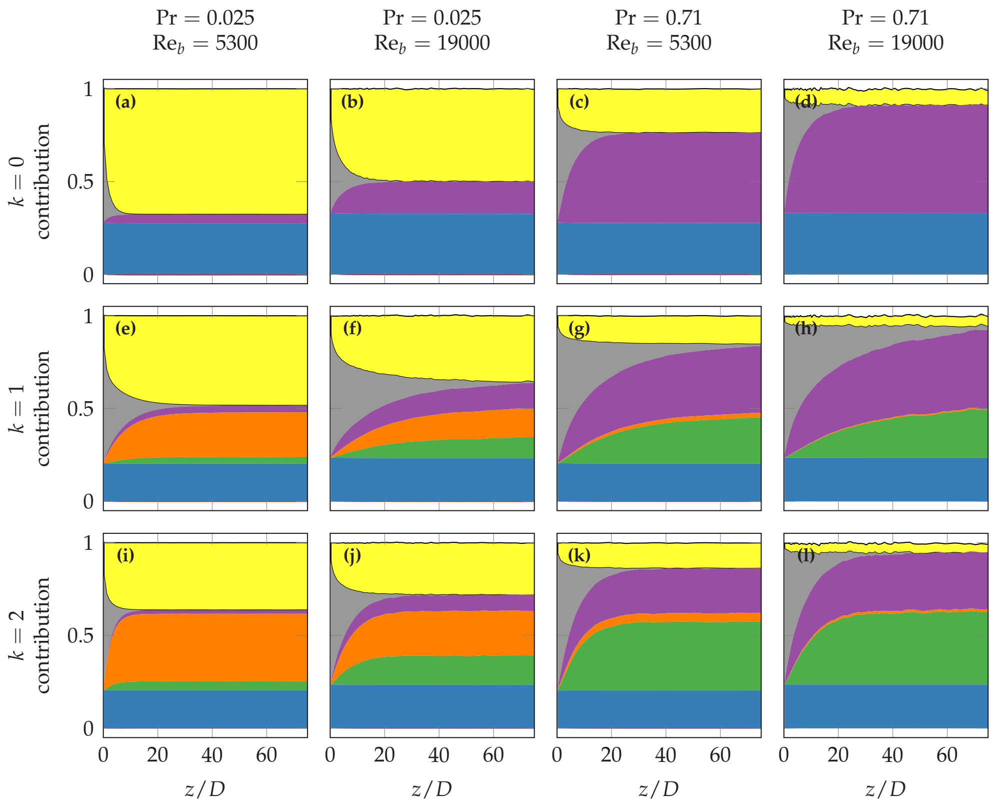

Figure 4.18: Individual contributions to Nu_l according to the decomposition eq. (4.40), as a function of z. Rows: wavenumbers $k = 0$ (top), $k = 1$ (middle), $k = 2$ (bottom); columns: $(\mathrm{Re}_b, \mathrm{Pr})$ sorted by increasing Pe from left to right. Contributions: yellow: $\mathrm{Nu}_{lam}/\mathrm{Nu}_l$, blue: $\mathrm{Nu}_{lam}/\mathrm{Nu}_{RSS}$, purple: $\mathrm{Nu}_{lam}/\mathrm{Nu}_{HF,r}$, green: $\mathrm{Nu}_{lam}/\mathrm{Nu}_{HF,\varphi}$, orange: $\mathrm{Nu}_{lam}/\mathrm{Nu}_{az.cond}$, red: $\mathrm{Nu}_{lam}/\mathrm{Nu}_{HF,z}$, grey: $\mathrm{Nu}_{lam}/\mathrm{Nu}_{dev.}$. Extended from [NGF26].

[NGF26]

fully developed value; the same monotonic behaviour was found in laminar flow.[17] For Pr = 0.025, increasing Re_b increases the development length by a factor of 2–3 [for all k]. For $Pr = 0.71$, the development lengths [of all k only change] marginally when increasing Re_b. [As in the laminar case, the $k = 1$ mode shows a much longer development length than $k = 0$, and the $k = 2$ case has a similar development length compared to the $k = 0$ case.]

[17] In buoyancy-aided flow with otherwise the same configuration, the deformation of the velocity profile near the wall is known to trigger relaminarisation at moderate Reb, see Narasimha and Sreenivasan (1979), accompanied by a significant reduction of Nu. In the thermal entrance, this can lead to a non-monotonous behaviour of Nu (Vicente Cruz et al. 2025).

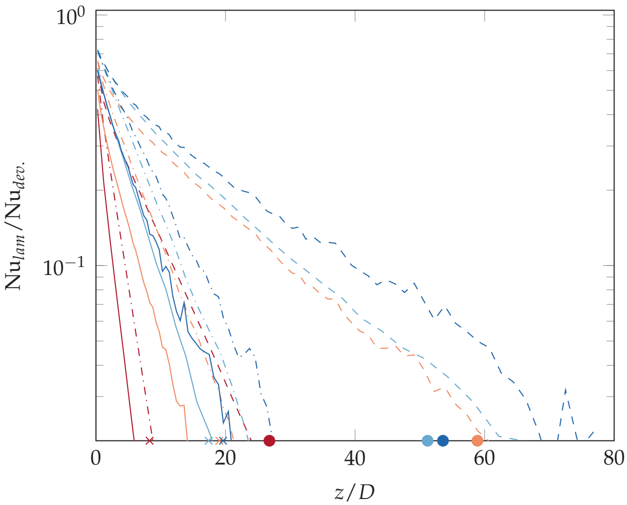

Figure 4.19: Contribution of the developing part to the decomposition eq. (4.40), i.e. $\mathrm{Nu}_{lam}/\mathrm{Nu}_{dev.}$. Colour in order of Pe; ——: $(\mathrm{Pr}, \mathrm{Re}_b) = (0.025, 5300)$, ——: $(0.025, 19000)$, ——: $(0.71, 5300)$, ——: $(0.71, 19000)$. Additionally marked on the bottom border of the plot is the 1 % development length of Nu_l, see fig. 4.17. Linestyle: $k = 0$ (solid, ×), $k = 1$ (dashed, ●), $k = 2$ (dash-dotted, [omitted to avoid cluttering]). Extended from [NGF26].

Decomposition of the Nusselt number Insight into the transport mechanisms in the developing region is obtained by evaluating the decomposition of Nu_l, using eq. (4.40). The resulting contributions are shown in fig. 4.18 [...]. [The top row shows the case $k = 0$, i.e. uniform heat flux.] Note that in all cases and for all z^*, the contributions sum up to approx. 1, verifying the decomposition eq. (4.40). The relevant contributions, in addition to Nu itself, are Nu_{RSS}, $\mathrm{Nu}_{HF,r}$ and $\mathrm{Nu}_{dev.}$. The term Nu_{RSS} depends only on the mean velocity profile, which is independent of z and determined by Re_b.

Close to $z^* = 0$, the developing term $\mathrm{Nu}_{dev.}$ dominates the balance. It consists of three parts: a positive contribution from the mean convection, a negative part from the axial turbulent heat flux (always smaller in magnitude), and a positive but extremely small part from axial conduction ($< 0.2\,\%$ even for the lowest Pe case). The ratio $\mathrm{Nu}_{lam}/\mathrm{Nu}_{dev.}$ is well approximated by an exponential decay after the temperature nonuniformity has been conducted through the viscous sublayer; this is illustrated in semi-logarithmic scaling in fig. 4.19. Its decay rate depends on the configuration: [for fixed k,] increasing either Re_b or Pr reduces the decay rate.

Increasing Pe (from left to right in fig. 4.18) enhances turbulent scalar mixing, so $\mathrm{Nu}_{HF,r}$ becomes more important. This radial heat flux contribution increases with z, because an increasing fraction of the turbulent eddies resides within the growing thermal boundary

[NGF26]

layer and contributes to wall-normal transport. For a given $(\mathrm{Pr}, \mathrm{Re}_b)$ configuration, the contributions $\mathrm{Nu}_{HF,r}$, $\mathrm{Nu}_{dev.}$ and Nu_l approach their fully developed values with similar convergence rates.

The middle and bottom rows of fig. 4.18 show the same decomposition for $k = 1$ and $k = 2$, respectively. Compared to $k = 0$, two additional terms appear: the azimuthal turbulent heat flux and azimuthal molecular conduction. Both terms converge at rates comparable to that of $\mathrm{Nu}_{dev.}$. Among all wavenumbers, $k = 1$ exhibits the slowest decay of $\mathrm{Nu}_{dev.}$ (see fig. 4.19). The location where $\mathrm{Nu}_{dev.}$ contributes only 1 % to the balance is shifted downstream by a factor 3–5 relative to $k = 0$. For $k = 2$, the decay rate consistently lies between those of $k = 0$ and $k = 1$ for all $(\mathrm{Pr}, \mathrm{Re}_b)$ considered. Thus, non-uniform heating with a dominant $k = 1$ produces a development region that is 3–5 times longer, during with the transport mechanisms responsible for $\mathrm{Nu}_{dev.}$ – changing mean convection, streamwise gradient of the axial turbulent heat flux, and axial conduction – remain significant. The development region characterised in this way agrees reasonably well with the development length of the local Nusselt number when taking into account that the contribution of Nu_l itself to the balance changes between cases.

Mean temperature profiles As discussed in the introduction of section 4.5, the (local) Nusselt number is an aggregate measure of all heat transfer mechanisms. Convergence of pointwise first-order statistics at a given z-plane is sufficient, but not necessary for the convergence of Nu_l. To better understand this relationship, fig. 4.20 shows contours of the mean modal temperature for the various Pr and k at $\mathrm{Re}_b = 19000$, together with the corresponding development length as a function of radial position (thick black line in each panel). For $k = 0$, the mean linear increase of the temperature has been removed to highlight the exponential approach to the fully developed profile. The shape of the contours, especially at low Pr, closely resemble the laminar ones in fig. 4.6.

For $k = 0$ (left column of fig. 4.20), the development length of the mean temperature agrees well with that of Nu (about $20D$) over most of the cross-section. An exception is a narrow region around $r = 0.3D$, where the difference between inlet and fully developed profile is small.

For $k = 1$ (middle column), the behaviour is very different. The centreline temperature is identically zero for all z, implying a development length of 0 at $r = 0$. In contrast, for $r > 0.25D$ the development length is almost constant and lies between $80D$ and $95D$ depending on Pr. Because Nu_l includes the (modal) bulk temperature, which is a cross-sectional average weighted with $u_z(r)$, regions near the centre contribute more

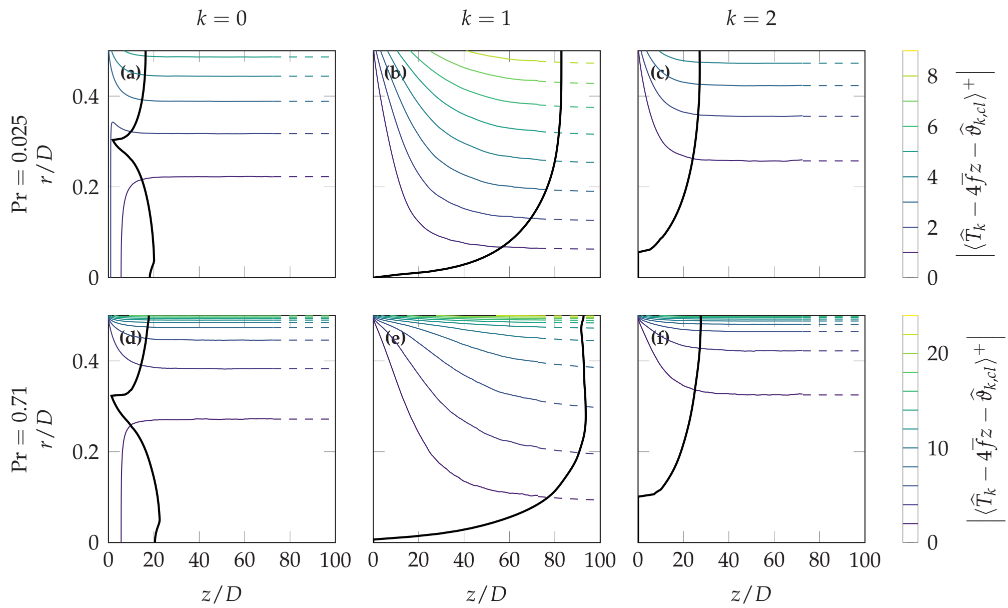

Figure 4.20: Contours of the (absolute) mean modal temperature $\widehat{T}_k$ as function of r and z for $\mathrm{Re}_b = 19000$. Top row: Pr $= 0.025$, bottom row: Pr $= 0.71$. Columns: $k = 0$ (left), $k = 1$ (center), $k = 2$ (right). The linear increase is removed from the $k = 0$ case by the term $-4\bar{f}z$, and the profile is normalised with the centreline temperature in the fully developed state. Beyond the simulation domain, the data is extrapolated using an exponential fit (dashed contours). The thick black line indicates the development length, which is for each radial location evaluated as the position from which on the displayed quantity deviates less than $0.01\left(\widehat{\langle\vartheta_k\rangle}\Big|_{r=0} - \widehat{\langle\vartheta_k\rangle}\Big|_{r=0.5}\right)$ from the fully developed state.

strongly than near-wall regions. As a result, the short development length at the centre offsets the long near-wall development, yielding an overall development length of Nu_l of only $50-60D$. A similar, but less pronounced, effect is observed for $k = 2$ (right column of fig. 4.20).

These results demonstrate that strongly asymmetric (half-sided) heating can delay the convergence of the pointwise mean temperature, in particular near the wall, well beyond what would be inferred from Nu_l alone. For the half-sinusoidal boundary condition, development lengths of order $100D$ are indeed observed in the numerical data.

Temperature fluctuations In a turbulent temperature field, temperature fluctuations are present. Streamwise invariance of $\langle T'T'\rangle$ therefore is an indication that the *turbulent* heat transfer can be considered fully developed. From the balance equation of $\langle T'T'\rangle$,

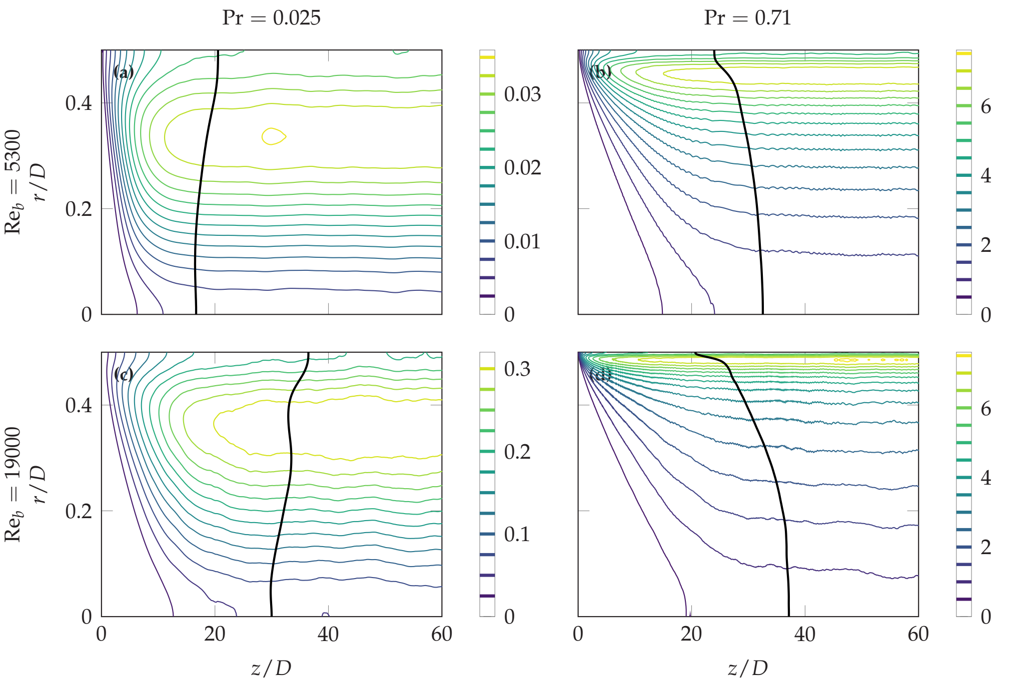

Figure 4.21: Contours of $\langle T'T'\rangle^+$ for uniform heat flux in the $r-z$-plane. Top row: $\mathrm{Re}_b = 5300$, bottom row: $\mathrm{Re}_b = 19000$; left column: $\mathrm{Pr} = 0.025$, right column: $\mathrm{Pr} = 0.71$. Black lines indicate the development length of this quantity, i.e. for each radial location the position where $\langle T'T'\rangle^+$ is within $0.01 \max_r \langle \vartheta'\vartheta'\rangle^+$ of the fully developed value, i.e. $\langle \vartheta'\vartheta'\rangle^+$. Adapted from [NGF26].

eq. (A.9), streamwise invariance of the production term [requires that] the mean radial and azimuthal temperature gradients, and thus the underlying mean temperature field, become invariant in the streamwise direction. One may therefore expect the development length of $\langle T'T'\rangle$ to exceed that of $\langle T\rangle$.[18]

Figure 4.21 shows contours of the temperature variance for uniform heat flux for both Re and Pr. The thick black line in each panel marks the development length at each radius (see figure caption for the precise definition). For all configurations, the development length of $\langle T'T'\rangle$ is nearly uniform across the pipe and approx. 50−100 % higher than the corresponding development lengths of Nu and $\langle T\rangle$. This is in line with the *hydraulic* development of turbulent pipe flows (Doherty et al. 2007).

[NGF26]

[18] Note that the dependence of the development length on r reverses when going from $\langle T\rangle$ to e.g. $\langle \partial T/\partial r\rangle$: this derivative has a development length of zero at the wall (fixed by the boundary condition) and maximum near the centreline.

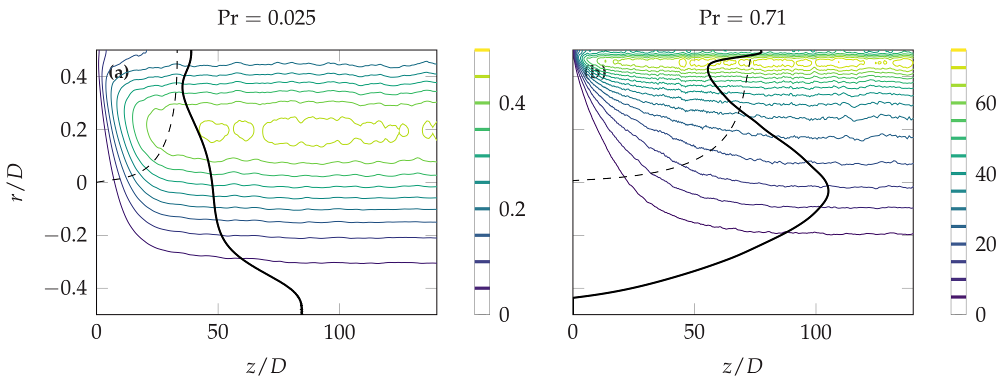

Figure 4.22: Contours of $\langle T'T' \rangle^+$ for half-sinusoidal heat flux in a slice of the pipe at $\varphi = \pi/2$, $\mathrm{Re}_b = 5300$. Left: $\mathrm{Pr} = 0.025$, right: $\mathrm{Pr} = 0.71$. Black lines indicate the development length of this quantity, i.e. for each radial location the position where $\langle T'T' \rangle^+$ is within $0.01 \max_{r,\varphi} \langle \vartheta'\vartheta' \rangle^+$ (where $\langle \vartheta'\vartheta' \rangle^+$ is the fully developed value). Additionally, the development length of $\widehat{\langle T \rangle}_{k=1}$ is shown with a dashed line in the upper half of the pipe (see fig. 4.20).

The nonlinearity of $\langle T'T' \rangle$ renders a decomposition in terms of azimuthal modes of the boundary condition futile. Instead, the half-sinusoidal case is again used as a representative case of non-uniform heating. Figure 4.22 presents $\langle T'T' \rangle$ for $\mathrm{Re}_b = 5300$ in a slice at the azimuthal location of maximum heat flux, $\varphi = \pi/2$. In the heated half, the development length of $\langle T'T' \rangle$ is in the same order of that of the $k = 1$ mean modal temperature (indicated by the dashed line, fig. 4.20). On the unheated side of the pipe (i.e. at $\varphi = 3\pi/2$), the fluctuation levels are lower, but the development region is considerably longer than on the heated side. The source term in the balance of temperature fluctuations corresponds to production in the near-wall region, which requires finite temperature gradients. On the heated side, the 'correct' production is established very close to the start of the heated section, so the variance budget can equilibrate over a relatively short distance. On the unheated side, production can only become representative of the fully developed state once turbulent and molecular diffusion have transported the effect of heating across the pipe. Only after this cross-stream transport has occurred can the local balance of $\langle T'T' \rangle$ begin to equilibrate, which explains the much longer development length there.

Temperature fluctuation data for $\mathrm{Re}_b = 19000$ is not shown in fig. 4.22 as the numerical domain is significantly too short to reach an acceptable level of convergence. An exponential extrapolation suggests development lengths exceeding $z/D \approx 300$ on the unheated side of the pipe, underlining how strongly non-uniform heating can delay the streamwise development of temperature fluctuations compared with mean quantities and with Nu_l.

Extrapolation to higher Reynolds and Prandtl numbers For laminar flow, [section 4.2.4 showed] that the thermal entry length of Nu_l (and of all other quantities) scales with $\mathrm{Pe} = \mathrm{Re}_b\,\mathrm{Pr}$. For turbulent flow, fig. 4.17 illustrated that the behaviour is more complex: for $\mathrm{Pr} = 0.025$ an increase in Re_b leads to a longer development length for all k, whereas for $\mathrm{Pr} = 0.71$ it is almost unchanged. In the following, the parameter space in $(\mathrm{Re}_b, \mathrm{Pr})$ is explored using a gradient-diffusion closure together with DNS data for the turbulent velocity profile and eddy viscosity.

The gradient-diffusion hypothesis eq. (4.79) in dimensionless form reads

$$\langle u_r' T' \rangle = -\frac{1}{\mathrm{Pe}} \alpha_{t,r} \frac{\partial \langle T \rangle}{\partial r}, \qquad \left[\langle u_\varphi' T' \rangle = -\frac{1}{\mathrm{Pe}} \alpha_{t,\varphi} \frac{1}{r} \frac{\partial \langle T \rangle}{\partial \varphi}, \right] \qquad \langle u_z' T' \rangle = -\frac{1}{\mathrm{Pe}} \frac{\alpha_{t,z}}{\alpha} \frac{\partial \langle T \rangle}{\partial z}, \tag{4.83}$$

[NGF26]

where $\alpha_{r,i}$ are the turbulent thermal diffusivities in the respective directions, non-dimensionalized with $\lambda_f/(\rho_f c_{p,f})$. These are inserted into eq. (4.11a):

$$\begin{aligned} \frac{\mathrm{Pe}}{\alpha} \langle u_z \rangle \frac{\partial \langle T \rangle}{\partial z} = & \left[\frac{1}{r} \frac{\partial}{\partial r} \left(r \frac{\partial \langle T \rangle}{\partial r} \right) + \frac{1}{r^2} \frac{\partial^2 \langle T \rangle}{\partial \varphi^2} + \frac{1}{\alpha^2} \frac{\partial^2 \langle T \rangle}{\partial z^2} \right] \\ & + \left[\frac{1}{r} \frac{\partial}{\partial r} \left(r \alpha_{t,r} \frac{\partial \langle T \rangle}{\partial r} \right) + \frac{1}{r^2} \frac{\partial}{\partial \varphi} \left(\alpha_{t,\varphi} \frac{\partial \langle T \rangle}{\partial \varphi} \right) + \frac{1}{\alpha^2} \frac{\partial}{\partial z} \left(\alpha_{t,z} \frac{\partial \langle T \rangle}{\partial z} \right) \right]. \end{aligned} \tag{4.84}$$

The turbulent thermal diffusivity is now approximated as isotropic, identical for all k and determined by the mean momentum equation, i.e.

$$\alpha_{t,r} = \alpha_{t,\varphi} = \alpha_{t,z} = \alpha_t(r). \tag{4.85}$$

In view of the fully developed results in section 4.4, this is a crude approximation, but it suffices to estimate trends in the development length. With this approximation, the temperature equation becomes

$$\frac{\mathrm{Pe}}{\alpha} \langle u_z \rangle \frac{\partial \langle T \rangle}{\partial z} = \frac{1}{r} \frac{\partial}{\partial r} \left(\alpha_{tot} r \frac{\partial \langle T \rangle}{\partial r} \right) + \alpha_{tot} \frac{1}{r^2} \frac{\partial^2 \langle T \rangle}{\partial \varphi^2} + \alpha_{tot} \frac{1}{\alpha^2} \frac{\partial^2 \langle T \rangle}{\partial z^2}, \tag{4.86}$$

with $\alpha_{tot} = 1 + \alpha_t(r)$. Introducing $\langle T \rangle = \sum_{-\infty}^{\infty} \widehat{\langle T \rangle}_k e^{jk\varphi}$, using $\alpha = \mathrm{Pe}$, and then comparing coefficients for each Fourier mode, yields

$$\langle u_z \rangle \frac{\partial \widehat{\langle T \rangle}_k}{\partial z} = \frac{1}{r} \frac{\partial}{\partial r} \left(\alpha_{tot} r \frac{\partial \widehat{\langle T \rangle}_k}{\partial r} \right) + \alpha_{tot} \frac{1}{\mathrm{Pe}^2} \frac{\partial^2 \widehat{\langle T \rangle}_k}{\partial z^2} \left[+ \alpha_{tot} \frac{k^2}{r^2} \widehat{\langle T \rangle}_k \right]. \tag{4.87}$$

[This equation is analogous to eq. (4.57) in section 4.2.4, which corresponds to the laminar case with $\alpha_t = 0$.] To close the model, the correlation of Kays (1994) is employed, i.e.

$$\alpha_{tot} = 1 + \alpha_t(r) = 1 + \frac{\mathrm{Pr}}{\mathrm{Pr}_t}\nu_t \quad \text{where } \mathrm{Pr}_t = 0.85 + \frac{0.7}{\mathrm{Pr}\nu_t} \tag{4.88}$$

where $\nu_t^* = \nu_t/\nu$ [...].

Together with the boundary conditions eqs. (4.41b), (4.41c) and (4.56), this equation can be solved numerically using $\langle u_z \rangle$ and ν_t from DNS. Data from Straub (2019) and Pirozzoli (2024) is used; the highest Re_b considered is 612 000. A second-order finite-difference discretisation is employed with suitably chosen domain length and grid resolution, and the resulting linear system is inverted directly. From the computed scalar fields, $\mathrm{Nu}_l(z)$ is evaluated and its development length determined. The results are shown in fig. 4.23.

Also indicated in fig. 4.23 are the points where well-resolved scalar data is available, i.e. $\mathrm{Pr} = \{0.025, 0.71\}$ and $\mathrm{Re}_b = \{5300, 19000\}$. Labels at these locations give the development length predicted by the simplified model, and in parentheses the value obtained from the resolved data. [For $k = 0$ and $k = 1$ the predictions agree within about 25 %,] indicating that the model captures the main trends in development length.

[For $k = 0$ (fig. 4.23a), the] dependence of the development length on Re_b is strongly influenced by Pr. For low $\mathrm{Pr} \ll 1$, the development length increases with Re_b (from about $5D$ to about $35D$), whereas for high $\mathrm{Pr} \gg 1$ it decreases with Re_b (from approx. $10D$ to $5D$). For intermediate $\mathrm{Pr} \approx 0.7-10$, the development length is weakly affected by Re_b and is roughly $20D$.[19]

These findings are explained as follows. Increasing Re_b has two competing effects on the development length. First, the mean convective time scale decreases (advection is faster), so for a given amount of diffusion (molecular and turbulent), a *longer* streamwise distance is needed to reach thermally fully developed conditions. Second, increasing Re_b increases turbulent mixing, which enhances turbulent diffusion and thus tends to *shorten* the development length. For low Pr, turbulent diffusion contributes less to radial transport, so the first effect dominates and the development length increases with Re_b. For high Pr, turbulent diffusion dominates and the second effect prevails. At a sufficiently high Re_b, an approximate balance between both mechanisms appears

[19] These trends are consistent with the results of Notter and Sleicher (1972), who used a different turbulent heat flux model and synthetic velocity profiles based on measurements.

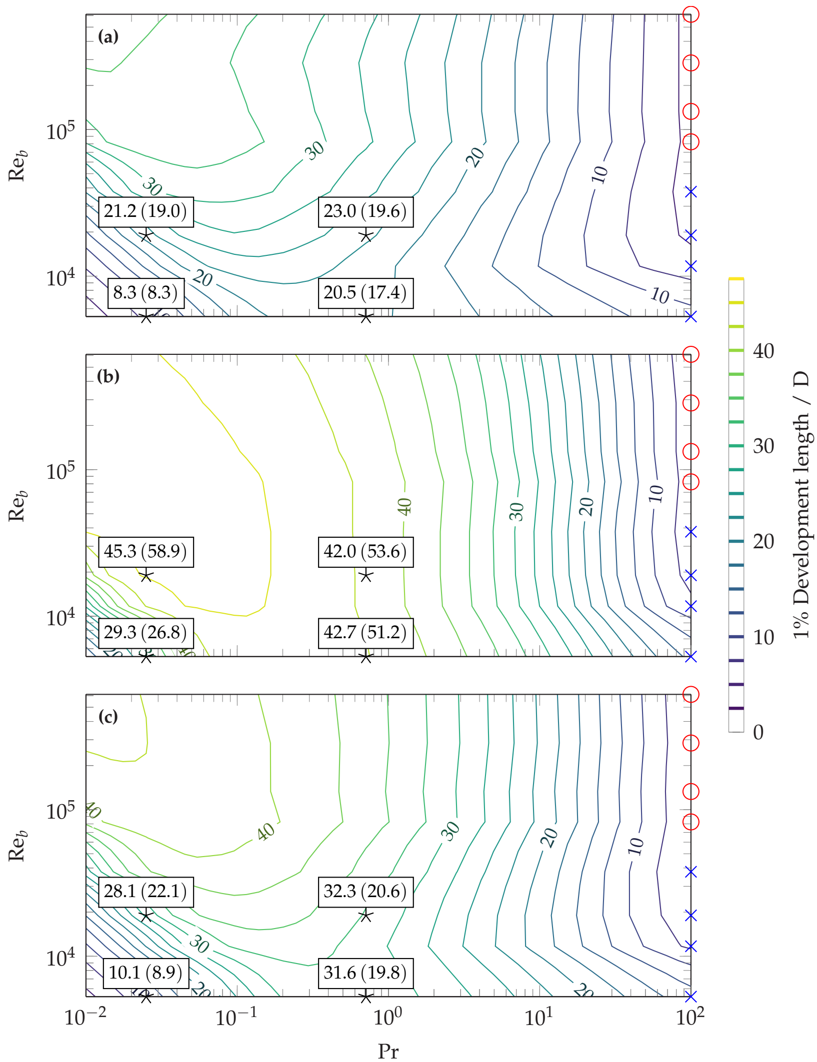

Figure 4.23: 1 % development length of Nu_l for wavenumbers $k = 0$ (top), $k = 1$ (centre), $k = 2$ (bottom) as a function of Pr and Re_b, based on the Kays correlation and DNS data for the momentum variables. On the right, markers indicate Re_b values at which DNS data was used: × (Straub 2019) for $\mathrm{Re}_b = \{5300, 11700, 19000, 37700\}$; ○ (Pirozzoli 2024) for $\mathrm{Re}_b = \{82500, 133000, 285000, 612000\}$. Points marked with ⋆ represent present (resolved) data. The label above each of those points contain the value predicted by the simplified model, and (in parentheses) the value as computed from the resolved data. Extended from [NGF26].

at all Pr: further increasing Re_b leaves the development length almost unchanged. For example, at $\mathrm{Pr} = 100$ the development length is nearly constant for $\mathrm{Re}_b > 19000$, whereas for $\mathrm{Pr} = 0.1$ this plateau is only reached for $\mathrm{Re}_b > 10^5$. [NGF26]

Figures 4.23b and 4.23c show the development length for $k = 1$ and $k = 2$, respectively. While the simplified model tends to underpredict the development lengths for $k = 1$ and overpredicts them for $k = 2$, the overall trends are well captured and consistent with those discussed for $k = 0$. In particular, the RANS-based model also predicts a significantly larger development length for $k = 1$ than for $k = 0$ over the entire (Re_b,Pr) range, with $k = 2$ falling in between.

4.6 Discussion and summary

This chapter investigates the impact of non-uniform heat flux on passive scalar transfer in laminar and turbulent pipe flow, using theoretical analysis and thermal DNS results.

From a theoretical perspective, an open question in the literature is whether the global Nusselt number Nu is affected by azimuthal inhomogeneities in the wall heat flux. A main result of this chapter is a definitive negative answer: in all cases considered (different Pr fluids, laminar vs. turbulent, CHT vs. non-CHT, fully developed and thermal inlet), the global heat transfer properties are independent of the azimuthal distribution of the imposed heat flux. This follows from a more general statement developed here, namely that the operator $\mathcal{L}_{\langle T^* u_i^{*n} \rangle}[f(\varphi)], n \geq 0$, is Fourier-diagonal in the azimuthal direction. This property also extends to plane channel flow. As a consequence, all first-order temperature statistics in this chapter are presented in terms of their azimuthal Fourier modes. This spectral structure is then used to derive a decomposition of the local Nusselt number Nu_l into individual heat transfer mechanisms, which takes into account axial and azimuthal heat flux inhomogeneities. In addition, a closed-form solution for the laminar, non-uniform Graetz problem is presented.

The azimuthal Fourier decomposition of the boundary condition $f(\varphi)$ introduces the wavenumber k, where a strong $k = 1$ mode is evoked by one-sided heating. For both laminar and turbulent flow, increasing k beyond $k = 1$ causes the (mean) temperature to vanish in a growing region around the pipe centre, and the fully developed state is reached earlier under otherwise identical conditions. The notable exception is the $k = 1$ mode, whose development length exceeds that of the $k = 0$ mode. The corresponding deformation of the (mean) temperature profile is caused by azimuthal conduction and azimuthal turbulent heat flux, as shown by the Nu_l decomposition; the latter becomes important only at sufficient Re or Pr. The turbulent heat flux is characterised by the turbulent Prandtl number Pr_t, and the present data show that this quantity becomes anisotropic under azimuthally inhomogeneous heat flux ($k > 0$), but approaches isotropy near the centreline. Moreover, Pr_t increases with k, particular for low-Pr fluids.

Conjugate heat transfer is then considered in the fully developed state, for both laminar and turbulent flow. With azimuthally uniform heat flux, the (mean) temperature depends mainly the ratio of thermal conductivities of solid and fluid, λ_{sf}, while the level of temperature fluctuations $\langle \vartheta' \vartheta' \rangle$ is primarily influenced by the ratio of effusivities K. An analysis of the streamwise temperature spectrum shows that, with increasing wall distance, all but the largest temperature scales become insensitive to the solid's properties. The stronger dependence of $\langle \vartheta' \vartheta' \rangle$ on K at low Pr is explained by the lack of small-scale thermal structures in such fluids. For non-uniform heat flux, a thick, well-conducting solid leads produces a flatter azimuthal distribution of the (mean) temperature as the distance from the outer wall increases; this effect is particularly strong for high k and low Pr. At low Pr, the turbulent heat flux and Pr_t are also more strongly affected by the solid's properties. As in the azimuthally uniform case, temperature fluctuations in the solid increase with K, but now λ_{sf} also plays a major role in determining the fluctuation level.

In the thermal inlet regime, the development length of various quantities, and the notion of the fully developed state, are examined as well. In general, Nu_l converges faster than the (mean) temperature $\langle T \rangle$ (or T for laminar flow). Using convergence of the global Nu alone as criterion for the fully developed state is shown to be misleading when non-uniform heating is present, or higher order statistics, such as temperature fluctuations, are of interest. In laminar flow, the dependence of the development length of various quantities on Re_b and Pr is simple: for $\mathrm{Pe} \gg 1$, it is linear in Pe. For turbulent flow, a reduced-order model based on the gradient-diffusion hypothesis and DNS velocity profiles reveals a more complex behaviour. At fixed Pr, the development length becomes nearly constant for sufficiently high Re_b, but this value is approached from above for high Pr and from below for low Pr, with low Pr fluids featuring much longer development lengths.

Temperature variance, as a nonlinear statistic, do not admit a straightforward spectral treatment in terms of azimuthal modes of the boundary condition. Nevertheless, the modal results enable a simple model for the variance in terms of $f(\varphi)^2$ and $f'(\varphi)^2$. The model correctly predicts the shape and magnitude of the fluctuation field and quantitatively explains the order-of-magnitude increase in fluctuation level for half-sinusoidal heating compared with uniform heat flux. The analysis of the developing flow further shows that, especially in configurations with an adiabatic side, temperature fluctuation statistics require significantly longer development lengths than first-order quantities. For the higher Reynolds number case, $\mathrm{Re}_b = 19000$, the development length of the temperature fluctuations on the adiabatic side by far exceeds the computational domain ($L_z = 77.5D$).

In summary, this chapter presents practical results for the design of systems featuring pipe flow subject to non-uniform heat flux. The demonstrated independence of the global Nusselt number Nu from the azimuthal heat flux distribution allows standard heat transfer correlations to be used also in non-uniform cases, while representing first-order temperature statistics as linear combination of azimuthal modes reduces the effective parameter space considerably. The chapter also identifies under which conditions, and for which statistics of interest, conjugate heat transfer must be accounted for, and shows how non-uniform heating modifies the development region and thus the heat-transfer behaviour without assuming thermally fully developed conditions.

5

Conclusion and outlook

This thesis investigates several types of spatially inhomogeneous boundary conditions and their impact on momentum and heat transfer. Novel analytical results are combined with well-resolved numerical simulations for two configurations: spanwise-alternating surface roughness in turbulent channel flow and azimuthally non-uniform heat flux in pipe flow. In both cases, the development from an initially homogeneous base flow to the inhomogeneous state is considered. Detailed conclusions for each configuration are given at the end of the respective chapters; only the main overarching findings are summarised here.

On the analytical side, the work focuses on a priori predictions of global drag (C_f) and global heat transfer (Nu). For channel flow, the wide-strip limit for skin friction is derived and validated for various surface configurations (ridge-type and strip-type roughness, laminar and turbulent). For heat transfer of a passive temperature variable, it is shown that the global Nusselt number Nu depends only on the azimuthal mean of the heat flux and not on its distribution around the circumference. This Nu-independence holds for any Re and Pr, and extends to both the thermal entrance region and conjugate heat transfer. The derivation is naturally formulated in Fourier space, which allows any first-order temperature statistic to be expressed as a linear combination of wavenumber modes weighted by the Fourier coefficients of the boundary condition. The Nu-independence then follows as a corollary. This analysis substantially reduces the parameter space of the subsequent DNS study. In addition, an analytical solution of the laminar Graetz problem for non-uniform heat flux is derived.

Well-resolved numerical data are generated for both configurations using high-order spatial discretisation (compact finite differences for channel flow, spectral elements for pipe flow). For spanwise-varying surface roughness, a piecewise-constant spanwise slip length is used and validated as a roughness model. This model correctly reproduces the topology of the mean flow observed in experiments, including the turbulent secondary motions, for various relative strip widths s/δ. It can be interpreted as the limiting case of infinite scale separation between outer flow scales and individual roughness elements, and preserves the laminar behaviour (i.e. laminar flow is unaffected by the roughness model). These properties make it an ideal tool to study the adaptation of the flow to spanwise heterogeneity when coming from a spanwise-uniform base flow. The control parameter in these simulations is the strip width s/δ.

For turbulent pipe flow with azimuthally non-uniform heat flux, the numerical setup is a standard, well-resolved LES, with two notable features: inclusion of unsteady heat conduction in the solid (conjugate heat transfer), and simulation of the thermal entrance region (turbulent Graetz problem). Data are generated at two bulk Reynolds numbers ($\mathrm{Re}_b \in \{5300, 19000\}$) and two Prandtl numbers ($\mathrm{Pr} \in \{0.025, 0.71\}$).

In fully developed flow over spanwise-heterogeneous surfaces, the DNS data confirms the predictions of the wide-strip-limit approach. For finite strip widths, turbulent secondary motions are observed, along with a spanwise redistribution of streamwise momentum. For roughness strips with $s \ll \delta$, both the secondary flow and the z-dependence of the mean streamwise momentum are confined to a region close to the wall.

In the case of heat transfer in turbulent pipe flow, the influence of high-wavenumber modes (corresponding to small azimuthal spacing between heating peaks) in the imposed heat flux is confined to near-wall regions (an analogous behaviour to that found for streamwise-aligned roughness strips). The usual CHT non-dimensionalisation using the ratio of conductivities λ_{sf} and the ratio of effusivities K is found to generalise well to non-uniform heat flux conditions, in the sense that the mean temperature distribution in a cross-section is only weakly affected by K. A decomposition of the local Nusselt number, separating azimuthal conduction from azimuthal turbulent transport, shows that the dominant heat transfer mechanisms differ between air ($\mathrm{Pr} = 0.71$) and liquid metals ($\mathrm{Pr} = 0.025$). Extending this analysis to higher Re_b would be a natural next step.

For developing flow over spanwise-heterogeneous surfaces, the simulations show a clear sequence in the adjustment process. After the onset of the structured surface, the near-wall turbulence over the rough patch adapts first. This is followed by the establishment of counter-rotating secondary vortices, which slowly increase in intensity and redistribute the streamwise momentum along the spanwise direction. A statistical analysis of filtered vorticity reveals that extreme events of large-scale vorticity do not become more frequent in the presence of secondary flow. This supports an interpretation of secondary motions as a statistical footprint of a preferential attachment of existing large-scale structures (Kawahara et al. 2012) rather than as energy-consuming generators of new ones. This analysis would benefit from additional numerical data for a configuration in which the fully developed homogeneous and spanwise-inhomogeneous share the same global flow rate and pressure gradient (the latter of which is constant in the spanwise direction by construction in fully developed flow). In such a case, their spanwise-averaged inner scaling would be identical. One way to realise such a configuration is to place spanwise-alternating roughness strips downstream of a homogeneous rough section with a smaller roughness function ΔU^+. No evidence is found for a significant impact of secondary motions on global drag.

It is also observed that the streamwise development length required for mean-flow statistics to reach their fully developed state increased with increasing s/δ, i.e. with the characteristic spanwise wavelength of the surface heterogeneity.

An analogous picture emerges for passive-scalar transfer in developing turbulent pipe flow. Low-wavenumber modes of the mean temperature (corresponding to large azimuthal spacing between heating peaks) exhibit longer development lengths than high-wavenumber modes, and (for $k = 1$) even longer than in the uniform heat flux case. The pointwise mean temperature requires a longer development region than Nu_l or the global Nu; which mirrors the behaviour on the momentum side, where C_f reaches its fully developed value earlier than the full mean velocity field in the case of spanwise non-uniform roughness.

The observed development length of Nu as a function of Re, Pr and k are, in general, consistent with the simplified analysis of Notter and Sleicher (1972). A similar analysis based on a heat-flux model, together with DNS data for the velocity field and eddy diffusivity, is carried out for the $k = 1$ and $k = 2$ heating modes. From well-resolved data, temperature fluctuations $\langle T'T' \rangle$ are found to have significantly longer development lengths than first-order temperature statistics, particularly for half-sided heating.

The decomposition of the local Nusselt number is extended to axially developing pipe flow as well. A logical next step is to move from passive-scalar transport to active scalars, i.e. to include buoyancy or temperature-dependent fluid properties, and to study how these additional couplings modify not only turbulent heat transport, but also turbulent *momentum* transport when subject to azimuthally non-uniform heating.

Bibliography

W. Anderson, J. M. Barros, K. T. Christensen, and A. Awasthi (2015). "Numerical and Experimental Study of Mechanisms Responsible for Turbulent Secondary Flows in Boundary Layer Flows over Spanwise Heterogeneous Roughness". In: *Journal of Fluid Mechanics* 768, pp. 316–347.

A. Andreolli, N. Hutchins, B. Frohnapfel, and D. Gatti (2025). "Temporal Decay of Secondary Motions in Turbulent Channel Flows". In: *Journal of Fluid Mechanics* 1007, A19.

J. Andreopoulos and D. H. Wood (1982). "The Response of a Turbulent Boundary Layer to a Short Length of Surface Roughness". In: *Journal of Fluid Mechanics* 118, pp. 143–164.

A. Antoranz, O. Flores, and M. García-Villalba (2025). "Turbulent Heat Transfer and Secondary Flows in a Non-Uniformly Heated Pipe with Temperature-Dependent Fluid Properties". In: *International Journal of Heat and Fluid Flow* 115, p. 109791.

A. Antoranz Perales (2017). "A Numerical Study of Turbulent Heat Transfer in Pipes". PhD thesis. Universidad Carlos III de Madrid.

R. Aris (1989). *Vectors, Tensors, and the Basic Equations of Fluid Mechanics*. 2nd ed. Dover Books on Mathematics. Dover Publications.

A. Barletta and S. Lazzari (2007). "Combined Forced and Free Flow in a Vertical Circular Duct Subjected to Non-Axisymmetric Wall Heating Conditions". In: *International Journal of Heat and Mass Transfer* 50.25–26, pp. 4927–4936.

A. Barletta, S. Lazzari, and E. Zanchini (2003). "Non-Axisymmetric Forced and Free Flow in a Vertical Circular Duct". In: *International Journal of Heat and Mass Transfer* 46.23, pp. 4499–4512.

P. Bartholomew, G. Deskos, R. A. S. Frantz, F. N. Schuch, E. Lamballais, and S. Laizet (2020). "Xcompact3D: An Open-Source Framework for Solving Turbulence Problems on a Cartesian Mesh". In: *SoftwareX* 12, p. 100550.

G. K. Batchelor (2010). *An Introduction to Fluid Dynamics*. 14th ed. Cambridge Mathematical Library. Cambridge University Press.

D. W. Bechert and M. Bartenwerfer (1989). “The Viscous Flow on Surfaces with Longitudinal Ribs”. In: *Journal of Fluid Mechanics* 206, pp. 105–129.

T. L. Bergman and F. P. Incropera, eds. (2011). *Fundamentals of Heat and Mass Transfer*. 7th ed. Wiley.

R. B. Bird, W. E. Stewart, and E. N. Lightfoot (2007). *Transport Phenomena*. Revised second edition. John Wiley & Sons, Inc.

A. W. Black and E. M. Sparrow (1967). “Experiments on Turbulent Heat Transfer in a Tube With Circumferentially Varying Thermal Boundary Conditions”. In: *Journal of Heat Transfer* 89.3, pp. 258–268.

K. Bürger, M. Treib, R. Westermann, S. Werner, C. C. Lalescu, A. Szalay, C. Meneveau, and G. L. Eyink (2023). *Vortices within Vortices: Hierarchical Nature of Vortex Tubes in Turbulence*. Pre-published.

A. Busse and N. D. Sandham (2012). “Influence of an Anisotropic Slip-Length Boundary Condition on Turbulent Channel Flow”. In: *Physics of Fluids* 24.5, p. 055111.

A. Carravetta and R. Della Morte (2004). “Response of Velocity to a Sudden Change of Bed Roughness in Sub Critical Open Channel Flow”. In: *Proceedings of the Second International Conference on Fluvial Hydraulics*. Second International Conference on Fluvial Hydraulics (Napoli). Vol. 1. A.A. Balkema Publishers, pp. 389–394.

X. Chen and Y.-M. Chiew (2003). “Response of Velocity and Turbulence to Sudden Change of Bed Roughness in Open-Channel Flow”. In: *Journal of Hydraulic Engineering* 129.1, pp. 35–43.

D. Chung, J. P. Monty, and N. Hutchins (2018). “Similarity and Structure of Wall Turbulence with Lateral Wall Shear Stress Variations”. In: *Journal of Fluid Mechanics* 847, pp. 591–613.

D. Chung, N. Hutchins, M. P. Schultz, and K. A. Flack (2021). “Predicting the Drag of Rough Surfaces”. In: *Annual Review of Fluid Mechanics* 53.1, pp. 439–471.

M. Colombini and G. Parker (1995). “Longitudinal Streaks”. In: *Journal of Fluid Mechanics* 304, pp. 161–183.

W. Couzy (1995). “Spectral Element Discretization of the Unsteady Navier-Stokes Equations and Its Iterative Solution on Parallel Computers”. PhD thesis. Lausanne, EPFL.

A. Dachwitz, C. Bauer, and C. Wagner (2022). “Direct Numerical Simulation of Turbulent Pipe Flow Subjected to Sinusoidally Varying Periodic Wall Heating”. In: Turbulence and Interactions.

R. B. Dean (1978). “Reynolds Number Dependence of Skin Friction and Other Bulk Flow Variables in Two-Dimensional Rectangular Duct Flow”. In: *Journal of Fluids Engineering* 100.2, pp. 215–223.

M. O. Deville, P. F. Fischer, and E. H. Mund (2002). *High-Order Methods for Incompressible Fluid Flow*. 1st ed. Cambridge University Press.

J. Doherty, P. Ngan, J. Monty, and M. Chong (2007). "The Development of Turbulent Pipe Flow". In: Australasian Fluid Mechanics Conference.

G. K. El Khoury, P. Schlatter, A. Noorani, P. F. Fischer, G. Brethouwer, and A. V. Johansson (2013). "Direct Numerical Simulation of Turbulent Pipe Flow at Moderately High Reynolds Numbers". In: *Flow, Turbulence and Combustion* 91.3, pp. 475–495.

W. P. Elliott (1958). "The Growth of the Atmospheric Internal Boundary Layer". In: *Transactions, American Geophysical Union* 39.6, pp. 1048–1054.

L. Elmlinger, T. Laube, B. Dietrich, and T. Wetzel (2026). "Experimental Investigation of Mixed Convection in a Horizontal Tube for a Liquid Metal Flow". In: *International Journal of Heat and Mass Transfer* 260, p. 128495.

P. Fischer, S. Kerkemeier, M. Min, Y.-H. Lan, M. Phillips, T. Rathnayake, E. Merzari, A. Tomboulides, A. Karakus, N. Chalmers, and T. Warburton (2022). "NekRS, a GPU-accelerated Spectral Element Navier–Stokes Solver". In: *Parallel Computing* 114, p. 102982.

C. Flageul (2016). "Création de bases de données fines par simulation directe pour les effets de la turbulence sur les transferts thermiques pariétaux". PhD thesis. Université de Poitiers.

C. Flageul, S. Benhamadouche, É. Lamballais, and D. Laurence (2015). "DNS of Turbulent Channel Flow with Conjugate Heat Transfer: Effect of Thermal Boundary Conditions on the Second Moments and Budgets". In: *International Journal of Heat and Fluid Flow* 55, pp. 34–44.

B. Frohnapfel, L. Von Deyn, J. Yang, J. Neuhauser, A. Stroh, R. Örlü, and D. Gatti (2024). "Flow Resistance over Heterogeneous Roughness Made of Spanwise-Alternating Sandpaper Strips". In: *Journal of Fluid Mechanics* 980, A31.

K. Fukagata, K. Iwamoto, and N. Kasagi (2002). "Contribution of Reynolds Stress Distribution to the Skin Friction in Wall-Bounded Flows". In: *Physics of Fluids* 14.11, pp. L73–L76.

K. Fukagata, N. Kasagi, and P. Koumoutsakos (2006). "A Theoretical Prediction of Friction Drag Reduction in Turbulent Flow by Superhydrophobic Surfaces". In: *Physics of Fluids* 18.5, p. 051703.

J. R. Garratt (1990). "The Internal Boundary Layer – A Review". In: *Boundary-Layer Meteorology* 50.1–4, pp. 171–203.

D. Gatti, A. Güttler, B. Frohnapfel, and C. Tropea (2015). "Experimental Assessment of Spanwise-Oscillating Dielectric Electroactive Surfaces for Turbulent Drag Reduction in an Air Channel Flow". In: *Experiments in Fluids* 56.5, p. 110.

D. Gatti and M. Quadrio (2016). “Reynolds-Number Dependence of Turbulent Skin-Friction Drag Reduction Induced by Spanwise Forcing”. In: *Journal of Fluid Mechanics* 802, pp. 553–582.

R. Ghorbani and O. R. Zadeh (2020). “Lessons Learned on 20 Years of Challenges to Internal Corrosion Protection of Subsea Pipelines-Corrosion Inhibitor or pH Stabilization?” In: *Pipeline Technology Journal*. Pipeline Technology Conference. Vol. 3.

G. Gómez-de-Segura and R. García-Mayoral (2020). “Imposing Virtual Origins on the Velocity Components in Direct Numerical Simulations”. In: *International Journal of Heat and Fluid Flow* 86, p. 108675.

L. Graetz (1882). “Über die Wärmeleitungsfähigkeit von Flüssigkeiten, Erste Abhandlung”. In: *Annalen der Physik* 254.1, pp. 79–94.

J. O. Hinze (1967). “Secondary Currents in Wall Turbulence”. In: *Physics of Fluids* 10, pp. 122–125.

N. Hutchins, B. Ganapathisubramani, M. Schultz, and D. Pullin (2023). “Defining an Equivalent Homogeneous Roughness Length for Turbulent Boundary Layers Developing over Patchy or Heterogeneous Surfaces”. In: *Ocean Engineering* 271, p. 113454.

H. G. Hwang and J. H. Lee (2018). “Secondary Flows in Turbulent Boundary Layers over Longitudinal Surface Roughness”. In: *Physical Review Fluids* 3.1, p. 014608.

U. Ismail, T. A. Zaki, and P. A. Durbin (2018). “Simulations of Rib-Roughened Rough-to-Smooth Turbulent Channel Flows”. In: *Journal of Fluid Mechanics* 843, pp. 419–449.

I. Jacobi and B. J. McKeon (2011). “New Perspectives on the Impulsive Roughness-Perturbation of a Turbulent Boundary Layer”. In: *Journal of Fluid Mechanics* 677, pp. 179–203.

N. Kasagi, Y. Tomita, and A. Kuroda (1992). “Direct Numerical Simulation of Passive Scalar Field in a Turbulent Channel Flow”. In: *Journal of Heat Transfer* 114.3, pp. 598–606.

Y. Katznelson (2004). *An Introduction to Harmonic Analysis*. 3rd ed. Cambridge Mathematical Library. Cambridge University Press.

G. Kawahara, M. Uhlmann, and L. Van Veen (2012). “The Significance of Simple Invariant Solutions in Turbulent Flows”. In: *Annual Review of Fluid Mechanics* 44.1, pp. 203–225.

W. M. Kays (1994). “Turbulent Prandtl Number—Where Are We?” In: *Journal of Heat Transfer* 116.2, pp. 284–295.

S. Laizet and E. Lamballais (2009). “High-Order Compact Schemes for Incompressible Flows: A Simple and Efficient Method with Quasi-Spectral Accuracy”. In: *Journal of Computational Physics* 228.16, pp. 5989–6015.

S. Laizet and N. Li (2011). "Incompact3d: A Powerful Tool to Tackle Turbulence Problems with up to O(105) Computational Cores". In: *International Journal for Numerical Methods in Fluids* 67.11, pp. 1735–1757.

E. Lamballais, V. Fortuné, and S. Laizet (2011). "Straightforward High-Order Numerical Dissipation via the Viscous Term for Direct and Large Eddy Simulation". In: *Journal of Computational Physics* 230.9, pp. 3270–3275.

T. Laube, B. Dietrich, L. Marocco, and T. Wetzel (2022). "Turbulent Heat Transfer in a Liquid Metal Tube Flow with Azimuthally Inhomogeneous Heat Flux". In: *International Journal of Heat and Mass Transfer* 189, p. 122734.

– (2023). *Heat Transfer and Pressure Drop Data of a Turbulent Tube Flow of Water and GaInSn with Azimuthally Inhomogeneous Heat Flux*. KITopen.

S. Lee, J. Yang, P. Forooghi, A. Stroh, and S. Bagheri (2022). "Predicting Drag on Rough Surfaces by Transfer Learning of Empirical Correlations". In: *Journal of Fluid Mechanics* 933, A18.

S.-H. Lee and H. J. Sung (2007). "Direct Numerical Simulation of the Turbulent Boundary Layer over a Rod-Roughened Wall". In: *Journal of Fluid Mechanics* 584, pp. 125–146.

S. K. Lele (1992). "Compact Finite Difference Schemes with Spectral-like Resolution". In: *Journal of Computational Physics* 103.1, pp. 16–42.

A. Lozano-Durán and J. Jiménez (2014). "Effect of the Computational Domain on Direct Simulations of Turbulent Channels up to $\mathrm{Re}_\tau = 4200$". In: *Physics of Fluids* 26.1, p. 011702.

P. Luchini (2013). "Linearized No-Slip Boundary Conditions at a Rough Surface". In: *Journal of Fluid Mechanics* 737, pp. 349–367.

P. Luchini, F. Manzo, and A. Pozzi (1991). "Resistance of a Grooved Surface to Parallel Flow and Cross-Flow". In: *Journal of Fluid Mechanics Digital Archive* 228, p. 87.

S. Manservisi and F. Menghini (2014). "A CFD Four Parameter Heat Transfer Turbulence Model for Engineering Applications in Heavy Liquid Metals". In: *International Journal of Heat and Mass Transfer* 69, pp. 312–326.

T. Mantel and R. Borghi (1994). "A New Model of Premixed Wrinkled Flame Propagation Based on a Scalar Dissipation Equation". In: *Combustion and Flame* 96.4, pp. 443–457.

L. Marocco, G. Cammi, J. Flesch, and T. Wetzel (2016). "Numerical Analysis of a Solar Tower Receiver Tube Operated with Liquid Metals". In: *International Journal of Thermal Sciences* 105, pp. 22–35.

T. Min and J. Kim (2004). "Effects of Hydrophobic Surface on Skin-Friction Drag". In: *Physics of Fluids* 16.7, pp. L55–L58.

D. Modesti and S. Pirozzoli (2022). "Direct Numerical Simulation of Forced Thermal Convection in Square Ducts up To". In: *Journal of Fluid Mechanics* 941, A16.

D. Modesti, S. Pirozzoli, P. Orlandi, and F. Grasso (2018). "On the Role of Secondary Motions in Turbulent Square Duct Flow". In: *Journal of Fluid Mechanics* 847, R1.

Y. Nagano and M. Shimada (1996). "Development of a Two-Equation Heat Transfer Model Based on Direct Simulations of Turbulent Flows with Different Prandtl Numbers". In: *Physics of Fluids* 8.12, pp. 3379–3402.

R. Narasimha and K. Sreenivasan (1979). "Relaminarization of Fluid Flows". In: *Advances in Applied Mechanics*. Vol. 19. Elsevier, pp. 221–309.

C. L. M. H. Navier (1823). "Mémoire sur les lois du mouvement des fluides". In: *Mémoires de l'Académie Royale des Sciences de l'Institut de France* 6.1823, pp. 389–440.

J. Neuhauser (2025). *Analytical Solutions of the Laminar (Extended) Graetz Problem*. GitHub repository. GitHub. URL: https://github.com/joneuhauser/graetz (visited on 05/05/2026).

– (2026a). *Dataset: Conjugate Heat Transfer in Turbulent Pipe Flows with Non-Uniform Heating Effects at Two Prandtl Numbers*. Karlsruhe Institute of Technology.

– (2026b). *Dataset: Developing Turbulent Secondary Flow over Streamwise-Aligned Roughness Strips*. Karlsruhe Institute of Technology.

– (2026c). *Dataset: Simulation of the Turbulent Graetz Problem with Neumann Boundary Conditions at Two Reynolds and Prandtl Numbers*. Karlsruhe Institute of Technology.

J. Neuhauser, K. Schäfer, D. Gatti, and B. Frohnapfel (2022a). *Dataset: Simulation of Turbulent Flow over Roughness Strips*. KITopen.

I. Nezu and H. Nakagawa (1991). "Response of Velocity and Shear Stress to Abrupt Irregularity of Bed Roughness in Streams". In: *Proceedings of the 24th IAHR World Congress*. IAHR World Congress (Madrid). Vol. 24.

V. I. Nikora, T. Stoesser, S. M. Cameron, M. Stewart, K. Papadopoulos, P. Ouro, R. McSherry, A. Zampiron, I. Marusic, and R. A. Falconer (2019). "Friction Factor Decomposition for Rough-Wall Flows: Theoretical Background and Application to Open-Channel Flows". In: *Journal of Fluid Mechanics* 872, pp. 626–664.

R. H. Notter and C. A. Sleicher (1972). "A Solution to the Turbulent Graetz Problem—III Fully Developed and Entry Region Heat Transfer Rates". In: *Chemical Engineering Science* 27.11, pp. 2073–2093.

P. Orlandi, ed. (2000). *Fluid Flow Phenomena*. Red. by R. Moreau. Vol. 55. Fluid Mechanics and Its Applications. Springer Netherlands.

E. Papoutsakis, D. Ramkrishna, and H. C. Lim (1980). "The Extended Graetz Problem with Prescribed Wall Flux". In: *AIChE Journal* 26.5, pp. 779–787.

A. T. Patera (1984). "A Spectral Element Method for Fluid Dynamics: Laminar Flow in a Channel Expansion". In: *Journal of Computational Physics* 54.3, pp. 468–488.

M. Piller (2005). "Direct Numerical Simulation of Turbulent Forced Convection in a Pipe". In: *International Journal for Numerical Methods in Fluids* 49.6, pp. 583–602.

A. Pinelli, M. Uhlmann, A. Sekimoto, and G. Kawahara (2010). "Reynolds Number Dependence of Mean Flow Structure in Square Duct Turbulence". In: *Journal of Fluid Mechanics* 644, pp. 107–122.

S. Pirozzoli (2018). "On Turbulent Friction in Straight Ducts with Complex Cross-Section: The Wall Law and the Hydraulic Diameter". In: *Journal of Fluid Mechanics* 846, R1.

– (2024). "On the Streamwise Velocity Variance in the Near-Wall Region of Turbulent Flows". In: *Journal of Fluid Mechanics* 989, A5.

S. Pirozzoli, J. Romero, M. Fatica, R. Verzicco, and P. Orlandi (2021). "One-Point Statistics for Turbulent Pipe Flow up to $Re_\tau \approx 6000$". In: *Journal of Fluid Mechanics* 926, A28.

S. B. Pope (2000). *Turbulent Flows*. Cambridge University Press.

V. Rathore, N. Penna, S. Dey, and R. Gaudio (2022). "Response of Open-Channel Flow to a Sudden Change from Smooth to Rough Bed". In: *Environmental Fluid Mechanics* 22.1, pp. 87–112.

W. Reynolds (1963a). "Turbulent Heat Transfer in a Circular Tube with Variable Circumferential Heat Flux". In: *International Journal of Heat and Mass Transfer* 6.6, pp. 445–454.

– (1963b). "Effect of Wall Heat Conduction on Convection in a Circular Tube with Arbitrary Circumferential Heat Input". In: *International Journal of Heat and Mass Transfer* 6.10, p. 925.

A. Rouhi, D. Chung, and N. Hutchins (2019). "Direct Numerical Simulation of Open-Channel Flow over Smooth-to-Rough and Rough-to-Smooth Step Changes". In: *Journal of Fluid Mechanics* 866, pp. 450–486.

F. Rousta and B. Lessani (2022). "Numerical Study of Thermally Developing Turbulent Internal Flows". In: *International Journal of Heat and Mass Transfer* 188, p. 122623.

N. Saito and D. Pullin (2014). "Large Eddy Simulation of Smooth–Rough–Smooth Transitions in Turbulent Channel Flows". In: *International Journal of Heat and Mass Transfer* 78, pp. 707–720.

K. Schäfer, A. Stroh, P. Forooghi, and B. Frohnapfel (2022). "Modelling Spanwise Heterogeneous Roughness through a Parametric Forcing Approach". In: *Journal of Fluid Mechanics* 930, A7.

P. Schlatter, S. Stolz, and L. Kleiser (2004). "LES of Transitional Flows Using the Approximate Deconvolution Model". In: *International Journal of Heat and Fluid Flow* 25.3, pp. 549–558.

R. K. Shah and A. L. London (1978). *Laminar Flow Forced Convection in Ducts: A Source Book for Compact Heat Exchanger Analytical Data*. Advances in Heat Transfer : Supplement 1. Academic Press.

R. Siegel, E. M. Sparrow, and T. M. Hallman (1958). “Steady Laminar Heat Transfer in a Circular Tube with Prescribed Wall Heat Flux”. In: *Applied Scientific Research* 7.5, pp. 386–392.

L. J. Slater and D. Lit (1960). *Confluent Hypergeometric Functions*. Cambridge University Press.

E. M. Sparrow, T. M. Hallman, and R. Siegel (1957). “Turbulent Heat Transfer in the Thermal Entrance Region of a Pipe with Uniform Heat Flux”. In: *Applied Scientific Research* 7.1, pp. 37–52.

E. M. Sparrow and S. H. Lin (1963). “Turbulent Heat Transfer in a Tube with Circumferentially-Varying Temperature or Heat Flux”. In: *International Journal of Heat and Mass Transfer* 6.9, pp. 866–867.

P. Stephan, S. Kabelac, M. Kind, D. Mewes, K. Schaber, and T. Wetzel, eds. (2019). *VDI-Wärmeatlas*. Springer Reference Technik. Springer Berlin Heidelberg.

S. Straub (2019). *Statistics on Turbulent Forced Convection Pipe Flow with Different Thermal Boundary Conditions for Two Prandtl Numbers*. KITopen.

– (2020). “Non-Homogeneous Thermal Boundary Conditions in Low to Medium Prandtl Number Turbulent Pipe Flows”. PhD thesis. Karlsruhe.

S. Straub, P. Forooghi, L. Marocco, T. Wetzel, and B. Frohnapfel (2019a). “Azimuthally Inhomogeneous Thermal Boundary Conditions in Turbulent Forced Convection Pipe Flow for Low to Medium Prandtl Numbers”. In: *International Journal of Heat and Fluid Flow* 77, pp. 352–358.

S. Straub, P. Forooghi, L. Marocco, T. Wetzel, R. Vinuesa, P. Schlatter, and B. Frohnapfel (2019b). “The Influence of Thermal Boundary Conditions on Turbulent Forced Convection Pipe Flow at Two Prandtl Numbers”. In: *International Journal of Heat and Mass Transfer* 144, p. 118601.

A. Stroh, K. Schäfer, P. Forooghi, and B. Frohnapfel (2020a). “Secondary Flow and Heat Transfer in Turbulent Flow over Streamwise Ridges”. In: *International Journal of Heat and Fluid Flow* 81, p. 108518.

A. Stroh, K. Schäfer, B. Frohnapfel, and P. Forooghi (2020b). “Rearrangement of Secondary Flow over Spanwise Heterogeneous Roughness”. In: *Journal of Fluid Mechanics* 885, R5.

F. X. Studerus (1982). “Sekundärströmungen im offenen Gerinne über rauhen Längsstreifen”. PhD thesis. ETH Zurich.

I. Tiselj (2014). “Tracking of Large-Scale Structures in Turbulent Channel with Direct Numerical Simulation of Low Prandtl Number Passive Scalar”. In: *Physics of Fluids* 26.12, p. 125111.

I. Tiselj, R. Bergant, B. Mavko, I. Bajsić, and G. Hetsroni (2001). “DNS of Turbulent Heat Transfer in Channel Flow With Heat Conduction in the Solid Wall”. In: *Journal of Heat Transfer* 123.5, pp. 849–857.

S. Toosi, J. Larsson, and P. Schlatter (2024). “Assessment of the Accuracy and Robustness of Different Numerical Methods in Wall-Bounded Flows”. In: 9th European Congress on Computational Methods in Applied Sciences and Engineering.

A. A. Townsend (1976). *The Structure of Turbulent Shear Flow*. 2nd ed. Cambridge University Press.

S. Türk, G. Daschiel, A. Stroh, Y. Hasegawa, and B. Frohnapfel (2014). “Turbulent Flow over Superhydrophobic Surfaces with Streamwise Grooves”. In: *Journal of Fluid Mechanics* 747, pp. 186–217.

T. Van Buren, D. Floryan, L. Ding, L. H. O. Hellström, and A. J. Smits (2020). “Turbulent Pipe Flow Response to a Step Change in Surface Roughness”. In: *Journal of Fluid Mechanics* 904, A38.

C. Vanderwel, A. Stroh, J. Kriegseis, B. Frohnapfel, and B. Ganapathisubramani (2019). “The Instantaneous Structure of Secondary Flows in Turbulent Boundary Layers”. In: *Journal of Fluid Mechanics* 862, pp. 845–870.

C. Vanderwel and B. Ganapathisubramani (2015). “Effects of Spanwise Spacing on Large-Scale Secondary Flows in Rough-Wall Turbulent Boundary Layers”. In: *Journal of Fluid Mechanics* 774, R2.

D. A. Vermaas, W. S. J. Uijttewaal, and A. J. F. Hoitink (2011). “Lateral Transfer of Streamwise Momentum Caused by a Roughness Transition across a Shallow Channel”. In: *Water Resources Research* 47.2, W02530.

R. Vicente Cruz, C. Flageul, É. Lamballais, J. C. Uribe, V. Duffal, E. Le Coupanec, and S. Benhamadouche (2025). “High-Fidelity Simulation of Developing Mixed Convection in a Bouyancy-Aided Vertical Pipe Flow”. In: Turbulence, Heat and Mass Transfer.

R. Vicente Cruz and E. Lamballais (2023). “A Versatile Immersed Boundary Method for High-Fidelity Simulation of Conjugate Heat Transfer”. In: *Journal of Computational Physics* 488, p. 112182.

L. H. Von Deyn, D. Gatti, and B. Frohnapfel (2022). “From Drag-Reducing Riblets to Drag-Increasing Ridges”. In: *Journal of Fluid Mechanics* 951, A16.

Z.-Q. Wang and N.-S. Cheng (2006). “Time-Mean Structure of Secondary Flows in Open Channel with Longitudinal Bedforms”. In: *Advances in Water Resources* 29.11, pp. 1634–1649.

D. D. Wangsawijaya, R. Baidya, D. Chung, I. Marusic, and N. Hutchins (2020). “The Effect of Spanwise Wavelength of Surface Heterogeneity on Turbulent Secondary Flows”. In: *Journal of Fluid Mechanics* 894, A7.

J. Yang, A. Stroh, S. Lee, S. Bagheri, B. Frohnapfel, and P. Forooghi (2023). “Prediction of Equivalent Sand-Grain Size and Identification of Drag-Relevant Scales of Roughness – a Data-Driven Approach”. In: *Journal of Fluid Mechanics* 975, A34.

X. Yang, X. Yang, J. Ding, Y. Shao, and H. Fan (2012). “Numerical Simulation Study on the Heat Transfer Characteristics of the Tube Receiver of the Solar Thermal Power Tower”. In: *Applied Energy* 90.1, pp. 142–147.

J. Yao, S. Rezaeiravesh, P. Schlatter, and F. Hussain (2023). “Direct Numerical Simulations of Turbulent Pipe Flow up to $\mathrm{Re}_\tau \approx 5200$”. In: *Journal of Fluid Mechanics* 956, A18.

Co-supervised student theses

[Wur23] D. Wurche (2023). “Heat Transfer in Liquid Metal Flows: Numerical Investigation and Validation”. Master’s thesis. Karlsruhe Institute of Technology.

[Kip24] M. Kippenberger (2024). “Azimuthally Inhomogenous Roughness in Turbulent Pipe Flows”. Master’s thesis. Karlsruhe Institute of Technology.

[Sch24] J. Schmitt (2024). “Heat Transfer in Liquid Metal Flows: Numerical Investigation of Thermal Turbulence Models using OpenFOAM”. Master’s thesis. Karlsruhe Institute of Technology.

[Bür25] L. Bürk (2025). “Heat Transfer in Turbulent Liquid Metal Flows: Investigation of the Thermal Entrance”. Master’s thesis. Karlsruhe Institute of Technology.

[Ded25] C. E. Dederichs (2025). “Convection Velocities of Passive Scalar and Velocity Fluctuations in Wall-Bounded Turbulence”. Master’s thesis. Karlsruhe Institute of Technology.

[Lan25] N. Langer (2025). “Numerical Simulation of Secondary Currents in Arterial Flows with Stents”. Master’s thesis. Karlsruhe Institute of Technology.

List of Figures

List of Tables

Nomenclature

Acronyms

BDF	Backward Difference Formula (SEM)
CHT	Conjugate Heat Transfer
CFR	Constant Flow Rate
CPG	Constant Pressure Gradient
DNS	Direct Numerical Simulation
EXT	Extrapolation scheme (SEM)
FEM	Finite Element Method
FIK	Fukagata-Iwamoto-Kasagi (identity, decomposition)
GLL	Gauss-Lobatto-Legendre
HMP	High-momentum pathway
IBL	Internal Boundary Layer
IF	Isoflux (prescribed heat flux)
LES	Large Eddy Simulation
LMP	Low-momentum pathway
MBC	Mixed Boundary Condition
PDF	Probability Density Function
PFA	Parametric Forcing Approach
RANS	Reynolds-averaged Navier-Stokes
SEM	Spectral Element Method
TKE	Turbulent Kinetic Energy

Greek symbols and variables

α	Thermal diffusivity ($\lambda/(\rho c_p)$)
$\alpha_{t,\varphi}; \alpha_{t,r}$	Azimuthal and radial turbulent thermal diffusivities
α_{tot}	Total thermal diffusivity ($1 + \alpha_t$)

β	Geometric scaling factor for reference radius (non-dimensionalisation parameter)
δ	Channel half-height
δ_i	Height of the internal boundary layer
δ_v	Viscous length scale (ν/u_τ)
ϵ_k	Dissipation of turbulent kinetic energy
η	Hydraulic channel height ratio (h_{hyd}/h); also transformed radial coordinate (non-uniform Graetz problem)
Γ	Radius ratio (R_o/R_i)
γ	Exponent for temperature reference scaling
κ	Scaled wavenumber ($k\Delta x$)
κ_s''	Modified wavenumber of the second derivative
λ	Thermal conductivity
λ_{sf}	Ratio of thermal conductivities (λ_s/λ_f)
μ	Dynamic viscosity
ν	Kinematic viscosity
ρ	Density
σ	Standard deviation
$\boldsymbol{\sigma}$	Stress tensor
$\boldsymbol{\tau}$	Deviatoric component of the stress tensor
τ_w	Wall shear stress
ϕ	Passive scalar (e.g., temperature)
ϕ_{kj}	Orthonormal eigenfunctions of $\mathcal{L}_k$ (non-uniform Graetz problem)
φ	Azimuthal coordinate
ψ	Angle of rotation
ω_x	Streamwise vorticity
$\tilde{\omega}_x$	Filtered streamwise vorticity
Π	Mean streamwise pressure gradient ($-\partial\langle p\rangle/\partial x$)
θ_i^*	General dimensionless temperature for the fully developed solution
θ_i	Dimensionless temperature for the fully developed solution (non-dimensionalisation of the non-uniform Graetz problem)
ϑ_i	Dimensionless temperature for the fully developed solution (non-dimensionalisation of turbulent pipe flow)
Θ_i	Dimensionless temperature for the developing solution (non-dimensionalisation of the non-uniform Graetz problem)

Latin symbols and variables

a_k, b_k, c_k	Coefficients for Runge-Kutta time stepping
A	Cross-sectional area
c_p	Heat capacity at constant pressure
C_1	Slope coefficient for bulk temperature growth
C_2	Scaling constant for fractional flow rate
C_f	Skin friction coefficient
D	Diffusivity of a general advective-diffusive scalar; also Pipe diameter in some contexts
$\mathcal{D}$	Domain
D_h	Hydraulic diameter
f	Heat flux distribution function $f(\varphi)$; also generic function
f_k	Complex Fourier coefficient of $f(\varphi)$
$\vec{f}$	Volumetric force density vector
f_j^e	Local forcing vector ofe element j (SEM)
$F[q_w]$	Functional for reference heat flux
g	Generic function in integration (derivation of the Nusselt number decomposition)
g^{ij}	Contravariant metric coefficients
h	Channel half-height (used interchangeably with δ)
h_{avg}	Average channel height
h_{empty}	Empty channel height (geometric maximum)
h_{hyd}	Hydraulic channel height
h_{lam}	Laminar flow reference height (ridges)
h_{turb}	Turbulent flow reference height (ridges)
$H(\varphi)$	Convolution kernel for temperature solution
H^2	Sobolev space of square-integrable functions with square-integrable first and second derivatives
$\boldsymbol{I}$	Identity tensor
Im	Imaginary part of complex number
I_r, I_φ, I_z	Radial, azimuthal, and axial contributions to energy equation (Nusselt number decomposition)
j	Imaginary unit
k	azimuthal wavenumber
K	Ratio of effusivities
K_{ij}^e	Local stiffness matrix (SEM)
k_s	Equivalent sand grain roughness

L_x, L_y, L_z	Domain lengths in x, y, z directions
$l_{s,u}$	Streamwise slip length
$l_{s,w}$	Spanwise slip length
L^2	Lebesgue space of square-integrable functions
$\mathcal{L}_k$	self-adjoint linear operator
M	Confluent hypergeometric function
M_{ij}^e	Local mass matrix (SEM)
N_p	Polynomial degree/order
Nu	Nusselt number
Nu_l	Local Nusselt number
p	Pressure, also probability density function
P_k	Production of turbulent kinetic energy
$P_{\vartheta'\vartheta'}$	Production of temperature variance
P_n	Legendre polynomial of order n
Pe	Péclet number ($\mathrm{Re}_b \, \mathrm{Pr}$)
Pr	Prandtl number
Pr_t	Turbulent Prandtl number
q	Heat flux, also generic quantity of interest
q_w	Wall heat flux
$R_{\dot{V}}$	Relative flow rate loss
$\Re$	Real part of complex number
R_i, R_o	Inner and outer pipe radii
Re_b	Bulk Reynolds number
Re_τ	Friction Reynolds number
r	Radial coordinate
s	Strip width (spanwise period of roughness)
t	Time
T	Temperature
T_0	Inlet temperature
T_i	Dimensionless temperature for the developing solution (non-dimensionalisation of turbulent pipe flow)
T_b	Bulk temperature
u, v, w	Velocity components in x, y, z direction (channel flow)
u_r, u_φ, u_z	Velocity components in r, φ, z direction (pipe flow)
u_b	Bulk velocity
u_τ	Friction velocity
$\overline{u_\tau}$	Global (spanwise-averaged) friction velocity
$\vec{u}$	Velocity vector, also displacement in the derivation of SEM

x, y, z	Streamwise, wall-normal, and spanwise coordinates (channel)
z	Axial coordinate (pipe)
X_q	Recovery magnitude of quantity q

Subscripts and superscripts

$(\cdot)'$	Fluctuation (Reynolds decomposition)
$(\cdot)^*$	non-dimensional variable; also intermediate velocity before pressure correction
$(\cdot)^+$	Non-dimensionalisation in viscous units
$(\cdot)_0$	Reference value (typically smooth wall or inflow)
$(\cdot)_b$	Bulk quantity
$(\cdot)_f, (\cdot)_s$	Fluid or solid phase
$(\cdot)_l$	Local quantity
$(\cdot)_{smooth}, (\cdot)_{rough}$	Quantity evaluated for smooth or rough homogeneous reference cases
$(\cdot)^e$	Quantity defined on the local element (SEM)
$(\cdot)^k$	Value at Runge-Kutta substep k
$(\cdot)''$	Second derivative
$\langle\cdot\rangle$	Statistical mean, or time mean estimate of the statistical mean
$\overline{(\cdot)}$	Spanwise or azimuthal average
$\tilde{(\cdot)}$	Filtered quantity (channel flow)
$\tilde{(\cdot)}$	Transformed temperature variable (pipe flow)
$\widehat{(\cdot)}_k$	Fourier coefficient for wavenumber k
$(\cdot)_{;j}$	Covariant derivative

A

Appendix

A.1 Transport equations in cylindrical coordinates

Starting from the conservation equations of mass, momentum and energy in general tensor form, this Appendix derives the balance equations of the heat flux vector, the temperature covariance and the dissipation of temperature covariance. These equations are then reduced to cylindrical coordinates. The sections assumes an incompressible Newtonian fluid without volume forces, constant density ρ and constant thermal conductivity λ. Viscous heating is neglected.

Standard tensor calculus in curvilinear coordinates is employed. A coordinate system (x^1, x^2, x^3) characterised by the (contravariant) metric coefficients g^{ij} is considered; the metric is torsion-free and compatible. The notation follows Aris (1989); u^j is the (contravariant) velocity vector and $a_{;j}$ denotes a covariant derivative; the summation convention applies.

Under these conditions, the Navier-Stokes equations are given by Aris (1989, eqs. (8.11.3), (8.21.10), (8.22.2)). Similarly the conservation equation of energy can be derived. The conservation equations are given by:

$$u^i_{;i} = 0 \tag{A.1a}$$

$$\rho \left(\frac{\partial u^i}{\partial t} + u^j u^i_{;j} \right) = -g^{ij} p_{;j} + \mu g^{jk} u^i_{;jk} \tag{A.1b}$$

$$\rho c_p \left(\frac{\partial T}{\partial t} + T_{;j} u^j \right) = g^{ij} \left(\lambda T_{;j} \right)_{;i} \tag{A.1c}$$

The RANS equations can be derived by applying the Reynolds decomposition to eqs. (A.1a) to (A.1c):

$$\langle u^i \rangle_{;i} = 0 \tag{A.2a}$$

$$\rho \frac{\partial \langle u^i \rangle}{\partial t} + \rho \langle u^j \rangle \langle u^i \rangle_{;j} = -g^{ij} \langle p \rangle_{;j} + \mu g^{jk} \langle u^i \rangle_{;jk} - \rho \langle u^{j\prime} u^{i\prime} \rangle_{;j} \tag{A.2b}$$

$$\rho c_p \left(\frac{\partial \langle T \rangle}{\partial t} + \langle u^j \rangle \langle T \rangle_{;j} \right) = g^{ij} \left(\lambda \langle T \rangle_{;j} \right)_{;i} - \rho c_p \langle u^{j\prime} T' \rangle_{;j} \tag{A.2c}$$

Subtracting the mean equations (eqs. (A.2a) to (A.2c)) from eqs. (A.1a) to (A.1c) yields the conservation of fluctuations:

$$u^{i\prime}_{;i} = 0 \tag{A.3a}$$

$$\rho \frac{\partial u^{i\prime}}{\partial t} + \rho u^j u^{i\prime}_{;j} = -g^{ij} p'_{;j} + \mu g^{jk} u^{i\prime}_{;jk} + \rho \langle u^{j\prime} u^{i\prime} \rangle_{;j} - \rho \langle u^i \rangle_{;j} u^{j\prime} \tag{A.3b}$$

$$\rho c_p \left(\frac{\partial T'}{\partial t} + u^j T'_{;j} \right) = g^{ij} \left(\lambda T'_{;j} \right)_{;i} + \rho c_p \langle u^{j\prime} T' \rangle_{;j} - \rho c_p \langle T \rangle_{;j} u^{j\prime} \tag{A.3c}$$

The remainder of this section will assume $\lambda = \text{const.}$ The conservation equation for the turbulent heat flux vector can then be computed as $\langle c_p T' \cdot (\text{A.3b}) + u^{i\prime} \cdot (\text{A.3c}) \rangle$ and applying the product rule:

$$\begin{aligned} \rho c_p \frac{\partial \langle u^{i\prime} T' \rangle}{\partial t} + \underbrace{\rho c_p \langle u^j \rangle \langle u^{i\prime} T' \rangle_{;j}}_{\mathrm{I}} + \underbrace{\rho c_p \langle u^{i\prime} u^{j\prime} T' \rangle_{;j}}_{\mathrm{II}} &= \underbrace{-c_p g^{ij} \langle p' T' \rangle_{;j}}_{\mathrm{III}} + \underbrace{c_p g^{ij} \langle p' T'_{;j} \rangle}_{\mathrm{IV}} \\ &\quad \underbrace{g^{jk} \left(\mu c_p \langle u^{i\prime}_{;j} T' \rangle_{;k} + \lambda \langle u^{i\prime} T'_{;j} \rangle_{;k} \right)}_{\mathrm{V}} \underbrace{- g^{jk} \left(\mu c_p + \lambda \right) \langle u^{i\prime}_{;j} T'_{;k} \rangle}_{\mathrm{VI}} \\ &\quad \underbrace{- \rho c_p \langle u^i \rangle_{;j} \langle u^{j\prime} T' \rangle - \rho c_p \langle T \rangle_{;j} \langle u^{i\prime} u^{j\prime} \rangle}_{\mathrm{VII}} \end{aligned} \tag{A.4}$$

The underbraced terms are given the interpretation of (I) mean convection, (II) turbulent difusion, (III) pressure diffusion, (IV) correlation of pressure and temperature gradient, (V) molecular diffusion, (VI) dissipation and (VII) production. Equation (A.4) is abbreviated as ($i = r, \varphi, z$)

$$\begin{aligned} c_p \rho \left(\frac{\partial \langle T' u'_i \rangle}{\partial t} + \mathrm{MC}_i + \mathrm{TD}_i \right) & \\ = c_p(-\mathrm{PD}_i + \mathrm{PT}_i) - c_p \rho \mathrm{P}_i + (c_p \mu \mathrm{MD1}_i + \lambda \mathrm{MD2}_i) - (c_p \mu + \lambda) \mathrm{D}_i & \end{aligned} \tag{A.5}$$

and in cylindrical coordinates, the physical components are given by the following terms for $i = r$:

$$\mathrm{MC}_r = \langle u_r \rangle \frac{\partial \langle T' u_r' \rangle}{\partial r} + \frac{\langle u_\varphi \rangle}{r} \frac{\partial \langle T' u_r' \rangle}{\partial \varphi} + \langle u_z \rangle \frac{\partial \langle T' u_r' \rangle}{\partial z} - \frac{\langle u_\varphi \rangle}{r} \langle T' u_\varphi' \rangle \tag{A.6a}$$

$$\mathrm{TD}_r = \frac{1}{r} \frac{\partial r \langle T' u_r' u_r' \rangle}{\partial r} + \frac{1}{r} \frac{\partial \langle T' u_r' u_\varphi' \rangle}{\partial \varphi} + \frac{\partial \langle T' u_r' u_z' \rangle}{\partial z} - \frac{1}{r} \langle T' u_\varphi' u_\varphi' \rangle \tag{A.6b}$$

$$\mathrm{PD}_r = \frac{\partial \langle T' p' \rangle}{\partial r} \tag{A.6c}$$

$$\mathrm{PT}_r = \left\langle p' \frac{\partial T'}{\partial r} \right\rangle \tag{A.6d}$$

$$\begin{aligned} \mathrm{P}_r = {} & \langle T' u_r' \rangle \frac{\partial \langle u_r \rangle}{\partial r} + \frac{\langle T' u_\varphi' \rangle}{r} \left(\frac{\partial \langle u_r \rangle}{\partial \varphi} - \langle u_\varphi \rangle \right) + \langle T' u_z' \rangle \frac{\partial \langle u_r \rangle}{\partial z} \\ & + \langle u_r' u_r' \rangle \frac{\partial \langle T \rangle}{\partial r} + \frac{\langle u_r' u_\varphi' \rangle}{r} \frac{\partial \langle T \rangle}{\partial \varphi} + \langle u_r' u_z' \rangle \frac{\partial \langle T \rangle}{\partial z} \end{aligned} \tag{A.6e}$$

$$\begin{aligned} \mathrm{MD1}_r = {} & \frac{1}{r} \frac{\partial}{\partial r} \left(r \left\langle T' \frac{\partial u_r{}'}{\partial r} \right\rangle \right) - \frac{\langle T' u_r' \rangle}{r^2} + \frac{1}{r^2} \frac{\partial}{\partial \varphi} \left\langle T' \frac{\partial u_r{}'}{\partial \varphi} \right\rangle + \frac{\partial}{\partial z} \left\langle T' \frac{\partial u_r{}'}{\partial z} \right\rangle \\ & - \frac{1}{r^2} \frac{\partial \langle T' u_\varphi' \rangle}{\partial \varphi} - \frac{1}{r^2} \left\langle T' \frac{\partial u_\varphi{}'}{\partial \varphi} \right\rangle \end{aligned} \tag{A.6f}$$

$$\mathrm{MD2}_r = \frac{1}{r} \frac{\partial}{\partial r} \left(r \left\langle u_r' \frac{\partial T'}{\partial r} \right\rangle \right) + \frac{1}{r^2} \frac{\partial}{\partial \varphi} \left\langle u_r' \frac{\partial T'}{\partial \varphi} \right\rangle - \frac{1}{r^2} \left\langle u_\varphi' \frac{\partial T'}{\partial \varphi} \right\rangle + \frac{\partial}{\partial z} \left\langle u_r' \frac{\partial T'}{\partial z} \right\rangle \tag{A.6g}$$

$$\mathrm{D}_r = \left\langle \frac{\partial T'}{\partial r} \frac{\partial u_r{}'}{\partial r} \right\rangle + \frac{1}{r^2} \left\langle \frac{\partial T'}{\partial \varphi} \frac{\partial u_r{}'}{\partial \varphi} \right\rangle - \frac{1}{r^2} \left\langle u_\varphi' \frac{\partial T'}{\partial \varphi} \right\rangle + \left\langle \frac{\partial T'}{\partial z} \frac{\partial u_r{}'}{\partial z} \right\rangle \tag{A.6h}$$

For $i = \varphi$:

$$\mathrm{MC}_\varphi = \langle u_r \rangle \frac{\partial \langle T' u_\varphi' \rangle}{\partial r} + \frac{\langle u_\varphi \rangle}{r} \frac{\partial \langle T' u_\varphi' \rangle}{\partial \varphi} + \langle u_z \rangle \frac{\partial \langle T' u_\varphi' \rangle}{\partial z} + \frac{\langle u_\varphi \rangle}{r} \langle T' u_r' \rangle \tag{A.7a}$$

$$\mathrm{TD}_\varphi = \frac{\partial \langle T' u_r' u_\varphi' \rangle}{\partial r} + \frac{2 \langle T' u_r' u_\varphi' \rangle}{r} + \frac{1}{r} \frac{\partial \langle T' u_\varphi' u_\varphi' \rangle}{\partial \varphi} + \frac{\partial \langle T' u_\varphi' u_z' \rangle}{\partial z} \tag{A.7b}$$

$$\mathrm{PD}_\varphi = \frac{1}{r} \frac{\partial \langle T' p' \rangle}{\partial \varphi} \tag{A.7c}$$

$$\mathrm{PT}_\varphi = \frac{1}{r} \left\langle p' \frac{\partial T'}{\partial \varphi} \right\rangle \tag{A.7d}$$

$$\mathrm{P}_\varphi = \langle T' u_r' \rangle \frac{\partial \langle u_\varphi \rangle}{\partial r} + \frac{\langle T' u_\varphi' \rangle}{r} \left(\frac{\partial \langle u_\varphi \rangle}{\partial \varphi} + \langle u_r \rangle \right) + \langle T' u_z' \rangle \frac{\partial \langle u_\varphi \rangle}{\partial z}$$

$$+ \langle u_r' u_\varphi' \rangle \frac{\partial \langle T \rangle}{\partial r} + \frac{\langle u_\varphi' u_\varphi' \rangle}{r} \frac{\partial \langle T \rangle}{\partial \varphi} + \langle u_\varphi' u_z' \rangle \frac{\partial \langle T \rangle}{\partial z} \tag{A.7e}$$

$$\mathrm{MD1}_\varphi = \frac{1}{r} \frac{\partial}{\partial r} \left(r \left\langle T' \frac{\partial u_\varphi{}'}{\partial r} \right\rangle \right) - \frac{\langle T' u_\varphi' \rangle}{r^2} + \frac{1}{r^2} \frac{\partial}{\partial \varphi} \left\langle T' \frac{\partial u_\varphi{}'}{\partial \varphi} \right\rangle$$

$$+ \frac{1}{r^2} \left\langle T' \frac{\partial u_r{}'}{\partial \varphi} \right\rangle + \frac{1}{r^2} \frac{\partial \langle T' u_r' \rangle}{\partial \varphi} + \frac{\partial}{\partial z} \left\langle T' \frac{\partial u_\varphi{}'}{\partial z} \right\rangle \tag{A.7f}$$

$$\mathrm{MD2}_\varphi = \frac{1}{r} \frac{\partial}{\partial r} \left(r \left\langle u_\varphi' \frac{\partial T'}{\partial r} \right\rangle \right) + \frac{1}{r^2} \frac{\partial}{\partial \varphi} \left\langle u_\varphi' \frac{\partial T'}{\partial \varphi} \right\rangle + \frac{1}{r^2} \left\langle u_r' \frac{\partial T'}{\partial \varphi} \right\rangle + \frac{\partial}{\partial z} \left\langle u_\varphi' \frac{\partial T'}{\partial z} \right\rangle \tag{A.7g}$$

$$\mathrm{D}_\varphi = \left\langle \frac{\partial u_\varphi{}'}{\partial r} \frac{\partial T'}{\partial r} \right\rangle + \frac{1}{r^2} \left\langle u_r' \frac{\partial T'}{\partial \varphi} \right\rangle + \frac{1}{r^2} \left\langle \frac{\partial T'}{\partial \varphi} \frac{\partial u_\varphi{}'}{\partial \varphi} \right\rangle + \left\langle \frac{\partial T'}{\partial z} \frac{\partial u_\varphi{}'}{\partial z} \right\rangle \tag{A.7h}$$

For $i = z$:

$$\mathrm{MC}_z = \langle u_r \rangle \frac{\partial \langle T' u_z' \rangle}{\partial r} + \frac{\langle u_\varphi \rangle}{r} \frac{\partial \langle T' u_z' \rangle}{\partial \varphi} + \langle u_z \rangle \frac{\partial \langle T' u_z' \rangle}{\partial z} \tag{A.8a}$$

$$\mathrm{TD}_z = \frac{1}{r} \frac{\partial r \langle T' u_r' u_z' \rangle}{\partial r} + \frac{1}{r} \frac{\partial \langle T' u_\varphi' u_z' \rangle}{\partial \varphi} + \frac{\partial \langle T' u_z' u_z' \rangle}{\partial z} \tag{A.8b}$$

$$\mathrm{PD}_z = \frac{\partial \langle T' p' \rangle}{\partial z} \tag{A.8c}$$

$$\mathrm{PT}_z = \left\langle p' \frac{\partial T'}{\partial z} \right\rangle \tag{A.8d}$$

$$\mathrm{P}_z = \langle T' u_r' \rangle \frac{\partial \langle u_z \rangle}{\partial r} + \frac{\langle T' u_\varphi' \rangle}{r} \frac{\partial \langle u_z \rangle}{\partial \varphi} + \langle T' u_z' \rangle \frac{\partial \langle u_z \rangle}{\partial z}$$

$$+ \langle u_r' u_z' \rangle \frac{\partial \langle T \rangle}{\partial r} + \frac{\langle u_\varphi' u_z' \rangle}{r} \frac{\partial \langle T \rangle}{\partial \varphi} + \langle u_z' u_z' \rangle \frac{\partial \langle T \rangle}{\partial z} \tag{A.8e}$$

$$\mathrm{MD1}_z = \frac{1}{r} \frac{\partial}{\partial r} \left(r \left\langle T' \frac{\partial u_z{}'}{\partial r} \right\rangle \right) + \frac{1}{r^2} \frac{\partial}{\partial \varphi} \left\langle T' \frac{\partial u_z{}'}{\partial \varphi} \right\rangle + \frac{\partial}{\partial z} \left\langle T' \frac{\partial u_z{}'}{\partial z} \right\rangle \tag{A.8f}$$

$$\mathrm{MD2}_z = \frac{1}{r} \frac{\partial}{\partial r} \left(r \left\langle u_z' \frac{\partial T'}{\partial r} \right\rangle \right) + \frac{1}{r^2} \frac{\partial}{\partial \varphi} \left\langle u_z' \frac{\partial T'}{\partial \varphi} \right\rangle + \frac{\partial}{\partial z} \left\langle u_z' \frac{\partial T'}{\partial z} \right\rangle \tag{A.8g}$$

$$\mathrm{D}_z = \left\langle \frac{\partial T'}{\partial r} \frac{\partial u_z{}'}{\partial r} \right\rangle + \frac{1}{r^2} \left\langle \frac{\partial T'}{\partial \varphi} \frac{\partial u_z{}'}{\partial \varphi} \right\rangle + \left\langle \frac{\partial T'}{\partial z} \frac{\partial u_z{}'}{\partial z} \right\rangle \tag{A.8h}$$

The equation for the temperature variance follows in a similar way from $2\langle(\text{A.3c}) \cdot T'\rangle$:

$$\rho c_p \left(\frac{\partial \langle T' T' \rangle}{\partial t} + \langle u^j \rangle \langle T' T' \rangle_{;j} + \langle u^{j\prime} T' T' \rangle_{;j} \right)$$

$$= g^{ij}\lambda\langle T'T'\rangle_{;ij} - 2g^{ij}\lambda\langle T'_{;i}T'_{;j}\rangle - 2\rho c_p\langle T\rangle_{;j}\langle u^{j\prime}T'\rangle \quad \text{(A.9)}$$

where the terms are abbreviated according to

$$c_p\rho\left(\frac{\partial\langle T'T'\rangle}{\partial t} + \mathrm{MC}_{T'T'} + \mathrm{TD}_{T'T'}\right) = \lambda\mathrm{MD}_{T'T'} - 2\lambda\mathrm{D}_{T'T'} - 2c_p\rho\mathrm{P}_{T'T'} \quad \text{(A.10)}$$

where

$$\mathrm{MC}_{T'T'} = \langle u_r\rangle\frac{\partial\langle T'T'\rangle}{\partial r} + \frac{\langle u_\varphi\rangle}{r}\frac{\partial\langle T'T'\rangle}{\partial\varphi} + \langle u_z\rangle\frac{\partial\langle T'T'\rangle}{\partial z} \quad \text{(A.11a)}$$

$$\mathrm{TD}_{T'T'} = \frac{1}{r}\frac{\partial r\langle T'T'u'_r\rangle}{\partial r} + \frac{1}{r}\frac{\partial\langle T'T'u'_\varphi\rangle}{\partial\varphi} + \frac{\partial\langle T'T'u'_z\rangle}{\partial z} \quad \text{(A.11b)}$$

$$\mathrm{MD}_{T'T'} = \frac{1}{r}\frac{\partial}{\partial r}\left(r\frac{\partial\langle T'T'\rangle}{\partial r}\right) + \frac{1}{r^2}\frac{\partial^2\langle T'T'\rangle}{\partial\varphi^2} + \frac{\partial^2\langle T'T'\rangle}{\partial z^2} \quad \text{(A.11c)}$$

$$\mathrm{D}_{T'T'} = \left\langle\frac{\partial T'}{\partial r}\frac{\partial T'}{\partial r}\right\rangle + \frac{1}{r^2}\left\langle\frac{\partial T'}{\partial\varphi}\frac{\partial T'}{\partial\varphi}\right\rangle + \left\langle\frac{\partial T'}{\partial z}\frac{\partial T'}{\partial z}\right\rangle \quad \text{(A.11d)}$$

$$\mathrm{P}_{T'T'} = \langle T'u'_r\rangle\frac{\partial\langle T\rangle}{\partial r} + \frac{\langle T'u'_\varphi\rangle}{r}\frac{\partial\langle T\rangle}{\partial\varphi} + \langle T'u'_z\rangle\frac{\partial\langle T\rangle}{\partial z} \quad \text{(A.11e)}$$

Turbulent heat flux models such as Nagano and Shimada (1996) and Manservisi and Menghini (2014) include a balance equation for the dissipation of $k_\theta = \frac{1}{2}\langle T'T'\rangle$. In general tensor notation, this balance follows from $\langle(\text{A.3c})_{;k}\cdot T'_{;l} + (\text{A.3c})_{;l}\cdot T'_{;k}\rangle$:

$$\underbrace{\frac{\partial\langle T'_{;k}T'_{;l}\rangle}{\partial t}}_{\mathrm{I}} + \underbrace{\langle u^j\rangle\langle T'_{;k}T'_{;l}\rangle_{;j}}_{\mathrm{II}} = \underbrace{\frac{\lambda g^{ij}}{\rho c_p}\langle T'_{;k}T'_{;l}\rangle_{;ji}}_{\mathrm{III}} \underbrace{-\langle u^{j\prime}T'_{;k}T'_{;l}\rangle_{;j}}_{\mathrm{IV}} \underbrace{-\langle T\rangle_{;j}\left(\langle u^{j\prime}_{;l}T'_{;k}\rangle + \langle u^{j\prime}_{;k}T'_{;l}\rangle\right)}_{\mathrm{V}}$$
$$+ \underbrace{\langle u^j\rangle_{;k}\langle T'_{;j}T'_{;l}\rangle + \langle u^j\rangle_{;l}\langle T'_{;j}T'_{;k}\rangle}_{\mathrm{VI}} \underbrace{-\left(\langle T\rangle_{;jl}\langle u^{j\prime}T'_{;k}\rangle + \langle T\rangle_{;jk}\langle u^{j\prime}T'_{;l}\rangle\right)}_{\mathrm{VIb}}$$
$$+ \underbrace{\langle u^{j\prime}_{;k}T'_{;j}T'_{;l}\rangle + \langle u^{j\prime}_{;l}T'_{;j}T'_{;k}\rangle}_{\mathrm{VII}} \underbrace{-2\frac{\lambda g^{ij}}{\rho c_p}\langle T'_{;li}T'_{;kj}\rangle}_{\mathrm{VIII}} + \underbrace{\frac{\lambda}{\rho c_p}\left(R_l{}^m\langle T'_{;m}T'_{;k}\rangle + \langle R_k{}^m T'_{;m}T'_{;l}\rangle\right)}_{\text{curvature term}} \quad \text{(A.12)}$$

The terms are labelled according to Mantel and Borghi (1994). They represent "(I) accumulation (I), convection (II), molecular diffusion (III), turbulent diffusion (IV), production by mean concentration gradients (V), production by mean velocity gradients (VI), production by curvature of the mean concentration field (VIb), production by stretching of the concentration field by the turbulent strain field (VII) [and] molecular dissipation (VIII)" (Mantel and Borghi 1994, p. 445). The curvature term includes the Ricci tensor R; it is zero in flat space and hence vanishes for cylindrical or Cartesian coordinates. After contraction with g^{kl} the individual components of the equation in cylindrical coordinates follow as:

$$g^{kl}\langle u^j\rangle\langle T'_{;k}T'_{;l}\rangle_{;j} = \langle u_r\rangle\frac{\partial}{\partial r}\mathrm{D}_{T'T'} + \frac{\langle u_\varphi\rangle}{r}\frac{\partial}{\partial\varphi}\mathrm{D}_{T'T'} + \langle u_z\rangle\frac{\partial}{\partial z}\mathrm{D}_{T'T'} \tag{A.13a}$$

$$g^{kl}g^{ij}\langle T'_{;k}T'_{;l}\rangle_{;ji} = \frac{1}{r}\frac{\partial}{\partial r}\left(r\frac{\partial}{\partial r}\mathrm{D}_{T'T'}\right) + \frac{1}{r^2}\frac{\partial^2}{\partial\varphi^2}\mathrm{D}_{T'T'} + \frac{\partial^2}{\partial z^2}\mathrm{D}_{T'T'} \tag{A.13b}$$

$$\begin{aligned} g^{kl}\langle u^{j\prime}T'_{;k}T'_{;l}\rangle_{;j} = {} & \frac{1}{r}\frac{\partial}{\partial r}\left(r\left\langle u'_r\frac{\partial T'}{\partial r}\frac{\partial T'}{\partial r}\right\rangle\right) + \frac{1}{r^2}\frac{\partial}{\partial r}\left\langle u'_r\frac{\partial T'}{\partial\varphi}\frac{\partial T'}{\partial\varphi}\right\rangle + \frac{1}{r}\frac{\partial}{\partial r}\left(r\left\langle u'_r\frac{\partial T'}{\partial z}\frac{\partial T'}{\partial z}\right\rangle\right) \\ & + \frac{\partial}{\partial z}\left\langle u'_z\frac{\partial T'}{\partial r}\frac{\partial T'}{\partial r}\right\rangle + \frac{1}{r^2}\frac{\partial}{\partial z}\left\langle u'_z\frac{\partial T'}{\partial\varphi}\frac{\partial T'}{\partial\varphi}\right\rangle + \frac{\partial}{\partial z}\left\langle u'_z\frac{\partial T'}{\partial z}\frac{\partial T'}{\partial z}\right\rangle \\ & + \frac{\partial}{\partial\varphi}\left(\frac{1}{r}\left\langle u'_\varphi\frac{\partial T'}{\partial r}\frac{\partial T'}{\partial r}\right\rangle + \frac{1}{r^3}\left\langle u'_\varphi\frac{\partial T'}{\partial\varphi}\frac{\partial T'}{\partial\varphi}\right\rangle + \frac{1}{r}\left\langle u'_\varphi\frac{\partial T'}{\partial z}\frac{\partial T'}{\partial z}\right\rangle\right) \\ & - \frac{1}{r^3}\left\langle u'_r\frac{\partial T'}{\partial\varphi}\frac{\partial T'}{\partial\varphi}\right\rangle \end{aligned} \tag{A.13c}$$

$$g^{kl}\langle T\rangle_{;j}\langle u^{j\prime}_{;l}T'_{;k}\rangle = \mathrm{D}_r\frac{\partial\langle T\rangle}{\partial r} + \frac{\mathrm{D}_\varphi}{r}\frac{\partial\langle T\rangle}{\partial\varphi} + \mathrm{D}_z\frac{\partial T}{\partial z} \tag{A.13d}$$

$$\begin{aligned} g^{kl}\langle u^j\rangle_{;k}\langle T'_{;j}T'_{;l}\rangle = {} & \left\langle\frac{\partial T'}{\partial r}\frac{\partial T'}{\partial r}\right\rangle\frac{\partial\langle u_r\rangle}{\partial r} + \frac{1}{r}\left\langle\frac{\partial T'}{\partial r}\frac{\partial T'}{\partial\varphi}\right\rangle\left(\frac{1}{r}\frac{\partial\langle u_r\rangle}{\partial\varphi} + \frac{\partial\langle u_\varphi\rangle}{\partial r} - \frac{1}{r}\langle u_\varphi\rangle\right) \\ & + \left\langle\frac{\partial T'}{\partial r}\frac{\partial T'}{\partial z}\right\rangle\left(\frac{\partial\langle u_r\rangle}{\partial z} + \frac{\partial\langle u_z\rangle}{\partial r}\right) \\ & + \frac{1}{r^3}\left\langle\frac{\partial T'}{\partial\varphi}\frac{\partial T'}{\partial\varphi}\right\rangle\left(\frac{\partial\langle u_\varphi\rangle}{\partial\varphi} + \langle u_r\rangle\right) \\ & + \frac{1}{r}\left\langle\frac{\partial T'}{\partial\varphi}\frac{\partial T'}{\partial z}\right\rangle\left(\frac{1}{r}\frac{\partial\langle u_z\rangle}{\partial\varphi} + \frac{\partial\langle u_\varphi\rangle}{\partial z}\right) + \left\langle\frac{\partial T'}{\partial z}\frac{\partial T'}{\partial z}\right\rangle\frac{\partial\langle u_z\rangle}{\partial z} \end{aligned} \tag{A.13e}$$

$$\begin{aligned} g^{kl}\langle T\rangle_{;jl}\langle u^{j\prime}T'_{;k}\rangle = {} & \left\langle u'_r\frac{\partial T'}{\partial r}\right\rangle\frac{\partial^2\langle T\rangle}{\partial r^2} + \frac{1}{r}\left\langle u'_r\frac{\partial T'}{\partial\varphi}\right\rangle\frac{\partial}{\partial r}\left(\frac{1}{r}\frac{\partial\langle T\rangle}{\partial\varphi}\right) + \left\langle u'_r\frac{\partial T'}{\partial z}\right\rangle\frac{\partial^2\langle T\rangle}{\partial r\partial z} \\ & + \left\langle u'_\varphi\frac{\partial T'}{\partial r}\right\rangle\frac{\partial}{\partial r}\left(\frac{1}{r}\frac{\partial\langle T\rangle}{\partial\varphi}\right) + \frac{1}{r^2}\left\langle u'_\varphi\frac{\partial T'}{\partial\varphi}\right\rangle\left(\frac{1}{r}\frac{\partial^2\langle T\rangle}{\partial\varphi^2} + \frac{\partial\langle T\rangle}{\partial r}\right) \\ & + \frac{1}{r}\left\langle u'_\varphi\frac{\partial T'}{\partial z}\right\rangle\frac{\partial^2\langle T\rangle}{\partial\varphi\partial z} + \left\langle u'_z\frac{\partial T'}{\partial r}\right\rangle\frac{\partial^2\langle T\rangle}{\partial r\partial z} \end{aligned}$$

$$+\frac{1}{r^2}\left\langle u_z' \frac{\partial T'}{\partial \varphi}\right\rangle \frac{\partial^2 \langle T\rangle}{\partial \varphi \partial z} + \left\langle u_z' \frac{\partial T'}{\partial z}\right\rangle \frac{\partial^2 \langle T\rangle}{\partial z^2} \tag{A.13f}$$

$$\begin{aligned} g^{kl}\langle u^{j\prime}_{;k} T'_{;j} T'_{;l}\rangle = & \left\langle \frac{\partial T'}{\partial r}\frac{\partial T'}{\partial r}\frac{\partial u_r{}'}{\partial r}\right\rangle + \frac{1}{r^2}\left\langle \frac{\partial T'}{\partial r}\frac{\partial T'}{\partial \varphi}\frac{\partial u_r{}'}{\partial \varphi}\right\rangle + \frac{1}{r^3}\left\langle \frac{\partial T'}{\partial \varphi}\frac{\partial T'}{\partial \varphi} u_r'\right\rangle \\ & + \left\langle \frac{\partial T'}{\partial r}\frac{\partial T'}{\partial z}\frac{\partial u_r{}'}{\partial z}\right\rangle + \frac{1}{r}\left\langle \frac{\partial u_\varphi{}'}{\partial r}\frac{\partial T'}{\partial r}\frac{\partial T'}{\partial \varphi}\right\rangle - \frac{1}{r^2}\left\langle u_\varphi' \frac{\partial T'}{\partial r}\frac{\partial T'}{\partial \varphi}\right\rangle \\ & + \frac{1}{r^3}\left\langle \frac{\partial T'}{\partial \varphi}\frac{\partial T'}{\partial \varphi}\frac{\partial u_\varphi{}'}{\partial \varphi}\right\rangle + \frac{1}{r}\left\langle \frac{\partial T'}{\partial \varphi}\frac{\partial T'}{\partial z}\frac{\partial u_\varphi{}'}{\partial z}\right\rangle + \left\langle \frac{\partial T'}{\partial r}\frac{\partial T'}{\partial z}\frac{\partial u_z{}'}{\partial r}\right\rangle \\ & + \frac{\left\langle \frac{\partial T'}{\partial \varphi}\frac{\partial T'}{\partial z}\frac{\partial u_z{}'}{\partial \varphi}\right\rangle}{r^2} + \left\langle \frac{\partial T'}{\partial z}\frac{\partial T'}{\partial z}\frac{\partial u_z{}'}{\partial z}\right\rangle \end{aligned} \tag{A.13g}$$

$$\begin{aligned} g^{kl}g^{ij}\langle T'_{;li} T'_{;kj}\rangle = & \left\langle \frac{\partial^2 T'}{\partial r^2}\frac{\partial^2 T'}{\partial r^2}\right\rangle + \frac{1}{r^2}\left\langle \frac{\partial T'}{\partial r}\frac{\partial T'}{\partial r}\right\rangle + \frac{2}{r^3}\left\langle \frac{\partial T'}{\partial r}\frac{\partial^2 T'}{\partial \varphi^2}\right\rangle \\ & + \frac{2}{r^2}\left\langle \frac{\partial^2 T}{\partial r \partial \varphi}' \frac{\partial^2 T}{\partial r \partial \varphi}'\right\rangle - \frac{4}{r^3}\left\langle \frac{\partial T'}{\partial \varphi}\frac{\partial^2 T}{\partial r \partial \varphi}'\right\rangle + 2\left\langle \frac{\partial^2 T}{\partial r \partial z}'\frac{\partial^2 T}{\partial r \partial z}'\right\rangle \\ & + \frac{1}{r^4}\left\langle \frac{\partial^2 T'}{\partial \varphi^2}\frac{\partial^2 T'}{\partial \varphi^2}\right\rangle + \frac{2}{r^4}\left\langle \frac{\partial T'}{\partial \varphi}\frac{\partial T'}{\partial \varphi}\right\rangle + \frac{2}{r^2}\left\langle \frac{\partial^2 T}{\partial \varphi \partial z}'\frac{\partial^2 T}{\partial \varphi \partial z}'\right\rangle \\ & + \left\langle \frac{\partial^2 T'}{\partial z^2}\frac{\partial^2 T'}{\partial z^2}\right\rangle \end{aligned} \tag{A.13h}$$

A.2 Extension of wide-strip limit to heat transfer

In this section, the wide-strip limit derived in section 3.2.1 is extended to heat transfer [NSGF25]. For the transport of a passive scalar, a local equilibrium limit expression for the global Nusselt number, similar to eq. (3.3), can be derived. Here, this derivation is shown exemplarily for laminar flow over streamwise-aligned ridges, see fig. 3.4. The analysis is possible in a similar fashion for turbulent flow or inhomogeneous wall roughness; however, such an attempt is not made because of the lack of experimental or numerical reference data.

As for pipe flow (cf. section 4.4), different boundary conditions can be chosen. For simplicity, the mixed boundary condition is selected, defined in the same way as for pipe flow (see Kasagi et al. (1992)), i.e. the temperature equation is forced proportionally to u_x, where the proportionality constant is determined by a global energy balance, and homogeneous Dirichlet conditions apply at the wall.

The dimensional steady-state temperature equation (eq. (2.7)) for fully developed laminar flow in x direction is given by

$$\rho c_p u_x \frac{\partial T}{\partial x} = \lambda \left(\frac{\partial^2 T}{\partial y^2} + \frac{\partial^2 T}{\partial z^2} \right). \tag{A.14}$$

In particular, the streamwise gradient of temperature must be identical everywhere. Under fully developed laminar conditions, the temperature profile for a channel with half-height h is given by Shah and London (1978) as

$$T(y) = T_w - \frac{3}{2} \frac{q}{h\lambda} \left(\frac{5}{12} h^2 - \frac{y^2}{2} + \frac{y^4}{12h^2} \right), \tag{A.15}$$

where q and T_w are the heat flux density and wall temperature, respectively. A suitable Nusselt number definition is presented by Shah and London (1978) as

$$\mathrm{Nu} = \frac{qD_h}{k(T_w - T_b)} = \frac{qD_h}{k} \left(T_w - \frac{\int_A T u_x \mathrm{d}A}{\int_A u_x \mathrm{d}A} \right)^{-1}, \tag{A.16}$$

with the classical hydraulic diameter $D_h = 4A/P$, four times the ratio of cross-sectional area and perimeter of the profile. In the wide-strip limit, we expect the profile given by eq. (A.15) to be obtained in a piecewise sense. The heat flux density q can be computed from a global energy balance: the total convective flux balances the total heat flux over the wall, and the streamwise temperature gradient is the same in both regions. The

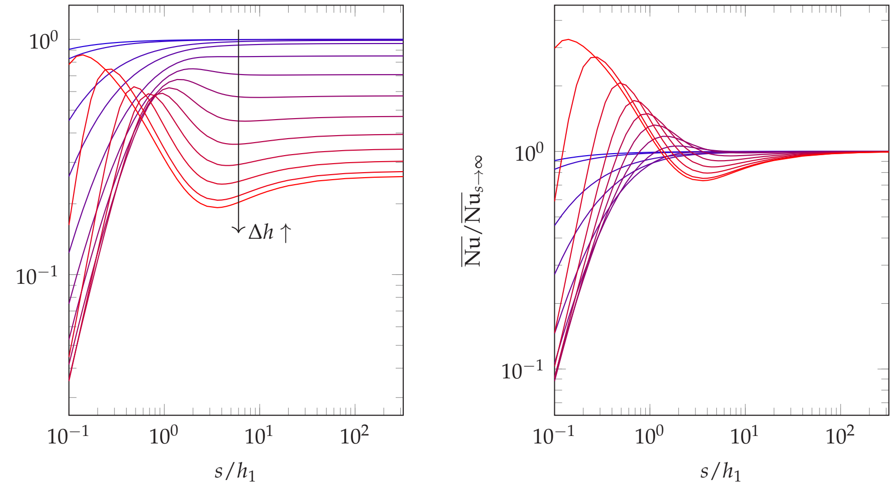

Figure A.1: Nusselt number normalised with the value of the flat-plate channel (a), as well as Nusselt number normalised with the wide-strip limit (b), see eq. (A.17), for laminar flow over streamwise-aligned ridges. Displayed are $\Delta h/h_1 = 0.001, 0.005, 0.01, 0.05, 0.1, 0.2, ..., 0.9, 0.095$, ranging from blue to red.

integrals in eq. (A.16) are readily obtained from the assumed profile in both regions. We finally obtain the wide-strip limit of the Nusselt number for laminar flow as

$$\overline{\mathrm{Nu}}_{s\to\infty} = \frac{140}{17}\frac{(h_1+h_2)(h_1^3+h_2^3)^2}{4(h_1^7+h_2^7)}. \tag{A.17}$$

The canonical value of $140/17 \approx 8.235$ (Shah and London 1978) for the flat-plate channel is recovered for $h_1 = h_2$.

Figure A.1a displays the Nusselt number, as defined by eq. (A.16), obtained from laminar, body-fitted OpenFOAM simulations, as a function of strip size s and the height ratio $\Delta h/h_1 = (h_2 - h_1)/h_1$. Figure A.1b displays the Nusselt number normalised with the wide-strip limit for each Δh according to eq. (A.17). While the full picture is more complex than for the streamwise momentum (see fig. 3.5), we observe that, for all height ratios, the wide-strip limit correctly captures the behaviour for large s, and the deviation from the wide-strip limit generally increases with $\Delta h/h_1$. [NSGF25]

A.3 Properties of $\mathcal{L}_k$

Let $\mathcal{D} := \{\varphi \in H^2((0,1)), \varphi'(1) = 0\}$. Here, the boundary condition is to be understood in the sense of the Sobolev trace. We equip $\mathcal{D}$ with the inner product defined by eq. (4.60). Then, for all k, the operator $\mathcal{L}_k$ is self-adjoint on $\mathcal{D}$ as can be shown by means of partial integration, i.e.

$$\begin{aligned}
\langle \mathcal{L}_k u, v\rangle - \langle u, \mathcal{L}_k v\rangle &= \int_0^1 (ru')'v - \frac{k^2}{r}uv - (rv')'u + \frac{k^2}{r}uv\mathrm{d}r \\
&= \int_0^1 (ru')'v - (rv')'u\mathrm{d}r \\
&= \left[(ru')v - (rv')u\right]_0^1 - \int_0^1 (ru')v' - (rv')u'\mathrm{d}r \\
&= u'(1)v(1) - v'(1)u(1) \\
&= 0.
\end{aligned} \tag{A.18}$$

Moreover, for $k \neq 0$, the operator is negative definite, since

$$\begin{aligned}
\langle \mathcal{L}_k u, u\rangle &= \int_0^1 (ru')'u - \frac{k^2}{r}u^2\mathrm{d}r \\
&= \left[ru'u\right]_0^1 - \int_0^1 r(u')^2 - \int_0^1 \frac{k^2}{r}u^2\mathrm{d}r \\
&= -\int_0^1 r(u')^2 - \int_0^1 \frac{k^2}{r}u^2\mathrm{d}r.
\end{aligned} \tag{A.19}$$

[NMGF25] For $k \neq 0$, this expression is strictly negative unless $u \equiv 0$. In particular, all eigenvalues must be negative. For $k = 0$, the function $\varphi \equiv 2$ is a (normalised) eigenvector corresponding to $\lambda = 0$. Hence, the operator is only negative semi-definite.